UDK 621.3:(53+54+621+66)(05)(497.1)=00 ISSN 0352-9045

INFORMACIJE MIDEM

Strokovno društvo za mikroelektroniko elektronske sestavne dele in materiale

3°2011

Strokovna revija za mikroelektroniko, elektronske sestavne dele in materiale
Journal of Microelectronics, Electronic Components and Materials

INFORMACIJE MIDEM, LETNIK 41, ŠT. 3(139), LJUBLJANA, september 2011

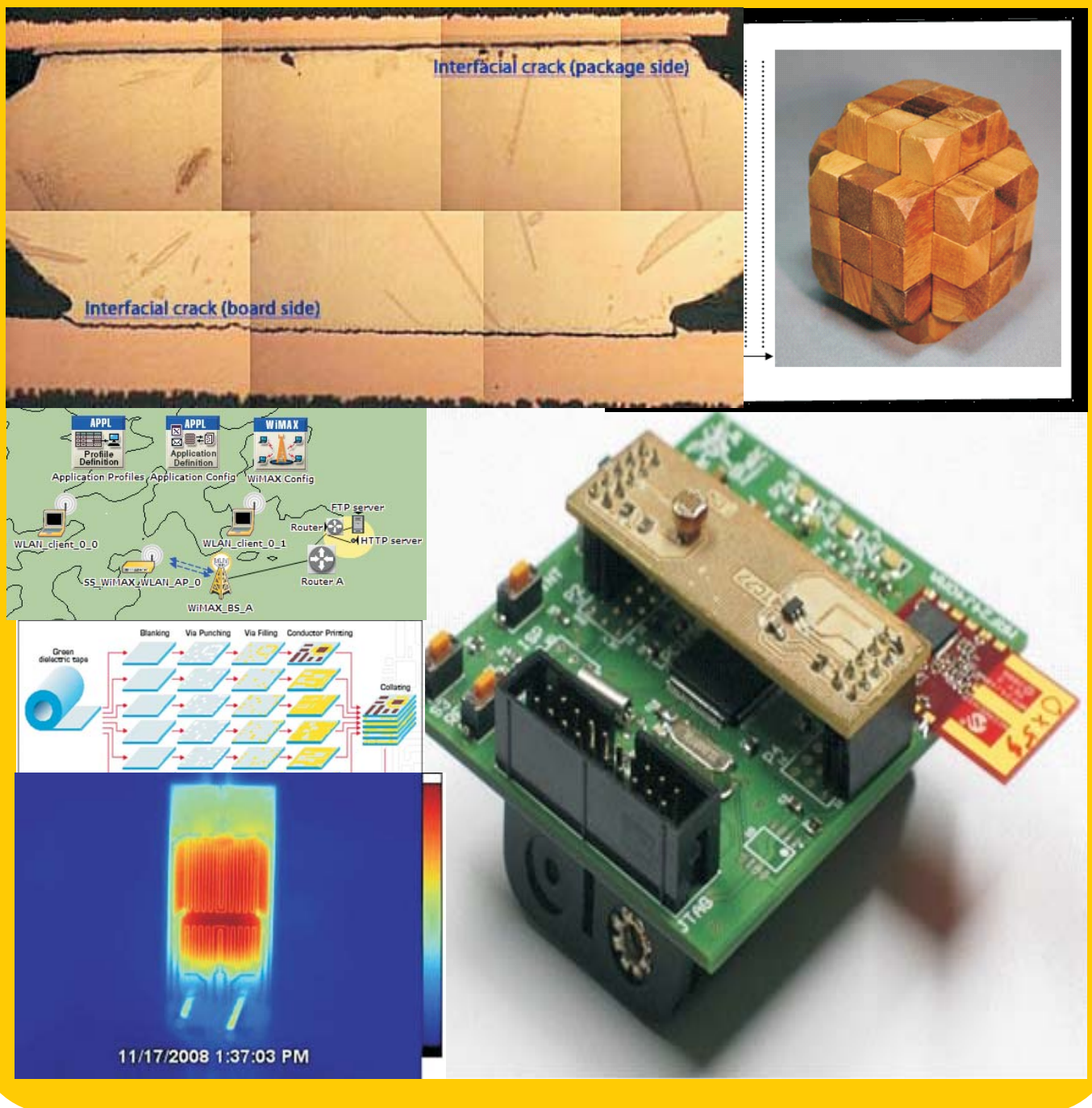

UDK 621.3:(53+54+621+66)(05)(497.1)=00 ISSN 0352-9045

INFORMACIJE MIDEM 2 0 2011

INFORMACIJE MIDEM LETNIK 41, ŠT. 2(138), LJUBLJANA, JUNIJ 2011
INFORMACIJE MIDEM VOLUME 41, NO. 2(138), LJUBLJANA, JUNE 2011

Revija izhaja trimesečno (marec, junij, september, december). Izdaja strokovno društvo za mikroelektroniko, elektronske sestavne dele in materiale - MIDEM.
Published quarterly (march, june, september, december) by Society for Microelectronics, Electronic Components and Materials - MIDEM.

Naslov uredništva
Headquarters
Uredništvo Informacije MIDEM
MIDEM pri MIKROIKS
Stegne 11, 1521 Ljubljana, Slovenija
tel.: + 386 (0)1 51 33 768
faks: + 386 (0)1 51 33 771
e-pošta: Iztok.Sorli@guest.arnes.si
http://www.midem-drustvo.si/

Letna naročnina je 100 EUR, cena posamezne številke pa 25 EUR. Člani in sponzorji MIDEM prejemajo Informacije MIDEM brezplačno.
Annual subscription rate is EUR 100, separate issue is EUR 25. MIDEM members and Society sponsors receive Informacije MIDEM for free.

Znanstveni svet za tehnične vede je podal pozitivno mnenje o reviji kot znanstveno-strokovni reviji za mikroelektroniko, elektronske sestavne dele in materiale. Izdajo revije sofinancirajo JAKRS in sponzorji društva.
Scientific Council for Technical Sciences of Slovene Research Agency has recognized Informacije MIDEM as scientific Journal for microelectronics, electronic components and materials.
Publishing of the Journal is financed by Slovenian Book Agency and by Society sponsors.

Znanstveno-strokovne prispevke objavljene v Informacijah MIDEM zajemamo v podatkovne baze COBISS in INSPEC.

Prispevke iz revije zajema ISI® v naslednje svoje produkte: Sci Search®, Research Alert® in Materials Science Citation Index™

Scientific and professional papers published in Informacije MIDEM are assessed into COBISS and INSPEC databases.

The Journal is indexed by ISI® for Sci Search®, Research Alert® and Material Science Citation Index™

Po mnenju Ministrstva za informiranje št.23/300-92 šteje glasilo Informacije MIDEM med proizvode informativnega značaja.

Grafična priprava in tisk
Printed by
BIRO M, Ljubljana

Naklada
Circulation
1000 izvodov
1000 issues

Poštnina plačana pri pošti 1102 Ljubljana
Slovenia Taxe Percue

UDK621.3:(53+54+621+66), ISSN0352-9045 Informacije MIDEM 41(2011)3, Ljubljana

Obnovitev članstva v strokovnem društvu MIDEM in iz tega izhajajoče ugodnosti in obveznosti

Spoštovani,

V svojem več desetletij dolgem obstoju in delovanju smo si prizadevali narediti društvo privlačno in koristno vsem članom.Z delovanjem društva ste se srečali tudi vi in se odločili, da se v društvo včlanite. Življenske poti, zaposlitev in strokovno zanimanje pa se z leti spreminjajo, najrazličnejši dogodki, izzivi in odločitve so vas morda usmerili v povsem druga področja in vaš interes za delovanje ali članstvo v društvu se je z leti močno spremenil, morda izginil. Morda pa vas aktivnosti društva kljub temu še vedno zanimajo, če ne drugače, kot spomin na prijetne čase, ki smo jih skupaj preživeli. Spremenili so se tudi naslovi in način komuniciranja.

Ker je seznam članstva postal dolg, očitno pa je, da mnogi nekdanji člani nimajo več interesa za sodelovanje v društvu, se je Izvršilni odbor društva odločil, da stanje članstva uredi in **vas zato prosi, da izpolnite in nam pošljete obrazec priložen na koncu revije.**

Naj vas ponovno spomnimo na ugodnosti, ki izhajajo iz vašega članstva. Kot član strokovnega društva prejemate revijo »Informacije MIDEM«, povabljeni ste na strokovne konference, kjer lahko predstavite svoje raziskovalne in razvojne dosežke ali srečate stare znance in nove, povabljene predavatelje s področja, ki vas zanima. O svojih dosežkih in problemih lahko poročate v strokovni reviji, ki ima ugleden IMPACT faktor. S svojimi predlogi lahko usmerjate delovanje društva.

Vaša obveza je plačilo članarine 25 EUR na leto. Članarino lahko plačate na transakcijski račun društva pri A-banki: 051008010631192. Pri nakazilu ne pozabite navesti svojega imena!

Upamo, da vas delovanje društva še vedno zanima in da boste članstvo obnovili. Žal pa bomo morali dosedanje člane, ki članstva ne boste obnovili do konca leta 2011, brisati iz seznama članstva.

Prijavnice pošljite na naslov:

MIDEM pri MIKROIKS

Stegne 11

1521 Ljubljana

Ljubljana, september 2011

Izvršilni odbor društva

EFFECT OF DANGLING BONDS ON TRANSIENT RESPONSE OF P-I-N A-SI:H PHOTODIODE

Vera Gradišnik, Antonio Linić and Mladen Šverko

Faculty of Engineering, University of Rijeka, Croatia

Key words: Amorphous silicon, transient response, trapping and recombination, photodiode

Abstract: The transient photocurrent of a-Si:H p-i-n photodiode as a three-color detector under simultaneously pulsed visible light illumination and forward voltage pulse at low reverse bias voltage and low frequency conditions were studied. The characteristic transient response properties are attributed to the effect of the spatial distribution of defect states in the i-layer. They act temporally as recombination or generation centers. The results are useful in directing further investigation of the observed effect regard light illumination energy with application in color sensor in an active pixel sensor.

Vpliv bingljajočih vezi na odziv p-i-n a-Si:H fotodiode

Kjučne besede: amorfni silicij, prehodni pojav, zajem in rekombinacija, fotodioda

Izvleček: V prispevku preučujemo nizkofrekvenčni prehodni odziv a-Si:H p-i-n fotodiode kot tribarvnega detektorja pri reverzni napetosti, osvetlitvi s pulzno vidno svetlobo in pulzni napetosti v prevodni smeri. Karakteristični prehodni odziv smo pripisali prostorski porazdelitvi energijskih stanj defektov v i-plasti. Le-te delujejo hkrati kot generacijski in rekombinacijski centri. Rezultati služijo kot smernica za nadaljnje raziskave vpliva energije svetlobe pri preučevanju barvnih senzorjev v aktivni matriki svetlobnih senzorjev

1. Introduction

Hydrogenated amorphous silicon (a-Si:H) p-i-n photodiodes are important for photodetection in imaging sensors. The reverse current-voltage characteristic is controlled by thermal emission of hole-electron pairs from deep states and can give useful information about the mid-gap states and their spatial distribution in the i-layer. The dark current mainly arises from thermal generation in i-layer and emission of carriers from the p-i and i-n interfaces. There is a significant voltage dependency of the steady-state thermal generation current at low biases. The transient dark current and steady-state thermal generation current which give useful information about the mid-gap states and their spatial distribution in i-layer and at p^+-i interface are well documented /1-2/. Models of recombination and transport through localized states have also been well described by Fuhs /3/ and Dhariwal et al. /4-6/.

The signal shapes as a function of bias potential were analyzed in terms of mobilities and mean free paths of the electron and holes in amorphous silicon p-i-n detector response to a range of photon radiation /7/. It is important to have detailed information on the localized electronic states in a-Si:H to understand optical and electronic properties as the contribution of dangling bonds as the main recombination centers and their determination of transient current is relevant for device application. The influence of deeply-trapped charge on the transient photocurrent responses /8/, transient photocurrent spectroscopy /9/, has been studied by various authors using the transient photocurrent method TPC /10/ and the AC and DC constant photocurrent method CPM /10-12/. As Fuhs describes, /3/ transport and recombination mechanisms in low-temperature regime with the kinetics of carrier recombination is characterized by a broad distribution of lifetimes. For hopping conduction in photoconductivity, strong electric fields play a similar role to the temperature.

The responses of a-Si:H three-colour detectors have previously been described /13-15/. The characteristic transient response shapes as a response to the simultaneous forward voltage and visible light pulses are described. Under the assumption that the response is controlled by multi-trapping processes, the energy levels of trap states are determined from transit time using least-squares fitting techniques. Shen /16/ describes the response time includes the time that an electron spends in the extended states and the residence time in traps.

In this paper analysis of observed effect of dangling bond on transient response of p-i-n a-Si:H photodiode at simultaneously forward voltage and light pulse of visible light at low reverse bias and low frequency is presented. The model employed is an extension of the model of recombination proposed by Dhariwal and Rajvanshi /4, 5/ and the interpretation of transient response and methods for determination of defect densities proposed by Main et al. /10, 11/. Our results describe the effect of dangling bonds on transient response on concurrent forward voltage and light pulses of a-Si:H p-i-n photodiode at low reverse voltages. Their influence on space charge density and recombination rates are distributed in time and therefore analyzed through photocurrent transients. In-depth analysis, with respect to the energy of absorbed light, will be completed in future work.

After a description of the theory with used model in Section 2, a short recapitulation of the experiment follows in Section 3. The results and discussion are presented in Section 4 and finally the conclusions.

2. Model description

The characteristic shapes of transient response on simultaneous voltage and light pulses at low reverse bias voltage of amorphous silicon p-i-n photodiode have already been observed /13-15/. The densities of localized states (DOS) in the energy gap determine most of electronic properties. Their temporal activity as recombination centers is the cause of the observed characteristic response shapes

In a-Si:H, disorder causes the tails of localized states which extend deep into the energy gap. The localized and extended states are separated by a mobility gap. Unsaturated silicon bonds (Si dangling bonds), which are structural defects introduce additional deep electronic states. The non-radiative transition by tunneling of band-tail carriers to dangling-bond states is a dominant factor in the mobility gap. The proposed model by Dhariwal et al. /4-6/ of recombination statistic through dangling bonds include dangling bonds in the analysis and compare the relative contribution of tail states and dangling bonds in the recombination mechanism and the formation of the space charge region. They characterize the excitation of a semiconductor by an np product

$$np = n_i^2 e^{\frac{qU_A}{kT}} \tag{1}$$

where n and p are the concentration of free electrons and holes respectively, ni is the intrinsic carrier concentration and U_A the applied voltage. It is assumed that the dangling bonds have two energy states at fixed energies with respect to the conduction band and valence band. The effect of their statistical broadening has been neglected. The band tail states are exponential in nature and the quasi-equilibrium between the localized and free carriers separately for conduction and valance band has been assumed in their model.

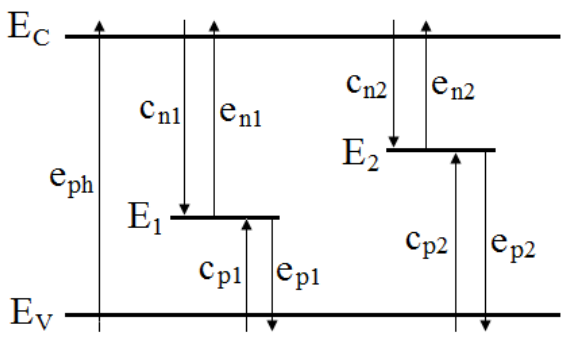

Fig. 1 Transition probabilities for capture and emission of free carriers at dangling bond states according to model described in /4/.

There are three charge states of dangling bonds: positive, D^+, negative, D^- and neutral, D^0. The transitions occur at correlated energy states with energy E_1 and E_2 from the valence band edge, E_V shown in Figure1

From the equations for net capture rates for electrons and holes at two correlated bond states and occupation probabilities for the three charge states in steady state the recombination rate in steady state is

$$R = N_{db}\left(U_{n1} + U_{n2}\right) = N_{db}\left(U_{p1} + U_{p2}\right) \tag{2}$$

or

$$R = N_{db} \cdot f^0 \left[nc_{n1}\left(\frac{pc_{p1} + n_1 c_{n1}}{nc_{n1} + p_1 c_{p1}}\right) + nc_{n2} - n_1 c_{n1} - n_2 c_{n2}\left(\frac{nc_{n2} + p_2 c_{p2}}{pc_{p2} + n_2 c_{n2}}\right)\right] \tag{3}$$

where N_{db} is concentration of dangling bond and is 10^{16} cm^{-3}; n, p free carrier concentrations of electrons and holes; n1, p1, n2, p2 concentrations of electrons and holes at energy levels E_1 and E_2, respectively; c_{p1}, c_{p2}, c_{n1}, c_{n2} equal to 10^{-9} cm^3s^{-1} are capture rates for neutral traps and for Coulomb attractive charged traps, respectively and f^0 occupation probability for the neutral charge states in steady state.

As described by Dhariwal /5/ the i-layer is divided into five regions. In one, the nearest p^+-i junction the space charge region is dominated by positive band tails. The following region is dominated by positive dangling bond, D^+. The central part of i-layer is assumed to be neutral semiconductor and near the n^+-i junction mainly negatively charged dangling bonds, D^- and finally close to the n^+-i junction there is negative charge in the conduction band tail.

In our analysis, we allow for absorption of visible light the intrinsic optical generation (photogeneration) rate, G_{opt} of electron-hole pairs in i-layer using

$$G_{opt}(\lambda, x) = \alpha(\lambda)(1-R)\phi_0 e^{-\alpha(\lambda)x} \tag{4}$$

where $\alpha(\lambda)$ -is absorption coefficient for specified wavelength of visible light, ϕ_0 - photon flux of incident light on the active surface of photodiode, R- reflectivity of incident light. The visible light of interest is quasi-uniformly absorbed in specified regions of our p-i-n a-Si:H sample. Small differences in results are observed for the region near n^+-i junction.

At low reverse bias voltages and in darkness the i-layer is depleted and the dark current arises due to thermal generation from deep defects in the i-layer /17/. The np product is very low and recombination rates (3) are negative. We assume in our analysis the high doped n^+ and p^+ layer are photoinactive. At low reverse bias the doped layers are extremely depleted. All changes of space charge density, electric field, recombination and thus the photocurrent happen in i-layer.

In our experiments, the p-i-n photodiode is illuminated through the p^+ layer. We assume complete depletion of the

i-layer at 2 V reverse bias voltage and mainly the changes of space charge density arise from time variation in charging and discharging of positive D^+ dangling bond in region near p^+-i junction and negative D^- dangling bonds near n^+-i junction. At illumination with RGB light the level of excitation is characterized from the excess carrier electrons and holes photogenerated in the region of voltage bias created positive space charge density near p^+-i junction and negative space charge density near n^+-i junction, respectively. This is described by Kazanskii /12/ by the relation

$$|\Delta n_0| = \frac{G_{opt}\tau_n}{\sqrt{1+\omega^2\tau_n^2}} \tag{5}$$

where the τ_n is effective electron lifetime and G_{opt} optical generation rate amplitude (4). We assume the electron lifetime 0.8 ns as the estimated value for $b = \mu_n n/\mu_p p = \mu_n \tau_n/\mu_p \tau_p = 10$, from /18/, for undoped a-Si:H. At low bias voltages and low modulation frequency, the influence of an applied field in case of steady state /2/ and the influence of modulated illumination /12/ can be neglected. Excess electron and hole concentration, respectively become

$$n = G_{opt}\tau_n \quad p = G_{opt}\tau_p \tag{6}$$

The corresponding density of space charge in the i-layer is calculated dependently on free and trapped charges as given by Dhariwal et al. /4/

$$\rho = q\left[p + p_t - n - n_t + N_{db}\left(f^+ - f^-\right)\right] \tag{7}$$

Here, p and n represent free hole and electron concentrations, p_t, n_t density of holes and electrons in the conduction band tail, N_{db} density of dangling bond, f^+, f^- occupation probability of a state D^+, D^- at energy E. The dangling bond states energy levels are 0.6 eV and 0.9 eV, respectively in /4/.

The dangling bond states activation energy, E is calculated from $t_r = \nu_o^{-1}\exp(E/kT)$, where ν_o is attempt-to-escape frequency on the order of 10^{12} s^{-1} for gap states of a-Si:H, k the Boltzman constant and T the temperature of 300 K. The average time spent in the DOS, t_r is determined by measured response curve fitting to the sums of exponential functions. This approach follows that previously described by Gradišnik et al. /19, 20/.

In this analysis, we assume the transition probabilities occurring between free carriers and two correlated dangling bond states with energies: (a) $E_1 = E\text{-}E_V$, and E_2 equal to the referent energy, $E_2 = E_{2r} = 0.9$ eV, or (b) E_1 equal to referent energy, $E_1 = E_{1r} = 0.6$ eV, and $E_2 = E_C - E$.

3. Experimental

The device p-i-n structure and experimental system are described in details elsewhere /19/. Illumination was introduced through the p-type layer. The transient response of a-Si:H p-i-n photodiode was measured as a response to the simultaneous pulses of light and bias voltage. The photovoltage was measured on the 220 kΩ load resistor at illumination from multicolour LED lamps emitting at 470, 565 and 624 nm, corresponding to the blue (B), green (G), and red (R) light, respectively and for their combinations. The optical powers were 8.25 μW, 10.35 μW, and 14.42 μW for red, green and blue light sources, respectively. The light and voltage pulse period was 3 ms with 50 % duty cycle, and the device was reversely biased at 2 V dc voltage. For the transient response analysis, the experimental curves with characteristic shape were divided into 7 intervals, the rise and the decay components.

4. Results and discussion

The measured photocurrent transient response to light pulses at 2 V reverse bias voltage and response on simultaneous light pulse and forward voltage pulse of 1 V amplitude are shown in Figure 2 as the lower and upper curves. The calculated energy levels are 0.482 eV and 0.508 eV, respectively. The overshoot is not present on these two responses as is in the case of responses on voltage pulse with magnitude between 0 V and 1 V. The response on light pulse at constant reverse bias voltage shows photocurrent increase with respect to the direct photogeneration of free carriers and enough high electric field for their separation. At simultaneous 1 V amplitude forward voltage pulse and light pulse the decrease of space charge region and capture of photogenerated free carriers in deep energy level as 0.508 eV was found to occur. The reduced electric field results in photucurrent decrease. In Figure 3 the densities of space charge are shown for both responses in the case a) when the calculated energy level is on E1 below Fermi level and b) when the calculated energy is on E2 above Fermi level. The transitions take place at energy level of 0.482 eV and 0.508 eV, respectively.

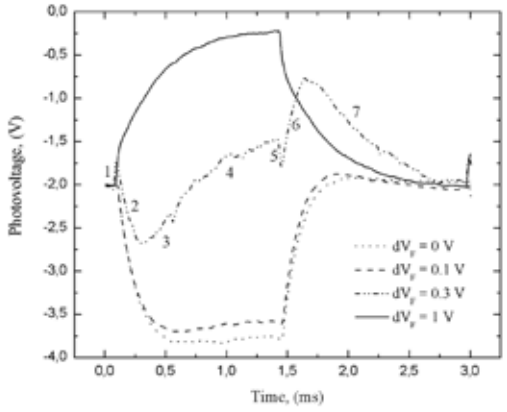

Fig. 2 Transient responses on simultaneous voltage and light pulses at bias voltage magnitude of 0 V, 0.1 V, 0.3 V and 1 V.

Figure 4 shows the generation rate (negative recombination rate shown as absolute value) for light pulses at constant reverse bias voltage of 2 V and recombination rate for simultaneous light and 1 V forward voltage pulse at two possible levels of calculated energies.

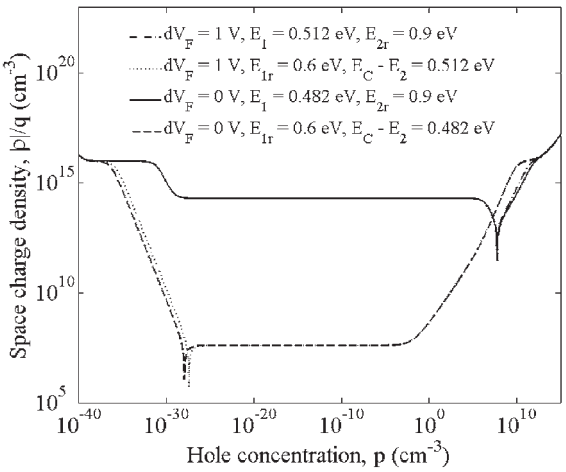

Fig. 3 Magnitudes of space charge density against hole concentration for transient responses at: dV_F = 0 V and a) energy states E_1 = 0.482 eV, E_{2r} = 0.9 eV; b) E_{1r} = 0.6 eV, $E_C - E_2$ = 0.482 eV; dV_F = 1 V and c) energy states E_1 = 0.512 eV, E_{2r} = 0.9 eV and d) E_{1r} = 0.6 eV, E_2 = 0.512 eV.

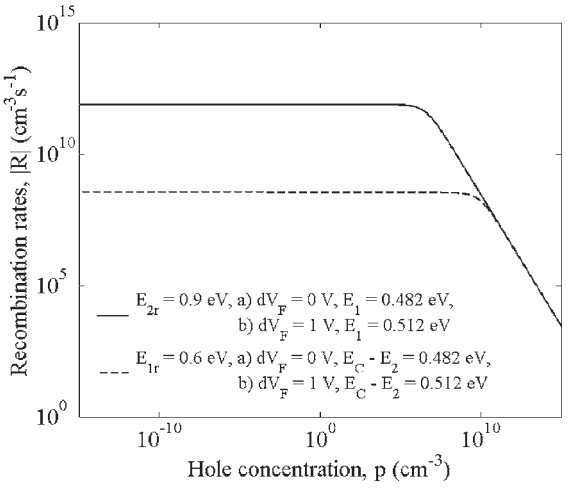

Fig. 4 Recombination rates against hole concentration for transient responses at: dV_F = 0V and a) energy states E_1 = 0.482 eV, E_{2r} = 0.9 eV; b) E_{1r} = 0.6 eV, $E_C - E_2$ = 0.482 eV; dV_F = 1 V and c) energy states E_1 = 0.512 eV, E_{2r} = 0.9 eV and d) E_{1r} = 0.6 eV, $E_C - E_2$ = 0.512 eV.

At a 2 V reverse bias voltage the electric filed is constant and all the photogenerated free carriers are collected. Small part is captured by dangling bond at p^+-i and n^+-i interfaces. The photogeneration occurs through the direct transition and small part through dangling bond states at an energy level of 0.482 eV in first 0.5 ms. This agrees with computed energy distribution of trapped charge thermally released by multi-trapping processes, as obtained by Main /10/. As the forward voltage pulse amplitude increases, the photocurrent shows an overshoot as is evident in the Figure 2. The photocurrent maxima delay also decrease. At 0.6 V forward voltage pulse magnitude the overshoot disappear /14/. Further increase in forward voltage pulse amplitude leads to the greater neutralization of D^+ dangling bond and the injection of holes from p^+-type. Valence band tail states capture the holes as is evident in Figure 2. The electric filed versus central part of i-layer decreases and electrons and holes become less separated. The recombination at D^- and D^+ states leads to observed current decrease. The recombination rate at an energy level of 0.508 eV (at 1 V voltage pulse amplitude) locally exceeds the generation rate, so holes and electrons diffuse back into the i-layer region. The photocurrent exponentially decrease as shown in Figure 2 for 1 V forward voltage pulse transient response.

The measured characteristic photovoltage transient response on 0.3 V forward voltage pulse at 2 V reverse bias and simultaneous RGB light illumination is shown in Figure 2. The observed characteristic p-i-n a-Si:H photodiode response shape enables us to divide it into seven intervals of photocurrent rise or decay corresponding to the generation or recombination prevalence.

1. At t < 0 the photodiode is reverse biased at 2 V and in the dark. The reverse current is controlled by thermal generation from deep states. The positive D^+ dangling bonds are activated in the vicinity of p-i junction and negative D- in vicinity of the n-i junction inside the i-layer.
2. At t = t_0 the low forward voltage pulse of 0.3 V magnitude and RGB light pulse through the p^+ layer are simultaneously applied to the p-i-n a-Si:H photodiode. The quasi-uniform photogenerated free carriers are in part captured by dangling bond inside i-layer. The recombination also includes the capture of carriers injected from the n^+ and p^+ layers into the tail states in

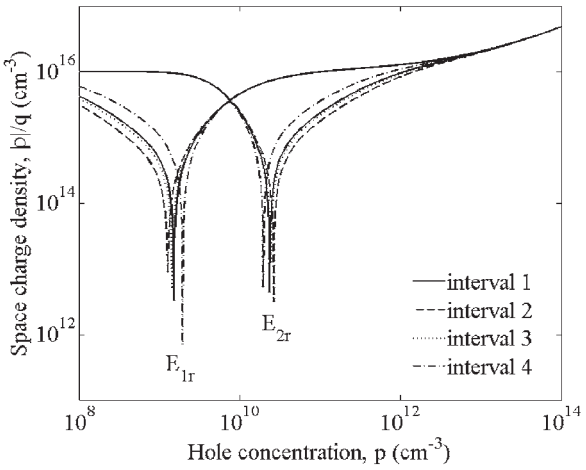

Fig. 5 Magnitudes of space charge density against hole concentration for transient responses at E_1r and E_2r for calculated energies for E_2 and E_1, respectively in time intervals from 1 to 4 signed in Fig. 2 on characteristic transient response for dV_F = 0.3 V

the intrinsic region, as was previously mentioned. The recombination through dangling bond prevails away from the p^+-i interface. In the first 20 μs the space charge region is reduced and consequently the drift current component decreases with decreasing electric field. The photodiode comport as a discharging capacitor. The space charge resulting from dangling bond is shown in Figure 5 and recombination rate in Figure 6 where the calculated energy is on level E_1 and E_2, respectively.

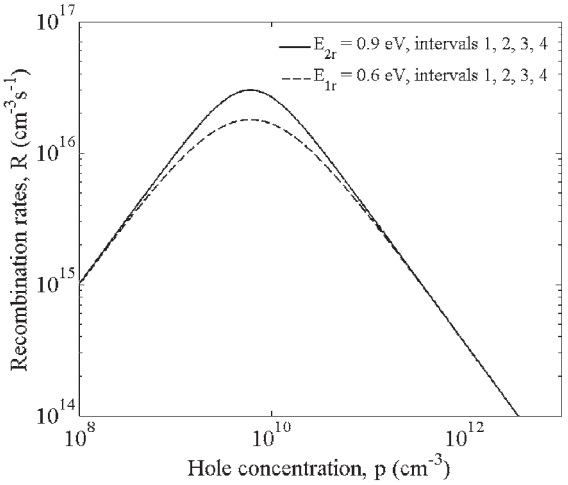

Fig. 6 Recombination rates at E_1r and E_2r for calculated energies for E_2 and E_1, respectively in time intervals from 1 to 4 signed in Fig. 2 on characteristic transient response for dV_F = 0.3 V.

3. In the second time interval in duration of 210 μs in Figure 2, the photocurrent rises as consequence of the photogenerated free carrier drift current. The transient photocurrent is from the holes, which are collected promptly and the electrons drift through the i-layer to the n side. The concentration of photogenerated free carriers is calculated by (4) and (5) at τ= 0.8 ns. The space charge provided from the dangling bonds reduces after a recombination of potogenerated carriers and injected carriers on dangling bonds at energy of 0.482 eV. A wavelength-dependent quasi-uniform absorption of light occurs (blue light component with higher energy and lower absorption depth contribute more to the free carriers in vicinity of surface), more space charge is neutralized in vicinity of the p^+-i interface than in vicinity of the n^+-i interface. The capture of electrons through the dangling bond in the vicinity of p^+-i prevails as shown in Figure 6. Consequently, the electric field begins to reduce and the photocurrent reaches the maximum value.
4. In time intervals 3 and 4 in Figure 2, the photocurrent begins to reduce as the space charge continues to reduce with recombination through the dangling bonds since the new steady state condition is reached. The calculated energies in these two intervals are 0.491 eV for interval 3 and 0.512 eV for interval 4, respectively. The photogenerated electrons are captured by dangling bond with deep energy levels below Fermi level. The minimum of the space charge density shifts toward the p-i junction and an increased recombination takes place via deeper energy levels seen in Figure 5 and Figure 6. This happens in the first part of time interval 3. The holes are captured by dangling bond with energy level above Fermi level in vicinity of n^+-i junction in the time of about 1 ms corresponding to the time interval 4. The greatest recombination rate is on the deeper energy level.
5. After the end of the illumination and on reverse bias voltage pulse the electric field suddenly increases. Trapped electrons within the energy level above the Fermi level are thermally emitted to the conduction band. Thermal electron emission from deep states at energy of 0.441 eV occurs. In this first short time of 30 μs the space charge region increases (Figure 7). The undoped a-Si:H i-layer is sufficiently thin that the recombination (Figure 8) of remaining photogenerated free carriers is negligible and the photocurrent suddenly rises.

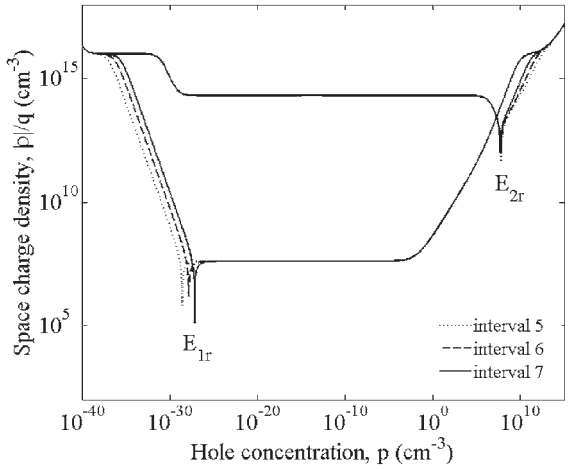

Fig. 7 Magnitudes of space charge density against hole concentration for transient responses at E_{1r} and E_{2r} for calculated energies for E_2 and E_1, respectively in time intervals from 5 to 7 signed in Fig. 2 on characteristic transient response for dV_F = 0.3 V

In the next 200 μs the current fall as an overshoot is observed in accordance with /9/. The holes' capture to the deeper states at energy of 0.486 eV activate positively dangling bond at which the free electrons are trapped before reaching the p-i junction. The free holes are trapped at the D- trap at n-i junction. The resulting space charge density is shown in Figure 7. Simultaneous decrease of the electric field in the i-layer increases the recombination during the recharging of dangling bonds (Figure 8).

A 1 ms long current tail arises from detrapping of carriers from the deep level of 0.525 eV, before the steady state is

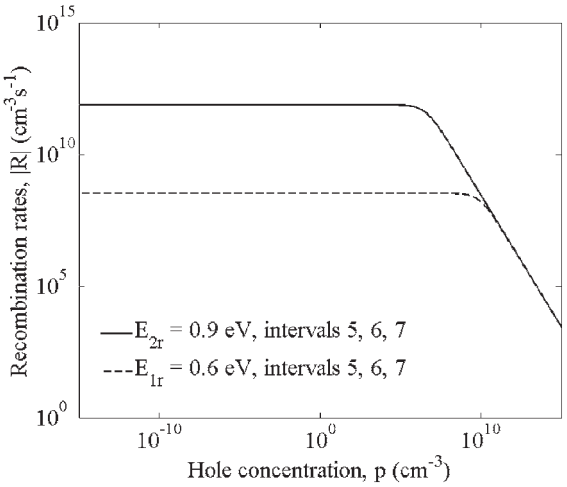

Fig. 8 Recombination rates at E_{1r} and E_{2r} for calculated energies for E_2 and E_1, respectively in time intervals from 5 to 7 signed in Fig. 2 on characteristic transient response for dV_F = 0.3 V.

reached . The influence of applied reverse bias voltage and the thermal generation is observed in agreement with Shen /16/. The corresponding space charge and recombination rates are shown in Figure 7 and Figure 8, respectively. The rise of energy level and consequently the shift of space charge toward the middle of the i-layer is evident in Figure 7 after light is going off.

The observed changes in overshoot by varying the bias voltage at simultaneously pulsed light illumination is present at the beginning and at the end of voltage and light pulses. The very small overshoot is observed at constant reverse voltage and pulsed light. Further increase of forward bias voltage at constant light pulse magnitude increases the overshoot. At 0.6 V there is only a small local maximum before the photocurrent reaches the stationary value. For the highest voltages photocurrent exhibits an exponential fall to a new steady-state. The maximum point of the overshoot moves from 0.88 to 1.43 ms from the stationary value and the corresponding overshoot magnitude from 0.047 to 1.337 V. The symmetric overshoot is observed at the end of the signal pulses.

5. Conclusions

The characteristic transient response shapes of a-Si:H p-i-n three-colour detectors are analyzed in depth using the model of recombination rate proposed by Dhariwal and Rajvanshi /4, 5/. The obtained results describe the effect of dangling bonds and tail states on transient response with increasing forward voltage pulse amplitude at low reverse voltages and low simultaneous voltage and light pulse frequencies, respectively. The time-distributed trapping and release are detected by simultaneous voltage and light excitation.

We observed the changes in overshoot by varying the voltage pulse amplitude at concurrent pulsed light illumination with constant amplitude. The overshoot is very small at constant reverse voltage and pulsed light. At forward bias voltage pulse of 0.6 V the overshoot disappears. For highest voltages photocurrent exhibits exponential decrease to a new steady-state value. Further investigation of observed effect regarding light illumination energy would be informative for color detection in photodiodes as active pixels in active pixel sensors.

References:

/1/ R.V.R. Murthy, V. Dutta, Underlying reverse current mechanisms in a-Si:H p^+-i-n^+ solar cell and compact SPICE modeling, J. Non-Cryst. Solids, no. 354, 2008, pp. 3780-3784.

/2/ S.A. Mahmood. M. Z. Kabir, Modling of transient and steady-state dark current in amorphous silicon p-i-n photodiodes, Current Appl. Phys., no. 9, 2009, pp. 1393-1396.

/3/ W.Fuhs, Recombination and transport through localized states in hydrogenated amorpohus and microcrystalline silicon, J. Non-Cryst. Solids, no. 354, 2008, pp. 2067-2078.

/4/ S.R. Dhariwal, S.Rajvanshi, Theory of amorphous silicon solar cell (a): numerical analysis, Sol. Energy Mater. Sol. Cells, no. 79, 2003, pp. 199-213.

/5/ S.R. Dhariwal, S.Rajvanshi, Theory of amorphous silicon solar cell (b): a five layer analytical model, Sol. Energy Mater. Sol. Cells, no. 79, 2003, pp. 215-233.

/6/ S.R. Dhariwal, M. Smirty, On the sensitivity of open-circuit voltage and fill factor on dangling bond density and Fermi level position in amorphous silicon p-i-n solar cell, Sol. Energy Mater. Sol. Cells, no. 90, 2006, pp. 1254-1272.

/7/ S. Qureshi, V. Perez-Mendez, S. N. Kaplan, I. Fujieda, G. Cho, R. A. Street, Signal Generation in a Hydrogenated amorphous silicon detector, IEEE Trans. on Nuclear Science NS- 36, no. 1, Feb. 1989, pp.194-198.

/8/ B. Stannowski, H. Cordes, R. Brüggemann, Th. Eickhoff, S. Bröcheler, H. Wagner, The influence of deeply-trapped charge on the transient photocurrent response of a-Si:H solar cells, J. Non-Cryst. Solids, n. 227-230, 1998, pp. 1295-1299.

/9/ C. Ulrichs, Th. Eickhoft, H. Wagner, Transient Photocurrent Spectroscopy on amorphous silicon solar cells, Conf. Rec. of the IEEE Photovoltaic Spec. Conf., 1993, pp. 981-985.

/10/ C. Main, Interpretation of photocurrent transient in amorphous semiconductors, J. Non-Cryst. Solids, no.. 299-302, 2002, pp. 525-530.

/11/ C. Main, S. Reynolds, I. Zrinščak, A. Merazga, Comparison of AC and DC constant photocurrent methods for determinaiton of defect densities, J. Non-Cryst. Solids, no.. 338-340 , 2004, pp. 228-231.

/12/ A. G. Kazanskii, K. Yu Khabarova, E. I. Terukov, Modulated photoconductivity method for investigation of band gap states distribution in silicon-based thin films, J. Non-Cryst. Solids, no.. 352, 2006, pp. 1176-1179.

/13/ V. Gradišnik, M. Pavlović, Characteristic Transient Response Shapes of a-Si:H Three-Colour Detectors, In Proc. of 44th International Conference on Microelectronics, Devices and Materials and the Workshop on Advanced Plasma Technologies, Sep 17.-19., 2008, Fiesa, Slovenia , 2008. pp. 297-300.

/14/ V. Gradišnik, Ž. Milanović, Effect of Light and Voltage-Induced Defects on a-Si:H Three-Color Detector Transient Response, In Proc. of 45th International Conference on Microelectronics, Devices and Materials and the Workshop on Advanced Photovoltaic Devices and Technologies, Postojna, Slovenia, 2009. pp. 301-304.

/15/ V. Gradišnik, Observed similar behaviour of a-Si:H p-i-n photodiode and retina response, In Proc. of the 7th IASETD International Conf. on Biomedical Engineering, BioMed 2010, Innsbruck, Austria: IASTED, 2010, pp. 176-180.

/16/ D.S. Shen, Transient opto-electric response in hydrogenated amorphous silicon and implications for high speed sensor devices, In Proc. 4th Int. Conf. on Solid-State and Integrated Circuit Technology, 1995, Beijing China, pp.718-720.

/17/ Rambhatla V. R. Murthy, V. Dutta, Underlying reverse current mechanisms in a-Si:H p^+-i-n^+ solar cell and compact SPICE modeling, J. Non-Cryst. Solids, no. 354, 2008, pp. 3780-3784.

/18/ R. Brüggemann, Parameters for photoelectronic characterisation and the Fermi level in amorphous silicon, Thin Solid Films, no. 427, 2003, pp. 355-357.

/19/ V. Gradišnik, M. Pavlović, B. Pivac, and I. Zulim, Study of the color detection of a-Si:H by transient response in the visible range, IEEE Trans. Electron Devices, vol. 49, no. 4, Apr. 2002, pp. 550-556.

/20/ V. Gradišnik, M. Pavlović, B. Pivac, and I. Zulim, Transient response times of a-Si:H p-i-n color detector, IEEE Trans. Electron Devices, vol. 53, no. 10, Oct. 2006, pp. 2485-2491.

Assoc. Prof. Dr.sc. Vera Gradišnik, dipl.ing.*
*Faculty of Engineering, University of Rijeka, Croatia
Vukovarska 58, Rijeka, HR-51000, Croatia
e-mail:Vera.Gradisnik@riteh.hr,
tel. +385 51 651 557, fax. +385 51 651 416
Antonio Linić, mag. ing. el., Šojska 27b,
Kostrena, HR-51221
Mladen Šverko, mag. ing. el., Rabarova 8,
Pula, HR-52100

Prispelo: 26.11.2010 *Sprejeto: 23.08.2011*

EXPERIMENTAL INVESTIGATION OF Si-SiO_2 INTERFACE TRAPS USING EQUILIBRIUM VOLTAGE STEP TECHNIQUE

M.S. Benlatreche[1], F. Rahmoune[1], O.Toumiat[2]

[1]University M'hamed Bougara of Boumerdes, Faculty of science, Physics department. Algeria
[2]University of Constantine, Faculty of science, Physics department. Algeria

Key words: Si-SiO_2 interface traps; Equilibrium Voltage Step technique; traps.

Abstract: The concentration profile of Si-SiO_2 interface traps in metal-oxide-semiconductor transistors has been studied using an equilibrium voltage step techniques. The Equilibrium Voltage Step (EVS), usually applied to extract the slow states profile in 3 dimensions, was used to deduce the in-depth profile of the slow states of the Si-SiO_2 interface. The profile of the slow states decreased between 7Å and 17Å awing.

Eksperimentalne raziskave pasti na mejni plasti Si-SiO_2 z uporabo napetostne tehnike EVS

Kjučne besede: pasti na meji Si-SiO_2 , napetostna tehnika EVS, pasti

Izvleček: V prispevku preučujemo koncentracijski profil pasti na meji Si-SiO_2 v MOS tranzistorju z uporabo napetostne tehnike EVS. Tehniko EVS, ki jo običajno uporabimo za študij počasnih energijskih stanj v treh dimenzijah, smo tokrat uporabili za določanje globinskega profila le-teh na meji Si-SiO_2. Ugotovili smo, da koncentracija počasnih stanj močno pade na razdalji med 7Å in 17Å od meje.

1. Introduction

Because of their limitation on the scaling of SiO_2 based metal-oxide semiconductors (MOS), the understanding of Si-SiO_2 interface traps is necessary. Many methods and theoretical models have been proposed to study Si-SiO_2 interface traps. The "1/f" noise method was the first technique, which supposed a distribution of traps in the direction of the oxide /1-2/. Recently, different methods have been proposed for the study of slow states /3-5/. A capture time constant distribution of traps has been confirmed by Bauza et al /6/, using the in-depth approach of charge pumping. This technique consists of measuring the charge pumping current as a function of frequency evaluated at the maximum of the Elliot curves. The Equilibrium Voltage Step (EVS) technique, developed by Tanner et al /5/, has been used to simultaneously extract the trap response time, density and energy in the silicon band gap of traps located near the Si-SiO_2 interface. The technique is simple and direct and consists of scanning the gate voltage of a MOS capacitor with different delay times and then measuring the resulting current transients. In this article, the trap profile, assuming only pure tunneling for capture, using data obtained by the EVS techniques.

2. Extraction of Si-SiO_2 interface trap profile using the equilibrium voltage step technique

The EVS technique has been mainly used to characterize slow traps in the Si-SiO_2 interface/4/. Then, it was extended to extract slow trap profiles in MOS capacitors with plasma damaged oxides /10/ and with NO and N_2O nitride oxides grown on Si and SiC substrates /11/. It has been later validated by Spillane et al. /12/.

This technique is based on the extraction of the current-voltage-time information in MOS capacitors /4/. It consists of scanning the gate voltage in a staircase manner and then measuring the resulting current transients after a delay time which is composed of the measurement time of the instrument, t_0 and a time td which is adjusted by the operator. The transient current measured at time $t_0 + t_d$ corresponds to the trap density with that response time. After scanning the gate voltage with different delay times, it is possible to extract directly the trap density as a function of response time at each energy position in the silicon band gap.

To extract the slow trap profile, the measured transient substrate current shown in Fig. 1 is divided by ($q \times A \times \Delta E$), where q is the absolute electronic charge, A the area of the gate and ΔE the change in the surface Fermi level resulting from the gate voltage step.

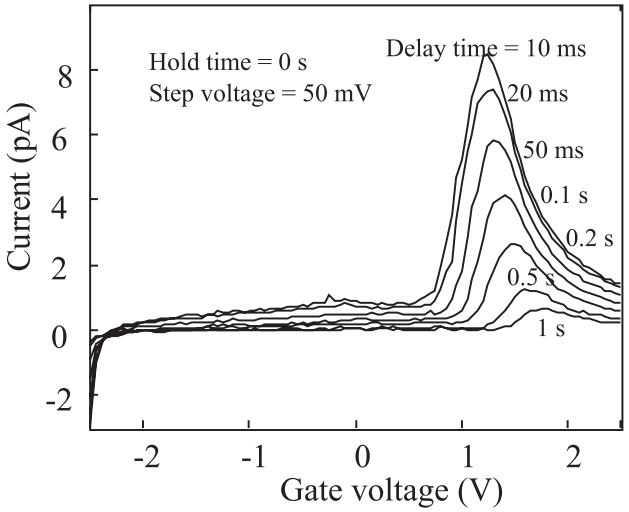

Fig 1: Transient substrate current due to the gate v oltage step at different delay times (p-type substrate MOS capacitor).

If we consider a set of slow traps at the Fermi level at equilibrium, then the capture time constant is equal to the emission time constant $\tau_c=\tau_e$ such that :

$$\tau = \frac{1}{n\sigma v_{th}} \quad (1)$$

where σ is the capture cross section, n the carrier concentration at the surface and Vth the carrier thermal velocity. If we suppose a uniform distribution of traps into the oxide, then according to the Heiman-Wrafield tunneling model /9/, the capture cross section at distance x from the interface can be written as:

$$\sigma(x) = \sigma(0)\exp(\frac{-x}{\lambda}) \quad (2)$$

Then, solving for the tunneling depth x we find /12/:

$$x = \lambda\left[\ln(N_c v_{th}\sigma(0)\tau) - (E_c - E_F)/KT\right] \quad (3)$$

where N_c is the effective density of states in the conduction band, (E_c –E_F) the Fermi energy level relative to the conduction band and KT is the thermal energy.

We assume that traps are distributed through the oxide both in energy and space with density N_t. By stepping the gate voltage, the Fermi energy changes by an amount ΔE If the device is in equilibrium before the step, then after the voltage step traps up to depth x will have changed charge (through emission or capture processes). Thus, the number of these states per unit area can be written as :

$$N(x) = xN_t\Delta E \quad (4)$$

Introducing the expression of the tunneling depth x in Equation (2) and solving for N_t we get:

$$N_t = \frac{I_{sub}(t)t}{\lambda Aq\Delta E} \quad (5)$$

where $I_{sub}(t)$ is the transient current measured at the substrate.

In this part, a MOS p-type capacitor with a thick oxide is used. When the surface of the semiconductor is swept from accumulation to inversion using a staircase gate signal with increment V_{step}= 50 mV, and a variable delay time from 10ms to 2s, we obtain positive transient current peaks attributed to emission of holes to the substrate, this peak decreases as the delay time increases, as shown in Fig.3. Applying the model of Tanner et al. /4/, which consists of dividing the measured current density by (q x ΔE), where q is the absolute electronic charge and ΔE the energy swept by the surface Fermi level, one obtains the 3D trap profile illustrated in Fig.2. This figure is attributed to the slow trap profile having response times from 70 ms to 2060 ms (since the measuring time of the instrument is 60ms). One can see the existence of a peak at 0.25 eV above the mid-gap which decreases as the response time is increased. This device has a Dit value of 10^{12} $ev^{-1}cm^{-2}$ measured using a conventional charge pumping technique. By applying now the theory of charge tunneling through energy barriers, one obtains the in-depth profile of traps, as shown in Fig.3.

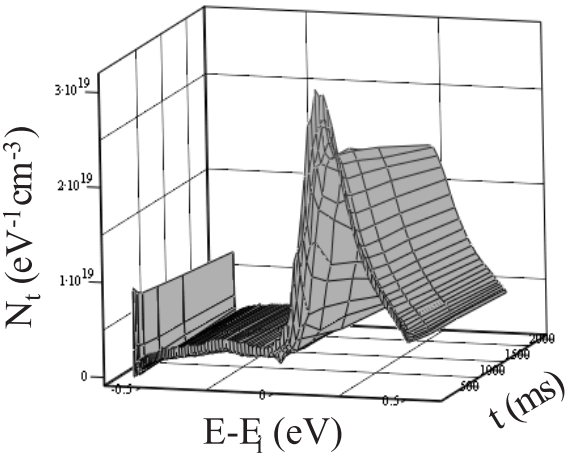

Fig 2: 3D slow trap profile of a p-type substrate MOS capacitor measured with delay times between 10 ms and 2s.

3. Resultants and discussion

The EVS technique allows the exploration of trap concentration into the oxide near the Si-SiO_2 interface, between 7 and 17Å, which corresponds to slow traps. Nevertheless, the charge pumping technique not only explores these types of traps, represented by the plateau of the profile, but probes also the fast states, which correspond to the exponential part of the profile /14/. The difference between the two techniques is that in charge pumping we measure a constant value of trap concentration for tunneling depth greater than 5 to 6Å, while with EVS we measure a decreasing value of the trap concentration between 7 and 17Å into the oxide. Another main difference concerns the energetic distribution of traps probed by each technique. The CP interface states located up to ±0.42eV around the mid-gap of silicon, depending on measuring conditions /13-14/, contribute to the recombination process and hence to the charge pumping current. However, in the EVS technique only slow traps located at specific energy

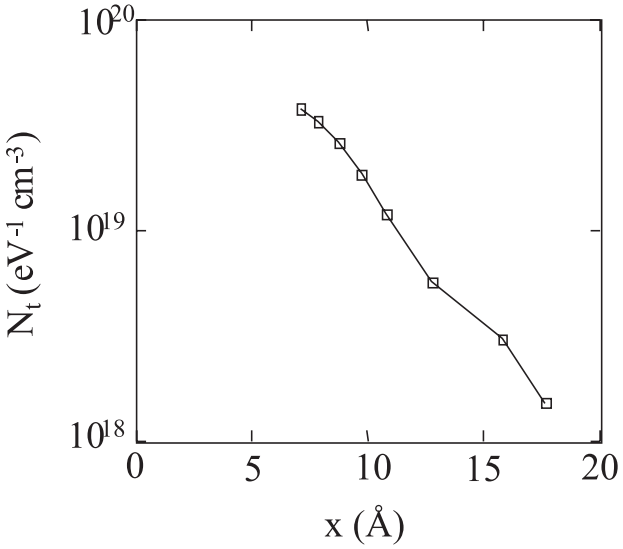

Fig. 3: Tunneling depth distribution obtained from the measured 3D profile of Fig. 2.

levels in the silicon band-gap contribute to the measured transient current.

4. Conclusion

The EVS technique has proven to be a simple and direct tool to simultaneously measure both the energy and response time distribution of traps located in the oxide near the Si-SiO_2 interface by scanning the gate voltage with different delay times. By applying the theory of carrier tunneling through energy barriers, the trap response time has been related to the tunneling depths into the oxide. The EVS technique only the slow traps located near the Si-SiO_2 interface and at specific energy levels in the silicon mid-gap are probed. This profile shows a decreasing trap concentration between 7 and 17Å from the Si-SiO_2 interface.

5. References

/1/ A. L. McWhorter, Semiconductor surface physics, Pennsylvania university press, Philadelphia, 1957 , p.293.

/2/ S. Christenson, I. Lundström and C. Svensson, Solid-St. Electron. 11,797 (1968).

/3/ R. E. Paulsen and M. H. White, IEEE Trans. Electron Devices ED-41, 1213(1994).

/4/ P. Tanner, S. Dimitrijev and H. B. Harrisson, Electron Letters 31, 1880 (1995).

/5/ S. Dimitrijev, P. Tanner, Z.-Q Yao and H. B. Harrisson, Microelectronics Reliability 37, 1143(1997).

/6/ D. Bauza and Y. Maneglia, IEEE Trans. Electron Devices, ED-44, 2262 (1997).

/8/ R. A. Wachnik and J. R. Lowney, Solid-St. Electron. 29,447 (1986).

/9/ P. Tanner, S. Dimitrijev, Y-T. Yeow and H. B. Harrison, IEEE Electron Device Letters 17, 515 (1996).

/10/ S. Dimitrijev, P Tanner, and H. B. Harrisson, Microelectronics Reliability 39, 441 (1999).

/11/ M. P. Spillane, S. Taylor and M. J. Uren, Microelectronic Engineering 48, 155(1999).

/12/ F. Hofmann and W. Hansch, J. Appl. Phys. 66, 3092, 1989.

/13/ F. Rahmoune, Contribution à l'étude des défauts de l'interface Silicium/Isolant dans les transistors MOS avancés. Ph.D Thesis, INPG , Grenoble, 2004.

M.S. Benlatreche[1], F. Rahmoune[1], O.Toumiat[2]
bmshakim35@umbb.dz; hakim2535@gmail.com
[1]University M'hamed Bougara of Boumerdes, Faculty of science, Physics department. Algeria
[2]University of Constantine, Faculty of science, Physics department. Algeria

Prispelo: 07.01.2011 *Sprejeto: 23.08.2011*

THE REALIZATION OF MICRO-REACTORS IN LTCC TECHNOLOGY FOR HYDROGEN PRODUCTION

Marko Hrovat[a,f], Darko Belavič[b,f], Gregor Dolanc[a], Primož Fajdiga[a], Marina Santo-Zarnik[b,f], Janez Holc[a.f], Mitja Jerlah[c,f], Kostja Makarovič[a,f], Stanko Hočevar[d], Iztok Stegel[e]

[a] Jožef Stefan Institute, Ljubljana, Slovenia
[b] HIPOT-R&D, d.o.o., Otočec, Slovenia
[c] Hyb, d.o.o., LŠentjernej, Slovenia
[d] National Institute of Chemistry, Ljubljana, Slovenia
[e] Ministry of Defence, Ljubljana, Slovenia
[f] Centre of Excellence NAMASTE, Ljubljana, Slovenia

Key words: LTCC technology, micro-reactor, buried channels, steam reforming

Abstract: One of the possibilities for achieving portable power systems is a low-temperature fuel-cell system integrated with a fuel processor. A fuel processor is needed to make the hydrogen from liquid fuels (mainly methanol), as the required fuel for PEM (polymer-electrolyte membrane) fuel cells. LTCC (Low Temperature Co-fired Ceramics) technology was used to prepare prototypes of fuel processors for low-temperature fuel cells. The planar integrated LTCC structure with buried cavities and channels including two evaporators (fuel and water for steam reforming), the mixing chambers and the reformer was designed and successfully realized. The length of the buried channels is nearly 2 m. The carbon-based thick-film pastes were evaluated for sacrificial layers and were used to form the buried channels. Platinum-based heaters and temperature sensors were integrated onto the top of the structure. The fuel-processor micro-channels were covered with the required catalyst, using either the sol-gel or wash-coating techniques. A laboratory experimental environment for testing was also provided. Preliminary results on the steam reforming of the liquid fuel (methanol) and the water are presented.

Realizacija keramičnih mikro reaktorjev v tehnologiji LTCC za izdelavo vodika

Kjučne besede: LTCC tehnologija, mikro rektorji, pokopani kanal, parni reforming

Izvleček: Nizko temperaturne gorivne celice s polimerno membrano (PEM – Proton Exchange Membrane), integrirane s procesorjem goriva, so ena od možnosti za prenosne vire električne energije. Procesor goriva potrebujemo, da s pomočjo kanalizirane reakcije pridobimo vodik, ki je gorivo za gorivne celice, iz tekočih goriv, v glavnem metanola in vode. Prototipi keramičnih mikro reaktorjev so bili realizirani s pomočjo LTCC tehnologije (Low Temperature Co-fired Ceramics – keramika z nizko temperature žganja). Planarne integrirane LTCC strukture s pokopanimi votlinami in kanali so bile načrtane in izdelane. Te 3D strukture vsebujejo dva uparjalnika, za vodo in gorivi, mešalne komore in reformer za reakcijo med tekočim gorivom in vodo. Dolžina pokopanih kanalov je okrog 2m. Debeloplastne paste na osnovi ogljika so bile uporabljene za izdelavo pokopanih kanalov. Grelci in temperaturno senzorji na osnovi Pt debeloplastnih prevodnikov so bili integrirani na površini. Notranje površine mikro kanalov procesorskega dela so bile pokrite s katalizatorjem, ki je bil nanesen s sol-gel tehnologijo. Razvili smo eksperimentalno laboratorijsko okolje za testiranje. Predstavljeni so preliminarni rezultati kataliziranih reakcij med metanolom in vodo.

1. Introduction

2.1. LTCC ceramics

Advanced ceramic micro-systems are in many cases created with multilayer ceramic modules that integrate screen-printed thick-film electronic components and sub-circuits as well as 3D buried structures, for example, cavities or channels. Low Temperature Co-fired Ceramics (LTCC) technology is considered as one of the more suitable technologies for the fabrication of ceramic micro-systems. These LTCC materials are sintered at the low temperatures typically used for thick-film processing, i.e., around 850°C. To sinter to a dense and non-porous structure at these, rather low, temperatures, LTCC materials have to contain some (or a great deal of) low-melting-point glass phase. Unfired LTCC tapes are a mixture of glass and ceramic particles, for example, alumina, and an organic phase. During firing, first the organics burn out at around 450°C, leaving a mixture of glass and ceramic particles. At higher temperatures the glass phase melts and the material sinters to a dense and non-porous structure. The whole process is schematically shown in Fig. 1. During the high-temperature processing some part of the glass crystallizes ([1-5]). This increases the viscosity of the remaining glass phase and the glass does not soften during subsequent re-firings.

The microstructures of the green and the fired LTCC material (Du Pont 951) are shown in Figs. 2.a and 2.b, respectively ([4,6]). The unfired material is a mixture of darker

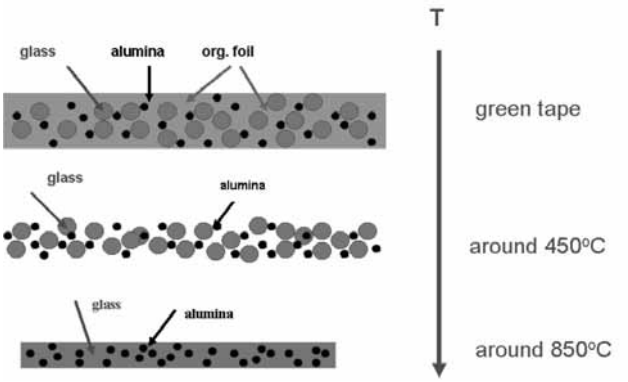

Fig. 1. Cross-sections of the LTCC tape at different temperatures during firing (schematic).

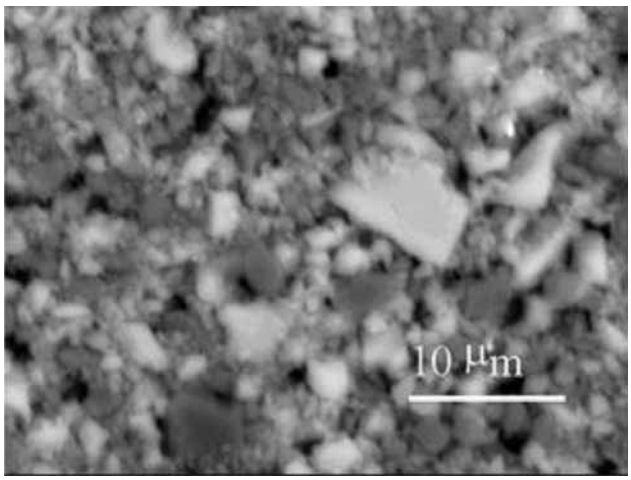

Fig. 2.a: Microstructure of a green LTCC tape. The darker grains are alumina and the lighter grains are glass particles

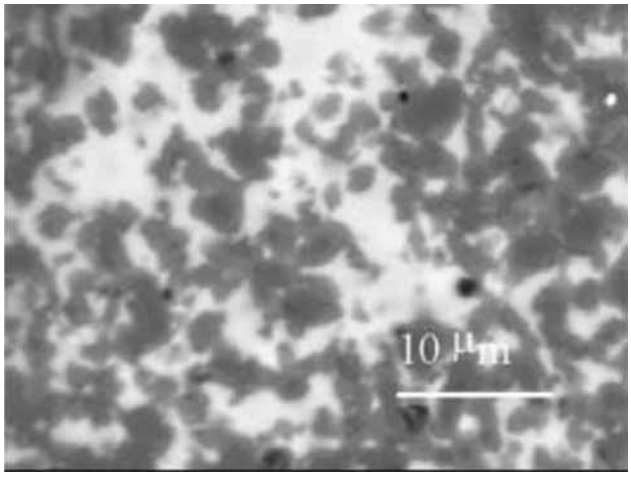

Fig. 2.b: Microstructure of a CC tape fired at 850°C. The material is densely sintered. The darker grains of alumina are embedded in the lighter glass matrix.

alumina and lighter glass particles. After firing the material is densely sintered with dark alumina grains in the glass matrix.

The whole process flow of the LTCC technology is schematically shown in Fig. 3. The green tapes are cut into the required dimensions. Vias are punched and filled with a conductor material. After this the conducting layers are screen printed. The substrates are then visually examined and put together into multilayer "packets. These "packets" are laminated under a pressure at temperatures around 80°C and fired at relatively low temperatures of around 850°C, which are typically used for thick-film processing,

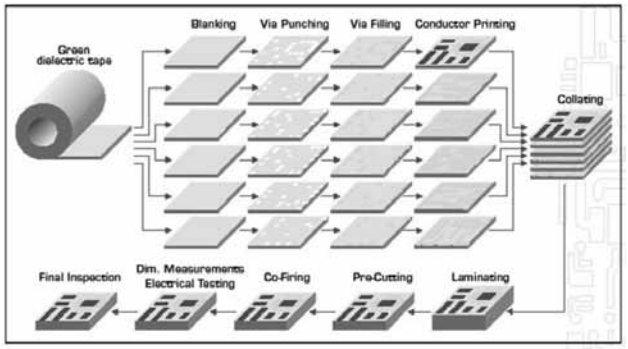

Fig. 3. The LTCC process flow.

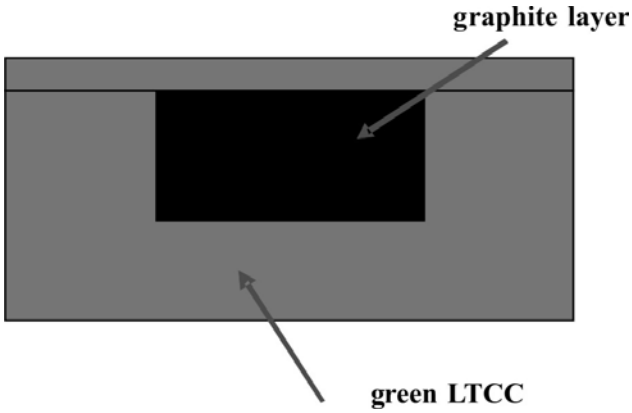

Fig. 4.a: Unfired LTCC structure. Graphite layer is laminated within the structure (schematic).

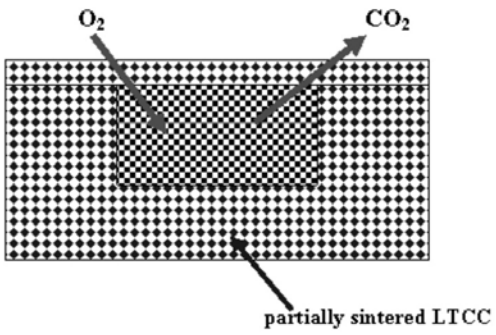

Fig. 4.b: Partially sintered LTCC structure with open porosity. The oxygen and carbon dioxide are diffusing through the porous structure (schematic).

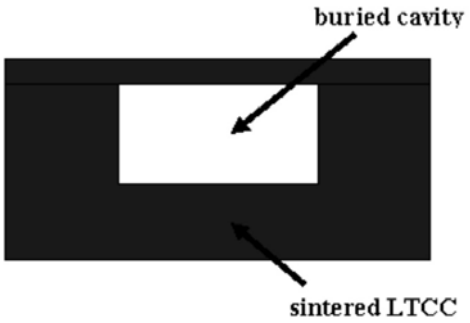

Fig.. 4.c: LTCC material is fully densified (schematic).

2.2. Sacrificial materials

LTCC technology is inherently efficient for producing 3D structures, e.g., buried cavities or channels, for different applications, ranging from pressure sensors to "laboratory-on-chip" systems ([7,8]). However, as mentioned above, LTCC tapes contain a relatively high concentration of low-melting-point glass, enabling the materials to sinter densely at relatively low firing temperatures. During the firing the top parts of the structures over the buried cavities tend to deform; generally they tend to sag. One of the possible solutions is to use so-called sacrificial carbon-based layers within the 3D LTCC structures ([9-11]). These sacrificial layers are either screen-printed (pastes) or inserted (tapes) into the green LTCC structures before the lamination. During the lamination and the earlier stages of the firing they must support the desired 3D structure and prevent deformations. Later, the sacrificial layers ought to burn out. The temperatures for the oxidation of the carbon material must be a little higher than the temperature for the onset of sintering of the LTCC 3D structures. This means that while the LTCC tapes start to sinter they are still porous enough so that the oxygen from the air can diffuse to the inside of the LTCC structures and the CO_2 can diffuse to the outside. All the carbon most be oxidized before the LTCC layers are fully densified. This is shown very schematically in Figure 4.a (unfired structure), 4.b (porously sintered LTCC structure) and 4.c (densely sintered LTCC structure), respectively.

A typical sintering/densification curve for the LTCC material (951, Du Pont) is shown in Figure 5 ([12]). The material starts to sinter at temperatures around 700°C and is more or less fully densified at 800°C. However, note that the sintering curve is a "dynamic" one – the temperature is increasing. However, if the samples were to be held at some temperature the material will still shrink, albeit at a slower rate. Suitable temperatures for the oxidation of the sacrificial layers would be a little over 700°C.

2.3. Micro-reactors for hydrogen production

Small, compact fuel cells that operate on liquid fuels offer lightweight alternatives to batteries, thus allowing the greater portability of electronic devices, e.g., laptop computers.

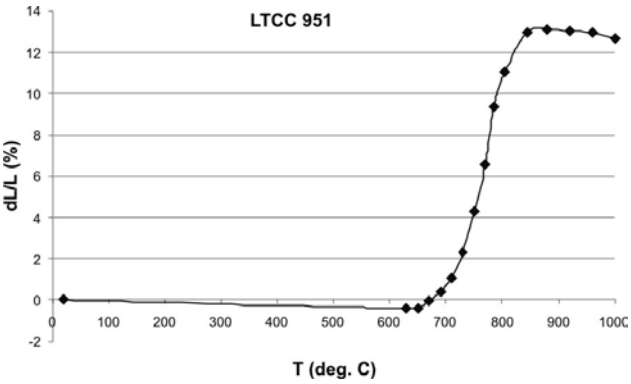

Fig. 5: Sintering curve of a typical LTCC material ([12])

These fuel cells are mainly based on low-temperature (under 100°C) PEM electrolytes (Proton Exchange polymer Membranes or Polymer Electrolyte Membranes). The required fuel for these fuel cells is pure hydrogen. To supply this fuel, water and a liquid fuel are steam reformed into hydrogen-rich gases with the help of appropriate catalysts.

A very schematic representation of a combination of the fuel processor and the PEM fuel cell is shown in Figure 6. A liquid fuel and water and/or air are fed into the fuel processor and the resulting hydrogen-rich gas is used as a fuel for the PEM fuel cell.

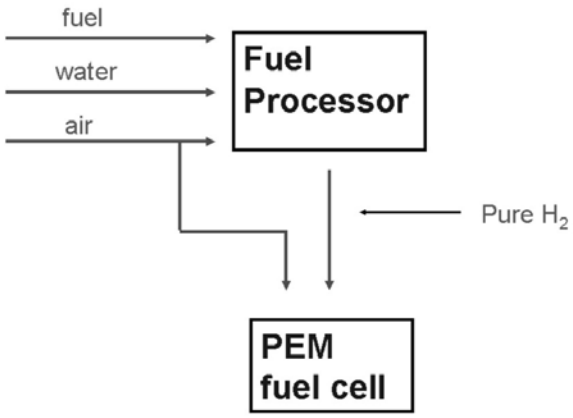

Fig. 6: Schematic presentation of a combination of the fuel processor and the PEM fuel cell. Liquid fuel and water and/or air are fed into the processor.

The ideal catalyst-assisted reaction would result, for example, for methanol and water:

$$CH_3OH + H_2O \rightarrow CO_2 + 3\,H_2 \qquad (1)$$

However, some side reactions also produce some small quantities of the undesirable (i.e., harmful) CO, which must be removed after the reforming. Therefore, complete fuel processors for the conversion of liquid fuels into (more or less) pure hydrogen consist basically of fuel vaporisers, fuel reformers and gas clean-up units (mainly to remove the excess carbon monoxide). A schematic outline of the fuel processor is shown in Figure 7. The two modules on the right are the water gas shift rector (WGS) and the preferential oxidation reactor (PrOx) for removing the carbon

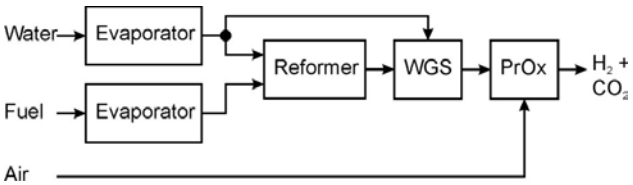

Fig. 7: Schematic outline of the fuel processor. WGS – water gas shift. PrOx – partial oxidation.

monoxide from the gas mixture by reactions with water and oxygen, respectively. The catalyst-assisted reactions are:

Reformer – fuel + H_2O + (O_2) → H_2 + CO_2 + CO (2)

WGS (water gas shift) – CO + H_2O → CO_2 + H_2 (3)

PrOx (preferential oxidation) – CO + O_2 → CO_2 (4)

Ceramic fuel processors based on LTCC technology for the catalyst-assisted production of hydrogen from liquid fuels (mainly methanol) for PEM (polymer-electrolyte membrane) fuel cells have been reported in the open literature. A. Kundu et al. ([13]) made an extensive overview of micro-processors with over 100 references. Most of the described devices are realized on single-crystal silicon wafers. However, some are made with LTCC or other ceramic materials. Koripella et al. ([14]) (Motorola) patented the compact design of an LTCC-based fuel processor with an integrated PEM fuel cell. Y. Shin et al. ([15]) reported simple, three-layered LTCC structures for micro-reformers and PrOX (preferential oxidation of the carbon monoxide) units.

In the paper the design and development of the planar ceramic micro-reactor will be described. The reactor was made using LTCC technology and sacrificial materials. Carbon-based materials for sacrificial layers will be briefly discussed. The planar LTCC structure includes two evaporators - fuel and water for steam reforming, mixing chambers and the reformer. Preliminary experiments were made with the water/methane steam reforming.

3. Experimental

3.1. Sacrificial layers

The evaluated carbon-based pastes for sacrificial layers were Harmonics (Carb-Paste-1) and Electro Science Labs. (4440). They were analyzed by thermogravimetric analysis (TGA). The heating rate was 5K/min. In most cases the firing profile of the LTCC tapes was simulated. This means firing first for 1 hour at 450°C (LTCC tapes organic binder burnout). However, the highest firing temperatures were in most cases 720°C (and not 850°C, which is the firing temperature of the LTCC material) for some hours to determine how long it takes to completely oxidize the carbon-based materials at temperatures when the sintering of the LTCC materials starts, while the ceramic tapes still "possess" the open porosity. In the case of the Harmonics thick-film paste some residue of a brownish powder (less than 1 wt.%) was left after the firing. This residue was analyzed using an X-ray diffraction (XRD) analyser and a scanning electron microscope (SEM) equipped with an energy-dispersive X-ray analyzer (EDS).

3.2. Micro-reactor

The prototype LTCC reactor – a horizontally connected evaporator and reformer – was designed. It is shown schematically in Figure 8. The reactor is composed of two evaporators, two mixing chambers and a reformer. On the left-hand side are the buried cavities for the input of the fuel and the water. Two levels of buried channels (dimensions 400 μm x 50 μm) – the evaporator part – connect the entrance chambers and the two mixing chambers in the middle of the substrate. Three levels of channels lead from the mixing chambers into the "output" chamber, i.e., the reformer. The channels were made with the help of sacrificial layers. The chosen graphite-based thick-film paste was screen-printed onto the green LTCC foils. On the top of the structure two platinum heaters for separate green LTCC foils (951, Du Pont) were laser cut to the required dimensions. The graphite-based thick-film paste was screen-printed to form the buried channels. The 3D structures were made by laminating layers of 951 (Du Pont) LTCC tapes at 70°C and at a pressure of 200 bars. The prepared samples were fired first for 1 h at 450°C (burn-out of organics) and then fired at maximum temperatures of 850°C. On the top of the fired structures platinum heaters and temperature sensors, and palladium/silver connections were printed and fired at 850°C.

The CuO-CeO_2 catalyst containing 20 mol % CuO was directly prepared without the need for a calcination step, by co-precipitation from mixtures of cerium and copper aqueous nitrate solutions with ammonium hydroxide. The catalyst slurry was prepared by mixing the catalyst (6.5 wt. %), aluminium hydroxide sol and 2-propanol. The precursor was then injected into the micro-channels with the syringe

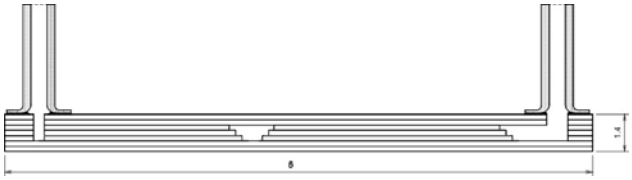

Fig. 8.a: Schematic longitudinal cross-section of the LTCC-based reactor comprising integrated evaporator and reformer. The evaporator is on the left-hand side and the reformer on the right-hand side. Buried cavities for the input of fuel and water on the left, mixing chambers in the middle and gas output cavity on the right are connected with buried channels

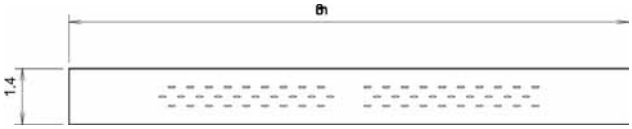

Fig. 8.b: Schematic transversal cross-section of the LTCC based reactor through three layers of buried channels on the right (reformer) part of the structure.

until it filled up the volume of all the micro-channels. The coating was then dried at 60°C for 12 h, and the process was repeated to achieve the desired weight of catalyst. After drying the samples were calcined in air at 450°C for 4h.

3.3. Integrated laboratory experimental environment

The experimental work (reforming) was performed within an integrated experimental environment, which supports various kinds of tests of the operation and efficiency of the reformer and its subsystems during the design and optimisation phase. The majority of the components of the integrated experimental environment are controlled via a computer, which simplifies the acquisition of the results and their documentation. The integrated experimental environment shown in Fig 9 contains the following subsystems:

- Temperature-profile measurement of the ceramic body surface is measured by a thermo-vision camera and is used to support the optimal thermal design of the ceramic structure.
- Temperature measurement and control is implemented independently for the evaporator and the reformer. The temperature is controlled using Pt sensors and heaters, which are integrated onto the reformer surface. Dedicated measurement and power-control electronic circuits are designed and provided.
- Flow rates of input reactants (water, methanol/diesel) must be carefully controlled and they have to be independent of the back pressure in the reformer. For the dosage, syringe-like cylinders are used and powered by step motors, allowing the adjustment of flow rates and quantities.
- Control software running on a personal computer is used for the data acquisition and control. Within the software the temperature evaluation and control is implemented, as well as the control of the flow rates and the quantities of the input reactants.

Preliminary experiments were made with methanol as the fuel and water for the steam reforming. The gas reaction products were bubbled through the water where the un-reacted methanol and water condensed in the water bath. The chemical analysis of the output products was performed using mass spectroscopy analyses.

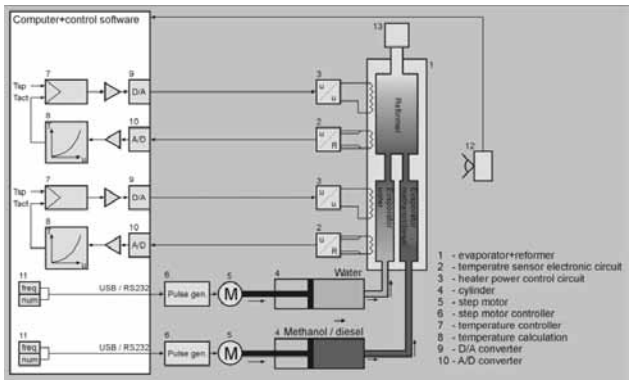

Fig. 9. The integrated experimental environment

4. Results and discussion

4.1. Carbon-based sacrificial layers

The TGA analyses of the carbon-based sacrificial materials are rather similar. The DTA analyses of the Harmonics and ESL (Electro Science Labs.) pastes are shown in Figures 10.a and 10.b, respectively. The weight loss is on the left "y" axis and the temperature is on the right. Samples were heated up to 450°C and held at this temperature for 1 hour to simulate the firing cycle of the LTCC green tapes. The temperature was increased to 720°C and the samples were then held at this temperature. The results for both pastes are similar. There is a noticeable weight decrease at 450°C, which is attributed to a burn-out of the organic vehicle in the pastes. The complete evaporation and burn-out of the added organic materials is mainly over before the 450°C "step" is reached and only a small (if any) further decrease of the samples' weight is observed during the one hour at 450°C. When the temperature reached 720°C a significant oxidation of the carbon-based materials starts. For both

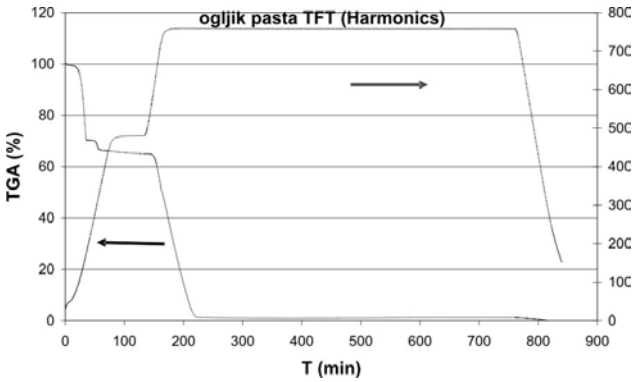

Fig. 10.a: TGA analysis (weight loss) of carbon-based sacrificial material (thick-film paste, Harmonics). The weight loss is on the left "y" axis and the temperature is on the right.

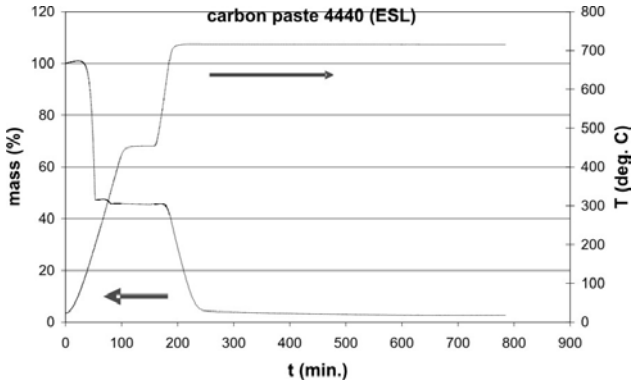

Fig.10.b: TGA analysis (weight loss) of carbon-based sacrificial material (thick-film paste, ESL, 4400). The weight loss is on the left "y" axis and the temperature on the right.

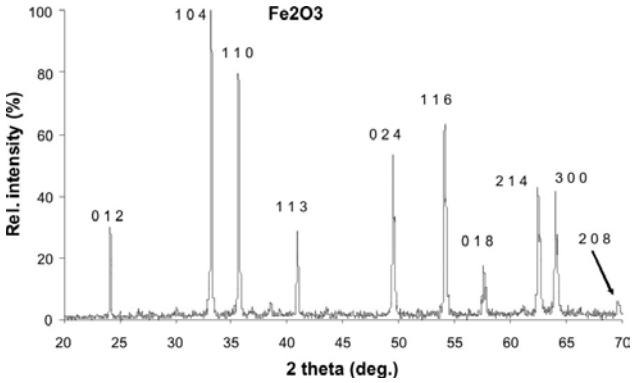

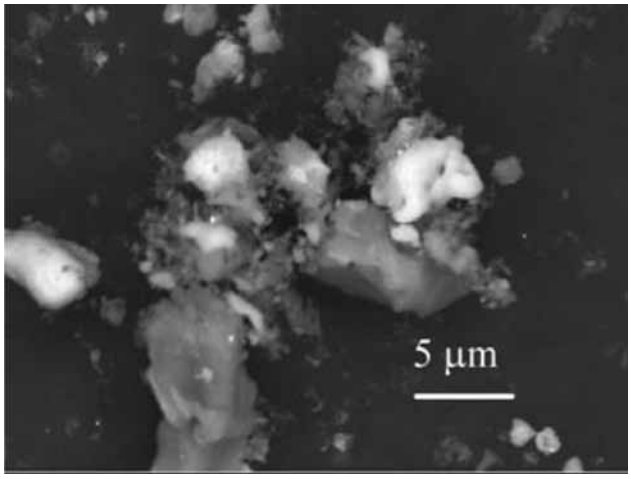

Fig. 11: The X-ray analysis of the brownish residue after the burn-out of some graphite-based sacrificial materials. The peaks of Fe_2O_3 are indexed.

the analyzed materials the oxidation is over in 100–150 min at 720°C. After that time no significant loss of weight can be detected.

As mentioned in the "Experimental" section, after the burn out the Harmonics thick-film paste leaves a small quantity (less than 1 wt.%) of brown residue. The X-ray analysis of the residue is shown in Figure 12.a and an SEM picture is presented in Figure 11.b. The X-ray analysis showed that this residue is an iron oxide (Fe_2O_3). This was confirmed by the EDS micro-analysis of the residual powder. The lighter particles observed in the microstructure in Fig. 12.b. are the iron oxide. Therefore the ESL 4440 which oxidises cleanly without any residue was used for sacrificial layers.

4.2. LTCC micro-reactor

The ceramic micro-reactor was prepared from eight layers of LTCC tapes. Carbon-based sacrificial layers were used to form the buried structures. The dimensions of the planar micro-reactor after firing are 70x30x1.45 mm^3. The surface of the horizontally integrated evaporator and the reformer realized in the LTCC technology reactor with the attached input and output "tubes" are shown in Figure 12.a. From left to right: the input openings for the fuel and water, the heater for both evaporators and the Pt-based resistive temperature sensor, the heater for the reformer

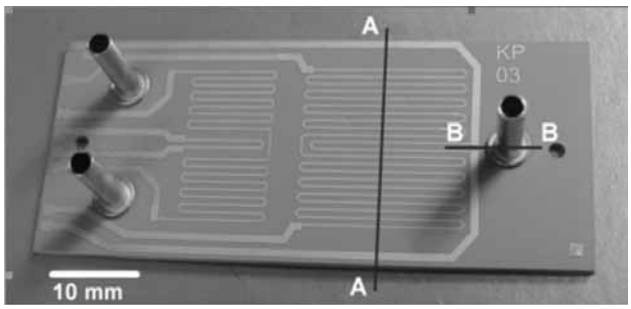

Fig. 12.a: The picture of the surface of the horizontally integrated evaporator and reformer realized in LTCC technology.

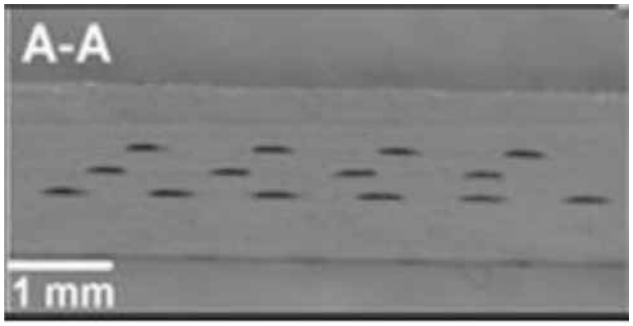

Fig. 12.b: The microstructural cross-section through the line A-A (see Fig. 7.b) is shown. Three layers of buried channels connect the mixing chambers and the output chamber.

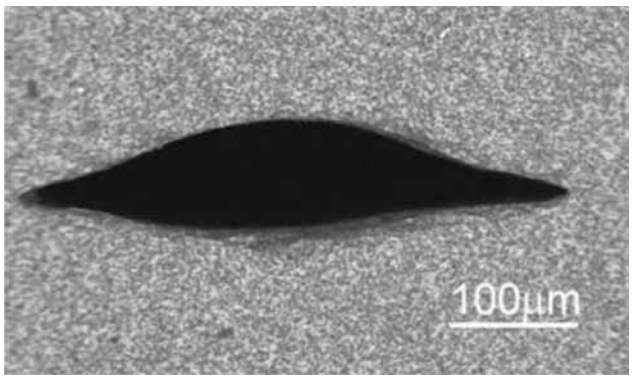

Fig.12.c: Cross-section of a channel.

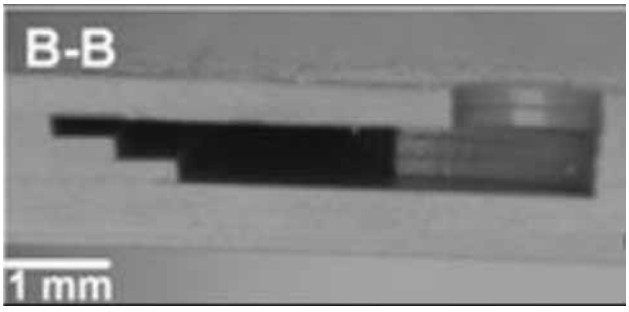

Fig. 12.d: The microstructure through the line B-B (see Fig. 7.b) represents the cross-section of the buried cavity at the output chamber.

and the second Pt-based resistive temperature sensor, and the output opening. In Figure 12.b the microstructural cross-section through the line A-A is shown. Three layers of buried channels connect the mixing chambers and the output chamber. The total length of the buried channels is around 2 m. A cross-section of one channel is shown in Figure 12.c. The microstructure (line B-B in Figure 13.b) presents the cross-section of the buried cavity at the outlet. The three-layered structure – three layers of channels – can be seen in Fig.12.d.

Within the experimental environment, which was described in the "Experimental" subsection, a number of experiments were performed. The first set of experiments was intended to test the thermal design of the ceramic body structure. We heated up the reactor structure to the working temperatures and observed the temperature profiles on the surface with a thermo-vision camera. Fig-13 shows an example of the temperature profile. The bottom region in the picture represents the area of the evaporator and the upper region is the reforming reactor.

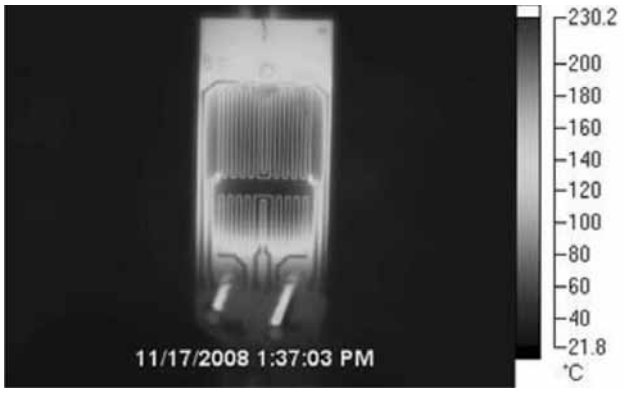

Fig. 13: An example of the temperature profile.

In the second set of experiments the operations of the reforming process were analysed and the preliminary analyses of the output products using the mass spectroscopy were performed. The preliminary results are shown in Table 1 where the concentrations of the output gases vs. the processing conditions are summarised. The table above contains seven different measurements. These measurements were conducted with the LTCC reformer at different temperatures and different flow rates of water and methanol. Generally, the produced hydrogen seems to be very pure. Note, however, that the molecular masses of N_2 and CO are the same i.e., 28, and therefore they cannot be distinguished using mass spectroscopy. At low temperatures (measurements 1 and 2) below the catalyst temperature window only very small amounts of hydrogen were produced. On the other hand, when the temperatures were within the required temperature window (measurements 3 and 4), the concentrations of hydrogen were increased significantly.

Table 1 – Mass spectroscopy results under various process conditions (temperatures., and flow rates of methanol and water)

No.	Temp. (°C)	Flow rate methanol (ml/h)	Flow rate water (ml/h)	H_2(%	CH_4(%)	N_2/CO(%)	O_2(%)	Ar(%)	CO_2(%)
1	200	22,6	34	5	0.6	69	23	0.9	1,6
2	200	11,3	34	7	0.6	68	23	1,1	1,1
3	270	11,3	34	35	0.5	45	15	0.6	3,9
4	370	11,3	23	55	0.2	34	7	0.3	3,8

5. Conclusions

The described ceramic micro-reactor was developed for the steam reforming of liquid fuels and water into hydrogen, which will fuel low-temperature fuel cells. The reactor was designed and made using LTCC technology. The planar LTCC structure with buried cavities and channels, including two evaporators - fuel and water for steam reforming, mixing chambers and the reformer was realized. Carbon-based sacrificial layers were evaluated and then used to form the buried structures. The total length of buried channels is around 2 m. Platinum-based heaters and temperature sensors were integrated onto the top of the structure. The CuO / CeO_2 catalyst was deposited within the channels of the structure. The reforming process was evaluated by analysing the output gas products using mass spectroscopy. These preliminary measurements validated the efficiency of the used catalyst.

The results confirm that Low Temperature Co-fired Ceramic (LTCC) technology has the potential to fulfil the process requirements meant for the conversion of fuels into a hydrogen-rich gas. Currently, the technology has demonstrated its suitability for the design and realisation of a planar micro-reactor with a reasonable yield of hydrogen.

Acknowledgement

The work was supported by the Ministry of Defence, Republic of Slovenia (Project KeraPro, No. 631-48/2007-78). The financial support of the Slovenian Research Agency is gratefully acknowledged.

References

/1./ L. C. Hoffman, Crystallizable dielectrics in multilayer structures for hybrid microcircuits: a review, Advances in Ceramics, 26, (1989), 249-253

/2./ A. A. Shapiro, D. F. Elwell, P. Imamura, M. L. MeCartney, Structure-property relationships in low-temperature cofired ceramic, Proc. 1994 Int. Symp. on Microelectronics ISHM-94, Boston, 1994, 306-311

/3. / J.-H. Jean, C.-R. Chang, Camber development during cofiring Ag-based low-dielectric-constant ceramic package, J. Mater. Res., 12, (10), (1997), 2743-2750

/4./ M. Hrovat, D. Belavič, J. Kita, J. Cilenšek, L. Golonka, A. Dziedzic, Thick film temperature sensors on alumina and LTCC substrates, J. Eur. Ceram,. Soc.., 25, (15), (2005), 3443-3450

/5. / Y. Imanaka, Multilayered Low Temperature Cofired Ceramics (LTCC) Technology, Fujitsu Laboratories, Ltd. Japan, Springer 2005

/6. / M. Hrovat, D. Belavič, J. Kta, J Holc, , J. Cilenšek, K. Golonka, A. Dziedzic, Thick-film resistors with low and high TCRS on LTCC substrates,. Inf. MIDEM, 35, (3), (2005), 114-121.

/7. / K. A. Peterson, K. D. Patel. C. K. Ho, S. B. Rohde, C. D. Nordquist, C. A. Walker, B. D. Wroblewski, M. Okandan, Novel microsystem applications with new techniques in low-temperature co-fired ceramics, Int. J. Appl. Ceram. Technol., 2, (5), (2005), 345-363

/8. / L. J. Golonka, H. Roguszezak, T. Zawada, R Radojewski, I. Grabowska, M. Chudy, A. Dybko, Z. Brzozka, D. Stadnik, LTCC based microfluidic system with optical detection, Sens. Act. B111-112, (2005), 396-402

/9. / H. Birol, T. Maeder, P. Ryser, Processing of graphite based sacrificial layer for microfabrication of low temperature co-fired ceramics (LTCC), Sensors Actuators, A 130-131, (2006), 560-567

/10. / H. Birol, T. Maeder, P. Rayser, Application of graphite-based sacrificial layers for fabrication of LTCC (low temperature co-fired ceramics) membranes and micro-channels, J. Micromechanics and Microengineering, 17, (1), (2007), 50-60

/11. / L. E. Khong, Y. M. Tan, Y. C. Lam, Carbon burnout and densification of self-constrained LTCC for fabrication of embedded structures in a multi-layer platform, J. Eur. Ceram. Soc., 29, (3), (2009), 457-463

/12. / M. Hrovat, D. Belavič, J. Holc, J. Cilenšek, The development of the microstructural and electrical characteristics of NTC thick-film thermistors during firing, J. Mater. Sci., 41, (18), (2006), 5900-5906

/13. / A. Kundu, J. H. Jang, J. H. Gil, C. R. Jung, H. R. Lee, S. H. Kim, B. Ku, Y. S. Oh, Micro-fuel cells – current development and applications, J. Power Sources, 170, (2007), 67-78

/14. / C, R. Koripella, C. K. Dyer, D. F. Gervasio, S. P. Rogers, D. Wilcox, W. J. Ooms, Fuel processor with integrated fuel cell utilizing ceramic technology, US patent 6569553, 2003

/15. / Y. Shin, H. Woochan, H. Seungjoo, C. Chanhwa, The development of micro-fuel processor using low temperature co-fired ceramics, Int. J. hydrogen energy, 31, (3), (2996), 1925-1933

Marko Hrovat[a,f], Darko Belavič[b,f], Gregor Dolanc[a], Primož Fajdiga[a] ,Marina Santo-Zarnik[b,f], Janez Holc[a.f], Mitja Jerlah[c,f], Kostja Makarovič[a,f], Stanko Hočevar[d], Iztok Stegel[e]

[a] Jožef Stefan Institute, Jamova 39, SI-1000 Ljubljana, Slovenia
[b] HIPOT-R&D, d.o.o., Šentpeter 18, SI-8222 Otočec, Slovenia
[c] Hyb, d.o.o., Levičnikova 34, SI-8310Šentjernej, Slovenia
[d] National Institute of Chemistry, Hajdrihova 19, SI-1001 Ljubljana, Slovenia
[e] Ministry of Defence, Vojkova 55, SI-1000 Ljubljana, Slovenia
[f] Centre of Excellence NAMASTE, Jamova 39, SI-1000 Ljubljana, Slovenia

E-mail: marko.hrovat@ijs.si

Prispelo: 17.11.2010 *Sprejeto: 23.08.2011*

ULTRA-COMPACT WIDEBAND ANTENNA FOR PORTABLE DEVICE APPLICATIONS

Ahmed Toaha Mobashsher[1], Norbahiah Misran[1], Mohammad Tariqul Islam[2]

[1]Dept. of Electrical, Electronic and Systems Engineering,
Universiti Kebangsaan Malaysia, Bangi, Selangor, Malaysia
[2]Institute of Space Science (ANGKASA), Universiti Kebangsaan Malaysia,
Bangi, Selangor, Malaysia

Key words: Compact antennas; portable device; wideband antenna.

Abstract: An ultra-compact broadband antenna easily integrable on portable devices is presented. The antenna is composed of **a printed rectangular radiating** element and a C-strip printed as the ground plane on the other side. The overall antenna occupies a compact area of 56.5 × 2 × 0.5 mm^3, yet generating two resonant modes to form 39% (850MHz) wide impedance bandwidth from 1.75 to 2.6GHz with stable omni-directional radiation pattern with low cross-polarization.

Ultra kompaktna širokopasovna antena za uporabo v prenosnih napravah

Kjučne besede: kompaktne antene, prenosne naprave, širokopasovna antena

Izvleček: Predstavljena je zelo kompaktna širokopasovna antena, ki se jo zlahka namesti v prenosne naprave. Sestavljena je iz tiskanega pravokotnega sevajočega elementa in ozemljitvijo v obliki tiskanega C-traku na drugi strani tiskanine. Celotna antena zavzema površino 56.5 × 2 × 0.5 *mm*^{3}, deluje v dveh resonančnih načinih, s pasovno širino 39% (850MHz) na frekvenčnem pasu od 1.75 do 2.6GHz s stabilnim večsmernim vzorcem sevanja in nizko navzkrižno polarizacijo.

1. Introduction

In the era of modern wireless communication systems, wideband or multi-band antennas with omni directional radiation characteristics play a vital role. Increasing demand for smaller size in portable devices results in a need for effective antenna miniaturization which is a critically challenging problem due to the inevitable trade-off between the size and the performance of the antenna due to the fact that antenna performance is bound with the fundamental limits based on the size of the antenna. This is especially true in the field of radio communications, where reducing the size of an antenna leads to smaller and light-weight systems, thereby enhancing portability and minimizing electromagnetic interference with other electronic devices. Therefore it is very desirable to miniaturize the antenna in order to scale down the system size.

Conventional internal antennas for portable device applications are generally in the forms of the planar inverted-F patch antenna, very-low-profile printed or metal-plate monopole antenna, and so on [1-3]. But such internal mobile antennas usually excite large surface currents on the system ground plane of the mobile phone, which functions as an effective radiation portion. Owing to the large excited surface currents on the system ground plane, especially in the region near the internal antenna, an isolation distance of about 7*mm* or larger between the antenna and the nearby conducting elements or electronic components in the mobile phone is usually required to avoid large degradation effects on the performances of the internal antenna[4,5]. This is a big limitation for the portable devices.

To eliminate the effect of large ground plane this paper presents an ultra-compact antenna for mobile applications in DCS-1900/PCS/**PHS (1850–1990MHz), WCDMA/IMT-2000 (1920–2170MHz), wireless broadband internet (WiBro) (2.3–2.39 GHz), WLAN-IEEE 802.11b (2400–2483MHz) bands. The antenna comprises a rectangular radiating** element and a C-strip printed as the ground plane. The antenna has the advantages of microstrip feeding and lack of big ground plane makes it suitable for co-existing integration on printed circuit board (PCB). Details of the antenna design and results are presented and discussed.

2. Antenna configuration

The configuration of the compact planar antenna is illustrated in Figure 1. The design of the antenna is based on an RT/Duroid RO4350B planar substrate that has a permittivity of 3.45 and a thickness of 20mils (0.5mm). The total dimension of the antennas is 56.5 × 2 × 0.5. It is also noticed that the antenna size at the lowest frequency

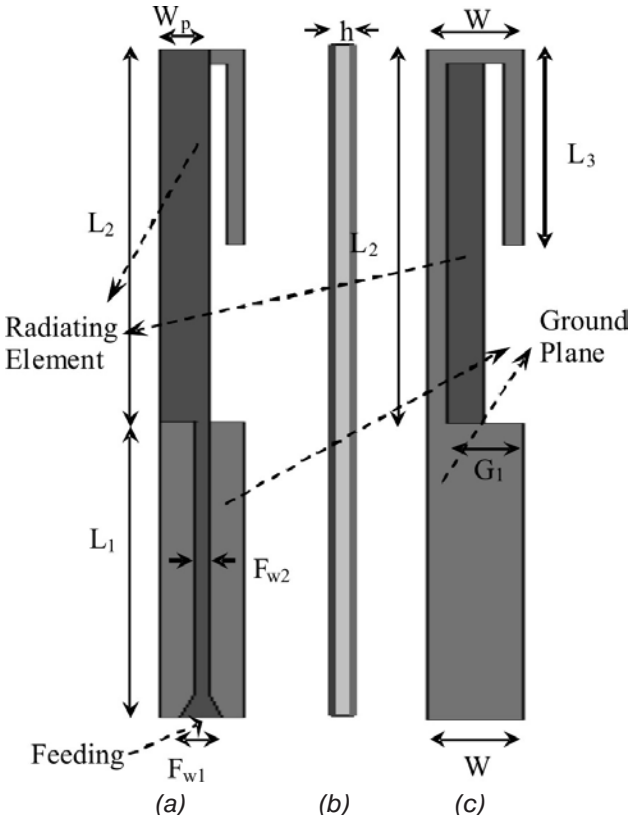

Fig. 1: Schematic Diagrams of proposed antenna (a) top view, (b) side view

(1.75GHz) is 0.33 λ_o × 0.012 λ_o × 0.003 λ_o. In one side of the antenna the rectangular ra**diating patch fed by a microstrip line of 0.4mm is designed. On the other side a C-strip a**cting as the ground plane. The feeding microstrip line is positioned at the middle of the antenna, while the rectangular patch is fed at the lower corner, which makes it only 1.5mm wide. The compactness of the planar antenna is attributed to the slim structure of the radiation element and the folded configuration of the C-strip, while the broad band performance is a result of the mutual coupling between the rectangular radiating patch and C-strip. However the tapped pad is added to enhance the lower limit of the operating frequency. The geometrical parameters of the antenna are shown in mm in the Table 1.

Table 1: Geometrical parameters of the slot-type antenna

L_1	25	h	0.5
L_2	31.5	W	2
L_3	16.5	W_p	1.2
F_{w1}	1	F_{w2}	0.4

3. Results & discussions

Generally, a 6-dBreturn loss is acceptable for the mobile phone applications [2]. The return loss of the antenna is exhibited in Figure 2. From the curve it is apparent that the antenna achieved -6dB return loss bandwidth of 850MHz, ranging from 1.75GHz to 2.6GHz, or about 39% with respect to the centre frequency at 2.18GHz.

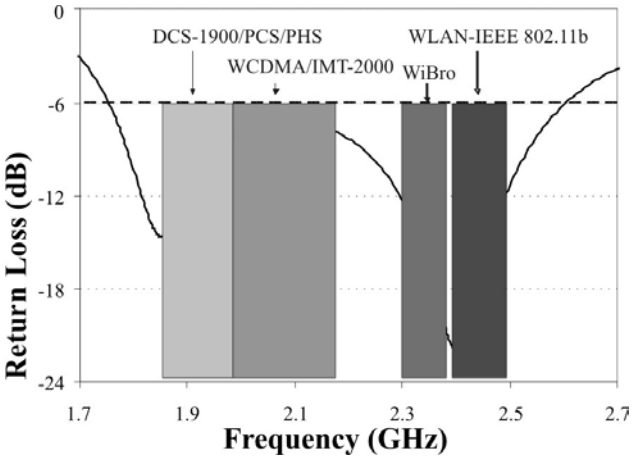

Fig. 2: Return loss of the designed antenna

The E and H plane radiation patterns of the proposed antenna at 1.85GHz and 2.4GHz has been shown in Figure 3. It can be realized that the antenna produces omnidirectional symmetrical radiation pattern in both the resonating frequencies. Moreover, a 30dB cross-polarization is observed in both E-and H-planes.

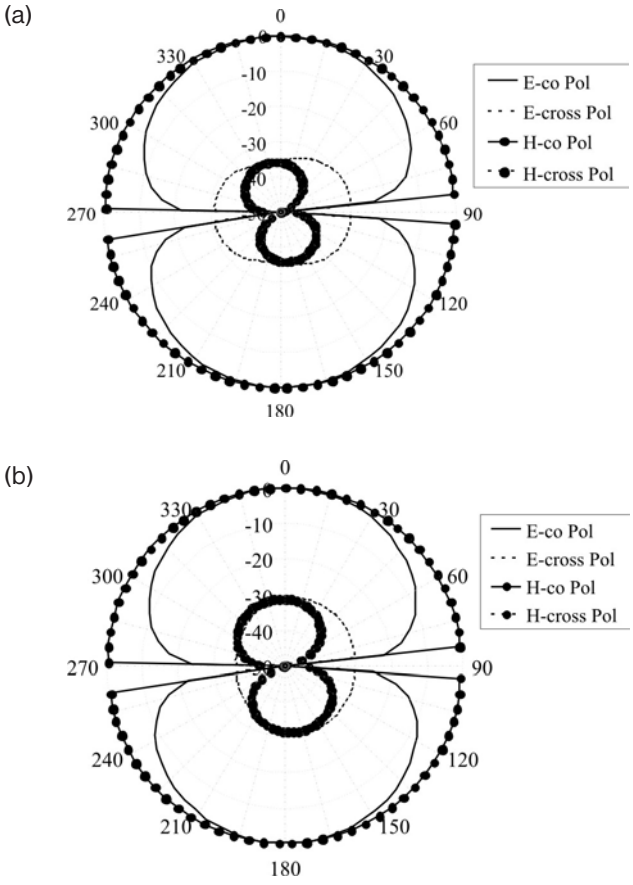

Fig. 3: Simulated radiation pattern of the proposed antenna at a) 1.85GHz, b) 2.4GHz

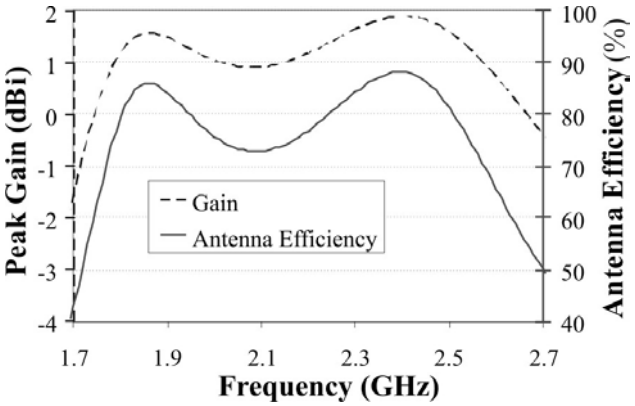

Fig. 4: Antenna gain of the proposed antenna (a) lower band and (b) upper band

Figure 4 depicts the peak gain and antenna efficiency of the proposed antenna. With a maximum gain of 1.9dBi, the antenna provides >0dBi over the whole resonating band of the antenna. The antenna efficiency takes into account the reflection losses, that is to say $\eta_a = \eta_r \times (1-|S_{11}|^2)$, where η_r is the radiation efficiency. A conductivity of $\sigma = 5.8 \times 10^7$ S/m for copper and a loss tangent of $\tan\delta = 0.0036$ for the low loss Duroide dielectric substrate were used in the simulation. A good antenna efficiency of 80% over operating band is observed for the antenna

4. Conclusion

The design of a low-profile microstrip-fed printed antenna with extremely small width, operating in the DCS-1900/ PCS/**PHS, WCDMA/IMT-2000, WiBro, WLAN-IEEE 802.11b** bands, has been proposed in this paper. The design is simple and compact with very few design parameters. The proposed antenna has small dimensions of $56.5 \times 2 \times 0.5$ mm^3 suitable for integration with application specific circuits. The present design stands out as a potential candidate for portable applications.

References

/1./ A. Cabedo, J. Anguera, C. Picher, M. Ribó, and C. Puente, "Multiband handset antenna combining a PIFA, slots, and ground plane modes," IEEE Trans. Antennas and Propagation, vol. 57, pp. 2526-2533, Sept. 2009.

/2./ C.-L. Liu, Y.-F. Lin, C.-M. Liang, S.-C. Pan, and H.-M. Chen, "Miniature internal penta-band monopole antenna for mobile phones," IEEE Trans. Antennas and Propagation, vol. 58, pp. 1008- 1011, Mar. 2010.

/3./ H.-W. Hsieh, Y.-C. Lee, K.-K. Tiong, and J.-S. Sun, "Design of a multiband antenna for mobile handset operations," IEEE Antennas and Wireless Propagation Letters, vol. 8, pp. 200-203, 2009.

/4./ K. L. Wong, S. W. Su, C. L. Tang, and S. H. Yeh, "Internal shorted patch antenna for a UMTS folder-type mobile phone," IEEE Trans. Antennas Propag., vol. 53, pp. 3391–3394, Oct. 2005.

/5./ S. W. Su, K. L. Wong, C. L. Tang, and S. H. Yeh, "Wideband monopole antenna integrated within the front-end module package," IEEE Trans. Antennas Propag., vol. 54, pp. 1888–1891, Jun. 2006.

Ahmed Toaha Mobashsher[1], Norbahiah Misran[2]
Dept. of Electrical, Electronic and Systems Engineering
Universiti Kebangsaan Malaysia,
Bangi, Selangor, Malaysia
[1]i_toaha@yahoo.com, [2]bahiah@vlsi.eng.ukm.my

Mohammad Tariqul Islam[3]
Institute of Space Science (ANGKASA)
Universiti Kebangsaan Malaysia,
Bangi, Selangor, Malaysia
[3]titareq@yahoo.com

Prispelo: 07.09.2010 *Sprejeto: 23.08.2011*

ANALYSIS OF NONLINEAR MICROWAVE CIRCUITS EXCITED BY MULTI-TONE SIGNALS USING ARTIFICIAL FREQUENCY MAPPING METHOD

Amir Vaezi, Abdolali Abdipour, Abbas Mohammadi

Microwave/mm-Wave & Wireless Communication Research Lab, Radio Communication Centre of Excellence, Electrical Engineering Department, Amirkabir University of Technology, Tehran .Iran

Key words: nonlinear microwave circuits, multi-tone signals, artificial frequency mapping method, WiMAX technology

Abstract: Artificial Frequency Mapping (AFM) is an effective method for analysis of memory-less microwave circuits excited by multi-tone signals. In this paper a new formulation for analysis of these circuits with nonlinear elements (nonlinear capacitance involved) is proposed. This is followed by introducing a linear amplifier suitable for WiMAX technology. Then, AFMT is used to evaluate the performance of the amplifier. So, the numerical results are presented and results of this CAD simulation are confirmed with other methods.

Analiza nelinearnih mikrovalovnih vezij vzbujenih z multitonskimi signali z uporabo metode umetne frekvenčne preslikave

Kjučne besede: nelinearna mikrovalovna vezja, multitonski signali, metoda umetne frekvenčne preslikave (AFM), WiMAX tehnologija

Izvleček: Umetna metoda frekvenčne preslikave, AFM, je učinkovita metoda za analizo mikrovalovnih vezij, ki so vzbujena z multitonskimi signali. V tem članku predlagamo novo metodo za analizo teh vezij z nelinearnimi elementi (nelinearne kapacitivnosti). Sledi predstavitev linearnega ojačevalnika ustreznega za uporabo v WiMAX tehnologiji. Delovanje tega ojačevalnika smo ocenili z metodo AFMT. Sledi predstavitev numeričnih rezultatov, ki jih na koncu potrdimo z drugimi metodami.

1. Introduction

The need for increased data transmission rates in wireless communications is driving the proposal of new types of wireless standards that achieve greater spectral efficiency. WiMAX based on IEEE 802.16 utilizes new modulation formats, require greater bandwidths, and necessitate multi-carrier modulation schemes, orthogonal frequency-division multiplexing (OFDM) /IEEE 802.16 standard/.

Information on system properties of analog and microwave circuits such as intermodulation distortion, noise or transfer characteristics can often be received from steady state behavior. Therefore accurate and reliable CAD tools and numerical algorithms are necessary to meet the design specifications.

As the characterization of nonlinear RF circuits using conventional single and two-tone tests is no longer sufficient to predict the circuit's response in its final operation regime. In order to follow the technology trends and meet the new standards requirements, more complicated analysis and tools is needed in the design process of nonlinear circuits such as RF power amplifiers. Therefore multitone harmonic balance (HB) proposes an appropriate analysis method. Commercial multitone HB utilizes almost periodic discrete Fourier transforms (APDFTs) /1/ or multidimensional Fourier transforms (N-FFTs) /2, 3/. Such schemes are practically limited to five or so discrete carriers. One commercial HB implementation using APDFT can handle up to ten carriers but with excessive simulation times./10/

Artificial Frequency-Mapping Technique (AFMT) is capable of modeling an arbitrary number of carriers and we have used it to handle systems with up to 150 noncommensurate tones /5/. Unfortunately, it is just applicable for memory-less nonlinear circuits /3/.

The main aim of this paper is to consider and formulate the multi-tone artificial frequency-mapping techniques (AFMTs) /2-6/ for applying to Microwave circuits with nonlinear elements – especially nonlinear capacitance – when driven with multi-tone excitation.

In this paper, first, we present the theoretical basis of AFMT applying to microwave circuits. Then, it is proposed a linear amplifier suitable for WiMAX technology. So, software is written to analyze this circuit. Also, numerical results of this CAD are confirmed with other methods. Finally the proposed CAD is used to obtain some important amplifier

characteristics such as Total Harmonic Distortion (THD), Power Added efficiency (P_{Added}), Intermodulation Distortion (IMD), Adjacent Channel Power Ratio (ACPR) and etc, play a fundamental role on correct specification of the power amplifier /2/.

2. Artificial frequency mapping :

Since Discrete Fourier Transform (DFT) is only directly applicable to periodic signals, common HB is not applicable to circuits with multitone excitation (with uncommensurated tones) /2/. If we restrict the nonlinearities' description to being memoryless /5/, their output spectrum coefficients no longer depend on input absolute frequency values, but only on their relative positions. AFMT proposes a method that converts our mixing component's vector into another one where the original proportions between frequency positions are preserved, and is both dense and harmonically related.

Generalization of AFMT, with important practical interest, uses the fact that a multi-tone signal composed of Q equally spaced tones is not characterized by Q independent base frequencies (as in the case of truly uncommensurated tones). Indeed, note that if the Q tones share an exact common separation Δf, then all Q tones can be uniquely identified by the frequency of one of them. It means that the lower frequency can defined as f_0 and others with separation of Δf which $f_q=f_0+(q-1)\,\Delta f$ where q=1, … , Q.

Thus, the total number of mixing products is $N_T=2QK^2-2K^2+2K+1$. (Eq.(1)) The mapping functions can be given by

$$\begin{aligned} f_1 &= [K(Q-1)-Q+2]\lambda \\ f_2 &= [K(Q-1)-Q+3]\lambda \\ &\vdots \\ f_q &= [K(Q-1)-Q+q+1]\lambda \\ &\vdots \\ f_Q &= [K(Q-1)+1]\lambda \end{aligned} \tag{1}$$

Therefore

$$f_k=\sum_{q=1}^{Q}k_q f_q \rightarrow \lambda_k=\left[\sum_{q=1}^{Q}k_q f_q\right]\lambda \tag{2}$$

By this mapping technique all positions are a multiple of λ, and the correspondent artificial time-domain signal is periodic, and the DFT can already be used. Therefore piecewise HB can be applied to the circuit. Since λ is arbitrary, $2\Pi\lambda$ or λ can be chosen 1.

So, the circuit is divided into two sub network linear and nonlinear part. According to HB lows Kirchhoffs current low should be satisfied At any harmonic of each port, or equivalently Eq.(3),

$$F(V_0)=Y_L V_0+j\Omega\tilde{Q}_{nl}(V_0)+\tilde{I}_{nl}(V_0)+\tilde{I}_S=0 \tag{3}$$

Where $Y_{LSNXSN}=\begin{bmatrix} y_{11} & \cdots & y_{1S} \\ \vdots & \ddots & \vdots \\ y_{S1} & \cdots & y_{SS} \end{bmatrix}$

$$Y_{ii\ NxN}=\begin{bmatrix} y_{ii}(0) & 0 & 0 \\ 0 & \ddots & 0 \\ 0 & 0 & y_{ii}(\omega_N) \end{bmatrix}$$

$V_{0\ SN\times SN}$ is voltage vector ports in form of

$$V_0=[V_1\cdots V_S]^T$$

and $V_i=[V_1(0)\cdots V_i(\omega_N)]^T$,

$$I_{nl}=[I_{nl1}\cdots I_{nlS})]^T$$

$$I_{nli}=[I_{nli}(0)\cdots I_{nli}(\omega_N))]^T$$

$$Q_{nl\ SNxSN}=\begin{bmatrix} Q_{11} & \cdots & Q_{1S} \\ \vdots & \ddots & \vdots \\ Q_{S1} & \cdots & Q_{SS} \end{bmatrix}$$ and

$$Q_{ii\ NxN}=\begin{bmatrix} Q_{ii}(0) & 0 & 0 \\ 0 & \ddots & 0 \\ 0 & 0 & Q_{ii}(\omega_N) \end{bmatrix}$$

also I_s is vector of equivalent current source at each port. S presents the number of nonlinear port and ω_i is related to any mixing component of basic frequencies that is mapped to 2Π ($\lambda_i = i\lambda$). Therefore N is the number of positive mixing frequency components including DC frequency ($N=(N_T+1)/2$).

But there are some differences between $F(v_0)$ in HB and AFM. Because Ω is the diagonal matrix of harmonic frequencies and in AFM absolute frequencies is changed. Since Ω is related to capacitive current it should be depend on original absolute frequencies (Eq.(4)). It means that frequency domain equivalent of $\frac{dq_{NL}(v_o(t))}{dt}$ is $j\omega_q Q_k$. Thus by substituting Ω by a diagonal matrix of original mixing frequency, OMEGA results in Eq.(5)

$$q_{NL}(v_0(t))=q_{NL}\left(\sum_k V_{0k}\ e^{jk\omega_0 t}\right)=\sum_k Q_k\ e^{jk\omega_0 t}$$

$$\frac{dq_{NL}(v_0(t))}{dt}=\frac{d(\Sigma_k Q_k e^{jk\omega_0 t})}{dt}=jk\omega_0\sum_k Q_k e^{jk\omega_0 t} \tag{4}$$

$$F(V_0)=Y_L V_0+jOMEGA\,\tilde{Q}_{nl}(V_0)+\tilde{I}_{nl}(V_0)+\tilde{I}_S=0 \tag{5}$$

Consequently

$$OMEGA_{SNxSN}=diagonal[\omega_{11}\cdots\omega_{SS}]^T\ and\ \omega_{ii}=diagonal[0\cdots\omega_N]^T$$

instead of:

$\Omega_{ii}=diagonal(2\Pi[\lambda_0\ \lambda_1\cdots\lambda_i\cdots\lambda_{N-1}]^T$ where $\lambda_i=i\lambda$

In the next section this method is applied to a power amplifier when driven by Multi-tone or two tone excitation signal.

3. Simulation and results

In this section one-stage class A power amplifier with 16 dBm of gain and output power of 18 dBm suitable for use in Fixed WiMAX technology based on IEEE 802.16 d standard. It is designed to work at WiMAX profile with 200MHz bandwidth centered at frequency of 3.5 GHz. The amplifier

includes input and output Micro-strip matching networks and the necessary DC bias circuitry. The Pseudomorahic InGaAs/ AlGaAS/GaAs HEMT /8/ is used to realized power amplifier. According to reduction of harmonic distortion on output power, it is biased in class A so V_d =6 V and V_g =0 V is chosen. Matching networks are designed and optimized to obtain maximum output power and minimum harmonic distortion.

Within the H-B simulator, they were represented by appropriate multi-port admittance matrices. The active device includes three nonlinear ports corresponding to gate-source, gate drain and drain-source control voltages and currents. For its equivalent circuit nonlinear elements, the nonlinear Curtice 3 model /9/ was adopted. Figure 1 shows the power amplifier circuit schematic. *This power-amplifier circuit was excited by four different types of signals:*

1) Sinusoidal input—one tone;
2) Sinusoidal input—two tones;
3) Sinusoidal multi-tone tone;

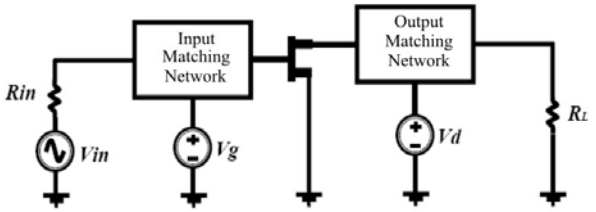

Fig. 1 .Schematic of circuit.

1) One-Tone Test: The first test step consisted of several continuous wave (CW) experiments to evaluate transducer power gain (Gain), output power , and PAE versus input drive level. Results of one-tone excitation is obtained from a one dimensional HB simulator. As seen in figure 2 the PA presents a 1-dB compression point of P1dB= 18.33 with an associated Gain of 16.23 dB and PAE of nearly 19%. Figure 3 shows the simulated output power and its harmonic levels at center frequency. So a Total Harmonic Distortion (THD) /3/ of THD 34.027 dBc, at this P1dB level, was deduced from Figure 3. Fundamental component of output power for the single tone input 2dBm at different frequencies are illustrated in Figure 4.

2) Two-Tone Test: As another classic linearity evaluation, the IMD performance was tested. The excitation was a two tone centered at 3.5GHz and separated by 100 MHz. The simulation is performed using AFMT. So two-tone spectrum, which was truncated to fifth order. The extension of this AFM to two-base frequencies diamond truncated up to order K gives 2K2+2K+1=61 as the total number of mixing products, therefore the mixing product matrix has a dimension of 31. By applying mapping technique, the output fundamental power per tone and single sideband IMD power results shown in Figure 5. A direct reading of this plot immediately provides IMR as a function of input drive level (shown in Figure 5), while the extrapolation of output fundamental and IMD power from the small-signal regime, leads to a third-order intercept point of nearly IP3 = 27.5 dBm.

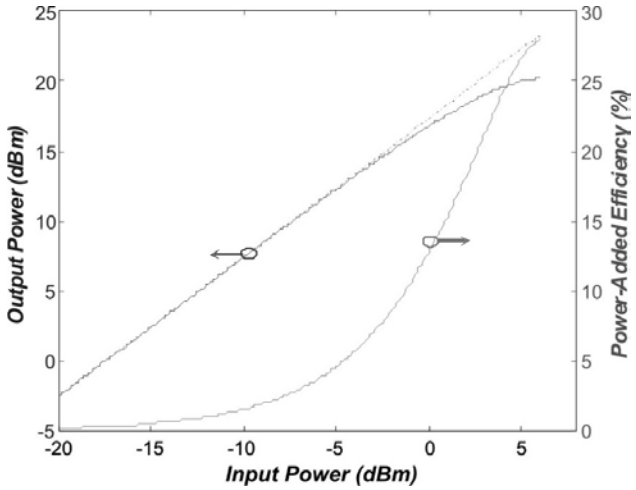

Fig. 2. PA output power and Power added Efficiency versus input drive level.

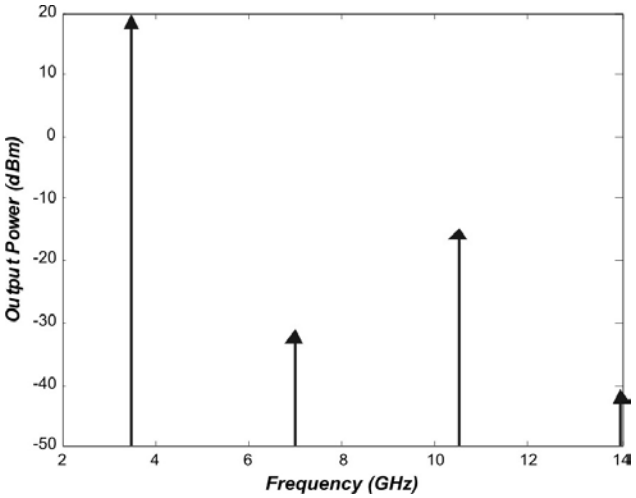

Fig. 3. Output power spectrum when subject to a one-tone excitation of P1dB (18.33 dBm) output power level.

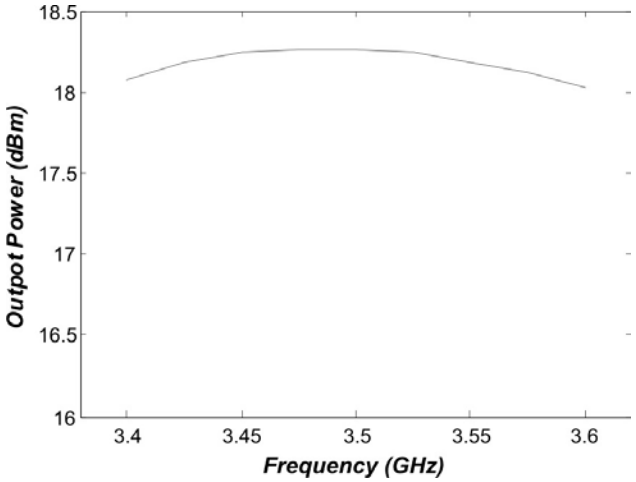

Fig. 4. Output spectrums for single tone input versus frequency in desired bandwidth

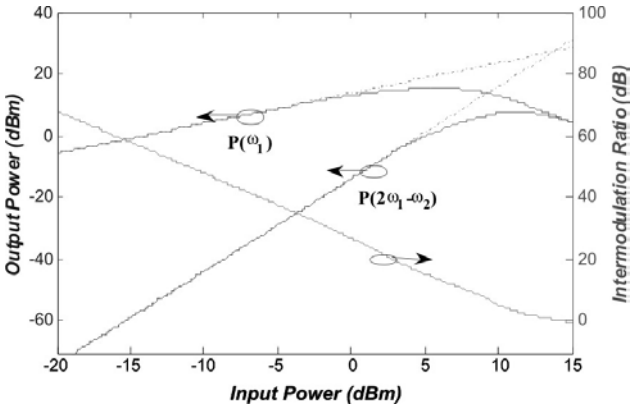

Fig. 5. Fundamental, IMD output power per tone, and inferred two-tone IMR, as a function of PA's input drive level per tone.

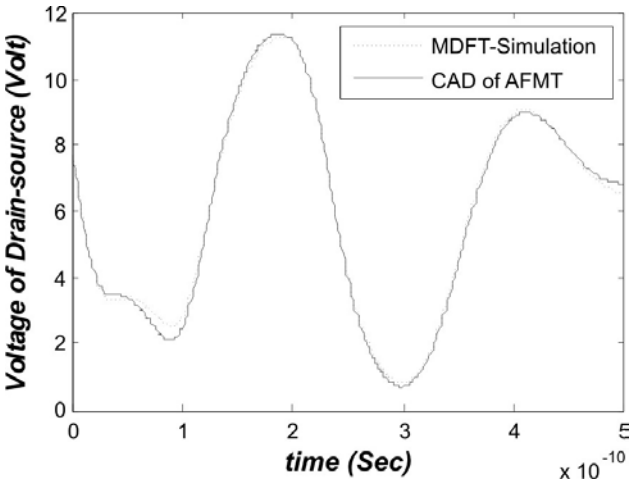

Fig. 6. Voltage of Drain-Source simulated with two different methods

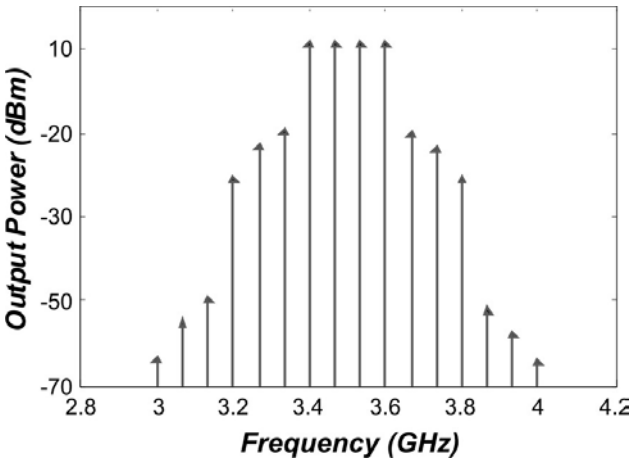

Fig. 7. Output power spectrum of PA exited by 2dBm multi-tone signal

3)Multi-Tone Test: After these two-tone tests, our designed amplifier was subject to a Multi-tone input signal. The amplifier's driving signal was composed of four tone distributed at desired bandwidth started at 3.4 GHz and exact common separation of 667 MHz. since Q=4 and K=5 according to Eq.(1) the number of mixing products is 161 and the dimension of mixing product matrix is 81. The results of simulation with AFM are confirmed with Multi Dimensional Discrete Fourier Transform (MDFT) method. It is illustrated in figure 6. Figure 7 shows the inband portion of the output spectrum. Calculated value of Total Adjacent-Channel Power Ratio /3/ ($ACPR_T$), about 22.1 dB was obtained.

Acknowledgment

This work was supported in part by Iran Telecommunication Research Center (ITRC).

References

/1/ Kundert, K.S.; Sorkin, G.B.; Sangiovanni-Vincentelli,A, **"Applying harmonic balance to almost-periodic circuits"** Microwave Theory and Techniques, IEEE Transactions on Volume 36, Issue 2, Feb 1988 Page(s):366 – 378

/1/ S. Maas, **"Nonlinear microwave circuits",** Artech House, Norwood, MA (1988).

/2/ J.C. Pedro and N.B. Carvalho, **"Intermodulation distortion in microwave and wireless circuits",** Artech House, Norwood, MA (2003).

/3/ Hente, D., and R. H. Jansen, **''Frequency Domain Continuation Method for the Analysis and Stability Investigation of Nonlinear Microwave Circuits,''** IEE Proceedings-H Microwaves Antennas and Propagation, Vol. 133, No. 5, 1986, pp. 351–362.

/4/ Carvalho, N.B.; Pedro, J.C.; Jang, W.; Steer, M.B. **,"Nonlinear RF circuits and systems simulation when driven by several modulated signals"** Microwave Theory and Techniques, IEEE Transactions on Volume 54, Issue 2, Feb. 2006 Page(s): 572 – 579

/5/ Carvalho, N.B.; Pedro, J.C.; Jang, W.; Steer, M.B **"simulation of mixers for assessing system-level performance",** International Journal of RF and Microwave Computer-Aided Engineering, Volume 15 , Issue 4 (July 2005) Pages: 350 – 361, 2005

/6/ Amir Vaezi, Abdolali Abdipour, Abbas Mohammadi, "A novel approach to analysis of nonlinear circuits excited by modulated signals" Informacije MIDEM, Journal of Microelectronics, Electronic Components and Materials, Volume 39, Issue 3, September 2009, Pages 156-161. ISSN 0352-9045

/7/ Siddiqui, M.K.; Sharma, A.K.; Callejo, L.G.; Lai, R.,**"A high-power and high-efficiency monolithic power amplifier at 28GHz for LMDS applications"** Microwave Theory and Techniques, IEEE Transactions on Volume 46, Issue 12, Dec 1998 Page(s):2226 - 2232

/8/ W. R. Curtice, and M. Ettenberg, **"A nonlinear GaAs-FET model for use in the design of output circuits for power amplifiers,"** IEEE Trans. Microwave Theory Tech., vol. 33, pp. 1383-1394, Dec. 1985.

/9/ Agilent Technologies, Advanced design system, Palo Alto, CA, 2006.

Amir Vaezi , Abdolali Abdipour , Abbas Mohammadi
Microwave/mm-Wave & Wireless Communication Research Lab, Radio Communication Centre of Excellence,
Electrical Engineering Department, Amirkabir University of Technology
424 Hafez. Ave, Tehran .Iran
E-mail: vaezi@aut.ac.ir

Prispelo: 03.11.2010 *Sprejeto: 23.08.2011*

A REVIEW ON THERMAL CYCLING AND DROP IMPACT RELIABILITY OF SOLDER JOINTS IN ELECTRONIC PACKAGES

Dhafer Abdulameer Shnawah, Mohd Faizul Mohd Sabri, Irfan Anjum Badruddin

Department of Mechanical Engineering, University of Malaya, Kuala Lumpur, Malaysia

Key words: Soldering, thermal cycling, drop impact, failure mode, material requirement

Abstract: Currently, the trend of miniaturization, light weight, high speed and multifunction are common in electronic assemblies, especially, for the mobile electronics. One of the most critical aspects of the package reliability is solder joint reliability. So, in that field, thermal cycling and drop/impact are the primary requirement for solder joint reliability. This paper discusses the reliability of solder joint in term of both temperature cycles load and drop/impact load from view points of failure mode and relevant material properties. High compliance and high grain-coarsening resistance are identified as key material properties for high thermal cycling and drop impact reliability respectively. The paper details the requirements solder joints have to meet to be qualified for the mobile electronics applications. Therefore, this contribution has its value in giving information on suitable material electronic devices under different loading condition.

Vpliv termičnih in fizičnih obremenitev na zanesljivost spajkanih spojev v elektronskih vezjih

Kjučne besede: spajkanje, termične in fizične obremenitve, načini odpovedi, lastnosti materiala

Izvleček: Miniaturizacija, zmanjševanje teže, velika hitrost in večopravilnost so trenutni trend lastnosti elektronskih vezij, še posebej namenjenih mobilnim napravam. Eden najbolj kritičnih vidikov zanesljivosti elektronskega modula je zanesljivost spajkanega spoja. Le-ta mora biti odporen na termične in fizične obremenitve. V prispevku obravnavamo zanesljivost spajkanega spoja ter vpliv materialnih lastnosti na vzroke odpovedi po termičnih in udarnih obremenitvah. Naštejemo vse zahteve, ki jih zanesljiv spoj mora zadovoljevati, da zadosti kvalitetnim kriterijem za uporabo v elektronskih modulih namenjenih mobilnim napravam.

1. Introduction

An electronic package integrates metal conductors, organic/ceramic dielectrics and semiconductors into a functional device. This variety of materials results in a complex system to build and, increasingly, retain high levels of reliability. Reliability is influenced by the operation of the device (e.g., power dissipated, current carried, etc.) and the environment (e.g., ambient temperature, temperature changes and imposed mechanical strains) (Frear et al., 2008). Traditionally, only temperature and power cycling were of concern for board level reliability, and coefficient of thermal expansion mismatch between the package and the board was considered as the primary failure mechanism. However, due to the proliferation of electronic devices across market segments, ranging from automotive to small, hand-held devices; electronic packages experience mechanical loading conditions other than just temperature cycling (Syed et al.). This additional failure mechanism has their implications on package material selection to design a robust package meeting reliability requirements for a particular end use application.

Thermal cycling and mechanical shock are two of major loads that lead to the failure of board-level solder joints for portable electronic product. Board-level package is a multi-material system. These various materials cause the mismatch of Coefficient of Thermal Expansion (CTE). The CTE mismatch between PCB (composed of FR4 material and polymer) and package (composed of substrate, die and mold cap) results in the thermo-mechanical fatigue damage of solder joints when the board-level package is subjected to thermal cycling load. The fatigue crack initiates and propagates through the bulk solder (Zhang et al., 2009). The increasing occurrence of drop-impact failure of portable electronics has been traced to the failure of the solder joints that interconnect the integrated circuit (IC) components to the printed circuit board (PCB). The drop-impact of portable electronics leads to bending of the PCB assembly within the portable electronic device; the interconnecting solder joints undergo severe deformation to accommodate the differential bending deformation between the IC component and the PCB (Wong et al., 2009). The strain rate of solder joint under mechanical shock load (e.g. drop impact) is much higher than that under thermal cycling load. The strength properties of the bulk solder will increase with the increasing of strain rate (Wong et al., 2008b, Zhu et al., 2007). The solder joints have less plastic deformation due to the higher strain rate under drop load compared with that under thermal cycling load, so the stress at the inter-metallic compound (IMC) layers increases and

exceeds the fracture strength of IMC. The crack initiates and propagates along the IMC layer (Mattila and Kivilahti, 2005). The failure mode, and therefore the reliability of interconnection, relies on the properties of solder matrix. This paper will discuss the thermal cycling and drop impact reliability of solder joints in electronic packaging from the view points of material properties, failure mechanism and crack propagation.

2. Drop impact reliability

For portable electronic applications, one of the greatest challenges for the package assembly is to survive a challenging use environment that includes being dropped, result at the end in electrical failure (Frear et al., 2008). "Drop-impact" refers to free fall under gravity followed by an impact on a target such as the ground. Upon impact, a fraction of the kinetic energy of portable electronic product will be converted to sound and frictional heat energy, a portion to elastic and plastic strain energy in the product housing, and the rest to elastic and plastic strain energy of the interior components including printed circuit board (PCB), integrated circuit (IC) components and interconnects (mainly solder joints) (Wong et al., 2008a). The literature on drop impact loading of electronic packages and assemblies is starting to grow (Alajoki et al., 2005, K. Mishiro, 2002, Mattila, 2005, Tee et al., 2003). The weak link in the package is the board level solder joint between the package and the printed circuit board.

The failure mode during drop impact loading is manifested in interfacial cracking along the solder joint (either on the package or board side (Suh et al., 2007, Syed et al., 2006) as shown in Figure 1 (M.P. Renavikar, 2008). In either case, shock failure is characterized by a lack of solder deformation and an absence of solder bulk cracking. This is due to the strain-rate sensitivity of metallic materials. Metallic materials including solders typically become stronger with increasing strain rates. Thus, the robustness of a solder joint is influenced by a complex combination of bulk solder and inter-metallic properties (Grafe et al.). Ductile failures through bulk solder typically progress slowly, but crack through brittle inter-metallic progress much faster (Frear et al., 2008). The outstanding question is whether "bulk" properties of solder can be optimized to suppress or delay this essentially interfacial" crack propagation along the solder joints. The so-called extrinsic toughening concept can be invoked to answer the question (Suh et al., 2007). The extrinsic toughening refers to a toughening mechanism by reducing effective crack driving force that the crack tip actually experiences through various energy dissipation processes without increasing inherent fracture resistance of the material or interface (Ritchie, 1988). High compliance (i.e., low elastic modulus) and high plastic energy dissipation (i.e., low yield strength) ability are identified as key material properties to be optimized for extrinsic toughening mechanism (Suh et al., 2007). Hence, solder alloy with low compliance and high plastic energy can help increase the drop performance because softer solder joint can help to absorb more dynamic energy to reduce the dynamic stress transformed from PCB to IMC/solder interface layer (Che et al.). There is a high variation in the life of similar solder joints since the cracks can change from ductile to inter-metallic due to random variation in the microstructure of individual joints.

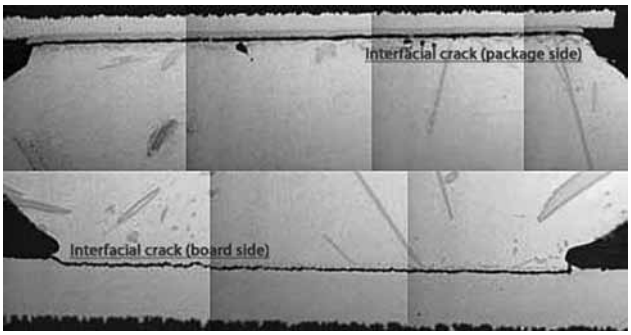

Fig. 1: SAC405 solders joint failure in shock conditions (M.P. Renavikar, 2008)

However, the strain rate experienced by solders joint or the boards during drop/shock testing is estimated to be10^2/sec., which belongs to dynamic-to-impact loading condition. Under these conditions the behavior of the metallic material is denominated by elasticity (Suh et al., 2007). In other words, plasticity is suppressed under these high strain rates; therefore, elastic compliance is becoming a key material property for drop impact performance. A high compliance solder is expected to be favorable for drop impact performance because it tends to lower stress transfer to vulnerable joint region (Garner, 2009, Kim et al., 2007). Figure 2 is a schematic diagram showing two different hypothetical solder joint behaviors during drop

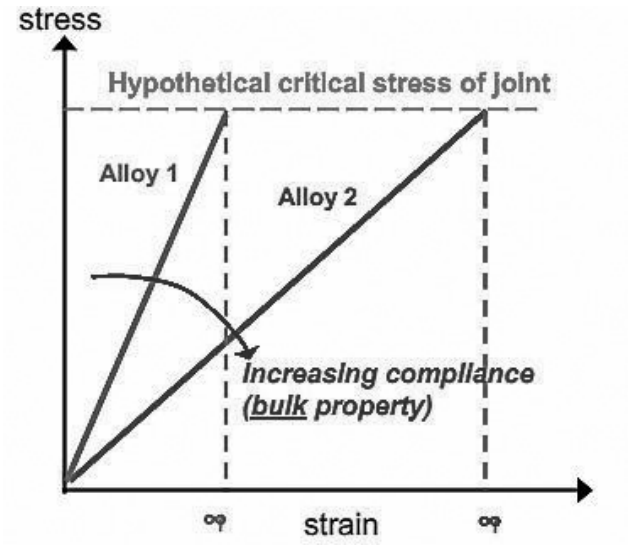

Fig. 2: Schematic stress-strain behavior of solder joint with two hypothetical alloys with different compliances. Note high compliance alloy (alloy 2) has lower stress under the same board displacement or strain (Suh et al., 2007)

testing. Alloy 2 has higher elastic compliance than alloy 1 and as a result, the stress at the solder joint of alloy 2 is lower than that of alloy 1 at the same board deflection (and therefore the same strain). Therefore, the solder joint with alloy 2 takes longer board deflection (or strain) to reach the same critical stress of the joint than the solder joint with alloy 1. In other words, a solder alloy with higher elastic compliance is expected to exhibit longer critical strain to failure (i.e., higher drop resistance) than a solder alloy with lower elastic compliance (Suh et al., 2007).

One of concerns for industry to address solder interconnect reliability under mechanical drop impact is the test methods for qualifying designs/materials and for quality assurance during manufacturing (Newman, 2005, Seah et al., 2006, Wong et al., 2005). Classic mechanical solder joint tests like shock, vibration and drop, result at the end mainly in electrical pass/fail information. More essential for solder joint characterization are test methods that provide more detailed information on the solder joint failure mode occurred. Fast Solder Ball Shear Test (see Figure 3) is recommended to address solder interconnect reliability (Grafe et al.). The interdependence between the various strength characteristics of a solder ball interconnect is depicted in Figure 4. A ductile/elastic solder alloy (1) is able to withstand higher strain rates compared to a stiffer solder alloy (2) before reaching the IMC fracture limit. The ability of a solder joint to deform in its bulk before IMC fracture is basically measured with FBST. The output from the FBST involves two basic parameters: (1) Energy before peak force (mJ) and (2) Fracture mode occurred in testing. The energy before peak is the area below the force plot till the peak force (see Figure 5), which directly correlates to the type of fracture which has happened and hence is useful for solder joint characterization (Grafe et al.).

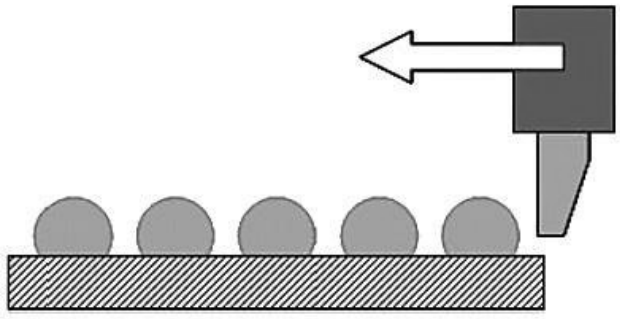

Fig. 3: Fast ball shear test arrangement (Grafe et al.)

The failure of board-level solder interconnects in drop tend to be more extensive in ball grid array BGA packages than land grid array because the joint is thicker and more dynamic strain is imposed (Frear et al., 2008). The drop impact failure behavior of the BGA joints was classified into three types in terms of the crack initiating points (see Figure 6); a crack initiating in the IMC layers (CI), a crack initiating in solder balls (CS), and a failure occurring as a result of large ductile deformation of solder balls (DD). For these three types of the failure, the corresponding three types of

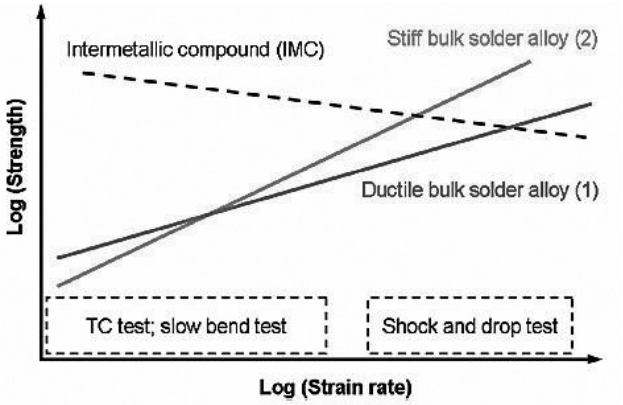

Fig. 4: Joint strength vs. strain rate (Grafe et al.)

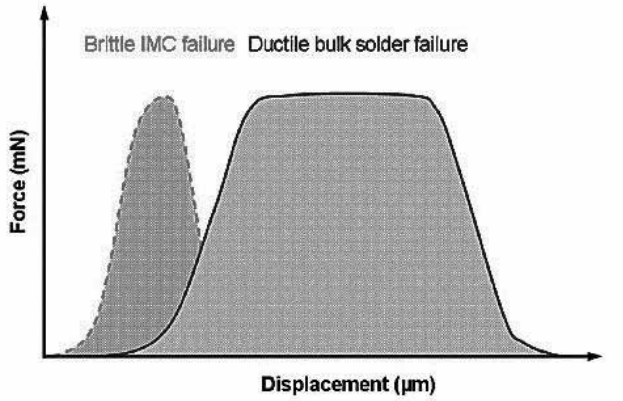

Fig. 5: FBST force vs. displacement (Grafe et al.)

practical failure situations can be considered (Tsukamoto et al., 2010). The CI-failure can occur in the practical situation that the BGA joints are subjected to high speed impact loadings such as drop conditions. The CS-failure can occur in the case that some objects bump into the solder balls in the packages. The DD-failure can occur in the case that the large shear deformation of solder parts occurs under low displacement- rate conditions (Tsukamoto et al., 2010).

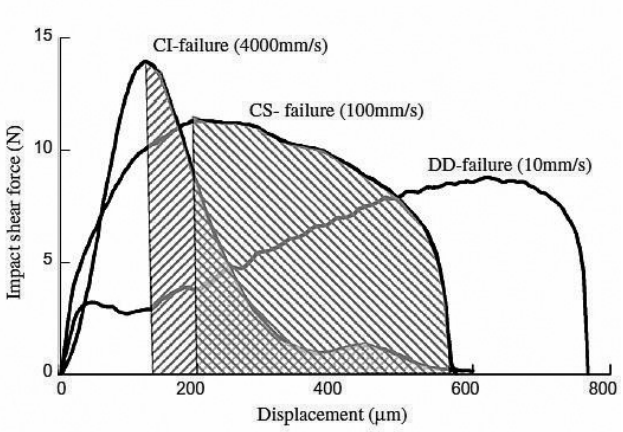

Fig. 6: Failure model of BGA joints subjected to shear loading (Tsukamoto et al., 2010)

3. Thermal cycling reliability

Thermo mechanical fatigue occurs when materials with different CTEs are joined and used in an environment that experiences cyclic temperature fluctuations resulting in imposed cycling strain. Thermo mechanical fatigue is a major deformation mechanism concern for solder joint in electronic packages (Frear et al., 2008). The type and magnitude of strains in solder joints under conditions of thermo mechanical fatigue is often quite complex. For surface mount applications, the strain is nominally in shear as shown in Figure 7. However, tensile and mixed-mode strains can occur due to bending of the chip- carrier or board as shown in Figure 8 (Abtew and Selvaduray, 2000, Frear, 1991, Frear et al., 1989).

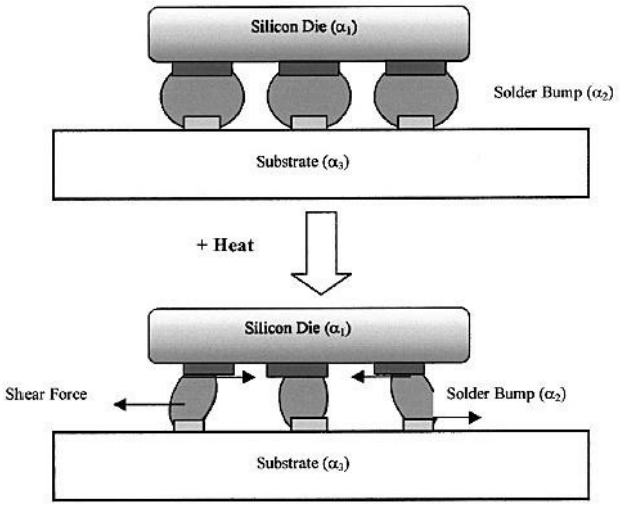

Fig. 7: solder joint subjected to shear strain during thermal cycling due to CTE mismatch (Abtew and Selvaduray, 2000)

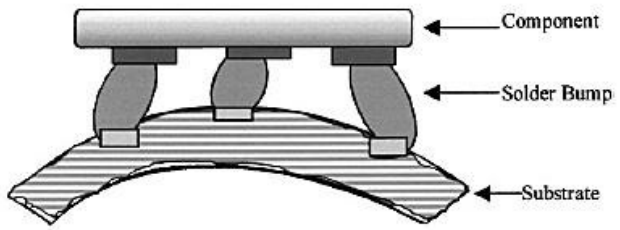

Fig. 8: solder joint subjected to tensile loading due to substrate flexing (Abtew and Selvaduray, 2000)

The combination of strain and temperature during thermo mechanical fatigue has a large effect on the microstructure, and micro structural evolution of solder joints (Frear, 1991, Frear et al., 1989). Strain concentration enhances diffusion leading to micro structural coarsening at elevated temperatures (Abell and Shen, 2002). It has been observed that typically only a fraction of the solder joint cross–section actually participates in cyclic deformation because strain distribution inside solder joints is seldom uniform. Deformation of the most highly strained areas of solder joints leads to localized deformation. The recrystallization or grain coarsening takes place first in the regions where the microstructure is most heavily deformed plastically and then gradually expands. Failure eventually occurs due to cracks that form in the coarsened regions of a joint. The thermal anisotropy of the recrystallized grains enhances the nucleation of micro cracks along their boundaries (Mattila, 2005). The failure mechanism under thermal cycling has been widely studied by many researchers (Hirano et al., 2001, Lee et al., 2002, Sohn, 2002). It was observed that cracks always take place inside the matrix of solder along or close to intermetallic layers closely parallel to the direction of imposed shear strain as shown in Figure 9. The propagation path of the crack shown in Figure 9a is enclosed entirely within the recrystallized region of the interconnection shown in Figure Figure 9b (Mattila et al.). The propagation of cracks, and therefore the reliability of interconnection, relies on the properties of solder matrix. The solder alloy with low strength facilitate plastic deformation of the solder alloy by external stress of solder joint and cracks are generated and grow more easily within the solder and shows poor fatigue resistance (Che et al.).

(a)

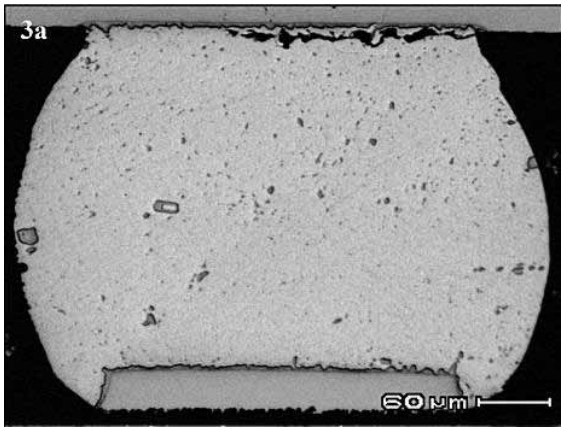

(b)

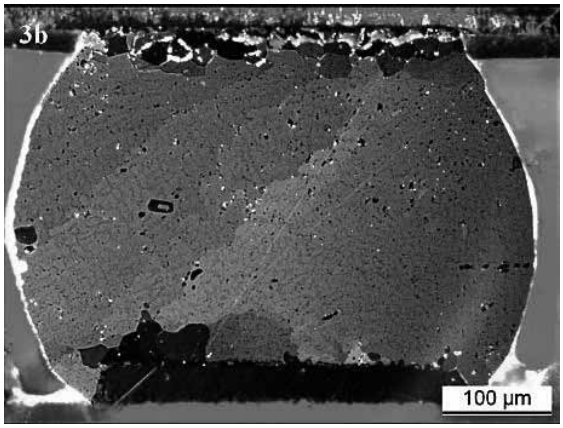

Fig. 9: Thermal cycle results (-40/125 OC) of SAC305 solder bump for a CSP BGA (Mattila et al.)

Standardized accelerated thermal cycling tests (ATC) are commonly used to evaluate the thermo mechanical reliability of electronic assemblies (Laurila et al., 2007, Li et

al., 2009, Zhang et al., 2005). During ATC, assemblies are uniformly heated up and cooled down in order to induce thermo mechanical strains and stresses in interconnections and interfaces of the assemblies. The main processing unit of the contemporary handheld multimedia smart Nokia N95 phone (see Figure 10), the Application engine (AE), was chosen for thermo mechanical reliability characterization under accelerated thermal cycling test. The AE component is a stacked-die BGA package-on-package design. The structure of the component is shown in Figure 11. A polarized image of the critical interconnection cross-section after testing is shown on the left side of Figure 12. The image shows that a crack has initiated and propagated through the interconnection close to the intermetallic compound layer on the PWB side of the interconnection. The image also shows recrystallization of the bulk solder. The calculated von Mises stress contour map of the critical interconnection cross-section at the time of the peak stress (at the end of the ATC-40°C low-temperature dwell) is shown on the right side of Figure 12. It can be seen from Figure 12 that the contour map agrees well with the observed crack location (Karppinen et al., 2010).

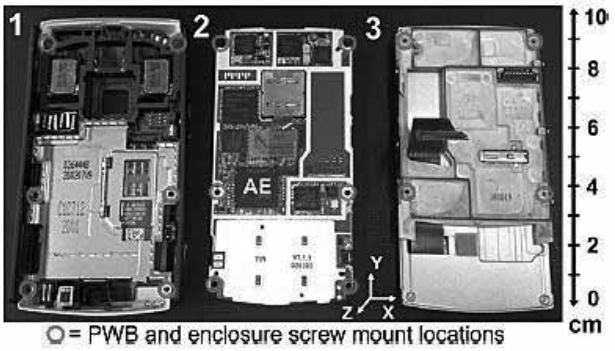

Fig. 10: Construction of the device: (1) lower enclosure, (2) main board and (3) display assembly. The Application engine (AE) component is marked for closer examination (Karppinen et al., 2010)

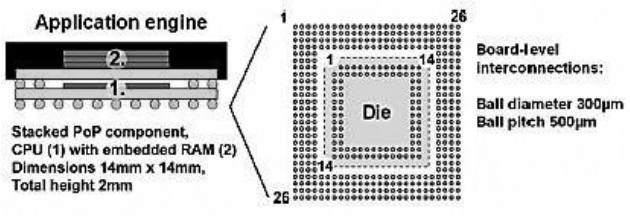

Fig. 11: Application engine component package (Karppinen et al., 2010)

4. Consecutive Multiple Loadings

Since portable electronics are often dropped after working for a period of time, usually interconnections are subjected to consecutive thermo-mechanical and mechanical loadings. The thermal cycling before drop test can introduce two different changes to the microstructure of interconnections: 1) The thermal mechanical strain and elevated

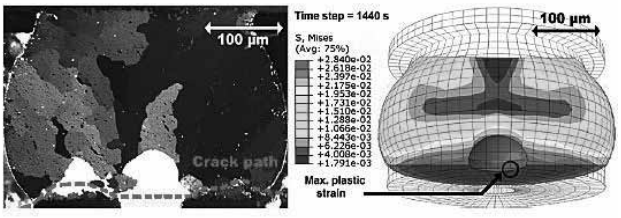

Fig. 12: Left: The polarized light cross-sectional image of the critical interconnection in ATC. Right: The calculated FEA stress contour map of the critical interconnection at the time of peak stress (end of low-temperature dwell at 40oC) (Karppinen et al., 2010)

temperature induces recrystallization in highly deformed region and fatigue cracks along large angle grain boundaries are developed; 2) The thickness of inter-metallic layers increases and the interfacial structure evolves with time. The first change weakens the mechanical properties of bulk solder under drop impact loading so that the cracking occurs partly through bulk solder (Mattila and Kivilahti, 2006).

Without temperature variation, the isothermal annealing has only the aging effects to interfacial microstructure. Since the effective time for inter-metallic growth is approximately only the total time of the upper soak stages in thermal cycling (Xu et al., 2005), inter-metallic layers have much more time to grow during isothermal annealing. If copper UBM is used on the component side, the formations of Cu_6Sn_5 and Cu_3Sn follow the typical growth kinetics (Mei et al., 1992, Paul, 2004, Rönkä et al., 1998). Given adequate time, the formation of "Kirkendall void" in the Cu_3Sn layer (Zeng et al., 2005) is much more severe during isothermal annealing and the rupture of inter-metallic layer becomes the primary failure mechanism, which degrades the drop loading reliability significantly (Mattila and Kivilahti, 2006).

5. Conclusion

Elevated operating temperatures can degrade/change the materials properties/ performance and the reliability of the solder joint.

The dominant failure mode under thermal cycling load is recrystallization-assisted crack nucleation and propagation. Hence, solder joint with a good fatigue resistance can be expected as result of inhibiting recrystallization.

High strength solder joint can exhibit a good fatigue resistance due to suppressing plastic deformation during thermal cycling loading.

The good drop performance can be attributed to extrinsic toughening mechanisms through high bulk compliance and high plastic energy dissipation during crack propagation.

Softer solder joint can help to absorb more dynamic energy during drop impact loading to reduce the dynamic stress transformed from PCB to IMC/solder interface layer.

Acknowledgement

The authors would like to acknowledge the financial support provided by the Institute of Research Management and Consultancy, University of Malaya (UM) under the IPPP Fund Project No.: PS117/2010B

Reference

/1/ ABELL, K. & SHEN, Y. L. 2002. Deformation induced phase rearrangement in near eutectic tin-lead alloy. Acta materialia, 50, 3193-3204.

/2/ ABTEW, M. & SELVADURAY, G. 2000. Lead-free solders in microelectronics. Materials Science and Engineering: R: Reports, 27, 95-141.

/3/ ALAJOKI, M., NGUYEN, L. & KIVILAHTI, J. Year. Drop test reliability of wafer level chip scale packages. In, 2005. IEEE, 637-644 Vol. 1.

/4/ CHE, F., POH, E. C., ZHU, W. & XIONG, B. Year. Ag Content Effect on Mechanical Properties of Sn-xAg-0.5 Cu Solders. In.: IEEE, 713-718.

/5/ FREAR, D. 1991. Microstructural evolution during the thermomechanical fatigue of solder joints. Sandia National Labs., Albuquerque, NM (United States).

/6/ FREAR, D., GRIVAS, D. & MORRIS, J. 1989. Parameters affecting thermal fatigue behavior of 60Sn-40Pb solder joints. Journal of Electronic Materials, 18, 671-680.

/7/ FREAR, D., RAMANATHAN, L., JANG, J. W. & OWENS, N. Year. Emerging reliability challenges in electronic packaging. In, 2008. IEEE, 450-454.

/8/ GARNER, S. S., D.SUH, T. BYRNE, A. DANE, T. MARTIN, M. MELLO, M. PATEL AND R. WILLIAM, 2009. Finding solutions to the challenges in package interconnect reliability. Intel Technology Journal,, 9, 297-308.

/9/ GRAFE, J., GARCIA, R., LABAYEN, M., GRASSME, O., GANESHAN, V., NOCKE, K., BREUER, D. & DRESDEN, Q. Reliability and Quality Aspects of FBGA Solder Joints.

/10/ HIRANO, T., FUKUDA, K., ITO, K., KIGA, T. & TANIGUCHI, Y. Year. Reliability of lead free solder joint by using chip size package. In, 2001. IEEE, 285-289.

/11/ K. MISHIRO, S. I., M. ABE, T. KUMAI, Y. HIGASHIGUCHI,K. TSEBONE 2002. Issues related to the implementation of Pb-free electronic solders. Microelectronics Reliability, 42, 77.

/12/ KARPPINEN, J., LI, J., MATTILA, T. & PAULASTO-KRÖCKEL, M. 2010. Thermomechanical reliability characterization of a handheld product in accelerated tests and use environment. Microelectronics Reliability.

/13/ KIM, D., SUH, D., MILLARD, T., KIM, H., KUMAR, C., ZHU, M. & XU, Y. Year. Evaluation of high compliant low Ag solder alloys on OSP as a drop solution for the 2nd level Pb-free interconnection. In, 2007. IEEE, 1614-1619.

/14/ LAURILA, T., MATTILA, T., VUORINEN, V., KARPPINEN, J., LI, J., SIPPOLA, M. & KIVILAHTI, J. 2007. Evolution of microstructure and failure mechanism of lead-free solder interconnections in power cycling and thermal shock tests. Microelectronics Reliability, 47, 1135-1144.

/15/ LEE, S. W. R., LUI, B. H. W., KONG, Y., BAYLON, B., LEUNG, T., UMALI, P. & AGTARAP, H. 2002. Assessment of board level solder joint reliability for PBGA assemblies with lead-free solders. Soldering & surface mount technology, 14, 46-50.

/16/ LI, J., KARPPINEN, J., LAURILA, T. & KIVILAHTI, J. K. 2009. Reliability of Lead-Free Solder Interconnections in Thermal and Power Cycling Tests. Components and Packaging Technologies, IEEE Transactions on, 32, 302-308.

/17/ M.P. RENAVIKAR, N. P., A. DANI, V. WAKHARKAR, G. ARRIGOTTI, V. VASUDEVAN, O. BCHIR, A.P. ALUR, C.K. GURUMURTHY, R.W. STAGE 2008. Materials technology for environmentally green micro-electronic packaging. Intel® Technology Journal, 12.

/18/ MATTILA, T. 2005. RELIABILITY OF HIGH-DENSITY LEAD-FREE SOLDER INTERCONNECTIONS UNDER THERMAL CYCLING AND MECHANICAL SHOCK LOADING. Helsinki University of Technology.

/19/ MATTILA, T. & KIVILAHTI, J. 2005. Failure mechanisms of lead-free chip scale package interconnections under fast mechanical loading. Journal of Electronic Materials, 34, 969-976.

/20/ MATTILA, T. & KIVILAHTI, J. 2006. Reliability of lead-free interconnections under consecutive thermal and mechanical loadings. Journal of Electronic Materials, 35, 250-256.

/21/ MATTILA, T., MUELLER, M., PAULASTO-KRO CKEL, M. & WOLTER, K. J. Year. Failure mechanism of solder interconnections under thermal cycling conditions. In.: IEEE, 1-8.

/22/ MEI, Z., SUNWOO, A. & MORRIS, J. 1992. Analysis of low-temperature intermetallic growth in copper-tin diffusion couples. Metallurgical and Materials Transactions A, 23, 857-864.

/23/ NEWMAN, K. Year. BGA brittle fracture-alternative solder joint integrity test methods. In, 2005. IEEE, 1194-1201 Vol. 2.

/24/ PAUL, A. 2004. The Kirkendall effect in solid state diffusion. Doctoral Deissertation, Technical University of Eindhoven.

/25/ RITCHIE, R. 1988. Mechanisms of fatigue crack propagation in metals, ceramics and composites: role of crack tip shielding. Materials Science and Engineering: A, 103, 15-28.

/26/ RÖNKÄ, K., VAN LOO, F. J. J. & KIVILAHTI, J. 1998. A diffusion-kinetic model for predicting solder/conductor interactions in high density interconnections. Metallurgical and Materials Transactions A, 29, 2951-2956.

/27/ SEAH, S., WONG, E., MAI, Y., RAJOO, R. & LIM, C. Year. High-speed bend test method and failure prediction for drop impact reliability. In, 2006. IEEE, 6 pp.

/28/ SOHN, J. E. 2002. Are lead-free solder joints reliable? Circuits Assembly, 13, 32-35.

/29/ SUH, D., KIM, D. W., LIU, P., KIM, H., WENINGER, J. A., KUMAR, C. M., PRASAD, A., GRIMSLEY, B. W. & TEJADA, H. B. 2007. Effects of Ag content on fracture resistance of Sn-Ag-Cu lead-free solders under high-strain rate conditions. Materials Science and Engineering: A, 460, 595-603.

/30/ SYED, A., KIM, T. S., CHO, Y. M., KIM, C. W. & YOO, M. Year. Alloying effect of Ni, Co, and Sb in SAC solder for improved drop performance of chip scale packages with Cu OSP pad finish. In, 2006. IEEE, 404-411.

/31/ SYED, A., SCANLAN, J., CHA, S. W., KANG, W. J., SOHN, E. S., KIM, T. S. & RYU, C. G. Year. Impact of package design and materials on reliability for temperature cycling, bend, and drop loading conditions. In.: IEEE, 1453-1461.

/32/ TEE, T. Y., NG, H. S., LIM, C. T., PEK, E. & ZHONG, Z. Year. Board level drop test and simulation of TFBGA packages for telecommunication applications. In, 2003. IEEE, 121-129.

/33/ TSUKAMOTO, H., NISHIMURA, T., SUENAGA, S., MCDONALD, S., SWEATMAN, K. & NOGITA, K. 2010. The influence of solder composition on the impact strength of lead-free solder ball grid array joints. Microelectronics Reliability.

/34/ WONG, E., RAJOO, R., MAI, Y., SEAN, S., TSAI, K. & YAP, L. Year. Drop impact: fundamentals and impact characterisation of solder joints. In, 2005. IEEE, 1202-1209.

/35/ WONG, E., SEAH, S. & SHIM, V. 2008a. A review of board level solder joints for mobile applications. Microelectronics Reliability, 48, 1747-1758.

/36/ WONG, E., SEAH, S., VAN DRIEL, W., CAERS, J., OWENS, N. & LAI, Y. S. 2009. Advances in the drop-impact reliability of solder joints for mobile applications. Microelectronics Reliability, 49, 139-149.

/37/ WONG, E., SELVANAYAGAM, C., SEAH, S., VAN DRIEL, W., CAERS, J., ZHAO, X., OWENS, N., TAN, L., FREAR, D. & LEONI, M. 2008b. Stress-strain characteristics of tin-based solder alloys for drop-impact modeling. Journal of Electronic Materials, 37, 829-836.

/38/ XU, L., PANG, J. H. L., PRAKASH, K. H. & LOW, T. 2005. Isothermal and thermal cycling aging on IMC growth rate in lead-free and lead-based solder interface. Components and Packaging Technologies, IEEE Transactions on, 28, 408-414.

/39/ ZENG, K., STIERMAN, R., CHIU, T. C., EDWARDS, D., ANO, K. & TU, K. 2005. Kirkendall void formation in eutectic SnPb solder joints on bare Cu and its effect on joint reliability. Journal of applied physics, 97, 024508.

/40/ ZHANG, B., DING, H. & SHENG, X. 2009. Reliability study of board-level lead-free interconnections under sequential thermal cycling and drop impact. Microelectronics Reliability, 49, 530-536.

/41/ ZHANG, Q., DASGUPTA, A., NELSON, D. & PALLAVICINI, H. 2005. Systematic study on thermo-mechanical durability of Pb-free assemblies: experiments and FE analysis. Journal of Electronic Packaging, 127, 415.

/42/ ZHU, F., ZHANG, H., GUAN, R. & LIU, S. 2007. The effect of temperature and strain rate on the tensile properties of a Sn99. 3Cu0. 7 (Ni) lead-free solder alloy. Microelectronic engineering, 84, 144-150.

Dhafer Abdulameer Shnawah, Mohd Faizul Mohd Sabri, Irfan Anjum Badruddin*
Department of Mechanical Engineering, University of Malaya, 50603 Kuala Lumpur, Malaysi
**Author correspondent/ Corresponding Author, Tel: +60 162375504, e-mail: dhafer_eng@yahoo.com*

Prispelo: 17.11.2010 *Sprejeto: 23.08.2011*

FABRICATION OF GLASS-BASED MICROFLUIDIC DEVICES WITH PHOTORESIST AS MASK

Alireza Bahadorimehr, Burhanuddin Yeop Majlis

Institute of Microengineering and Nanoelectronics (IMEN), Universiti Kebangsaan Malaysia, Selangor, Malaysia

Key words: Microfluidics, Photoresist, Glass, Wet etching

Abstract: This paper presents a low cost method for etching of glass based microfluidic devices. Microchannels with the depth up to 150µm were achieved by implementing a photoresist and wet etching process. In particular, a photoresist based mask method is introduced for glass etching which can strongly resist against etchant attacks up to 2 hours, showing high adhesion properties on glass substrate for fabrication of microfluidic microchannels. The width of the channels is determined by the width of the lines in photo-mask design and the rate of glass isotropic etching. The channel width range about 30µm to 350µm is fabricated. Commercially available inexpensive microscopic glass slides have been used as substrate. Achieving smooth and clear surface after wet etching process is an important factor for easily flowing fluid through channels and monitoring purposes. It is achieved by implementing special etchant with adding HCL in diluted BOE solution to get smooth and clear surface. The etch rate of the glass strongly depends on the concentration of the etchant. A mixture of different solutions with special ratios has been applied. Finally, typical UV curable glue is utilized for glass-glass bonding.

Izdelava mikrofluidnih vezij na osnovi stekla s pomočjo fotorezista kot maske

Kjučne besede: mikrofluiden, fotorezist, steklo, mokro jedkanje

Izvleček: V članku je predstavljena poceni metoda za jedkanje mikrofluidnih naprav na stekleni podlagi. Izdelali smo mikrokanale z globino do 150µm z uvedbo fotorezista in mokrega jedkanja. Uporabljeni fotorezist zdrži jedkanje v mokrem jedkalu dolgo do 2 uri in hkrati kaže odlično oprijemljivost na stekleno podlago. Širino kanalov v steklu določimo s širino linij na maski in jedkalno hitrostjo izotropnega jedkanja, oz. spodjedkavanjem. Na ta način nam uspe izdelati širine kanalov od 30µm do 350 µm. Za podlago smo uporabili komercialno dosegljive steklene ploščice namenjene mikroskopiranju. Pomembno je, da po jedkanju dosežemo čisto in gladko površino, ki omogoči normalen pretok tekočine po kanalih. Le-to dosežemo z uporabo posebnih jedkal z dodatkom HCl v razredčeno raztopino osnovnega jedkala BOE. Jedkalna hitrost stekla je močno odvisna od koncentracije jedkala. Poskusili smo različne koncentracijske mešanice raztopin. Za končno zlepljenje stekelc smo na koncu uporabili UV lepilo.

1. Introduction

Microfluidic systems have become increasingly well-known in different fields of studies. In recent years so many new commercialized microfluidic products has been emerged in the market. Microfluidic devices are going to become one of the most dynamic part of the BioMEMS technology trend. The main applications of microfluidics are medical diagnostics, genetic sequencing, chemistry production, drug discovery, and proteomics.

Depending on applications and suitability, different types of materials can be used as the substrate for the microchannels such as silicon /1/, glass /2, 3/, SU-8 /4/, polydimethyl-siloxan (PDMS) /5/ and Poly methyl methacrylate (PMMA) /6/. However, biocompatibility of the substrate material is very important in vivo and vitro analysis. Glass as a well-known material with the minimum chemical reaction issues is used in this paper. In terms of cost and simplicity, commercially available microscopic slides have been used.

Numerous fabrication techniques for microfluidic devices have been reported. Fabrication of microchannels as the main parts of the microfluidic systems plays an important role in operation of the entire system. Different techniques can be utilized for fabrication of microchannels. SU-8 as a low cost negative resist is a famous material to make vertical and high aspect ratio structures. Using SU-8 as a master mold and pouring PDMS on master is another well-known method for microchannel fabrication /4/. Microchannels with vertical and precise walls can be achieved using Deep Reactive Ion Etching (DRIE) on different substrates /7, 8/. Despite all the techniques, wet etching process is still used as a low cost and simple method for fabrication of microfluidic devices. However, various masking techniques are implemented to make a microchannel via glass substrate. Different mask layers for chemical wet etching of glass have been reported which use different materials such as Cr /9/, Cr/Au /10, 11/, polysilicon /12/ to deposit a layer as a mask on glass in order to make an open region for wet chemical etchant by different deposition methods such as CVD, LPCVD /12/, sputtering or other methods which needs special clean room instruments. The method in this paper includes coating the glass surface with a photoresists, AZ 5214, by spinning the sample on a spin-coater, and post baking procedure of photoresist followed by immersing the glass in an etchant with special concentrations of Hydrofluoric acid (HF), Ammonium Fluoride (NH-

4F), Hydrochloric acid (HCL) and DI water in a magnetic stirring bath. HF-based methods /13/ usually result in a rough surface, but the special recipe consisting of HCI, Buffered Oxide Etchant (BOE) and D.I. water provides a smooth surface /14/.

2. Experimental details

2.1. Cleaning procedure

The fabrication process starts with the glass substrate cleaning by ultra-sonication in acetone and methanol for 10 min respectively. Subsequently the glass substrates were boiled in piranha solution (H2SO4:H2O2= 3:1) for 15 min. The slides were then immersed in deionised water for 5 min and blow drying with nitrogen gas was applied later. Finally, the cleaned glass substrates were put in a conventional oven for 20 min at 85°C to demoisturize.

2.2. Photolithography and post-baking

Photolithography is a very important process due to the desire thickness of photoresist after spin coating, UV exposure time, and hard baking temperature to achieve the maximum adhesion between photoresist and substrate. In order to accomplish these conditions AZ5214, a positive photoresist, was utilized. Coating was obtained by spinning for 5 seconds at 500 rpm, followed by spinning for 20 seconds at different speeds to compare the results. The photoresist layer was soft baked on a hotplate at 100°C for 10 min, resulting moisture-free surface, allowing contact mode exposure. The dried photoresist was UV-exposed in a mask aligner at the wavelength of 365nm in hard contact mode for highest precision purposes. Immediately, after exposure the resist was subjected to a post-exposure bake on a hotplate at 100°C for 3 min for adhesion promotion. Development was done in diluted AZ400k developer (DI water: AZ400k = 3:1) at room temperature with a development time of 3-4 min and rinsing in DI water subsequently. A post-bake at 160°C for 90 min were applied on a hotplate in order to harden the photoresist against attacks of etchants.

2.3. Etching process

For producing microchannels a wet etching process was performed. The proper mixture of etchant concentrations can be greatly enhanced the resistant time of photoresist and etch rate as well. First, 10 parts of saturated NH4F solution was mixed with one part of 49% HF to form 10:1 BOE solution. HF-based etches usually result in a rough surface. However, by adding HCL to BOE solution, a smooth surface is attainable. The ratio of the BOE solution and HCL was 5:1. Putting the coating glass in this solution with magnetic stirring was lead to early attack on some parts of photoresist just in less than 10 min. To overcome this problem, DI water was used to dilute the solution. By adding 100% DI water to the solution, the resistivity time of the photoresist was increased up to more than 2 hours.

For removing photoresist from the glass surface, ultrasonic agitation in acetone was used for 10 min. Subsequently, the same procedure as stated in cleaning procedure section for cleaning etched glass for bonding purposes were performed.

2.4. Bonding with UV curable glue

The method involves UV curable glue that can be used for glass microfluidic chips bonding at room temperatures. The use of UV-curable glue was found to be a quick, easy, and inexpensive method for attachment of glass substrates together. The glue with low viscosity which ensures formation of a thin layer after spinning was selected (NOA 71). A thin layer of UV glue was applied on this slide by spinning it at 4000 rpm for 20s. The etched glass slide containing the microchannels was then brought in contact with the glue surface of the plain slide to permanently bond two glass slides together.

2.5. Tubings and Connections

In order to complete the entire device the tubing connection using PDMS was applied. Mixing 25 g of PDMS with 2.5 g (10%) hardening agent and pour it into the dish was the first step. Next the Petri dish was placed on a hot plate at 100°C and cure for 1h. For making holes through the PDMS, we used the typical needle and then cut the squares around each hole using a blade. The silicone glass sealant was used in order to adhere each square piece PDMS on glass substrate.

3. Results and discussions

Microscopic glass slides with easy accessibility were used as main material to fabricate the entire microfluidic chip. The standard glass slides with 25mm×75mm and 1mm thickness were utilized. The glass slides are naturally hydrophilic and the microchannels were made by etching process showed the same behavior (contact angle with water 18–20°).

AZ5214 is a thick positive photoresist which was coated with different speeds on glass substrates (600, 700, 800 and 900 rpm). The optimum thickness was determined to be about 7 µm in 700 rpm in order to withstand the attacks of etchant solutions for up to 120 min. Different baking process was used in this work. The primary purpose of baking is to removing moisture from the photoresist in order to avoid adherence of photoresist to the mask in mask aligner (prebake) and increase the surface adhesion (post-bake). In addition, heating affects on photoresist compounds to become a non-photosensitive product by changing chemical characteristics of photoresist. This can affect on exposure time too. Therefore, determining temperature and heating time have significant impacts on accuracy of the design. Different heating temperatures were utilized in order to optimize the photoresist patterning process for subsequent etching process. In particular, after photoresist

spin coating on glass, the substrate was put on a hotplate at 100°C for 10 min. Subsequently after UV exposure the coated substrates were put on a hotplate for 3 min at 100°C for prebake procedure. Post-bake process was performed after developing the exposed regions at 160°C for 90 min on a hotplate.

The wet etching process was performed in a plastic container using magnetic stirring plate. Different mixtures of NH4F/HF/HCL/DI-water were studied in order to achieve to a acceptable etch rate, smooth microchannel surface, no underlying glass etching effect, and clear glass slide in all regions without any signs of damages. Etching the glass can cause undercutting effect. Due to this effect width of the channels increase compare to the mask design. In order to compensate for undercutting effect of isotropic etching, determining glass etch rate is an important factor. We used scanning electron microscope (SEM) for etch rate measurements. Fig. 1 illustrates the depth of about 150μm after 90 min of etching using diluted etchant. In this figure the depth of the microchannel was measured using SEM every 15 min by Au sputtering. The results shows the etch rate of 1.75 μm/min. Although the etch rate can be achieved to more than this amount with less dilution, however, the smoothness of the substrate surface, undercutting effect and also sedimentation limit this factor. Fig. 2 presents a microscopic view of the effect of etchant concentration with a diluted etchant and without dilution. The less-diluted etchant can cause sedimentation on the etching area which is a reason of avoidance of more etching because of blocking of the open region for further etching. This can affect the smoothness of the etched surface as well because of high etching rate in some parts and low in other regions. It shows that the edges of the microchannel walls are not so smooth when a non-diluted etchant was applied in comparison with the diluted etchant. This is because of the undercutting effect when the dilution is not enough. It illustrates that the attacks against glass is more destructive especially on edges when no or less DI water is used. The dilution ratio was 2 part of DI water to 1 part of BOE: HCL=5:1. Fig. 3 shows the SEM view of a microchannel after 40 min wet etching. As can be seen the sharp edges and approximately smooth surface was achieved.

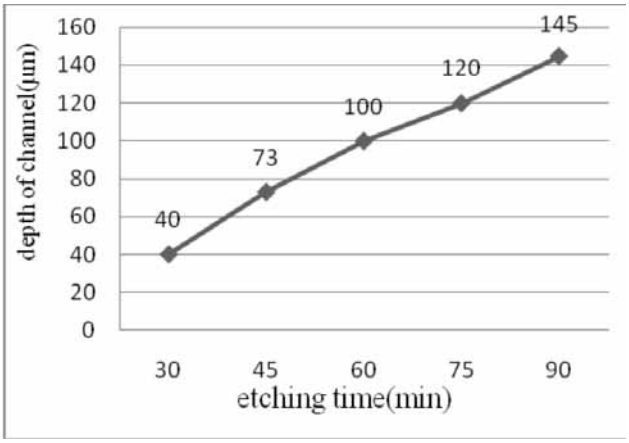

Fig. 1. Depth of channel vs. etching time

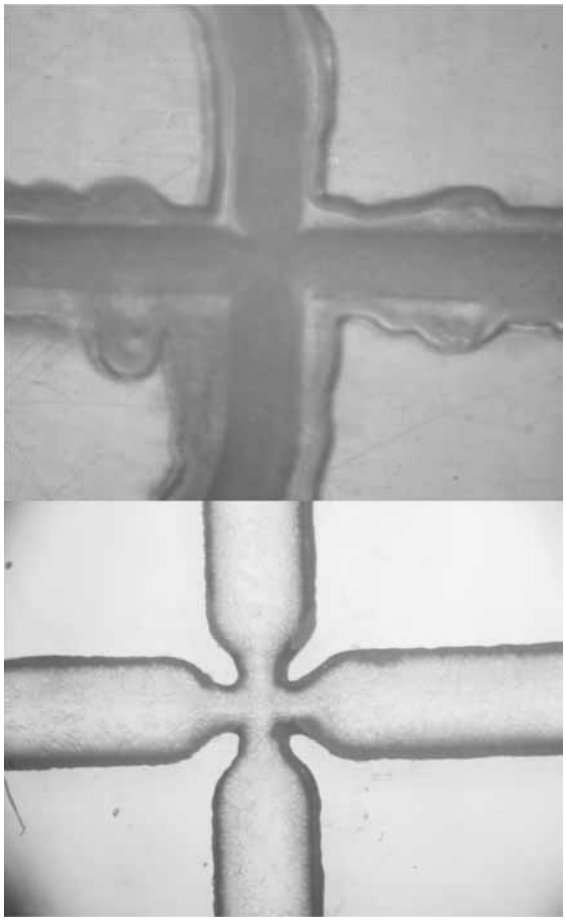

Fig. 2. Effect of the (a) non-diluted and (b) diluted etchant on side walls

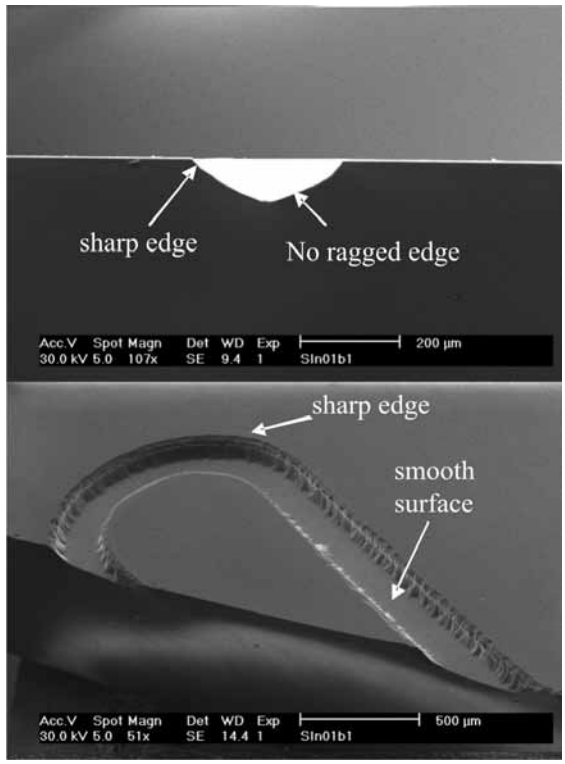

Fig. 3. SEM cross section view (a) and an angle view (b) of the microchannel

The bonding was applied using UV glue method. The results for UV glue are shown in Fig. 4(a) by filling the channels with dye water. This figure illustrates no penetration of dye water to other areas after sequential experiments. For making holes through the glass we used high speed drilling machine with diamond drill bits before bonding.

Leaking from connections and tubings in this microfluidic device was eliminated using special PDMS cubic parts. Fig. 4(b) shows the overall view of a microfluidic device. It shows the input and output channels have filled with dye water and the tubings are connected to the inlets and outlets without any leakage inside the channels and also via the connections. Also, it is clear that the UV glue has not clogged the micro-channels.

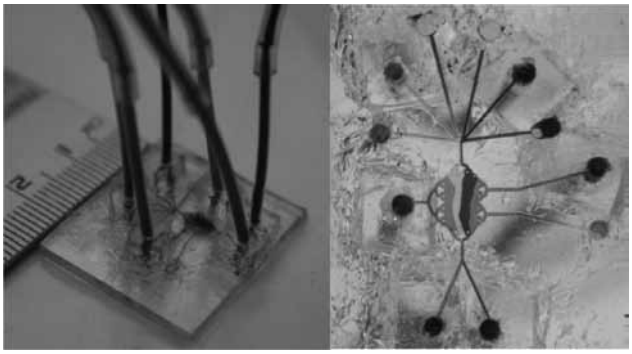

Fig. 4. (a)Tubings and connections and (b) Dye water inside the microchamber

4. Conclusions

In this paper we presented a simple and cost effective fabrication method for fabrication of microfluidic devices on glass substrate. This method uses typical microscopic glass slides as a substrate for fabrication of micro-channels. Using photo-resist as a mask led to gain precise results identical to other deposition methods which need sophisticated procedures and instruments. A smooth channel surface with acceptable sharp wall edges was achieved using specific etchant solution by adding HCL to diluted BOE. The UV glue was used to achieve promising bonding results. The tubings and connections also were performed using PDMS. The results show no leakage from connections and no penetration from the microchannels to other non-etched regions.

References

/1/ D. Lim, Y. Kamotani, B. Cho, J. Mazumder and S. Takayama, "Fabrication of microfluidic mixers and artificial vasculatures using a high-brightness diode-pumped Nd:YAG laser direct write method," Lab on a Chip - Miniaturisation for Chemistry and Biology, vol. 3, pp. 318-323, 2003.

/2/ M. Castanño-Álvarez, D. F. Pozo Ayuso, M. García Granda, M. T. Fernández-Abedul, J. Rodríguez García and A. Costa-García, "Critical points in the fabrication of microfluidic devices on glass substrates," Sensors and Actuators, B: Chemical, vol. 130, pp. 436-448, 2008.

/3/ P. Vulto, T. Huesgen, B. Albrecht and G. A. Urban, "A full-wafer fabrication process for glass microfluidic chips with integrated electroplated electrodes by direct bonding of dry film resist," J Micromech Microengineering, vol. 19, 2009.

/4/ H. Sato, H. Matsumura, S. Keino and S. Shoji, "An all SU-8 microfluidic chip with built-in 3D fine microstructures," J Micromech Microengineering, vol. 16, pp. 2318-2322, 2006.

/5/ M. A. Eddings, M. A. Johnson and B. K. Gale, "Determining the optimal PDMS-PDMS bonding technique for microfluidic devices," J Micromech Microengineering, vol. 18, 2008.

/6/ J. M. Li, C. Liu, X. D. Dai, H. H. Chen, Y. Liang, H. L. Sun, H. Tian and X. P. Ding, "PMMA microfluidic devices with three-dimensional features for blood cell filtration," J Micromech Microengineering, vol. 18, 2008.

/7/ T. N. T. Nguyen and N. -. Lee, "Deep reactive ion etching of polyimide for microfluidic applications," J. Korean Phys. Soc., vol. 51, pp. 984-988, 2007.

/8/ J. H. Park, N. -. Lee, J. Lee, J. S. Park and H. D. Park, "Deep dry etching of borosilicate glass using SF6 and SF 6/Ar inductively coupled plasmas," Microelectron Eng, vol. 82, pp. 119-128, 2005.

/9/ J. Park, Y. -. Yoon, M. R. Prausnitz and M. G. Allen, "High-aspect-ratio tapered structures using an integrated lens technique," in 17th IEEE International Conference on Micro Electro Mechanical Systems (MEMS): Maastricht MEMS 2004 Technical Digest, Maastricht, 2004, pp. 383-386.

/10/ T. Diepold and E. Obermeier, "Smoothing of ultrasonically drilled holes in borosilicate glass by wet chemical etching," J Micromech Microengineering, vol. 6, pp. 29-32, 1996.

/11/ F. E. H. Tay, C. Iliescu, J. Jing and J. Miao, "Defect-free wet etching through pyrex glass using Cr/Au mask," Microsyst Technol, vol. 12, pp. 935-939, 2006.

/12/ M. Grétillat, F. Paoletti, P. Thiébaud, S. Roth, M. Koudelka-Hep and N. F. De Rooij, "A new fabrication method for borosilicate glass capillary tubes with lateral inlets and outlets," Sens Actuators A Phys, vol. 60, pp. 219-222, 1997.

/13/ G. A. C. M. Spierings, "Wet chemical etching of silicate glasses in hydrofluoric acid based solutions," J. Mater. Sci., vol. 28, pp. 6261-6273, 1993.

/14/ H. Becker, K. Lowack and A. Manz, "Planar quartz chips with submicron channels for two-dimensional capillary electrophoresis applications," J Micromech Microengineering, vol. 8, pp. 24-28, 1998.

Alireza Bahadorimehr, Burhanuddin Yeop Majlis
Institute of Microengineering and Nanoelectronics (IMEN), Universiti Kebangsaan Malaysia, 43600 Bangi, Selangor, Malaysia
Email: bahadorimehr@gmail.com, burhamems@ukm.my

Prispelo: 03.01.2011 *Sprejeto: 23.08.2011*

IMPACT STUDY OF DISTURBANCE ON READABILITY OF TWO SIMILAR UHF RFID TAGS

Urška Bogataj[1], Marijan Maček[2], Tadeja Muck[3]

[1]Valkarton, Production of Corrugated Board and Packaging d. d., Logatec, Slovenia,
[2]University of Ljubljana, Faculty of Electrical Engineering, Ljubljana, Slovenia,
[3]University of Ljubljana, Faculty of Natural Sciences and Engineering, Chair of Information and Graphic Arts Technology, Ljubljana, Slovenia

Key words: RFID system, readability, water disturbance, metal disturbance.

Abstract: The radio frequency identification (RFID) is one of the automatic identification technologies describing the system which transmits the data about an object wirelessly using radio frequencies. The system consists of one or more RFID tags, a reader and antenna. Despite the system still presenting a costly solution, its use is on the increase in the supply chain management, especially for the labelling and identification of different packaging. Prior to the packaging labelling, the influence of the material on the radio frequency spreading has to be evaluated. This article describes the readability of two similarly folded dipole UHF RFID antennas in dependence on different packaging. The analysis was performed on three different packaging boxes made of corrugated cardboard. First, the boxes were empty (1), then the boxes had water inside (2) and in the last example, the Al foil was inside the boxes (3). The influence of packaging on the tag readability was determined. The 2-D field signal and the received signal strength were measured. The results showed that both tag antennas have almost the same response when they are labelled onto empty boxes, a slightly less similar response when labelled onto the packaging with water inside, but a quite different response when labelled onto the packaging which contains metal. It was established that although both tag antennas were labelled onto all three types of packaging and are similarly folded dipoles, the Alien tag is more suitable for labelling the packaging containing water and metal.

Študij vpliva motenj na čitljivost dveh podobnih UHF RFID značk

Kjučne besede: RFID sistem, čitljivost, vpliv vode, vpliv kovine.

Izvleček: Radijsko frekvenčna identifikacija (RFID) je ena izmed tehnologij avtomatske identifikacije, ki za prenos podatkov o določenem izdelku uporablja radijske frekvence. Sistem je sestavljen iz ene ali več RFID značk, čitalca in antene. Čeprav tehnologija še vedno predstavlja visok strošek vpeljave se vedno bolj uporablja predvsem v preskrbovalnih verigah, še posebno za označevanje in identifikacijo različne embalaže. Pred označevanjem embalaže z RFID značko, pa je pomembno preučiti vplive materialov na širjenje radijskih frekvenc. Članek opisuje čitljivost dveh podobno "zgibanih" dipolnih UHF RFID anten v odvisnosti od vsebine embalaže. Analiza je bila izvedena na treh različnih embalažnih škatlah narejenih iz valovitega kartona. Prva škatla je bila prazna, druga je vsebovala vrečko z vodo in tretja Al folijo. Tako je bil preučen vpliv embalaže na čitljivost značke. Predstavljen je signal delovanja v 2-D polju in moč signala, ki ga čitalec prejme od značke. Rezultati so pokazali, da imata obe anteni značk skoraj identičen odziv, ko sta nalepljeni na prazni škatli, delno različen odziv, ko sta nalepljeni na škatli z vodo in precej različen odziv, ko sta nalepljeni na škatli z Al. Dokazano je, da je Alien značka kljub temu, da sta si obe znački in njuni anteni med seboj zelo podobni, bolje prilagojena na motnje in zato bolj primerna za označevanje embalaže, ki vsebuje kovinske izdelke ali izdelke z visoko vsebnostjo vode.

1. Introduction

The radio frequency identification (RFID) has been existing for more than half a century /1/; however, even now, the RFID tags are not appropriately priced, compact, mechanically robust and readable from larger distances. Consequently, the RFID technology is still not widespread in our everyday lives. The RFID system consists of one or more RF tags, a reader, antenna and deployment environment /2/. The tags can be different depending on the communication method (active, passive and semi-passive) and operating frequency (low (LF), high (HF), ultra high (UHF)) /3/, and the reader and antenna have to be tuned to the tag frequency. In general, a higher frequency means on the one hand a longer read range and a higher data transfer rate, but on the other, a higher frequency (shorter wavelength) can be easily absorbed by the materials (water, metal) through which it is moving /4/. Many advantages, e.g. low cost (compared to active tags), long reading range and high data transfer, are the main reasons why the passive UHF RFID tags came to be applied in logistics first.

The products made of different materials can be placed inside the RFID tagged packaging. When the packed goods are made of metal, water or they contain high percentage of liquid or metal, the communication between the RFID tag and RFID reader deteriorates. The effective gain (G_{eff}) of the tag antenna (ability to increase the power or amplitude of the signal) can be defined as follows/5/:

$$G_{eff} = D_{\eta\tau} \quad (1)$$

where D is the directivity of the antenna, η is the antenna efficiency and τ is the power transfer efficiency. When the tag is labelled into the vicinity of metal, the directivity of an-

tenna increases, the efficiency decreases and the antenna impedance can change and cause poor power transfer efficiency /5/. When the tag is labelled onto the packaging with liquid or another high dielectric material inside, the directivity increases, while the efficiency decreases due to the dielectric loss. The antennas in such an environment undergo a significant shift in the resonant frequency and may lose efficiency /5/.

The power of the modulated signal that emits from the tag antenna and is received by the reader is proportional to r^{-4} and defined as a modified Friis equation:

$$P_{RX}^{rdr} = P_{TX}^{rdr} T_b G_{rdr}^2 G_{tag}^2 \left(\frac{\lambda}{4\pi r} \right)^4 \quad (2)$$

where P_{RX}^{rdr} presents the signal received by the reader, P_{TX}^{rdr} the signal transmitted from the reader, T_b the modulation efficiency, G_{rdr} is reader gain, G_{tag} tag gain, λ wavelength and r is the distance between the tag and reader.

When the tag is labelled onto the packaging, there are at least four effects the environment or material can have on tag readability, i.e. reflection, absorption, diffraction and interference /6/. The reflection and absorption are present especially when the packed goods are made of metal or liquid material /6, 7/, since metallic items reflect the radio frequency and detune the tag antenna from its resonance frequency. The tag does not absorb enough power from the RFID reader and the antenna cannot absorb enough energy to power up. Liquid materials absorb RF and reduce the strength of the original signal by absorbing or dissipating the power. This causes the tag to have insufficient energy to power up and backscatter the information to the reader.

The metal and water objects obviously have a high impact on tag readability. When tags are labelled onto the packaging that includes such products, the readability of tags can deteriorate or tags may even become unreadable. In our previous researches /7–10/, numerous analyses of tag readability in the vicinity of metal and water were conducted. In this research, the influence of three types of packaging on two different RFID tags readability was evaluated. The 2-D field of RFID tag readability, the signal strength in the line of sight and the signal strength when changing the position of a tag and Al plate were measured.

2. Experimental part

In the experimental part of the research, the measurements of RFID tag readability were performed. The influence of a packed product on the tag readability was analysed. For this purpose, three different cardboard boxes were used, the first being empty, the second with aluminium (Al) foil and the third with a water sack inside. The analyses of readability and signal strength of two different passive UHF RFID tag samples labelled onto all three packaging were conducted. The RFID tag samples (producers Alien (ALN-9649 Squiggle) and Avery Dennison (AD-224)) have a similarly folded dipole antenna shape and size (cf. Figure 1). They all support the EPC Gen 2 protocol and operate at frequencies 860–960 MHz.

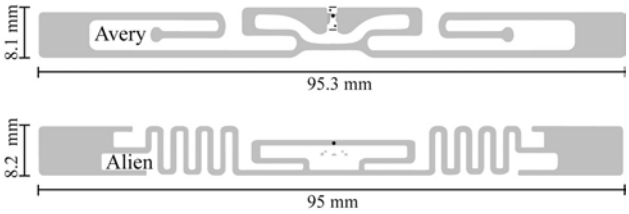

Fig. 1: RFID samples.

The measurements were accomplished in a real environment, i.e. a laboratory with numerous RF noises.

2.1. Encoding/decoding

Prior to the testing, the RFID tags were prepared for printing and encoding using the NiceLabel software. The labels with tag inlays were then printed and simultaneously encoded using the DataMax M Class Mark II UHF RFID printer/encoder. The decoding process was performed using two different RFID readers, namely Motorola RFID MC9090-G (for signal in 2-D field) and IDS-R902 reader (signal strength) with the characteristics as they follow below.

2.1.1. Motorola RFID MC9090-G reader

The Motorola reader has an integrated linearly polarized antenna that can emit the RF waving at approximately 70° zone measured from the nose of device. The reader operates at the UHF frequency 865.7–867.5 MHz. The reader supports the EPC Gen 2 standard and has the output power of 0.5 W (27 dBm).

2.1.2. IDS-R902 reader

The IDS reader consists of the IDS reader and Poynting Patch A0025 antenna that measures the received signal strength from the tag. The reader is based on the IDS-R902 circuit and supports the ISO18000-6C or EPC Gen2 protocol. It uses the UHF frequency at the frequency of 867 MHz. The reader output power is +26 dBm (0.4 W) and the output impedance is 50 Ω. The reader uses amplitude shift keying and has the maximum input sensitivity of –76 dBm. The antenna emits the signal that is circularly polarized, the antenna gain is 6.5 dBi and the input impedance is 50 Ω.

2.2. 2-D field signal measuring

All three types of packaging were labelled separately with all RFID tag samples. Using the Motorola reader, the tag readability or non-readability in different positions (x, y) in one quadrant was measured (cf. Figure 2). The measurements were carried out at centimetre intervals on the horizontal plane in the direction of the antenna radiation and perpendicularly to it.

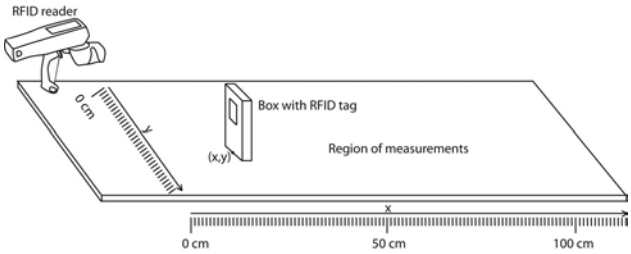

Fig. 2: Signal measurement in 2-D field.

2.3. Received signal strength

The tags were separately labelled onto all three types of packaging and the tag received signal strength (in dBm) was measured using the IDS reader. Firstly, the signal strength was measured in the straight line of sight between the tag and reader antenna. Afterwards, the signal strength when changing the position of a tag and Al plate was analysed.

2.3.1. Signal strength – straight line tag-reader

The signal strength backscattered from the tag antenna was measured at distances from 0 cm to the largest distance where the tag still responded on each cm. The measurements were performed in a straight line between the tag and reader antenna as it is seen from Figure 3.

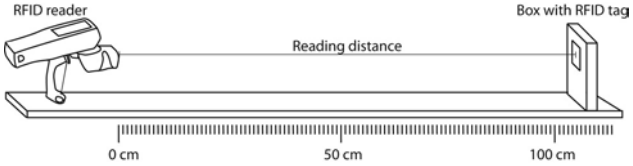

Fig. 3: Measurements of backscattered signal power from RFID tag labelled onto different packaging.

2.3.2. Signal strength – changing the position of tag and Al plate

Similarly, the backscattered signal strength at different distances between the RFID tag labelled onto an empty corrugated board packaging and Al plate was measured. The measurements were conducted at each cm from 0 to 40 cm as it is presented in Figure 4.

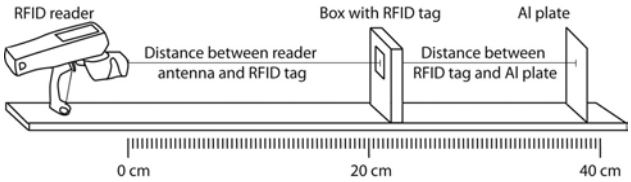

Fig. 4: Measurements of backscatter signal when changing the positions of RFID tag and Al plate.

3. Results and discussion

In the first part of the research, the evaluation of tag (labelled onto different types of packaging) readability ("yes/no") in the 2-D horizontal field was performed using the Motorola reader. The 2-D field figures were sketched and after that, the backscattered power (in dBm) coming from the tag antenna was measured with the IDS reader. In both cases, the differences in the response when different tags were labelled onto different packaging were evaluated. The results from both readers were compared and the correlation was observed. In the end, the backscattered power (dBm) from the tag antenna differentiating the position of the tag and Al plate was measured.

3.1. RFID tag labelled onto empty box

As Figure 5 shows, the reading distances of Alien and Avery tags are almost the same. The Alien sample has a larger uniform 2-D reading area (i.e. the clear grey-coloured area) closer to the reader than Avery. The Avery sample reading distance is only 3 cm shorter than the Alien sample reading distance in the direct line and 4 cm shorter in the perpendicular direction. The shape and size of samples are comparable, thus it can be seen that with no interruption (tag is labelled onto an empty corrugated box), the reading distances are almost the same. Comparing the results of 2-D sketches with the backscattered signal strength (cf. Figure 6), it is obvious that Alien and Avery have very similar signal strength, but a considerably shorter reading distance than in Figure 5. The reason for the mentioned deviations are the readers which have different characteristics (antenna polarizations (Motorola has a linearly and IDS a circularly polarized antenna), power and gain).

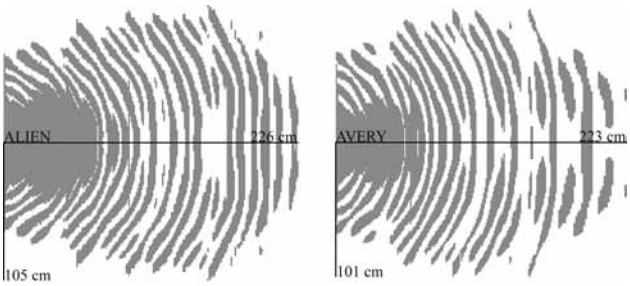

Fig. 5: 2-D horizontal field of readability of samples labelled onto empty boxes.

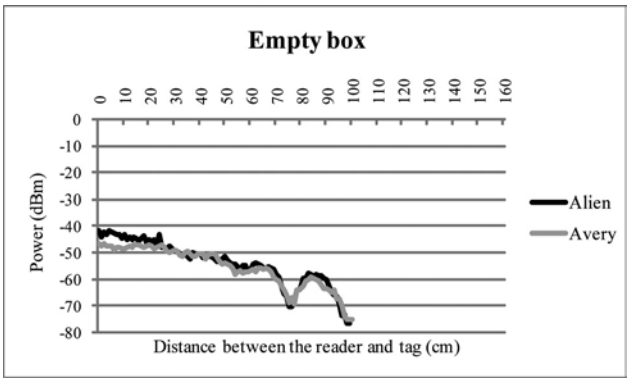

Fig. 6: Backscattered signal strength measured when tags were labelled onto empty box.

3.2. RFID tag labelled onto box with Al

Labelling the packaging that includes metal products or products that include metal can present a serious challenge for tag reading. The nearness of the metal substantially worsens the reading range and the behaviour of the RF waving. The reflection of waves causes shorter reading ranges and lowers the backscattered power strength. Comparing Figures 7 and 5, it is obvious that the reading range decreases twofold at both samples. The Alien sample shows a more uniform 2-D field (cf. Figure 7) in contrast to Avery, which has periodic reading/no-reading areas when increasing the distance between the tag and the reader.

The same deterioration was detected at the backscattered signal strength shown in Figure 8. All samples communicate with the reader only up to the distances of about 80 cm. Close to the reader nose (less than 10 cm), the signal is weak, reaching the maximum at 10 cm and monotonically decreasing by 20 dBm in the next 60 cm. There is a constant 10 dBm difference in the signal strength between the Alien (higher) and Avery (lower) labels during the whole range of readability.

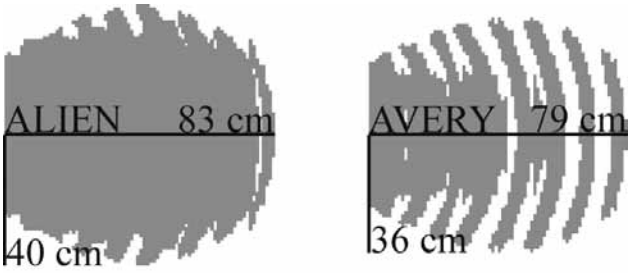

Fig. 7: 2-D horizontal field of readability of samples labelled onto boxes with Al inside.

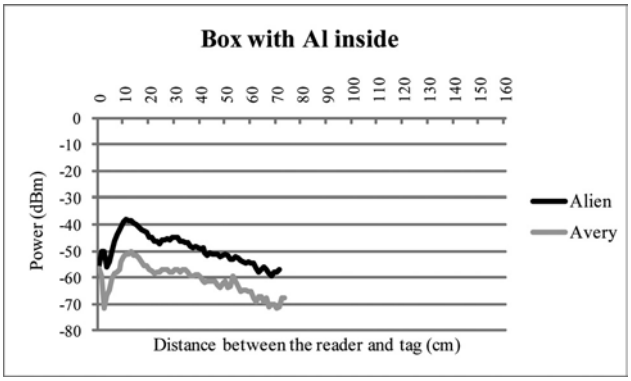

Fig. 8: Backscattered signal strength measured when tags were labelled onto box with Al inside.

3.3. RFID tag labelled onto box with water

When the tags were labelled onto boxes containing water, some unexpected results arose. The total reading area was larger than when the tags were labelled onto the packaging with Al inside, while the backscattered signal strength was lower. In this way, we proved that water absorbs RF and reduces the strength of the original signal by absorbing the power. This causes the tag to have insufficient energy to power up and backscatter the information to the reader. Focusing on the images of the 2-D field of readability (cf. Figure 9), Alien shows better readability in the x and y direction than Avery.

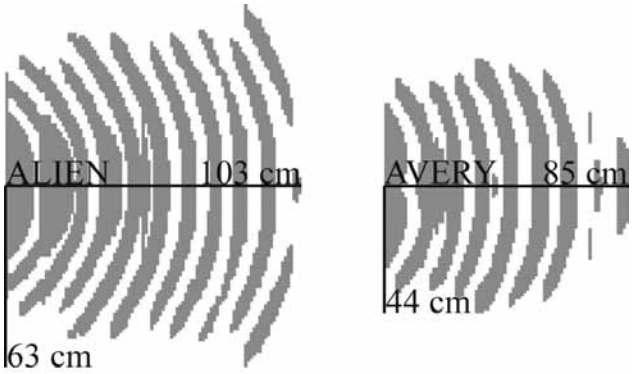

Fig. 9: 2-D horizontal field of readability of samples labelled onto box with water inside.

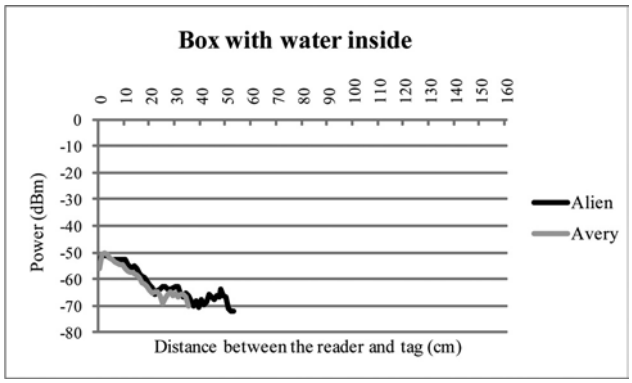

Fig. 10: Backscattered signal strength measured when tags were labelled onto box with water inside.

3.4. Signal strength – changing position of RFID tag and metal plate

The strength of the signal the tag backscatters to the reader antenna is very different, depending on the distance between the tag and antenna, and between the tag and Al plate. As Figures 11 and 12 show, the power varies from −75 to −30 dBm. The majority of signals respond with the power between −65 and −45 dBm. The Alien has slightly higher signal strength than the Avery tag. At all samples, it is also seen that the highest variability of power is detected when the tag is placed in the vicinity of the reader antenna and the Al foil is in close proximity to the RFID tag.

4. Conclusions

The RFID technology can facilitate the logistics, inventory or selling much faster and more accurate than barcodes or any other automated identification systems. When the

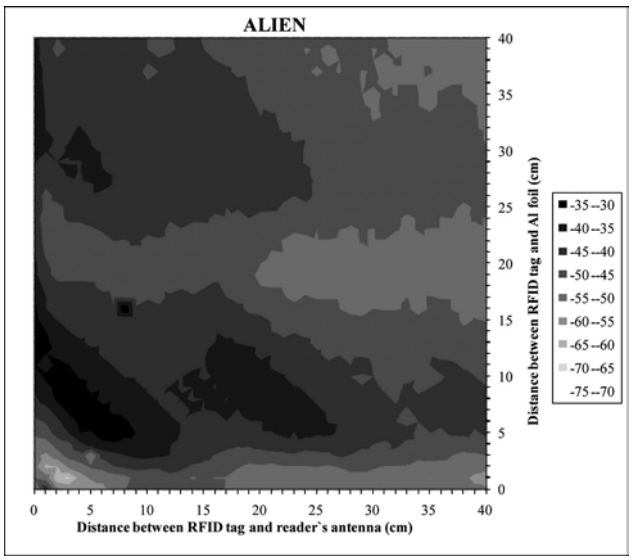

Fig. 11: Signal strength for Alien tag.

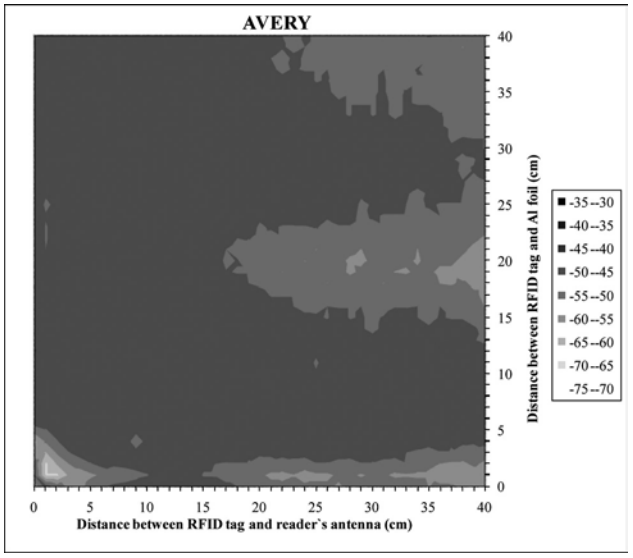

Fig. 12: Signal strength for Avery tag.

packaging and products that are packed are not made of metal or water, the passive UHF RFID tags work very well. The reading distance is long enough for the reading from at least 1 m, the backscattered signal strength is high and there is no particular reason for not using the RFID technology for labelling such products. Different characteristics are observed when the packed products are made of metal or contain a large amount of liquid. In that case, the reading distances shorten and the backscatter strength power becomes much lower. Despite both antennas are folded dipoles and are quite similar in shape and size, the Alien antenna works better than Avery and it seems more adjusted for the labelling onto metal- or water-containing, respectively, products. The total appropriateness of using RFID tags for labelling such products is questionable. In the research, two different passive UHF RFID tags were tested. The results showed that the type of reader antenna influences substantially the tag readability or backscatters the signal strength. The antenna polarization, efficiency and directivity are the most important for antenna gain and consequently, for the reading of frequencies and distances. Apart from the reader antenna, the shape, orientation and the size of tag antenna are of great importance as well.

5. Acknowledgements

The authors acknowledge the European Social Fund ("Operation part financed by the European Union, European Social Fund") for the financial support, the Slovenian Research Agency (Project no. L2-1097), and the company Valkarton.

References

/1/ D. M. Dobkin, *The RF in RFID*, Amsterdam etc: Elsevier, 2008.

/2/ M. Brown, S. Patadia, and S. Dua, *Mike Meyers` RFID+ Radio Frequency Identification Certification Passport*, New York: The McGraw-Hill Companies, 2007.

/3/ P. J. Sweeney, *CompTIA RFID+ Study Guide*, Indianapolis: Wiley, 2007.

/4/ P. Sanghera, and F. Thornton, "Selecting the RFID System Design," *How to Cheat at Deploying and Securing RFID*, pp. 119–146, Burlington: Syngress, 2007.

/5/ S. R. Aroor, and D. D. Deavours, "Evaluation of the State of Passive UHF RFID: An Experimental Approach," *Ieee Systems Journal,* vol. 1, no. 2, pp. 168–176, Dec, 2007.

/6/ P. J. Sweeney, *RFID for Dummies*, Indiana: Wiley publishing, 2005.

/7/ U. Bogataj, T. Muck, M. Maček *et al*, "**The study of UHF RFID tags readability in dependence of antenna design**." pp. **251–255**.

/8/ U. Bogataj, T. Muck, and M. Maček, "Readability of different UHF RFID tags."

/9/ T. Muck, U. Bogataj, D. Ličen *et al*, "**UHF RFID – a brief technology analysis**," in **5th International Symposium on Novelties in Graphics**, **Ljubljana, Slovenia**, 2010, pp. **573–577**.

/10/ T. Muck, M. Starešinič, U. Bogataj *et al*, "**UHF RFID in logistics – a brief technology analysis**," in **LOPE-C International Conference and Exhibition for the Organic and Printed Electronics Industry**, **Messe Frankfurt, Germany**, 2010, pp. **237–240**.

Urška Bogataj[1], Marijan Maček[2], Tadeja Muck[3]

[1]Valkarton, Production of Corrugated Board and Packaging d. d., Tržaška cesta 1, 1370 Logatec, Slovenia, e-mail address: urska.bogataj@gmail.com

[2] University of Ljubljana, Faculty of Electrical Engineering, Tržaška cesta 25, 1000 Ljubljana, Slovenia, e-mail address: marijan.macek@fe.uni-lj.si

[3] University of Ljubljana, Faculty of Natural Sciences and Engineering, Chair of Information and Graphic Arts Technology, Snežniška ulica 5, 1000 Ljubljana, Slovenia, e-mail address: tadeja.muck@gmail.com

Prispelo: 03.01.2011 *Sprejeto: 23.08.2011*

SYNTHESIS AND CHARACTERIZATION OF SILICA COATED MAGNETIC NANOPARTICLES

Ana Drmota[1], Andrej Žnidaršič[1]

[1]Nanotesla Institute Ljubljana, Ljubljana, Slovenia

Key words: magnetic nanoparticles, silica, microemulsion method

Abstract: Magnetic (γ-Fe_2O_3) nanoparticles coated with silica (SiO_2) and a narrow particle size distribution were prepared in microemulsion system: water/(SDS+1-butanol)/cyclohexane. The influence of the concentration of reactants in aqueous phase, the temperature of reaction, the pH value during the precipitation of hydroxides and the type of surfactant, on the nature of γ-Fe_2O_3 nanoparticles were investigated. The thickness of SiO_2 shell was carefully controlled by the amount of tetraethoxysilane (TEOS) added to the microemulsion after the precipitation step. Prepared uncoated and coated γ-Fe_2O_3 nanoparticles were characterized using transmission electron microscopy (TEM), X-ray diffractometry (XRD) and specific surface area measurements (BET). The specific magnetization (DSM-10, magneto-susceptometer) of the prepared samples was also measured. The specific magnetization of the γ-Fe_2O_3 nanoparticles depended on their size, ranging from 14 to 49 Am^2/kg. The specific magnetization of coated γ-Fe_2O_3 nanoparticles sharply decreased due to the non-magnetic nature of SiO_2 layer.

Sinteza in karakterizacija magnetnih nanodelcev s silikatno prevleko

Kjučne besede: magnetni nanodelci, silika, mikroemulzijska metoda

Izvleček: Magnetne (γ-Fe_2O_3) nanodelce s silikatno (SiO_2) prevleko smo sintetizirali v mikroemulzijskem sistemu: voda/(SDS+1-butanol)/cikloheksan. Raziskali smo vpliv koncentracije reaktantov vodne faze, temperature reakcije, pH vrednosti soobarjanja hidroksidov in tipa surfaktanta na naravo γ-Fe_2O_3 nanodelcev. Debelino nanosa SiO_2 smo kontrolirali s količino dodanega tetraetoksisilana (TEOS) v mikroemulzijo po končani reakciji soobarjanja. Neoblečene in s SiO_2 oblečene γ-Fe_2O_3 nanodelce smo karakterizirali s transmisijskim elektronskim mikroskopom (TEM), rentgensko praškovno difrakcijo (XRD) in merjenjem specifične površine delcev (BET). Pripravljenim vzorcem smo merili specifično magnetizacijo (M). V odvisnosti od velikosti delcev se je spreminjala od 14 do 49 Am^2/kg. Specifična magnetizacija oblečenih nanodelcev je močno padla zaradi nemagnetne narave SiO_2.

1. Introduction

The preparation of surface functionalized magnetic nanoparticles has a great interest for potential biomedical applications such as magnetic cell separations, therapeutic drug, gene and radionuclide delivery, hyperthermia treatments and MRI contrast enhancement.

In this field the main challenge is tailoring the surface of magnetic nanoparticles in order to functionalize and develop strong interactions with specific biological components (dye, drug or effector grafting). Therefore, chemical modification of the nanoparticle surface with biocompatible molecules, such as silica (SiO_2), is an important issue that provides biofunctionality and resistance to physiological conditions. Although there are many kinds of interesting magnetic nanoparticles, we have been focused our study on silica (SiO_2) coated maghemite (γ-Fe_2O_3) nanoparticles because of their non-toxic nature and lower susceptivity to physical and chemical changes.

Among many methods, a precipitation in microemulsion has been shown as a very perspective method to produce superparamagnetic core–shell nanoparticles. A microemulsion can be defined as a thermodynamically stable isotropic dispersion of two immiscible liquids consisting of nanosized domains of one or both liquids in the other, stabilized by an interfacial film of surface-active molecules /1,2/.

In this method, coprecipitation occurs in tiny droplets of water ("water pools") embedded with surfactant and homogenous distributed in an oil phase.

The size of these "water pools", so caled reverse micelles, which act as microreactors for the synthesis of the nanoparticles, is termodinamically define by the water-to surfactant molar ratio /3/.

In the present investigation, silica (SiO_2) coated maghemite (γ-Fe_2O_3) nanoparticles were performed in-situ via the precipitation in microemulsion system water/SDS,1-butanol/cyclohexane according to Schikorr´s reaction:

$$Fe^{2+} + Fe^{3+} + 2OH^- + O_2 \Rightarrow \gamma\text{-}Fe_2O_3 + H_2O.$$

In this synthesis, the Fe(II) and Fe(III) hydroxides were precipitated during the reaction between two different microemulsions containing an aqueous solution of corresponding ions (MEI) and precipitating reagent (MEII). In the second step of the synthesis, the Fe(II) hydroxide is oxidized, resulting in the formation of the spinel maghemite (γ-Fe_2O_3) phase. The surface of γ-Fe_2O_3 nanoparticles prepared in microemulsion systems was functionalized using tetraethoxysilane TEOS.

2. Experimental

The chemical reagents used in this synthesis process were iron (II) sulfate heptahydrate ($FeSO_4 \times 7H_2O$, ACS, 99+%), iron (III) sulfate hydrate ($Fe_2(SO_4)_3 \times xH_2O$, Reagent Grade), ammonium hydroxide solution (25%, puriss p.a.), sodium n-dodecyl sulfate (SDS) ($CH_3(CH_2)_{11}OSO_3Na$, 99%), 1-Butanol ($CH_3(CH_2)_3OH$, 99%), cyclohexane (C_6H_{12}, ACS, 99+%), tetraethoxysilane (TEOS), and ethanol (CH_3CH_2OH, 96%).

Two aqueous solutions were prepared (aqueous solution of Fe^{2+}/Fe^{3+} ions (0.4 or 0.15 M) and 5 % aqueous solution of NH_4OH). Aqueous solution of Fe^{2+}/Fe^{3+} ions with a molar ratio 1.85:1 was prepared by dissolving of an appropriate amounts of **iron (II) sulfate heptahydrate,** $FeSO_4 \times 7H_2O$, and **iron (III) sulfate hydrate**, $Fe_2(SO_4)_3 \times xH_2O$.

To chose a suitable composition that formed a stable water-in-oil (w/o) microemulsion in the system water/SDS,1-butanol/cyclohexane the region of microemulsion stability within which the microemulsion is optically transparent was determined by the titration method in connection with conductivity measurements. These are pseudo-ternary phase diagrams, in which every point represents a quaternary system whose overall composition is entirely defined by any pair among the three weight fractions: f_w (aqueous phase), f_s (surfactant + cosurfactant) and f_o (oil phase).

Prior to the synthesis two microemulsions of the same composition were prepared. The microemulsion I (MEI) contained 0.4 M or 0.15 M aqueous solution of Fe^{2+}/Fe^{3+} ions whereas the microemulsion II (MEII) contained 5 % aqueous solution of the ammonium hydroxide (NH_4OH) served as precipitation agent. The SDS to 1-butanol weight ratio was kept constant at 1:1.3, respectively. In the second step, MEI and MEII were mixed at diferrent temperatures and diferrent pH values for 1 h. A black precipitate was formed immediately. In the last step, the surface of g-Fe_2O_3 nanoparticles prepared in microemulsion systems with the same molar ratio (R=7) and the following composition: 39 wt.% of water phase, 31 wt.% of SDS/1-butanol, 31 wt.% of cyclohexane was functionalized using TEOS. The thickness of silica shell was carefully controlled by the amount of TEOS added to the microemulsion after the precipitation step. Finally, the product was centrifuged and washed several times with mixture of ethanol and water and dried at 100°C.

Synthesized SiO_2 coated g-Fe_2O_3 nanoparticles were characterized using transmission electron microscopy (TEM), X-ray diffractometry (XRD) and specific surface area measurements (BET). The specific magnetization (DSM-10, magneto-susceptometer) of the prepared samples was also measured.

3. Results and discussion

Figure 1 shows the X-ray diffraction patterns of the prepared samples. Except in the case of sample S2 (pH of synthesis was 6), the difractograms confirmed the formation of the spinel structure, characteristic of magnetite (Fe_3O_4) and maghemite (γ-Fe_2O_3) with different Fe^{2+} content. The chemical analysis of the synthesized nanoparticles showed that they contain only around 0,5 % of Fe^{2+}. From this we confirmed the formation of γ-Fe_2O_3 nanoparticles.

To estimate the average particle size (D_{XRD}) a Debye-Scherrer formula was used. The values are shown in Table 1.

The difference in the patterns is in the broadening of the peaks. Broader peak indicates smaller crystallite size. From the graph, it is observed that the crystallite size for sample S1 is the smalest and it follow by samples S6, S4 and S3. With increasing the concentration of aqueous solution of Fe^{2+}/Fe^{3+} ions from 0.15 M to 0.4 M the average size of the nanoparticles increased from 5.6 nm to 7.5 nm (samples S6 and S4) and with increasing the reaction temperature from 20 °C to 50 °C the average size of the nanoparticles increased from 3.3 nm to 7.3 nm (samples S1 and S4). The pH value had a strong influence to average particle size and phase composition. At pH 6 a nonmagnetic phase was formed. With increasing the pH value from 8.6 to 10.2 the average size of the nanoparticles decreased from 12.8 nm to 7.3 nm (samples S3 and S4).

Figure 2 left shows TEM image of uncoated γ-Fe_2O_3 nanoparticles which were spherical in shape and highly agglomerated, in compare to the γ-Fe_2O_3 nanoparticles obtained after the surface coating (Figure 2 right) with a thin layer of SiO_2.

The resultes obtained in this research show that concentration of aqueous solution of Fe^{2+}/Fe^{3+} ions, the reaction temperature and the pH value had a strong influence to average particle size distribution and as consequence to specific magnetization.

The results in table 1 show that with decreasing of concentration of aqueous solution of Fe^{2+}/Fe^{3+} ions from 0.4 M to 0.15 M the average particle size determined from BET measurements decreases from 6.5 nm to 4.5 nm (samles S4 and S6). The minimum average particle size was obtained at 20 °C. The average particle size increased from 5.4 nm to 6.5 nm (samles S1 and S4) with increasing the reaction temperature from 20 °C to 50 °C. At pH 6 a nonmagnetic phase was formed with the average particle size 9.3 nm and specific magnetization 1.4 Am^2/kg (samle S2). With increasing the pH value from 8.6 to 10.3 the average particle size decreased from 12.2 nm to 5.8 nm (samples S3, S4 and S5).

Figure 3 shows that specific magnetization (M) of the prepared γ-Fe_2O_3 nanoparticles increased from 19 Am^2/kg for the sample with average particle size 5.4 nm (sample S1) to 49 Am^2/kg for the sample with average particle size 12.2 nm (sample S3). The thickness of silica shell was carefully controlled by the amount of TEOS added to the microemulsion mixture during the precipitation step. Specific magnetization of the uncoated γ-Fe_2O_3 nanoparticles

prepared in microemulsion system was 48 Am^2/kg (sample S4) and decreased to 25 Am^2/kg for the nanoparticles with 3 nm thickness of silica shell.

Table 1 Results of the prepared samples

Sample	MEI (M)	$T_{(syn.)}$ (°C)	$pH_{(syn.)}$	BET (m^2/g)	D_{BET} (nm)	D_{XRD} (nm)	M (Am^2/kg)
S1	0,4	20	10,2	226	5,4	3,3	19
S2		50	6,0	132	9,3	-	1,4
S3			8,6	100	12,2	12,8	49
S4			10,2	189	6,5	7,3	48
S5			10,4	213	5,8	-	31
S6	0,15		10,2	274	4,5	5,6	14

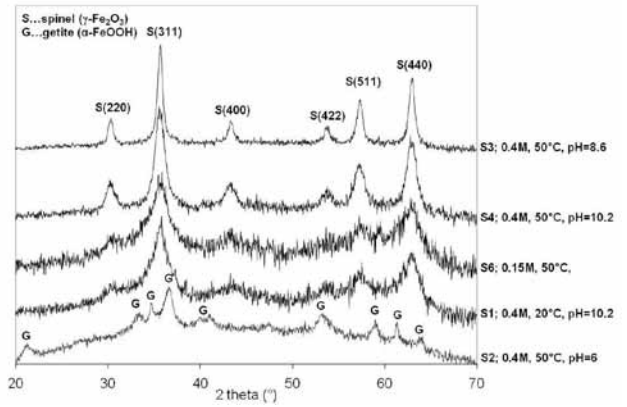

Fig. 1 XRD patterns of synthesized samples.

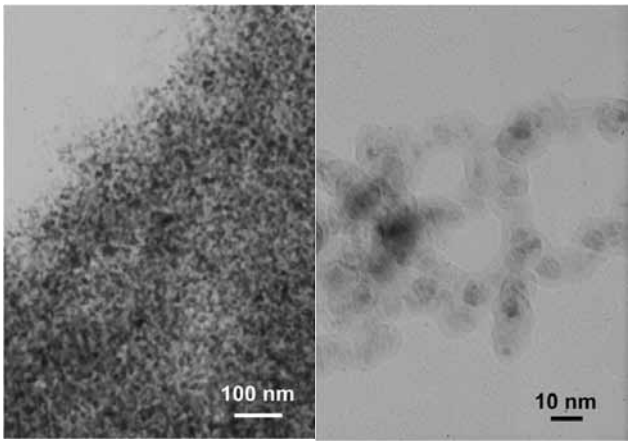

Fig. 2 TEM micrograph of (left) uncoated γ-Fe_2O_3 nanoparticles and (right) γ-Fe_2O_3 nanoparticles obtained with a thin layer of SiO_2.

4. Conclusions

In the present investigation γ-Fe_2O_3-SiO_2 core-shell nanoparticles were prepared via the precipitation in microemulsion system consisted of SDS as anionic surfactant, 1-butanol as co-surfactant, cyclohexane as an oil phase and aqueous solution of reactants.

We concluded that conductivity measurement can be used to characterize the microemulsion system and determine

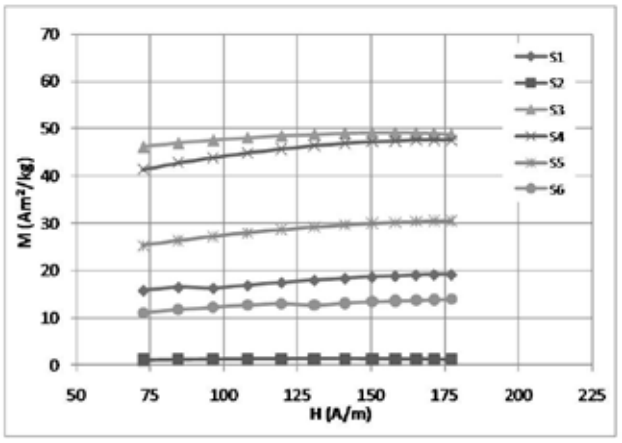

Fig. 3 Specific magnetization of uncoated γ-Fe2O3 nanoparticles.

the maximum amount of water that can be added to maintain the water-in-oil system.

The resultes obtained in this research show that the type of surfactant, concentration of aqueous solution of Fe^{2+}/Fe^{3+} ions, the reaction temperature and the pH value had a strong influence to average particle size distribution and as consequence to specific magnetization.

Results in Table 1, Figure 1 and Figure 2 show that smaller γ-Fe_2O_3 nanoparticles with high specific magnetization were prepared in the microemulsion system water/SDS,1-butanol/cyclohexane.

Prepared uncoated γ-Fe_2O_3 nanoparticles were spherical in shape and highly agglomerated. After the surface coating with a thin layer of SiO_2 core-shell nanoparticles were a tiny bit agglomerated.

The magnetic measurements indicate reduction of magnetization of the coated γ-Fe_2O_3 nanoparticles compared with the uncoated γ-Fe_2O_3 nanoparticles because of the contribution of the volume of the non-magnetic SiO_2 coating layer to the total sample volume.

References

/1/ S. Mornet, F. Grasset, J. Portier, E. Duguet, Maghemite@silica nanoparticles for biological applications, European Cells and Materials 3/2 (2002) p. 110-113.

/2/ J. Vidal-Vidal, J. Rivas, M.A. López-Quintela, Synthesis of monodisperse maghemite nanoparticles by the microemulsion method, Colloids and Surfaces A: Physicochemical and Engineering Aspects 288/1-3 (2006) p. 44-51.

/3/ D. Makovec, A. Košak, The synthesis of spinel–ferrite nanoparticles using precipitation in microemulsions for ferrofluid applications, Journal of Magnetism and Magnetic Materials 289 (2005) p. 32-35.

Ana Drmota[1], Andrej Žnidaršič[1]
[1]Nanotesla Institute Ljubljana, Stegne 29, 1000 Ljubljana, Slovenia

Prispelo: 02.12.2010 *Sprejeto: 23.08.2011*

SIMULATION OF RADIO-VISIBILITY IMPACT ON THE PROVIDED QUALITY OF SERVICE WITHIN THE WIMAX NETWORK

Saša Klampfer[1], Jože Mohorko[2], Žarko Čučej[2], Amor Chowdhury[1]

[1]Margento R&D d.o.o., Maribor, Slovenia
[2]Univerza v Mariboru, Fakulteta za elektrotehniko, računalništvo in informatiko, Maribor, Slovenia

Key words: signal attenuation, radiation, base station, WiMax, intermediate barriers, simulation, OPNET Modeler, model, elevation mapping, DTED, visibility, end user, signal strength, cross section, equipment allocation.

Abstract: This paper presents the latest generation of wireless networks, which includes WiMax networks. WiMax allows wireless broadband internet access in areas where a physical connection (optical connection, wired connection) is not possible or available. Because of many benefits, and good user properties of the WiMax network (a relatively large amount of available channel bandwidth (up to 70 Mbit/s) and a comprehensive range (up to 50 km)) such networks have in the last year become popular all around the world, especially in Africa. The abovementioned benefits are also the main reason for an increasing popularity of WiMax technology in Slovenia which also has high terrain roughness and large dispersion of the population in rural areas. Since the beginning many questions about WiMax are being posed on various internet forums: how far away from the main base station can a potential user be to receive a good quality of service, how many potential users can one base station cover, how do intermediate barriers (houses, hills, woods etc.) influence the WiMax signal strength, should a potential user of the WiMax technology have direct radio-visibility to the base station in order to receive a good quality of service, etc. The main aim of this paper is to answer some of the mentioned questions by using a WiMax simulation model in the OPNET Modeler simulation tool. Simulation results must be precise, and that preciseness depends on model accuracy, which is why we have also included DTED elevation mapping covering a wide range of Pohorje area beside a precise WiMax network model. With such elevation mapping we imitate intermediate barriers, and the effect of the terrain on dissemination and diffusion of radio signal emitted into the landscape. Elevation mapping allows us to observe a cross-section of the terrain between a potential user and a WiMax base station. It is also possible to observe the influence of the distance of the WiMax user from the base station, the changes of the signal strength due to terrain barriers etc. Each included scenario has a different geographical placement of the end-user unit in relation to the base station. In each simulation scenario we have observed the signal strength level, signal to noise ratio, ratio between all sent and all received packets between the base station and the end-user unit, etc. With all the obtained results and the observed parameters we try to provide answers to some of the abovementioned questions. Simulation and the simulation model are our starting points for the research presented in this paper.

Simulacija vpliva vidnosti na sprejem radio signala in kvalitete storitve znotraj omrežja WiMax

Kjučne besede: slabljenje signala, radiacija, bazna postaja, WiMax, vmesne ovire, simulacija, OPNET Modeler, model, višinska kartografija, DTED, vidljivost, končni uporabnik, jakost signala, prečni preprez, pozicioniranje opreme

Izvleček: V članku predstavljamo simulacijo WiMax brezžičnega omrežja. Ker takšno omrežje omogoča brezžičen širokopasovni dostop do sodobnih aplikacij na večje razdalje (do 70 km), je slednji še kako dobrodošel na neurbanih področjih, kjer je poseljenost redka, dostop preko fizičnega medija pa ni dostopen. Takšnih področij je še dandanes kar nekaj tudi v Sloveniji, zato postaja zanimanje za takšne storitve še kako zanimivo. V ta namen smo izvedli raziskavo v simulacijskem orodju OPNET Modeler, s katero smo želileli odgovoriti na vprašanja, ki jih vsakodnevno srečujemo na številnih spletnih portalih. Med takšna vprašanja sodijo npr.; ali vmesne ovire vplivajo na sprejem signala?, kako se vmesna ovira (npr. hrib) odraža na kvaliteti storitev?, kolikšen je domet? ipd. V ta namen smo v simulacijski model vključili višinsko kartografijo DTED, ki pokriva predel Pohorja in bližnjo okolico, prilagodili oddajno/sprejemno WiMax anteno, ustvarili odjemalca WiMax storitev, kateremu smo v različnih scenarijih spreminjali lokacijo postavitve (oddaljenost, vmesne ovire, ipd.), prilagodili frekvenčni pas, ter nenazadnje uporabili TIREM4 propagacijski model razširjanja radijskega valovanja, ki upošteva tudi faktorje prenosnega medija (zrak), kot so; vlažnost, nasičenost, refleksija ipd. Z upoštevanimi faktorji smo v simulaciji ustvarili, kar se da natančni približek dogajanja v realnem okolju.

1 Introduction

Use of mobile wireless communications, applications and mobile data transfer is nowadays rapidly increasing. Standardization of GSM-based systems has begun in the 1980s, when the development of a unique radio-communications system for Europe at 900MHz started. Since then many modifications have been made in order to fulfill increasing demands from the operators as well as cellular users.

This paper describes a Worldwide Interoperability for Microwave Access (WiMax) network and the influence of intermediate barriers on service reception (for example; data reception, when a VoIP application is in use). WiMax represents the next generation of long-range wireless networks, which allows broadband packet-based transmission of text, video, digitized voice and multimedia at data rates up to 70 megabits per second (Mbps) /1/. WiMax is intended for a consistent set of services provided to users, who do

not have the option to connect to any other communication media, such ADSL, FTTH, and VDSL.

Because WiMax is today fully available, internet service providers can also provide WiMax networks; mostly in rural areas where population dispersion is relatively high, and an ISP can for example cover such users with only one transmitting/receiving base station without using any optical or other cables to end-users. WiMax clients will have exactly the same set of possibilities and applications as users using wired broadband connections (xDSL, FTTH, etc.). WiMax offers many different applications, such as: light and heavy web browsing, reading web mail, VoIP quality speech, video conferencing, base access, telnet session, file transfer, file copy, e-mail, and so on. For simulation purposes, described further on, we have chosen only one application, i.e. VoIP, which is today widely used among most of the world's population, because it allows the user to communicate with the world at any place and time. WiMax networks are a part of making such communication available. This research work is mostly concentrated on the radio-visibility impact on service quality (VoIP), and the influence of distance on service quality. These are two major problems which are going to be exposed in the paper. With the obtained simulation results we are going to see how intermediate barriers between the base station and the WiMax end-user influence service quality, how distance affects the same provided service (VoIP), etc. The paper is organized into seven sections. The second section is devoted to the presentation of a WiMax network, its main constitutive parts and their properties and descriptions. The third section shortly presents the main problem, which is explained and argued with different simulation scenarios described in further sections. The fourth section presents the OPNET Modeler simulation tool as an essential part of a precise simulation procedure /5, 6, 9/. Within this section a description of the elevation maps (DTED) is also given, together with their impact on the simulation model and their presentation in a geographical form. Under the fifth section the TIREM4 signal propagation model, used in our case, is presented. The sixth section presents three simulation scenarios used for testing different impacts on the service quality provided by the WiMax network (first scenario – without barriers and at a short distance, second scenario – without barriers and at a large distance, and third scenario – with barriers between the base station and the end user). The first two scenarios are intended for testing the influence of distance on the services provided by WiMax. A modeled WiMax network corresponding to the abovementioned testing scenarios is also presented and explained in this section, together with the simulation results, which give us answers to questions posed on many different forums. The seventh section concludes the paper.

2 WiMax network and main parts presentation

Worldwide Interoperability for Microwave Access or shortly WiMax is at the moment one of the most popular wireless technologies in the world. The IEEE organization (Institute of Electrical and Electronics Engineers) in 2004 issued the IEEE standard 802.16 known as Revision D. It was published for the needs of WiMax and fixed applications. One year latter the same organization published Revision E of the 802.16 standard, which includes also the mobility options. WiMax typically operates in the 2.5GHz, 3.5GHz and 5.8GHz frequency bands licensed by many government authorities. It uses RF technology and OFDM (Orthogonal Frequency Division Multiplexing) multiplexing technology. OFDM is very effective in cases when carriers have a bandwidth equal to 5MHz or grater. WiMax can be used for many applications, including the so-called 'last mile' broadband connections, where the WiMax base station spreads the wireless link around.

The WiMax system consists of two main parts /4/:

- a WiMax base station, and
- a WiMax receiver station

The WiMax base station consists of interior electronics and a WiMax antenna. Such base station can usually cover a radius up to 10km, in theory even up to 50km. Any receivers node placed within the mentioned radius can receive the WiMax RF signal. These specifications will be tested in the OPNET Modeler simulation tool, as the original contribution of this paper. Nowadays, all WiMax networks are cellular, which means that the WiMax network is constructed by using many base stations. Several base stations can be interconnected using the so-called 'backhaul' microwave links. According to Revision E, this allows a WiMax subscriber to roam from one base station area to another base station area. The roaming procedure is quite similar to that known in the GSM/UMTS networks /3/.

The WiMax receiver station could be a stand-alone set-top-box or a PC, PCI or PCIe card, or simply a USB receiver dongle. The base station acts as an access point, so the access is similar as in case of WiFi.

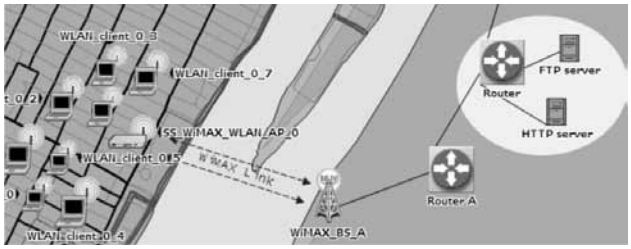

Fig. 1. A WiMax network example with a base station, a core network, and WiMax receivers.

In such a network it is necessary to provide logical separation between IP addressing, routing and connectivity management procedures and protocols to enable the primitives and interworking deployment.

The network reference model developed by the WiMax Forum NWG defines a number of functional entities and interfaces between them. Figure 2 below shows some of

the more important functional entities. The WiMax network core consists of the following elements:

A base station (BS) which is responsible for providing an air interface to the MS (Main Station). Additional functions that may be a part of the BS are micro mobility management functions, such as handoff triggering and tunnel establishment, radio resource management, QoS policy enforcement, traffic classification, DHCP (Dynamic Host Control Protocol) proxy, key management, session management, multicast group management etc.

Access service network gateway (ASN-GW) which typically acts as a layer 2 traffic aggregation point within the ASN. Additional functions that may be a part of the ASN gateway include intra-ASN location management and paging, radio resource management and admission control, caching of subscriber profiles and encryption keys, AAA (Authorization And Accounting platform) client functionality, establishment and management of a mobility tunnel with base stations, QoS and policy enforcement, foreign agent functionality for mobile IP, and routing to the selected CSN (see below).

Connectivity service network (CSN) which provides connectivity to the Internet, ASP, other public networks, and corporate networks. CSN is owned by the NSP (Network Service Provider) and includes AAA servers that support authentication for the devices, users, and specific services. CSN also provides per-user policy management of QoS and security. CSN is also responsible for IP address management, support for roaming between different NSPs, location management between ASNs, and mobility and roaming between ASNs.

The WiMax architecture framework allows for a flexible decomposition and/or combination of functional entities when building the physical entities. For example: ASN may be decomposed into base station transceivers (BST), base station controllers (BSC), and an ASN-GW analogous to the GSM model of BTS, BSC, and Serving GPRS Support Node (SGSN) /2, 3 and 4/.

3 Research area and limitations

Our aim at this research work is to answer some questions which can be found on many internet forums. With a WiMax simulation model and the OPNET simulation tool we will demonstrate how distance affects WiMax applications such is VoIP etc., how intermediate barriers affect service availability, if direct radio visibility is necessary or not, etc. In order to obtain relevant results and to prevent other traffic from affecting our simulation results we have used use the same traffic generators (same traffic amount) and the same number of clients in all simulation scenarios. We were thus able to compare delays at short and large distances as well as see what happens with end-to-end delay in case when an obstacle is placed between the transmitter and the receiver.

4 OPNET Modeler simulation tool

OPNET Modeler is one of the most useful simulation tools in the area of communication industry. The tool enables designing and studying telecommunication infrastructures, individual devices, protocols, applications, etc. It is based on object-oriented modeling. Individual modules included in specific libraries are representative of real building blocks used in real communication infrastructure. The created simulation models thus present a good approach compared to equivalent real networks. Support for modeling of all types of communication networks, included in advanced technologies such as Wi-Fi, UMTS, GSM, Fast Ethernet, etc. is also available. The tool allows modeling of PSTN, ISDN, xDSL, as well as optical networks. The user interface is based on a series of hierarchical graphic interfaces, which enable editing at every stage, as well as illustrate the structure of protocols, devices and networks. The tool also supports animations, which can provide a better understanding of the simulation results and events appearing in the simulated networks. The user can observe how individual packets travel during the execution of the simulation (slow motion support). OPNET Modeler offers a rich existing model library of standard equipment and protocols, including the possibility of modeling new or upgrading existing ones, which can be done by using code level in C/C++ programming languages /9/.

5 The used radio-signal propagation model (TIREM4)

TIREM is an abbreviation for the English phrase Terrain Integrated Rough Earth Model, which means an integrated land undulating terrain. TIREM includes two models, TIREM4 and TIREM3 which are often used when we model wireless links. TIREM3 has been developed by the Department of Defense (United States of America). In recent years it has been replaced with a more detailed model of radio-wave propagation: TIREM4, which offers a faster path-loss calculation, especially in cases when we have to deal with sophisticated 3D terrain landscape cartography. TIREM has the ability to anticipate loss-distribution of radio waves (RF) for the frequency bands between 1MHz and 40 GHz for land and open sea areas. The signal propagation model allows us to change the soil conductivity (ground conductivity) parameters, relative permeability, humidity, wave reflection and dispersion surface refractivity as well

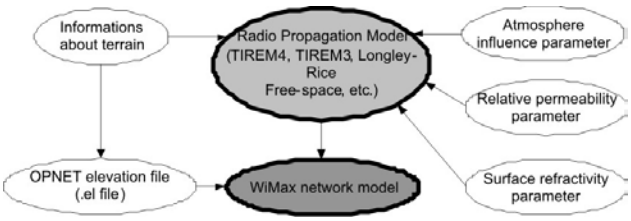

Fig. 2. The correlation between a radio propagation model and its parameters and a WiMax network model.

as resolution defined by the distance between isohypses on the elevation map /7, 8, 9/.

6 Simulated network presentation, simulation scenarios and simulation results

We have conducted the tests in the experimental part with the OPNET Modeler simulation tool where we have modeled the WiMax network structure serving as an example for the testing scenarios which will be described later. This is the simplest example with only one WiMax base station and two WiMax clients. We were focused on observing how the distance affects the VoIP application (a representative of time-sensitive applications) provided by the WiMax network, how intermediate barriers influence the WiMax RF-signal reception etc. Other WiMax users were not included, because we did not want to observe their impact on voice delay. Figure 3 presents a fictitious network. Our main goal in these simulations was to show the reader how the distance-parameter and intermediate barriers affect network's performance regarding the VoIP end-to-end delay, received power level, SNR etc.

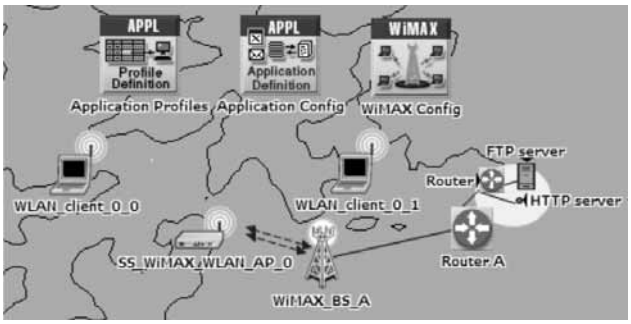

Fig. 3. Simulated WiMax network structure.

The whole network is constructed of two main parts:

- a wired network,
- the WiMax network.

The wired network structure consists of servers, such as Web Server, FTP server, etc, which are connected through a 100BaseT connection through an 8-port router. From this router, the 100BaseT connection is connected to Router A, which is intended to have WiMax base stations (in our case only one) connected to it. A WiMax base station with an Omni transmitting/receiving antenna produces a WiMax RF signal in the 3.5GHz frequency band /1/, which is then redistributed through a WiMax wireless access point.

Two WiMax clients establish a VoIP session through the WiMax wireless access point. Such VoIP application is defined by the 'Applications' node shown on the top-left side in Figure 3. With the 'Profiles' node (beside the 'Applications' node) client profiles are defined, i.e. what should the User Equipment (UE) do, or in other words, which application is such UE capable of using (in our case VoIP).

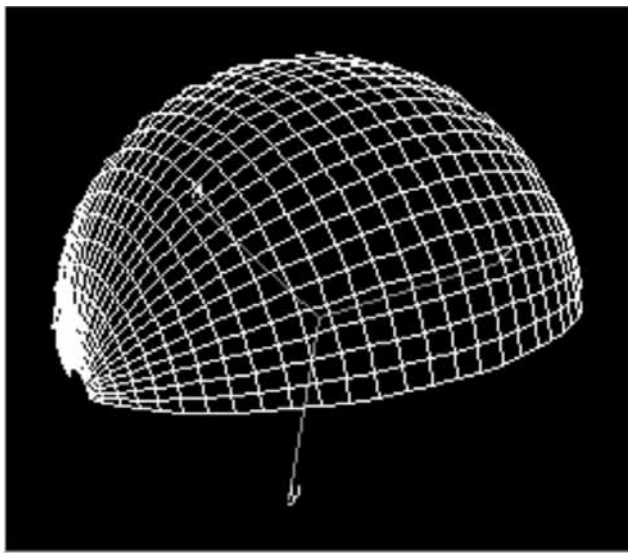

Fig. 4. WiMax Omni antenna radiation pattern.

Scenario 1: A short distance without barriers

In this scenario, the end-user equipment was placed near the WiMax access point. The distance between them was 820m and there was free space between them, so no obstacle (hill, building etc.) was presented. The transmitter power was in this case set to 0.05W. Figure 5 presents the described scenario.

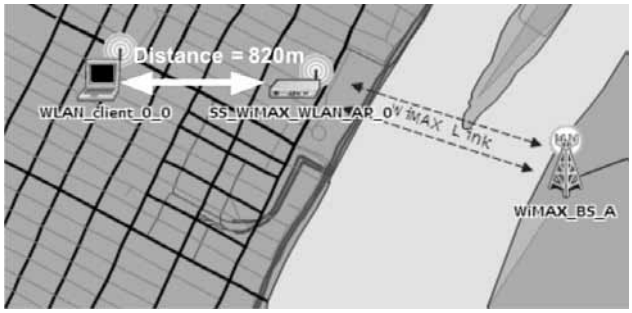

Fig. 5. A short distance (820m) between the WiMax access point and the WiMax client.

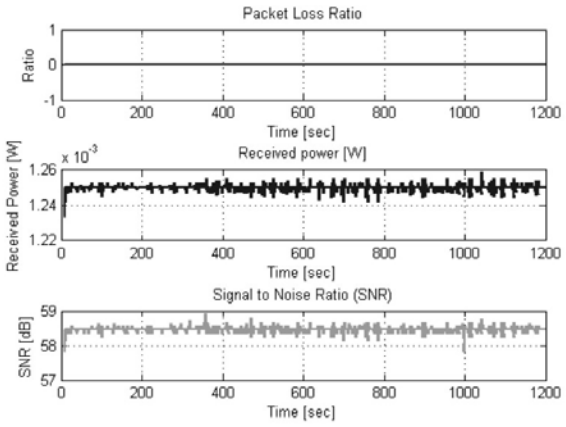

Fig. 6. Packet Loss ratio, received power and SNR for a WiMax client at a short distance (820m) and with a transmitting power 0.05W.

During the simulation process we have obtained the results presented in Figure 6. Data transfer was clear, so no data was lost. The received power was within acceptable borders and was fairly constant during the whole VoIP transfer process. The same can be said for signal-to-noise ratio (SNR).

The VoIP delay and the delay in the wireless network were minimal and also within the expected borders /10/. This is shown in the figure below (Figure 7).

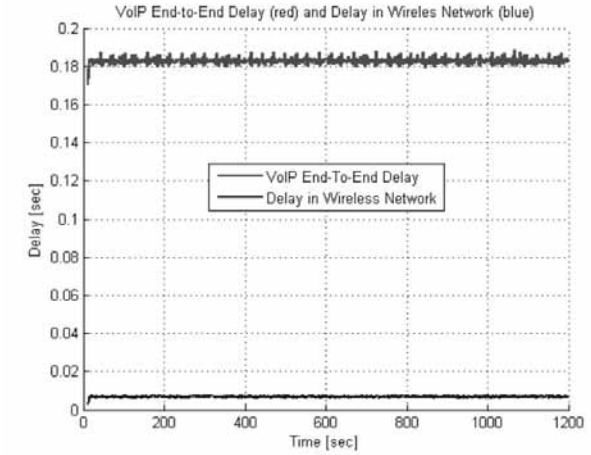

Fig. 7. VoIP end-to-end delay (red) and the delay in the WiMax wireless network for a WiMax client at a short distance (820m) and with a transmitting power 0.05W.

This scenario shows that at a short distance without intermediate barriers between the WiMax client and the base station there are no problems in the communication process.

Scenario 2: Large distance without barriers

In the second scenario we have moved the client node to a different position, which was 9.7km away from the WiMax access point.

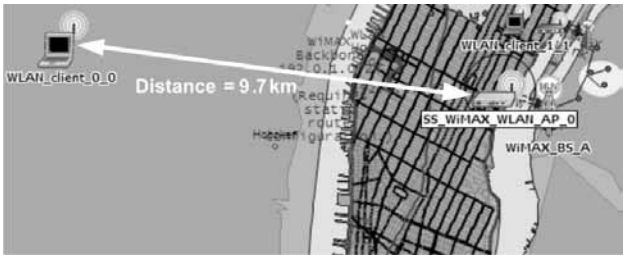

Fig. 8. A long distance (9.7km) between the WiMax access point and the WiMax client.

Like above there were no intermediate barriers between the client and the base station, and other settings and the traffic amount were also the same as in the first simulation scenario. This simulation scenario is presented in Figure 8.

With this simulation scenario we have obtained similar results as in the first scenario. They are presented in Figure 9. Also in this case data transfer was clear, and no data was lost. The received power was within acceptable limits and was also in this case fairly constant (1.6mW) during the whole VoIP transfer process. The same applies for signal-to-noise ratio (SNR). From this we can conclude that distance has a minimal influence on the power of the received signal. The difference between the first and the second scenario was in the base station transmitting power, which was in first scenario set to 0.05W, and in t

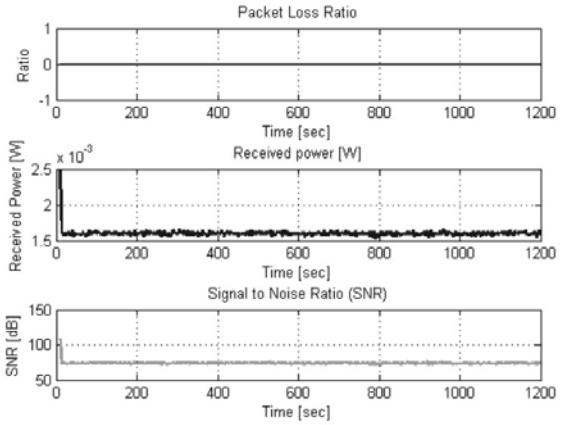

Fig. 9. Packet Loss ratio, received power and SNR for a WiMax client at a long distance (9.7km) with a transmitting power 1W.

However a completely different story appears when we observe the VoIP delay and the delay in the wireless network. Those delays have rapidly increased, but this was the consequence of a larger SNR factor in the first few seconds of the simulation. Such a case is presented in Figure 10. When we repeat the same scenario and ensure a constant SNR and received power, we obtain pretty similar results

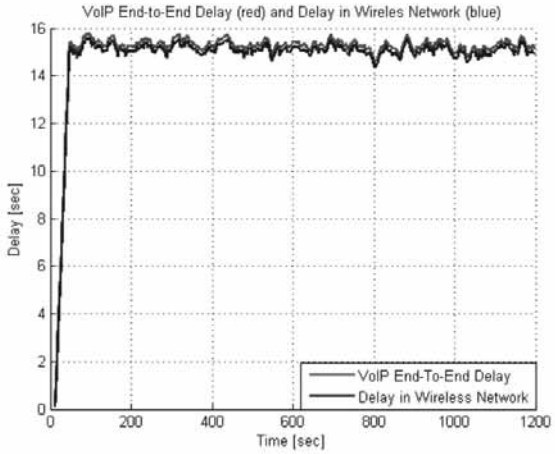

Fig. 10. VoIP end-to-end delay (red) and the delay in the WiMax wireless network for the WiMax client at a long distance (9.7km) with a transmitting power 1W (the receiver operates in the saturation area).

as those presented in Figure 7 (first scenario). Figures 9 and 10 show only a worst-case example, which happens when the SNR is increased and when the receiver operates in the saturation area. Under normal circumstances the differences in the delay between the first and the second scenario are minor and negligible. According to the obtained results we can confirm that the delay only minimally depends on the distance, but we have to be very careful with the transmitting power and the receiver density so that it does not pass into the saturated area.

A higher delay in Figure 10 is a consequence of the receiver saturation where the SNR also exceeds all allowed limits.

Scenario 3: Intermediate barriers between the WiMax client and the WiMax access point

The distance between the WiMax client and the WiMax access point was 5.26km in this simulation case. Between both units there were many intermediate barriers (hills) as shown in Figure 11 where the cross-section of the terrain between both units is presented. Traffic generator parameters were the same in this scenario as in both previous cases, so the traffic amount was equal in all three scenarios. Because of the nature of the frequencies that the WiMax uses, intermediate barriers should not have a noticeable influence on the service quality, which our last scenario has confirmed. In this scenario we have used the DTED cartography which simulates the geographical properties around the Pohorje area. Because of the DTED cartography and the used TIREM4 RF signal-propagation model, the terrain influence on signal dispersion is included.

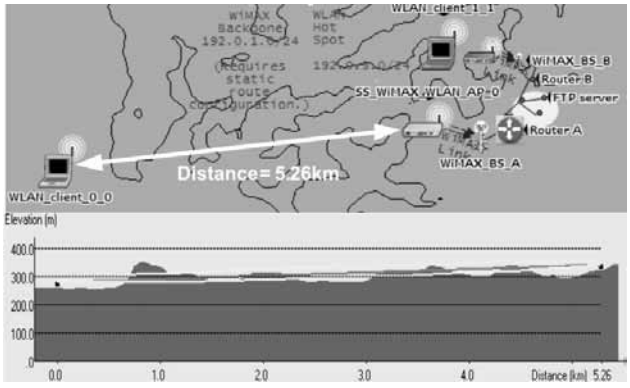

Fig. 11. Intermediate barriers between the WiMax access point and the WiMax client.

As shown in Figure 12, the abovementioned thesis on the WiMax frequency operation band is confirmed; meaning that intermediate barriers do not have a significant influence on the quality of the provided application.

Like in previous scenarios data transfer was clear, and no data was lost. The received power was within acceptable limits and was also in this case fairly constant. Compared to previous scenarios the received power was only slightly lower than in cases where there were no obstacles between the client and the base station.

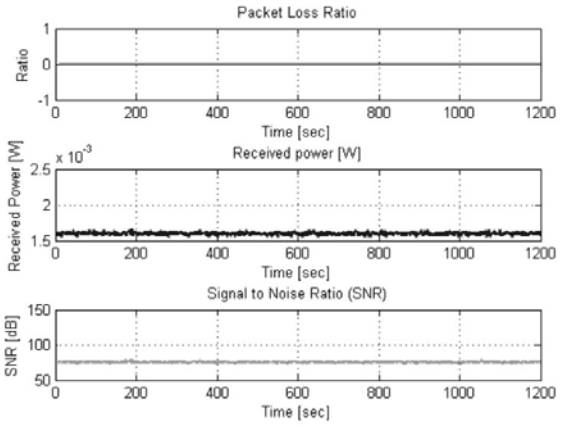

Fig. 12. Packet Loss ratio, received power and SNR for a WiMax client at a 5.26km distance with intermediate obstacles (hills). Transmitting power = 1W.

7 Conclusion

According to the obtained simulation results we can confirm that the WiMax network is very robust in terms of its frequency band operation. Intermediate obstacles, such as woods and hills, do not affect the quality of the provided service significantly. Distance also does not present a problem in the communication process, when it is within the specified borders. But as we have already mentioned, properly set transmitting power and configuration are very important for an undisturbed service delivery to the end-user. To conclude, we can say, that intermediate barriers and large distances which are within specified areas have only a small influence on the provided WiMax service.

Literatura

/1/ Frank Ohrtman, WiMax Handbook – Building 802.16 Wireless Networks, McGraw-Hill, June 2004

/2/ Kalai Kalaichelvan, Lawrence Harte, WiMax Explained (System Fundamentals), 2007

/3/ Jeffrey G. Andrews, Fundamentals of WiMax: Understanding Broadband Wireless Networking, Department of Electrical and Computer Engineering, The University of Texas at Austin, February 2007

/4/ G.S.V. Radha, K. Rao, G. Radhamani, WiMax: A Wireless Technology Revolution, Auerbach Publications, October 2007

/5/ Mohorko Jože, Matjaž Fras, Žarko Čučej, Modeling of IRIS Replication Mechanism in Tactical Communication Network with OPNET

/6/ J. Mohorko, M. Fras, Ž. Čučej, Modeling methods in OPNET simulations of Tactical Command and Control Information Systems

/7/ M. Fras, J. Mohorko, Ž. Čučej, A new approach to the modeling of network traffic in simulations, Informacije MIDEM 2008 (Junij)

/8/ M. Fras, J. Mohorko, Simulacija komunikacijskih sistemov v realnem času z realno komunikacijsko opremo v simulacijski zanki, Informacije MIDEM 2008 (Junij)

/9/ Opnet Documentation. http://www.opnet.com/

/10/ Jeffrey E. Wieselthier, Craig M. Barnhart and Anthony Ephremides, Data-delay evaluation in integrated wireless networks based on local product-form solutions for voice occupancy, Volume 2, Number 4, 297-314, DOI: 10.1007/BF01262049, March 29, 2005

Authors' presentation

Saša Klampfer graduated in 2007 from the Faculty of Electrical Engineering and Computer Science in Maribor, with a thesis title: "Networks simulation in OPNET Modeler". At the same faculty he defended his Master thesis: "Expert system for automatic analysis of tactical radio network properties" in 2009. His research work is focused on simulations and planning of telecommunication (UMTS) and computer networks (Fast Ethernet, Wi-Fi), and the influence of individual applications on individual networks in terms of delays, utilization of transfer channels, packet losses, etc.

Jože Mohorko received his B.Sc., M.Sc., and Ph.D. degrees in electrical engineering from the University of Maribor, Slovenia, in 1990, 1994 and 2002, respectively. He is a docent and researcher at the Faculty of Electrical Engineering and Computer Science in Maribor, University of Maribor. His research interests include image processing, modeling, simulating and evaluating telecommunication infrastructures.

Žarko Čučej is a full professor for automatic control and robotics, and telecommunications at the Faculty of Electrical Engineering and Computer Science of the University of Maribor. His recent research interests include signal processing and industrial data networks. He is a member of the IEEE.

Amor Chowdhury graduated in 1994 from the Faculty of Electrical Engineering and Computer Science in Maribor, with a thesis title: "Design of discrete regulation systems on a personal computer" In 1997 he defended his Master thesis: "The theory of robust synthesis" at the same Faculty. Four years later (2001) he finished his postgraduate studies with a doctoral dissertation: "Robust synthesis of control systems with consideration of performance criteria". He is an excellent innovator and researcher, which is proved by the number of granted patents and patent applications which are currently in the registration procedure, such as for example patent 11643 Terminal Device for Monitoring, Maintenance and Service Data.

Saša Klampfer[1], Jože Mohorko[2],
Žarko Čučej[2], Amor Chowdhury[1]

[1]Margento R&D d.o.o., Gosposvetska cesta 84,
2000 Maribor, Slovenia
[2]Univerza v Mariboru, Fakulteta za elektrotehniko,
računalništvo in informatiko, Smetanova 17,
2000 Maribor, Slovenia
E-pošta: sasa.klampfer@margento.com

Prispelo: 31.01.2011 *Sprejeto: 23.08.2011*

LICENCE PLATE RECOGNITION USING FEEDFORWARD NEURAL NETWORKS

Matej Kseneman[1], Dušan Gleich[1]

[1]Fakulteta za elektrotehniko, računalništvo in informatiko, Maribor, Slovenija

Key words: licence plate recognition, colour segmentation, colour space, feedforward neural networks, OCR engine

Abstract: Licence plate recognition presented in this paper is used to identify vehicles by their licence plate numbers. This technology can be widely used for paying pay-rolls, in opening parking garage door, traffic control /1/, etc. This paper presents an algorithm for licence plate recognition, shown in Fig. 1. The algorithm itself is divided into two parts, the first part extracts licence plate and the optical character recognition is described in the second part of the paper. In the first part of the paper three methods for licence plate recognition are presented. White pixels in an image can be detected using threshold method. Reference photo is shown in Fig. 2; meanwhile the experimental result of threshold method is shown in Fig. 3. The second method is based on 2D correlation, which uses segmentation in order to limit search area. The segmentation technique is performed using (1), but it is computationally very demanding (2). The result of this phase is shown in Fig 4. The method with Euclidian norm (3) uses Freeman chain code with interior pixels, but it is user dependent, because the user has to input one licence plate pixel (the result is shown in Fig. 5). The first method is used as method for licence plate recognition. The dilatation algorithm is used to fill up the whole plate with the same pixels. The dilated picture is shown in Fig 6. The algorithm detects the angle of licence plate, as shown in Fig. 7. Rotated and isolated licence plate is quantised and rescaled using a histogram method. The extracted licence plate is further shown in Fig. 8. The edges cut from detected licence plate and extracted binary images are shown in Figs. 9–10, respectively. A method called peak-to-valley is used to extract each individual character, which sums picture's columns and creates a histogram. By comparing sums to specified threshold, characters are detected. Characters are recognised using feed-forward neural networks. This network has 200 input neurons and 36 output neurons. Learning is accomplished through supervised learning of back-propagation technique. The whole structure of neural network is shown in Fig. 11. The results presented in Table 1 show that the overall efficiency of OCR engine is 96% when the recognition is applied on extracted licence plate

Razpoznava registrskih tablic vozila z uporabo feedforward nevronskih mrež

Kjučne besede: razpoznava registrske tablice, segmentacija barve, barvni prostor, nevronske mreže, OCR sistem

Izvleček: Ideja razpoznave registrskih tablic vozila (RTV) je relativno stara. Z razvojem informacijskih tehnologij in zmogljivih računalniških centralno-procesnih enot je postala implementacija zelo zahtevnih algoritmov zanimiva in uporabna. V tem članku bomo predstavili zmogljiv in robusten algoritem za zaznavo slovenskih RTV in zaznavo njenih znakov z uporabo t.i. feedforward nevronskih mrež. V prvem delu članka predstavljamo tri algoritme za izločitev RTV, in sicer s pomočjo pragovne funkcije, 2D korelacije in Evklidske norme. Nad prepoznano RTV se opravi kvantizacija in normalizacija za odstranitev šuma v sliki, skaliranje in rotacija na privzeto velikost in orientiranost. V drugem delu članka pa predstavljamo algoritem za prepoznavo znakov na RTV s pomočjo sistema za prepoznavo znakov (ang. Optical Character Recognition - OCR). Sistem OCR je sestavljen iz feedforward tipa nevronske mreže. Predlagani algoritem je zmožen prepoznati 96% izmed vseh testiranih RTV.

1. Uvod

S povečanjem zmogljivosti današnjih centralnih procesorskih enot in uporabi multimedijskih tehnologij v vsakdanjem življenju se prav tako povečuje potreba po avtomatizaciji vsakdanjih procesov. V tem članku bomo predstavili avtomatsko razpoznavanje RTV. Implementacijo predstavljenega algoritma je možno uvesti v plačilo cestnin, odpiranje zapornic garažnih hiš, pri nadzoru prometa, itd. Obstaja mnogo rešitev za avtomatizacijo RTV.

Yohimori /2/ je predlagal algoritem, ki primerja povprečne osvetlitve registrske tablice s podanimi pragovi. Porikli /3/ razpoznava RTV preko kovariančne matrike in nevronskih mrež. Podobno stori tudi Matas /4/, kateri za povečanje robustnosti pri razpoznavi uporabi invariantne deskriptorje in te rezultate pelje na nevronsko mrežo.

Prav to delo nas je motiviralo, da smo izvedli algoritem s pomočjo nevronskih mrež. V tem članku smo avtomatizirali razpoznavo RTV. Slika 1 prikazuje predlagani algoritem za razpoznavo RTV.

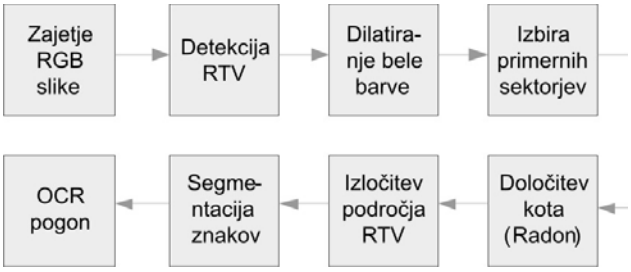

Slika 1. Blok diagram poteka razpoznave.
Fig. 1. Block diagram of recognition sequence.

Na izvorni sliki algoritem prične z iskanjem bele barve, kjer se nato v sliki belih segmentov išče pravokotnik. Na tem mestu se lahko pojavi nepravilna izbira pravokotnika, kajti slika belih segmentov je polna artefaktov (majhnih segmentov bele barve), ki so posledica leska in drugih stvari bele barve. Problem poskusimo odpraviti z uporabo segmentacije slike, nad katero napravimo 2D konvolucijo oz. korelacijo. Podoben pristop napravimo tudi s tretjo metodo, kjer algoritem za iskanje tablice uporablja Evklidsko normo /5/.

Iskanje pravokotnika se vrši preko dilatacije (odebelitve) belih segmentov, katere smisel je zapolniti črna področja na registrski tablici, na katerih se prvotno nahajajo znaki vključno z grbom. Z izbiro manjšega področja registrske tablice, se algoritem osredotoči na iskanje ravnih linij, preko katerih določi kot rotacije RTV. Kot rotacije določimo z uporabo Radonove trans-formacije /6/, s katero se nato celotna slika rotira tako, da se RTV pomakne v horizontalni položaj. Vzrok nagnjenosti gre iskati v krivinah na cestišču in kotom gledanja kamere.

Na manjši sliki ponovno opravimo iskanje pravokotnika, rezultat tega pa je slika registrske tablice v naravni velikosti slike in horizontalnem položaju. Na koncu se izvede še segmentacija znakov, kjer izločimo regije posameznih znakov, z OCR sistemom temelječim na nevronskih mrežah pa izvedemo razpoznavo znakov.

2. Zaznavanje registrske tablice

To poglavju podaja podrobno predstavitev posameznih korakov predlaganega algoritma, in sicer si koraki sledijo v vrstnem redu, kot so predstavljeni na sliki 1.

2.1. Uporaba različnih metod zaznavanja

Iskanje bele barve

Iskanje bele barve izvedemo v barvnem prostoru XYZ /7/, v katerem se prvotne 3 dimenzije RGB prostora pretvorijo v 2 dimenziji, tretja komponenta pa predstavlja svetlost. Na ta način lažje podamo meje, v katerih se nahaja bela barva, kar je ključnega pomena pri snovanju algoritma. Algoritem preveri ali je dani slikovni element bele barve ali ne. V primeru, da je, ga označi na izhodni sliki, kar prikazuje slika 3, medtem ko slika 2 prikazuje referenčno sliko.

2D korelacija

Razčlenjevanje slike v segmente s podobnimi lastnostmi imenujemo segmentacija slike. Pogosto predstavlja atribut svetlost barve pri monokromatski sliki, barvne komponente

Slika 2. Referenčna fotografija.
Fig. 2. Reference photography.

pri barvni sliki, lahko pa upoštevamo tudi robove objektov in njihove teksture, skratka možnosti je veliko. Po drugi strani pa nam segmentacija ne daje informacij o klasifikaciji segmentov, prav tako tudi o njihovih medsebojnih relacijah. Segmentacija je odvisna od osvetlitve slike, kar pa vpliva tudi na zaznavanje registrske tablice. Efekt ublažimo z izvedbo normalizacije barvnih komponent z vsoto trojice RGB /8-10/.

Slika 3. Najdeni beli slikovni elementi.
Fig. 3. Extracted white pixels.

Algoritem segmentacije deluje na sledeč način: najprej se izvede inicializacija, ki predstavi vse piksle kot neoznačene elemente, nato pa algoritem izbere prvi neoznačeni piksel, preko katerega se s pomočjo enačbe (1) izračuna razdalja pripadnosti 1. segmentu.

$$d_{ij} = \sqrt{\left(R_p - R_{i,j}\right)^2 + \left(G_p - G_{i,j}\right)^2 + \left(B_p - B_{i,j}\right)^2} \quad (1)$$

kjer je:

- d – razdalja,
- i, j – indeksa simbolično nakazujeta, da gre za matriko, kjer indeks i predstavlja vrstico in indeks j predstavlja stolpec trenutno izbranega slikovnega elementa,
- p – vrednosti barvnih komponent slikovnega elementa, s katerim računamo razdaljo in
- R, G, B – barvne komponente.

S 1. segmentom se označijo tudi slikovni elementi, katerih vrednost razdalje je pod vnaprej podano vrednostjo praga, ki eksperimentalno določeno znaša 0.1 (vrednost je manjša od 1 zaradi normalizacije barv). Slika 2 prikazuje referenčno fotografijo, za katero algoritem najde 52 segmentov.

Iz dobljenih segmentov določimo področje RTV preko 2D konvolucije oz. korelacije, kar opisuje enačba (2) /11/.

$$c(n_1, n_2) = \sum_{k_1=-\infty}^{\infty} \sum_{k_2=-\infty}^{\infty} a(k_1, k_2)\, b(n_1 - k_1, n_2 - k_2) \quad (2)$$

kjer sta: a in b parametra funkcije diskretnega argumenta n_1 in n_2.

Poudariti je potrebno, da se v enačbi (2) meji vsot spremenita na vrednost, ki zaznamuje širino in višino slike.

Algoritem korelacije se izvede s pravokotno masko, katere dimenzije so izbrane glede na velikost RTV. Prvotna maska dimenzije 60×190 je sestavljena tako, da znaša vrednost 1 na področju med 10. in 50. vrstico, kot tudi med 25. in 165. stolpcem, vendar so te vrednosti do prvotne dimenzije obrobljene z nasprotnimi vrednostmi, torej −1. Algoritem išče RTV na vseh segmentih, a le na enem segmentu ima korelacijska funkcija maksimalno vrednost. Za prikaz rezultata se v sliki uporabi točko z maksimalno vrednostjo, kateri očrtamo pravokotnik velikosti 140×40, kar prikazuje slika 4.

Slika 4. Rezultat segmentacije in 2D korelacije.
Fig. 4. Result of segmentation and 2D correlation.

Evklidska norma

Algoritem temelji na principu iskanja najprej v širino /12/. Zaradi samega koncepta delovanja algoritma potrebujemo dva seznama, in sicer označenih in neoznačenih slikovnih elementov. Evklidsko normo izračunamo preko enačbe (3) /5/.

(3)

Algoritem pri kreiranju polja označenih slikovnih elementov uporablja strategijo iskanja v vseh osmih smereh (gor, dol, levo in desno ter v ostalih 4 glavnih diagonalnih smereh). Ob zagonu algoritma, se le-ta postavi na mesto prvega neoznačenega elementa, ga označi v seznamu označenih slikovnih elementov in izračuna Evklidsko normo. Iz tega mesta pričnemo iskanje v vseh osmih smereh, kjer se v seznam označenih elementov vnesejo le neoznačeni elementi. Prag je nastavljen na 10% vrednosti trenutno obravnavanega slikovnega elementa, kjer se slikovni elementi vnašajo v posebno matriko, v kateri so le slikovni elementi, ki zadovoljujejo vse opisane pogoje. Algoritem se konča, ko v seznamu neoznačenih elementov ne najdemo več novega še neoznačenega elementa.

Pri tej metodi je najpomembnejši začetni slikovni element, ki se mora nahajati znotraj področja RTV, saj se z njim nastavi vrednost praga in prične se iskanje ostalih slikovnih elementov. To je sicer velika slabost, saj s tem izgubimo avtonomnost sistema, a je sam algoritem računsko zelo učinkovit. Problem odpravimo tako, da kombiniramo več metod. Kombinacija metode 2D korelacije in izračuna Evklidske norme dajeta dobre rezultate, saj metoda 2D korelacije vrne centralno točko, kjer je potrebno biti pazljiv, da le-ta ni drugačne barve (npr. črne). Tako je algoritem potrebno nadgraditi, da le-ta sam preveri ali je centralna točka primerna ali ne in v slednjem primeru se premakne do prve primerne točke oz. slikovnega elementa. Rezultat tega algoritma prikazuje slika 5. Kombinacija obeh metod je sila učinkovita, a je računsko izjemno potratna.

Slika 5. Rezultat uporabe Evklidske norme.
Fig. 5. Result using Euclidian norm.

Slika 6. Dilatacija področij bele barve.
Fig. 6. Dilatation of white colour areas.

2.2. Omejitev področja iskanja registrske tablice

V sliki z zaznano RTV, ki jo dobimo po eni izmed prej naštetih metod algoritem išče pravokotnik. Smiselno je izvesti dilatacijo slike (razširjanje slike) /13/, saj se s tem doseže zapolnitev praznih regij, ki so ostale na mestih znakov in grba. To zelo olajša iskanje pravokotnika, kajti ta korak dodobra zapolni področje registrske tablice. Rezultat

dilatacije slike opravljene nad izhodno sliko metode iskanja bele barve prikazuje slika 6.

2.3. Rotacija tablice

RTV je lahko poljubno orientirana na sliki, zato je potrebno najti kot rotacije, saj preko tega kota algoritem rotira registrsko tablico v horizontalni položaj potreben pri klasifikaciji znakov. Najprej izvedemo pretvorbo iz barvne slike v sliko s sivimi odtenki barve in predpostavimo, da so paralelne linije prisotne v okolici RTV. Na sliki zaznamo robove predmetov, nato izvedemo izračun Radonove transformacije /6/, in sicer v področju med 0° in 179°. Najdenih linij je navadno veliko, zato algoritem uporabi le najdaljše, kar stori s preprostim odštetjem neke konstantne vrednosti, ki v našem primeru znaša 25. Za kot zasuka se izmed vseh najdenih linij izbere maksimalna dolžina, ki navadno predstavlja sprednji ali zadnji odbijač. Slika 7 prikazuje primer vrisa najdenih linij.

Slika 7. Vris linij potrebnih pri določitvi kota zasuka.
Fig. 7. Lines drown needed for angle determination.

Naslednji korak je rotacija slike za najedeni kot. Rotirano sliko pretvorimo v binarno sliko, kjer zopet opravimo dilatacijo slike. Tukaj za razširitev uporabimo elemente oblike karo. Algoritem ponovno izvede iskanje pravokotnika v manjši sliki, kjer kot rezultat dobimo točno področje registrske tablice. Povečano področje najdene registrske tablice je prikazano na sliki 8.

Slika 8. Izločena registrska tablica.
Fig. 8. Extracted licence plate.

S slike 8 se kaj hitro opazi, da se poleg RTV nahaja nekaj dodatnega prostora. Problem odpravimo z določitvijo mejnih točk kontur, za to uporabimo metodo izračuna histograma, ki izračuna vsoto vrstic in stolpcev. Rezultat predstavljata dva stolpična vektorja, kjer eden vsebuje vsoto stolpcev, drugi pa vsoto vrstic. Začetne in končne vrednosti obeh vektorjev so enake nič (gre za binarno sliko) tako, da lahko algoritem izračuna točke, na katerih se nahaja področje registrske tablice, kot je prikazano na sliki 9.

Slika 9. Registrska tablica po obdelavi kontur.
Fig. 9. Licence plate after analysing contours.

Naslednji korak je filtriranje slike, s katerim se poudarijo znaki registrske tablice. Ta korak je ključnega pomena pri kasnejši razpoznavi znakov. Sliko najprej pretvorimo v sliko sivih odtenkov, nato izvedemo kvantizacijo in izenačevanje z izračunom histograma slike. Eksperimentalno nastavimo parametra oz. limiti, ki navzdol omejita vrednosti na 0, navzgor pa na 1 (gre za normalizirano sivinsko sliko). Za vse ostale vrednosti, ki se nahajajo znotraj teh mej, izračunamo optimalen prag. V primeru, kadar je histogram slike pretežno bimodalen, t.j. ima dva ločena vrhova, vrednost praga nastavimo na minimalno vrednost med vrhovoma. Težje je to v primerih, ko se vrhova prekrivata. Optimalen prag dejansko minimizira napako interpretacije ozadja kot objekta na sliki. Ta metoda je poenostavitev mnogo kompleksnejše statistične metode, vendar daje zelo dobre rezultate tudi pri majhnem številu iteracij. Primer kvantizacije in izenačevanja prikazuje slika 10.

Slika 10. Kvantizacija in izenačevanje.
Fig. 10. Quantization and equalization.

3. Razpoznava znakov na RTV

Sledeče poglavje podaja postopke, ki smo jih uporabili za razpoznavanje zrakov registrskih tablic. Vsi omenjeni algoritmi se navezujejo na stanje, ko smo že uspešno razpoznali registrsko tablico in je le-ta predstavljena kot npr. Slika 10.

3.1. Razčlenitev znakov

Binarno sliko RTV razčlenimo z uporabo metode izračuna histograma, in sicer vsote stolpcev slike (ang. Peak-to-valley). Pri razčlenjevanju slike sta algoritmu v pomoč dva statistična parametra, in sicer sta to minimalna širina in minimalna površina regije. Ta dva parametra sta potrebna, saj z njuno pomočjo lahko algoritem izloči nepotrebne znake, ki se pojavijo na registrski tablici, kot so grbi in pomišljaji. Razčlenjevanje poteka od leve proti desni, kjer izračunamo vsote stolpcev slike in jih primerjamo s podanima parametroma. V primeru, da najden znak s končno vsoto stolpcev ustreza pogojema, potem algoritem vrne začetno in končno mejo znaka ter nadaljuje iskanje na desni strani meje oz. za tem znakom.

Nad pravkar dobljenimi mejami znakov, v katerih se nahajajo znaki registrske tablice, izvedemo dilatacijo, ki zmanjša šum v sliki, ki je posledica predvsem slabe kakovosti slike. Metoda tudi poveča razmik med znaki, kar napravi lažjo

separacijo med znaki in ozadjem. Slednje je ključnega pomena pri razpoznavi z OCR sistemom.

Vsakemu najdenemu znaku prilagodimo konture, kar izvedemo s podobnimi postopki, ki so že bili opisani tako v horizontalni, kot tudi vertikalni smeri. Znak je potrebno skalirati na izbrano dimenzijo 20×10 slikovnih elementov, saj znaša število vhodnih nevronov ravno 200. To predstavlja zelo pomemben korak, saj so v učni množici nevronske mreže shranjeni znaki točno takšnih dimenzij. Razpoznava RTV z uporabo nevronskih mrež je sicer izjemno robustna, a kljub temu je ključnega pomena pridobitev dobrih kontur. Jalove konture direktno vplivajo na uspešnost OCR sistema pri razpoznavi znakov.

3.2. Nevronska mreža in razpoznava znakov

Nevronske mreže sestavljajo elementarni elementi t.i. nevroni, kateri delujejo paralelno. Ti elementi so le poenostavljena izpeljanka biološkega nevrološkega sistema. Podobno kot je to v naravi biološkega delovanja, se tudi tukaj determinira sposobnost reševanja problema s številom povezav med nevroni. Učenje nevronske mreže torej vpliva na povezave med nevroni tako, da se postavijo določeni pragovi (povezavam med nevroni se dodajo uteži), kateri vplivajo na nadaljnje odvijanje reševanja problema.

Vhodno skalirano sliko velikosti 20×10 pretvorimo v stolpični vektor, ki nosi informacijo o znaku. Tako se skladata dimenziji in število vhodnih nevronov, ki znaša 200. Podrobni prikaz za številko 3 prikazuje slika 11, kjer je potrebno poudariti, da je tukaj razpoznava izvedena le za numerični del znakov /14/.

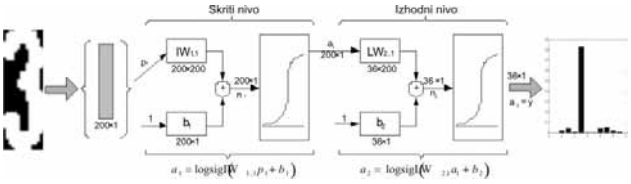

Slika 11. Arhitektura nevronske mreže.
Fig. 11. Neural network architecture.

Pri klasifikaciji znakov uporabljamo feedforward (predkrmiljeno) nevronsko mrežo, in sicer gre za dvonivojsko log-sigmoid/log-sigmoid nevronsko mrežo. Vseh možnih znakov je 36, izmed katerih je 26 črk in 10 številk, zato je smiselno uvesti 36 izhodnih nevronov. Izhod iz nevronske mreže predstavlja vektor dimenzije 36×1, v katerem so na vsakem mestu podane verjetnosti, ki opisujejo podobnost vhodnega znaka z znaki v učni množici. Identifikacijo iskanega znaka določimo z maksimalno verjetnostjo. Nevronska mreža je sposobna identificirati znake na popačenih slikah, v katerih je prisoten šum. Zajem slik v naravi pogosto privede do šumne slike, saj so v naravi prisotni različni vremenski pogoji, na šumnost slike pa vpliva tudi šumnost CCD tipala oz. njegovega CMOS ekvivalenta. Eksperimentalno je določeno, da se pri razpoznavi znakov najmanj napak pojavi pri šumu s srednjo vrednostjo enako 0 in standardno deviacijo 0.2 ali manj.

Robustno nevronsko mrežo, ki bi bila kar najmanj občutljiva na vhodni šum, najprej učimo na idealnih primerih, v katerih ni prisotnega šuma. V vse te idealne primere umetno vnesemo šum in nevronsko mrežo ponovno učimo na šumnih primerih. Učenje nevronske mreže traja vse dokler ni dosežena vrednost kvadratične vsote napake 10^{-5} ali se učenje zaključi po maksimalno 5000 epohah. Ker se ob takšnem postopku pojavijo problemi pri klasifikaciji idealnih primerov, je potrebno nevronsko mrežo ponovno učiti na idealnih primerih. Učenje nevronske mreže uporablja taktiko vračanja v primeru napake (ang. Backpropagation), ki poteka tako z adaptivnim učenjem kot tudi z momenti.

Zadnjih nekaj let so se na področju razpoznave znakov zelo razširile metode z uporabo nevronskih mrež, katere v določenih primerih pravilno interpretirajo vhodne signale, medtem ko ostale metode odpovedo. Problematika uporabljene metode nevronskih mrež pri OCR sistemu postane očitna, saj je za uspešno razpoznavo potrebna čim večja učna množica. V tej učni množici se mora nahajati čim več različnih primerov istega znaka, ki naj bo idealen, šumen, rotiran, itd. Posledica nepravilnih interpretacij znakov je predvsem majhno število znakov v učni množici, saj je bilo vseh skupaj komaj 360 (za vsak znak po 10 različnih primerov). Izboljšanje delovanja OCR sistema je pričakovati z razširitvijo učne množice.

4. Razpoznava znakov na RTV

Testiranje algoritma je potekalo na 50-ih naključno izbranih fotografijah avtomobilov s slovenskimi in evropskimi registrskimi tablicami. Tabela 1 podaja eksperimentalne rezultate, ki so razdeljeni na dva dela. V prvem delu primerjamo 3 metode razpoznave registrske tablice in njihovo učinkovitost, medtem ko v drugem delu merimo učinkovitost razpoznave znakov. Poudariti je potrebno dejstvo, da je metoda Evklidske norme že imela najden slikovni element iz področja registrske tablice. Iz Tabele 1 izhaja tudi dejstvo, da je sistem klasifikacije znakov izjemno robusten, a kljub vsemu učinkovit.

Tabela 1. Učinkovitost različnih metod.
Table 1. Overall efficiency of various used methods.

	Bela barva	2D korelacija	Evklidska norma
Pravilna razpoznana tablica	72%	54%	90%
Stopnja klasifikacije znakov	96%		

5. Sklep

Uporaba predstavljenega algoritma pri zaznavanju registrskih tablic z uporabo feedforward nevronskih mrež se izkaže kot zanesljiva rešitev. Največjo učinkovitost doseže metoda, ki temelji na izračunu Evklidske norme, vendar je pri tej metodi potreben vnos enega slikovnega elementa

znotraj področja registrske tablice, kar napravi celotni algoritem neavtonomen. Najnižjo učinkovitost izkazuje metoda 2D korelacije, ki pa je povrhu še izjemno računalniško potratna oz. kompliciran. Torej je v celotno integracijo algoritma smiselno vpeljati razpoznavo registrske tablice po metodi iskanja bele barve v XYZ barvnem prostoru.

Ko algoritem pravilno razpozna registrsko tablico, postane klasifikacija znakov prisotnih v registrski tablici dokaj visoka, saj procentualno znaša kar 96%. Stanje bi se še izboljšalo z razširitvijo učne množica, katera bi vključevala več primerov posameznega znaka.

Nadaljnje delo bo zajemalo implementacijo predlaganega postopka razpoznave registrskih tablic z uporabo feedforward nevronskih mrež na avtonomnem digitalnem signalnem procesorju, ki bo deloval v realnih pogojih. Ti pogoji zajemajo spremembe vremenskih razmer, razpoznavanje tudi v nočnih razmerah in pri različnih hitrostih premikanja objektov. Kot temeljni cilj bo postavljeno delovanje v strogem sprotnem času.

Literatura

/1/ License Plate Recognition, URL:
http://www.licenseplaterecognition.com/

/2/ S. Yohimori, Y. Mitsukura, M. Fukumi, N. Akamatsu, N. Pedrycz, License plate detection system by using threshold function and improved template matching method, 27-30 June 2004.

/3/ F. Porikli, T. Kocak, Robust License Plate Detection Using Covariance Descriptor in a Neural Network Framework, IEEE International Conference on Advanced Video and Signal Based Surveillance, pp. 107, November 2006.

/4/ J. Matas, K. Zimmermann, Unconstrained licence plate and text localization and recognition, Intelligent Transportation Systems, 13-15 Sept. 2005.

/5/ J. Dattorro, Convex Optimization & Euclidean Distance Geometry, Meboo Publishing, 2005.

/6/ Bracewell, Ronald, Two-Dimensional Imaging, Englewood Cliffs, NJ, Prentice Hall, 1995.

/7/ CIE XYZ, URL:
http://en.wikipedia.org/wiki/CIE_1931_color_space

/8/ William K. Pratt, Digital Image Processing 3rd Edition, Wiley-Interscience Publication, 2001.

/9/ R.C. Gonzales, R. E. Woods, S. L. Eddins, Digital Image Processing using MATLAB, Pearson Prentise Hall, 2004.

/10/ I. Kramberger, Z. Kačič, Enota za zajemanje stereo slike za delovanje v realnem času s strojno izvedenim digitalnim filtrom, Inf. MIDEM, Vol. 33(3), pp. 178-188, 2003.

/11/ Matlab Help, URL: http://www.mathworks.com/access/helpdesk/help/techdoc/index.html?/access/helpdesk/help/techdoc/ref/conv2.html;

/12/ R. Svečko, skripta: Inteligentni sistemi.

/13/ Haralick, R.M. and L. G. Shapiro, Computer and Robot Vision, Vol. I, Addison-Wesley, 1992, pp. 158-205.

/14/ B. Kröse, P. Smagt, An introduction to neural networks, November 1996.

Matej Kseneman[1], Dušan Gleich[1]

[1]Fakulteta za elektrotehniko, računalništvo in informatiko, Smetanova ulica 17, 2000 Maribor
E-pošta: matej.kseneman@gmail.com

Prispelo: 31.01.2011 *Sprejeto: 23.08.2011*

UWB FAST-HOPPING CARRIER FREQUENCY GENERATOR

Arjuna Marzuki,[1] Zaliman Sauli,[2] and Ali Yeon Md Shakaff[2]

[1]School of Electrical and Electronic, Universiti Sains Malaysia, Engineering Campus, Penang, Malaysia
[2]Universiti Malaysia Perlis, Perlis, Malaysia

Key words: Ultra Wide band (UWB), NMOS switch, oscillator, multi-band OFDM alliance (MBOA)

Abstract: This paper discusses on the UWB carrier frequency generator that is capable of fast switching between different center frequencies. By using a switching network, the different frequencies from different local oscillators are switched within 4ns. A new topology of NMOS switch based on series-shunt configuration is proposed so that it is able to pass the signal from oscillators to output without transition spike. The performance of our carrier frequency generator is estimated through post layout simulation with a target technology of Silterra 0.18 µm CMOS at a supply voltage of 1.8 V. The post layout simulation results indicate that our carrier frequency generator is able to produce a signal with three center frequencies, i.e. 3432 MHz, 3960 MHz, and 4488 MHz at 400mV peak-to-peak swing within every 4ns.

Zelo hiter generator nosilne frekvence

Kjučne besede: širokopasovni, UWB, NMOS stikalo, oscilator, MBOA združenje, multi-band OFDM alliance

Izvleček: V članku je predstavljen UWB generator nosilne frekvence, ki je zmožen hitrega preklapljanja med različnimi centralnimi frekvencami. Z uporabo stikalnega vezja uspemo v času 4ns preklopiti različne frekvence iz različnih lokalnih oscilatorjev. V prispevku predstavimo novo tipologijo NMOS stikala, ki omogoča prenos signala od oscilatorja do izhoda brez prehodne špice. Delovanje generatorja nosilne frekvence smo ovrednotili s simulacijami na osnovi parametrov 0.18 µm CMOS tehnologije Silterra pri napetosti 1.8 V. Rezultati nam pokažejo, da je generator sposoben proizvesti signal s tremi centralnimi frekvencami in sicer 3432 MHz, 3960 MHz in 4488 MHz vsake 4ns z vrhnjo napetostjo 400mV.

1. Introduction

The center frequencies for the three mandatory bands (i.e., "mode-1") for MBOA are 3432 MHz, 3960 MHz, and 4488 MHz /1/, /2/. The MBOA proposal assumes per-OFDM-symbol frequency hopping over these bands with a transition time below 9.5 ns, while remaining in a band for around 300 ns. Various different UWB LO concepts have already been proposed /3–5/, but none of them seems to give a clear advantage over the other. The required ability of hopping from one LO frequency to the other within 9 ns /1/ prevents the use of a conventional approach based on a single wide-band PLL. Single-sideband (SSB) mixers can be used to offset a fixed frequency to simultaneously generate the required carriers which are dynamically selected by a multiplexer /3-4/. This approach, however, in CMOS requires a huge power consumption to achieve low spurious. Another possibility is to use an array of PLLs /5/, leading to a large area. A recent paper /6/ focus on using sub-harmonic injection locking technique, but it seems to achieve the worst hop time.

In this paper, we will describe a fully integrated carrier frequency generator to generate the three mandatory carrier frequencies. The post-layout simulation of the design able to achieve settling time between bands less than 1 ns, which is the fastest reported so far.

2. Concept

The concept of the design is similar to array of PLLs /5/. The carrier frequency generator employs three local oscillators with center frequency of 3432 MHz, 3960 MHz, and 4488 MHz respectively based on the UWB specification. A switching network instead of a multiplexer as in /5/ is used to switch between the center frequencies. Fig. 1(a) shows the architecture of carrier frequency generator with active oscillators topology. A sequence pulse generator that is used to control the switch is assumed ideal and external.

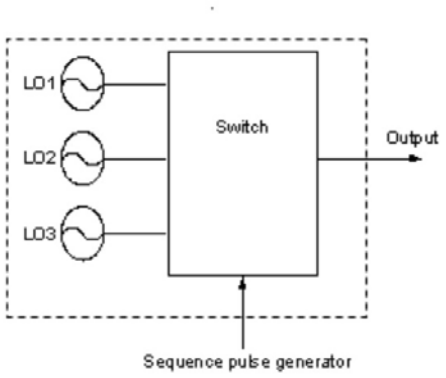

Fig. 1a. Block diagram of active oscillator solution

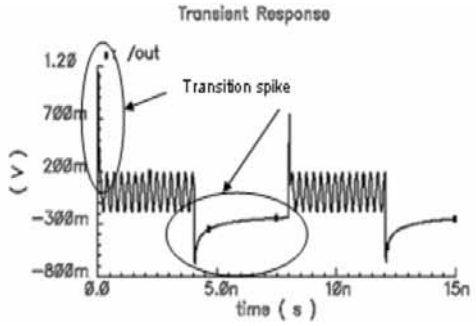

Fig. 1b. Transient response of NMOS switch

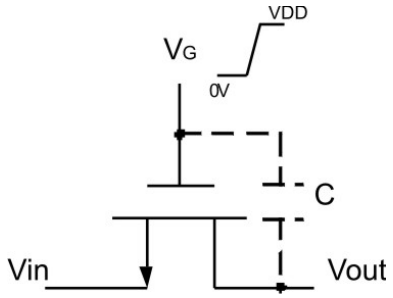

Fig. 1c. NMOS switch with parasitic capacitance

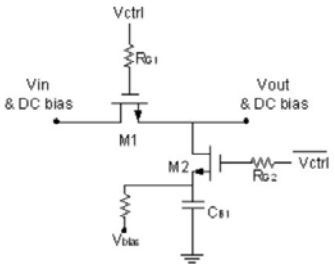

Fig. 1d. Schematic of series-shunt switch.

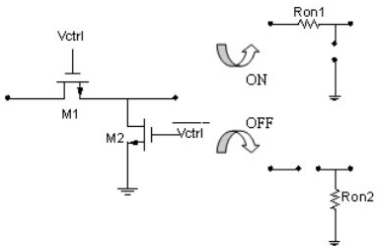

Fig. 1e. Equivalent circuit of series-shunt switch when it is turned on or off.

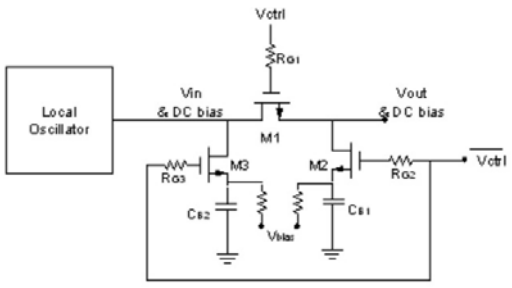

Fig. 1f . Modified series-shunt switch with additional shunt transistor at the input node.

2.1 NMOS Switch

A single NMOS can form a switch by its natural behavior. With the gate voltage acts as the control voltage, the NMOS can provide a path for the signal to pass through from drain to source or vice versa when it operates in linear region; and it blocks the signal when it operates in cutoff region. However a single NMOS switch is not a perfect switch. Fig.1(b) shows transient response of single NMOS switch.

There are two major issues in the NMOS switch that need to be eliminated in order to get a good switch. They are: transient spike at the transition from the switch "off" to switch "on"; and the negative going voltage when the switch is off. A MOS device exhibits inherent parasitic capacitances. These capacitances cannot be avoided. Fig.1(c) shows the NMOS switch with parasitic capacitance between the gate and output node.

We know that C = dQ/dV, where dQ is the magnitude of differential change in charge on one plate as a function of the differential change in voltage dV across the capacitor. The fundamental property of capacitor is it resists any sudden change of voltage across it. Thus when there is a sudden change in V_G, from 0V to VDD, the voltage at the output node is increased for the amount that is sufficient to maintain the charge between the capacitor. Hence a voltage spike equal to the difference occurs at the output node.

When the switch is on, there is a channel conducting under the NMOS gate and between the source and drain to allow the input signal passes to output node. Certainly there are some charges present in the channel. The charge in the channel is on the order of $C_{OX}(V_{GS}-V_{TH})$. When the switch is turned off, these charges either flow to the input source or the output node. The total charges flow to the input source or output node is a function of several parameters, which include input impedance, source impedance, control voltage falling edge and etc. To the first order, 50% distribution between the input source and output node can be assumed. This charge injection phenomenon makes the switch is not totally off in off state.

2.2 Series Shunt Topology

Series-shunt topology is proposed mainly to solve the charge injection phenomenon. In addition to charge injection, since the switch designed is operating at high frequency, the parasitic drain-source capacitance C_{DS} provides a path for signals to pass through from drain to source. This is unwanted because it will degrade the off-state of the switch /7/. Fig. 1(d) shows the schematic of a series-shunt switch.

Transistor M1 performs the main switching function, while the shunt transistor M2 is used to improve the isolation of the switch /8/. When the main switch transistor is on and the shunt transistor is off, the switch performs as a usual NMOS switch. When the main switch is off, the shunt transistor is on to ground the leakage signal due to the parasitic drain-source capacitance. The shunt transistor

also provides a path for the output to ground and the extra charge to be shorted to ground, and hence reduce the charge injection problem. The width of the shunt transistor is half of the main switch. This ratio can be intuitively selected based on the assumption that 50% of charges stored in the M1 channel are distributed to the output node when M1 turns off.

C_{B1} is the bypass capacitor, which allows DC biasing of the output node of the switch. By applying the same DC voltage on the top plate of the bypass capacitor as the output node, DC power consumption is made negligible. R_{G1} and R_{G2} are gate bias resistances used to improve DC bias isolation. The typical value of the gate bias resistance is about 5kΩ /9/. Without the gate bias resistances, the fluctuations of V_{GD} and V_{GS} of the transistors will be higher. These fluctuations will affect the channel resistance and also result in excessive voltage across the gate dielectric and cause breakdown /8/.

The top plate of bypass capacitor, the output node, as well as the input node are biased at the same DC voltage to reverse bias the drain/source-to-substrate p-n junctions. This is purposely to reduce the junction capacitances and RF signal coupled to the substrate and thus decrease the insertion loss /8/.

2.3 Integration of Switch and Oscillators

The switch directly connected to the oscillator definitely brings the effect of loading to the oscillator. As known, a transistor is approximate to a resistor with the value of on-resistance when it is operating in triode region. When the transistor is cut-off, its resistance is very high and approximate to open-circuit. So when the series-shunt switch directly connected to the oscillator circuit, the loading effect is mainly comes from the main switch, M1 and the effect are different when the switch is on and off.

Now we consider the condition when the switch is turned on and turned off as shown in Fig. 1(e). It is clear that when the switch is on, the load connected to oscillator is the on-resistance of transistor M1. When the switch is off, M1 acts as open-circuit and we can assume that no load is connected to oscillator. So it is expected that the amplitude of the oscillating signal will be different when the switch is on and off. When the signal amplitude becomes not stable, we can also expect the occurrence transition noise.

Thus a modification is done on the switch by adding another shunt transistor at the input node as shown in Fig. 1(f). This brings a more symmetrical solution of switch and when the switch is off, transistor M3 is turned on and acts as R_{ON3}. If we choose the width of M3 to be same as M1, the R_{ON3} is equal to R_{ON1}. As a result, no matter the switch is on or off, there is a same load connected to the oscillator. Hence the amplitude of the oscillating signal would be stable regardless the switch is on or off. Finally three oscillators and three switches are integrated to form a complete carrier frequency generator. By properly controlling the pulse generator, we can switch between the three oscillators within 4ns.

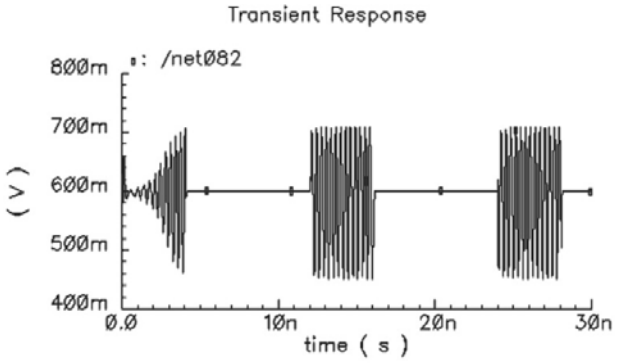

Fig. 2a. Smooth transition of signal generated with modified differential series-shunt switch

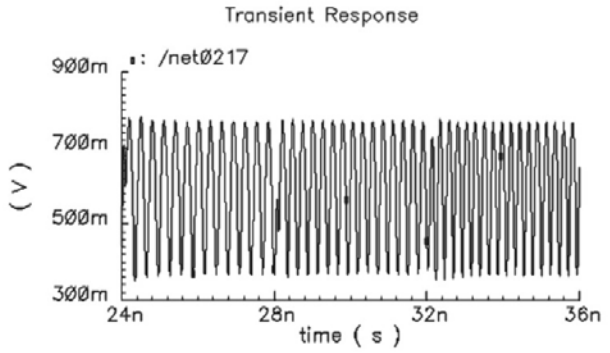

Fig. 2b. Transient response of signal generated from UWB carrier frequency generator

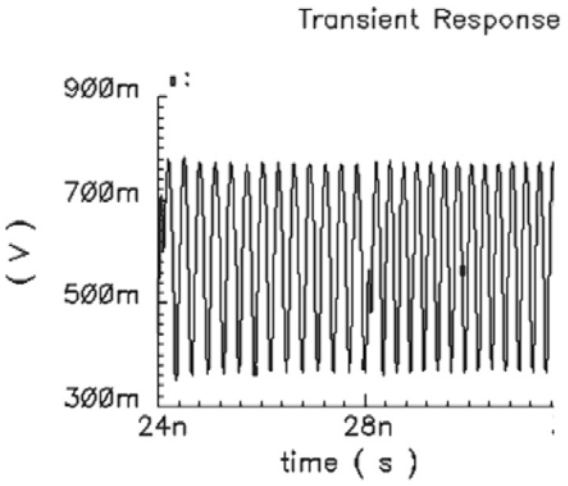

Fig. 2c. Hop time between 3.43 GHz to 3.96 GHz.

3. Simulation Results

Fig. 2(a) shows the signal generated from the local oscillator with center frequency of 3.43GHz integrated with the modified shunt-series switch. The switch is able to

eliminate the spike charge injection problem. In addition, the modified switch had improved the switch performance during transition period

Fig. 2(b) shows the signal generated from the full carrier frequency generator. It can be clearly seen that the signal generated is sinusoidal waveform without clipping and the frequency is different for every 4ns. The amplitude of the signal swing is stable and the transition is considered smooth.

Fig. 2(c) shows the hop time between 3.43 GHz to 3.96 GHz, the settling time is clearly less than 1ns.

Table I shows comparison of this work with other UWB LO Generation system.

Table I. Summary of the performance and comparison to other UWB LO Generation system

	/5/	/6/	This work
Tech/µm/	0.13	0.09	0.18
Band Group	#1	#6	#1
Area /mm^2/	1.9	0.074	2
P_{DC} /mW/	39	36	10.8
Spur Level /dBc/	<-28	<-19	<-20
Hop time /ns/	<2	<4	< 1

This work: Post-Layout simulation result, P_{DC} = 1.8x6 mA (three oscillators).

4. Conclusion

In this work, the design of carrier frequency generator, targeting fast switching between three different center frequencies that are suitable for UWB wireless application is presented. The design is done by using Silterra 0.18µm CMOS technology and the simulation is done by Cadence. A switch is developed that is able to pass the signal from oscillators to output without transition spike. The switch was designed such that it would not give unbalance-loading effect to the oscillator circuit when it is turned on or turned off. The optimization of transistor size was the key point to determine the switch performance. The weakness of a single NMOS switch is investigated then a topology developed that is capable to pass the signal with good transient response. The designed carrier frequency generator is capable to produce a signal with three center frequencies, i.e. 3432 MHz, 3960 MHz, and 4488 MHz at 400mV peak-to-peak swing. The frequency is switched in every 4ns with negligible transition noise. Hop time between frequencies is achieved within less than 1ns.

References

/1./ IEEE 802.15 High Rate Alternative PHY Task Group (TG3a) for Wireless Personal Area Networks (WPANs), IEEE802.15.3a / Online/. Available: http://www.ieee802.org/15/pub/TG3a.html

/2./ A. Batra et al., "Multi-Band OFDM Physical Layer Proposal for IEEE 802.15 Task Group 3a," doc.IEEE 802.15-03/268r3, Mar. 2004.2.

/3./ C.-F. Liang, S.-I. Liu, Y.-H. Chen, T.-Y. Yang, and G.-K. Ma, "A 14-band frequency synthesizer for MB-OFDM UWB application," in IEEE ISSCC Dig. Tech. Papers, 2006, pp. 126–127.

/4./ C. Sandner, S. Derksen, D. Draxelmayr, S. Ek, V. Filimon, G. Leach, S. Marsili, D. Matveev, K. L. R. Mertens, F. Michl, H. Paule, M. Punzenberger, C. Reindl, R. Salerno, M. Tiebout, A.Wiesbauer, I.Winter, and Z. Zhang, "A WiMedia/MBOA-compliant CMOS RF transceiver for UWB," IEEE J. Solid-State Circuits, vol. 41, no. 12, pp. 2787–2794, Dec. 2006.

/5./ K. Stadius, T. Rapinoja, J. Kaukovuori, J. Ryynanen, and K. Halonen, "Multitone fast frequency-hopping synthesizer for UWB radio," IEEE Trans. Microw. Theory Tech., vol. 55, no. 8, pp. 1633–1641, Aug. 2007.

/6./ Dal Toso, S.; Bevilacqua, A.; Tiebout, M.; Marsili, S.; Sandner, C.; Gerosa, A.; Neviani, A., "UWB Fast-Hopping Frequency Generation Based on Sub-Harmonic Injection Locking," Solid-State Circuits, IEEE Journal of , vol.43, no.12, pp.2844-2852, Dec. 2008

/7./ Y. Jin and C. Nguyen, " A 0.25-µm CMOS T/R Switch for UWB Wireless Communications", IEEE Microwave and Wireless Components Letters, vol.15, no.8, pp. 502-564, August 2005.

/8./ C. Lillebrekke, C. Wulff and T. Ytterdal, " Bootstrapped Switch in Low-voltage Digital 90nm CMOS technology", Department of Electronics and Telecommunications, 2002.

/9./ Z. Li and K.K.O, " 15-GHz Fully Integrated NMOS Switches in a 0.13-µm CMOS Process"' IEEE Journal of Solid-State Circuits, vol.40, no.11, pp.2323-2328, November 2005.

Arjuna Marzuki,[1a)] Zaliman Sauli,[2] and Ali Yeon Md Shakaff[2]

[1]School of Electrical and Electronic, Universiti Sains Malaysia, Engineering Campus, 14300 Nibong Tebal, Penang, Malaysia

[2]Universiti Malaysia Perlis, 02600 Arau, Perlis, Malaysia
a) eemarzuki@eng.usm.my

Prispelo: 07.01.2011 *Sprejeto: 23.08.2011*

EFFICIENT BUILT-IN SELF-TEST OF A HIGH-PRECISION ELECTRONIC WATT-HOUR METER

Rok Ribnikar[1], Uroš Bizjak[1,3], Drago Strle[2,3]

[1]Iskraemeco, d.d. Kranj, Slovenia
[2]University of Ljubljana, Faculty of Electrical Engineering, Ljubljana
[3]Center odličnosti NAMASTE, Ljubljana, Slovenia

Key words: built-in self-test, sigma-delta modulator, watt-hour meter

Abstract: To simplify the testing procedure of a mixed signal integrated circuit, which requires low noise equipment and a powerful computer, a built-in self-test is proposed in this paper. The test signal source is integrated in the ASICs and requires only small additional circuitry. The main benefits of using a built-in self-test are shorter testing time, no need for expensive testing equipment and the possibility of performing the test in the field. In this paper we describe an integrated signal generator, an algorithm for accurate evaluation of the system and some simulation results, which prove that conventional FFT analysis can be replaced by RMS function calculations.

Učinkovito vgrajeno testiranje v precizijskem elektronskem števcu električne energije

Kjučne besede: vgrajeno testiranje, sigma-delta modulator, števec električne energije

Izvleček: Za poenostavitev testnega postopka mešanega analogno digitalnega integriranega vezja, ki potrebuje nizko šumno opremo in zmogljiv računalnik, je predlagano vgrajeno testiranje. Test je integriran v ASIC-u in za svoje delovanje potrebuje minimalno število dodatnih komponent. Glavne prednosti uporabe vgrajenega testiranja so zmanjšanje časa testiranja, ne potrebujemo drage testne opreme ter možnost opravljanja testa na terenu ne samo med proizvodnjo ali na servisu. V članku je opisan integriran signalni generator, algoritem za ocenjevanje točnosti sistema in simulacijski rezultati, ki dokazujejo, da je FFT analizo mogoče nadomestiti z uporabo RMS funkcije.

1. Introduction

Watt-hour meters are very accurate devices and include many analog and digital circuits for precise measurement of electrical energy consumption /1/. Because different modules inside the instrument have to work accurately and reliably for a very long time, it is recommended that the instrument is able to monitor its most important parameters, not only during the manufacturing process, but also in the field. One of the most important modules inside the watt-hour meter is a high precision 2nd order sigma-delta modulator, the task of which is to accurately convert analog signal from the sensors to a digital representation, which is further processed and evaluated in the DSP. In general, for a reliable test, a low noise signal generator is needed as the input signal, while the response is usually analyzed using FFT. In the laboratory and during the test, we can use an accurate low noise signal generator as well as a Digital Signal Processor (DSP) to analyze the response characteristics. In field testing such equipment is not available. The solution to the testing problem is a Built-In Self-Test (BIST), where all the necessary equipment is integrated inside the circuit. The measurement accuracy of a BIST must be good enough to fulfill the accuracy requirements of the watt hour meter instrument.

Many different papers have been written about a built-in self-test of the mixed signal circuits. Usually, ramp or sine-wave signals are digitally generated and converted to analog domain /2/, /4/, /5/, /6/. Unfortunately, all such solutions need a lot of silicon area and have a high power consumption which makes them inappropriate for our application.

Different methods may be used for analyzing the output signal; the most accurate and complete is FFT which is very convenient if a powerful DSP is available /2/, /5/. However, this method is not efficient enough for the purpose of the BIST because it requires a lot of computational resources. Other methods are, for example, the sine-wave fitting method /2/, /4/ and the narrow-band filtering method /2/. With the sine-wave fitting method it is necessary to convolve the input sine-wave signal with the output signal. The given results enable the calculation of offset voltage, signal power and total-harmonic-distortion-and-noise (THD-N) values. From signal power and THD-N, one can further calculate the signal-to-noise and distortion ratio (SNDR) and the resolution in a specific frequency band. The ratio between the input and the output signal determines the gain and the accuracy. In the second method the narrow-band digital filter is used, which has two outputs: signal and notch output. At signal output the signal is band-pass filtered and contains only the input spectral component; the signal power can be estimated. At notch output the input signal is attenuated by the stop-band filter and only the noise and harmonic components pass-through the filter; the THD-N and noise power can be computed.

From both outputs the SNDR, resolution and accuracy of the conversion can be calculated.

Both methods are quite efficient, but require a lot of additional integrated digital circuits. In our watt-hour meter, a DSP circuits for calculation of energy consumption and RMS values of voltage and current are already available and therefore, it would be most efficient to use them. In this work we propose to calculate SNDR and accuracy of the measurements from the measurements of the RMS values.

In this paper the efficient BIST methodology used in the watt-hour meter is presented together with some simulation results. Section 2 presents BIST architecture, while a simple on-chip signal generator is presented in section 3. In section 4 modeling details of all important modules in the watt-hour meter are presented. In section 5, the theoretical basis for the BIST algorithm using built in RMS functions are described. Section 6 presents some simulation results that relate most important deviations of circuit parameters to the RMS result. The conclusions are given in section 7.

2. BIST architecture

The system for precision measurements of voltage and current signals consists of two 2nd order sigma-delta modulators; one for each measurement path (Figure 1). After A/D conversion, the digital signals have to be processed by digital filters, after which the RMS values are computed. The current measurement path is almost identical to the voltage measurement path except that it requires a preamplifier to amplify the "current" signal. Since both measurement paths are almost identical, all further descriptions and simulation results will be presented only for the voltage measurements path.

For BIST, the input signal generator has to be integrated in the ASIC. The signal generator consists of a digital generator, a D/A converter (DAC) and the chopper. The signal is connected directly to the ΔΣ modulator input via multiplexer. The result of the conversion is one bit digital bit-stream, which is processed by cascaded filters: a CIC, compensation and a high pass filter. The CIC filter attenuates high frequency components and shaped quantization noise, while compensation filters adjust the signal level in the pass-band. The attenuation of a DC component is accomplished with a high pass filter. The result of digital signal processing is a stream of the 24-bits parallel words. To compute the consumption of energy, the "voltage" and the "current" signals are multiplied and integrated. The RMS value can also be calculated using a built-in RMS function; this function is used during the BIST, which is controlled by the block control BIST (Figure 1). To evaluate the system accuracy, the data from RMS functions are collected. From this data the average RMS value and standard deviation of RMS values are calculated.

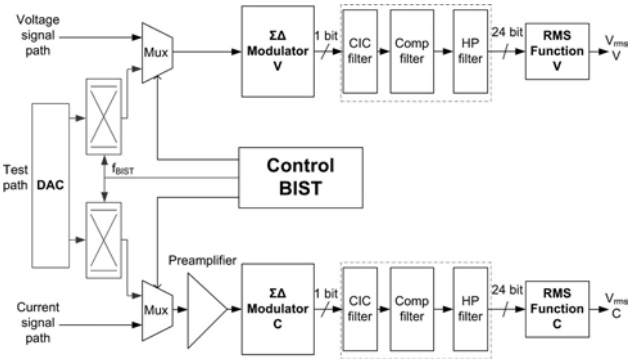

Fig. 1: Block diagram of energy meter ASIC

3. Stimulus generator

A square wave signal generator is used as a test signal source. It consists of a digital block, digital to analog converter (DAC) and a chopper. The DAC generates programmable DC voltages (Figure 2). Voltage levels can be selected to define different amplitudes of the square wave signals. For stable and low noise DC voltage we need a stable supply voltage and small resistance resistor divider. To see the mayor influences due to non-idealities the modulator must be tested at full scale defined by . To transform the DC signal into a square wave a chopper block is used that transforms DC voltage to a square-wave signal with chopper frequency (f_{BIST}). This frequency defines the fundamental frequency of the test signal and is generated in the digital "Control BIST" circuit.

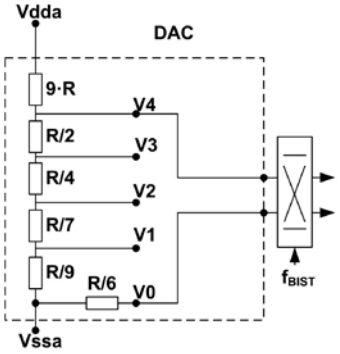

Fig. 2: Scheme of DAC and chopper at the input of modulator

$$V_4 = \frac{253}{2521} \cdot (Vdda - Vssa) \tag{1}$$

4. Modeling the BIST algorithm and circuits

4.1. Modeling and simulation of 2nd order sigma-delta modulator

To test the BIST effectiveness a Matlab model of the 2nd order sigma-delta modulator (Figure 3) /9/ was built. The model includes all important non-idealities /11/: open loop

gain, gain bandwidth, slew-rate, saturation nonlinearity, offset voltage, input noise density of the amplifiers etc.

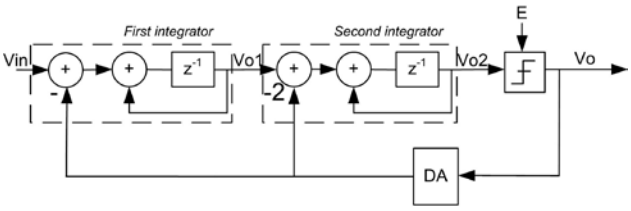

Fig. 3: 2nd order sigma-delta modulator

4.2. CIC filter

Output of the sigma-delta modulator is a digital bit-stream that consists of input signal, which contains all deviations due to eventual problems in the analog part of the circuit and high frequency noise shaped quantization noise. To remove out-of-band shaped quantization noise a 3rd order Cascaded integrator-comb (CIC) filter /7/, /8/ is used. The architecture of the CIC filter is such that the clock rate is reduced by a factor of R after the attenuation of HF part of the quantization noise. Its z-domain transfer function is defined by /9/. The architecture of the CIC filter is presented in Figure 4 /8/. In our simulations a bit-true model is used.

$$H_{CIC}(z)=\left(\frac{11}{R}\frac{-z^{-R}}{1-z^{-1}}\right)^{N} \tag{2}$$

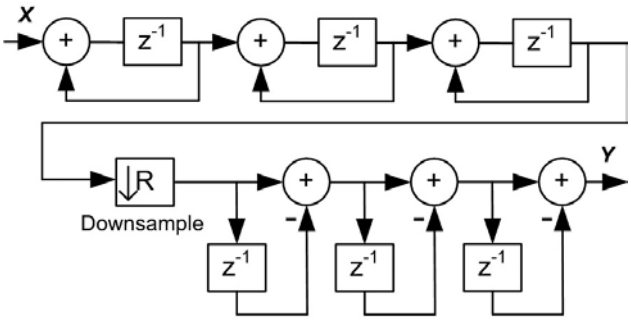

Fig. 4: Decimation using 3rd order CIC filter

4.3. Compensation filter

CIC filter's frequency characteristic is not-flat in the pass band and therefore, a compensation FIR (cFIR) filter is needed. The magnitude vs. the frequency response of the cFIR filter is an inverted function of the CIC filter's pass band response. The result of the two responses is a flattened magnitude characteristic in the signal band (Figure 6).

4.4. High pass filter

Before RMS calculation it is necessary to remove the remaining DC component that occur due to the imperfections of the switched-capacitor circuits and input offset voltage of the amplifiers; they are partly reduced using chopping technique /1/. Unfortunately, due to parasitic capacitances, some DC errors still remain and can be removed using a high pass filter that has the z-domain's characteristics given in. The filter architecture is presented in Figure 5.

$$H(z)=\frac{1-z^{-1}}{1-\alpha z^{-1}} \tag{3}$$

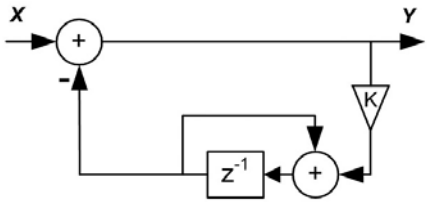

Fig. 5: High pass filter

Frequency responses of CIC, cFIR and high pass filter, together with their combined response, are presented in Figure 6.

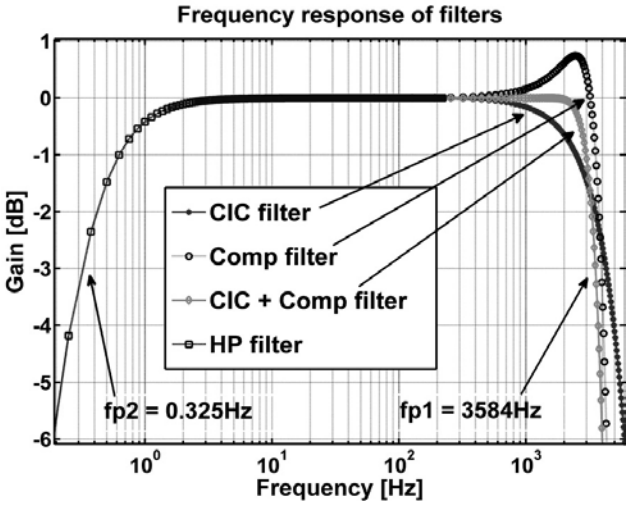

Fig. 6: Frequency response of all digital filters ($f_{clk}=2^{22}$ Hz)

5. RMS calculation, average RMS value and standard deviation

In this section the fundamental equations are presented that relate the FFT spectrum with the RMS result. Equation defines the calculation of RMS value:

$$V_{rms}=\sqrt{\frac{1}{n}\cdot\sum_{0}^{n}x^{2}(iT)} \tag{4}$$

where the meanings of the symbols are as follows: Vrms = RMS value; x(iT) is the sample of the signal after digital filtering; n is the number of samples and is defined with "time" period of input signal divided by the sampling period ($n=T_{signal}/T_{sampling}$).

To calculate the average Vrms value and standard deviation it is necessary to calculate first a series of Vrms values (Vrms(i); i=1,2,…,N).

$$\overline{V_{rms}} = \frac{1}{N} \cdot \sum_{i=1}^{N} V_{rms}(i) \quad (5)$$

Parameter N represents the number of Vrms values included in the calculation. The parameter N is calculated dividing the number of samples used for FFT calculations by the number of data needed for achieving RMS calculations with the desired resolution .

$$\sigma = \sqrt{\frac{1}{N-1} \cdot \sum_{i=1}^{N} \left(V_{rms}(i) - \overline{V_{rms}} \right)^2} \quad (6)$$

Standard deviation shows the variation from average RMS value.

$$V_{rms} = \sqrt{\frac{1}{n} \cdot \sum_{i=1}^{n} x^2(iT)} = \frac{1}{n} \sqrt{\sum_{i=1}^{n} |X(f)|^2} \quad (7)$$

Parseval's theorem /10/ shows the relation between time domain and frequency domain representation of RMS value calculations . The RMS value is calculated from the FFT by summing up the powers of all spectral components in a specified bandwidth. The bandwidth is defined with the digital filters at the output of the modulator according to , where fp1 is the pole frequency of the high pass filter and fp2 is the pole frequency of the combined CIC and cFIR filter (Figure 6).

$$BW = fp1 - fp2 \quad (8)$$

From a series of RMS values, an average RMS value ($\overline{Vrms}$) can be calculated. This average also equals to the sum of the power of spectral components according to Parseval's theorem . The average represents the sum of noise power, signal power and power of higher harmonic components in the specified frequency band. The standard deviation presents the statistical spread of the individual RMS values from the average RMS value. To get the relation between standard deviation and noise density, it is necessary to divide standard deviation with the square root of the bandwidth (BW) defined by the digital filters. The single RMS value is calculated from n_{RMS} samples ($n_{RMS}=T_{signal}/T_{sample}$) and has to be included in the equation that defines the relation between standard deviation and noise density .

$$V_{nd} = \frac{\sigma}{\sqrt{BW / n_{RMS}}} \quad (9)$$

$$BW = fp1 - fp2$$

6. Simulation Results

To verify the proposed methodology of the BIST a Matlab/ Simulink model was built. All blocks were modeled: digital filters, RMS function, voltage generator and 2nd order sigma delta modulator. The model of a sigma-delta modulator consists of the most important non-idealities such as: open loop gain (A0), unity gain bandwidth (GBW), slew-rate (SR), saturation (SAT), input noise density of the amplifiers, kT/C noise, etc., which significantly influences the accuracy, resolution and other parameters of the measurement channel. The results of BIST simulations using RMS calculations in time domain were compared to the FFT analysis results, some of which are presented below.

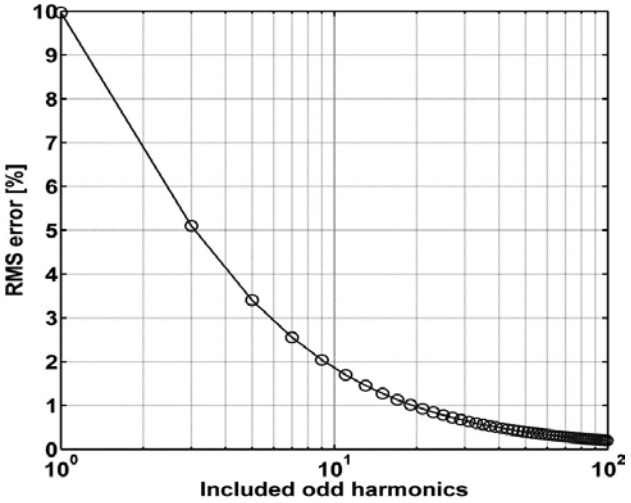

Fig. 7: RMS error in percentage depends on how many harmonics are included in ideal RMS calculation

The upper part of Figure 8 shows RMS value-error calculated by vs. open-loop gain, while the lower part of Figure 8 shows output noise density versus open-loop gain. FFT results are calculated from frequency specter and represented by a black line (marked with circles), while results obtained by RMS calculations are presented by the grey line (marked with X). In Figure 9, Figure 10, Figure 11 and Figure 12 the FFT and RMS values are shown as a function of slew-rate, unity gain bandwidth, saturation and input noise voltage of amplifier in the first integrator.

For easier comparison the average RMS values shown in the following figures are represented as a relative error. To calculate the relative error the ideal RMS value is needed. In theory, the RMS value of a square signal is equal to the amplitude of that signal. The frequency spectrum of a square wave signal is composed of fundamental and infinitive number of odd harmonic components. Digital filters attenuate HF components, so the correction must be included in the calculation of the ideal RMS value. Figure 7 shows the RMS error dependent on the number of odd harmonics included in the calculation.

The digital filters pass-through only 15 odd harmonic components of the square wave signal. Because of this filtering effect the ideal RMS value must be corrected (reduced) by 0.6%. The relative RMS error is calculated using .

$$RMSvalueerror = \frac{[IdealRMS - 0.6\%] - \overline{V_{RMS}}}{[IdealRMS - 0.6\%]} \cdot 100 \quad (10)$$

Figure 8 shows relative RMS error (top figure) and noise density (bottom figure) as a function of an open-loop gain of the first modulator's amplifier calculated from the FFT analysis and RMS calculation.

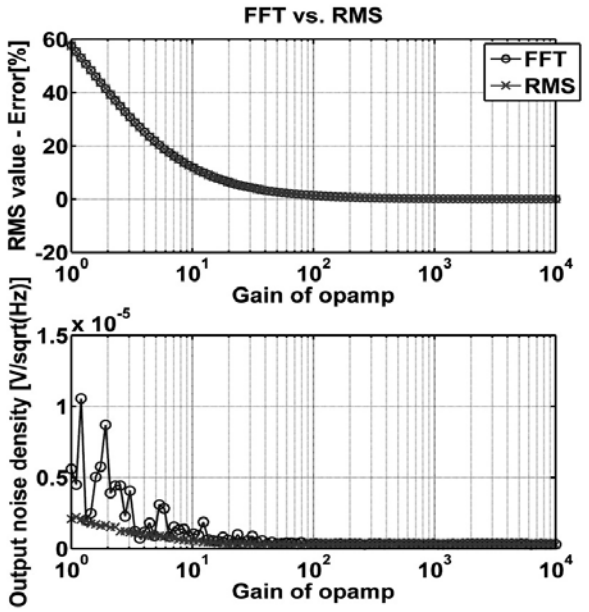

Fig. 8: RMS error and noise density of RMS as a function of open-loop gain (o : FFT results, x: RMS results)

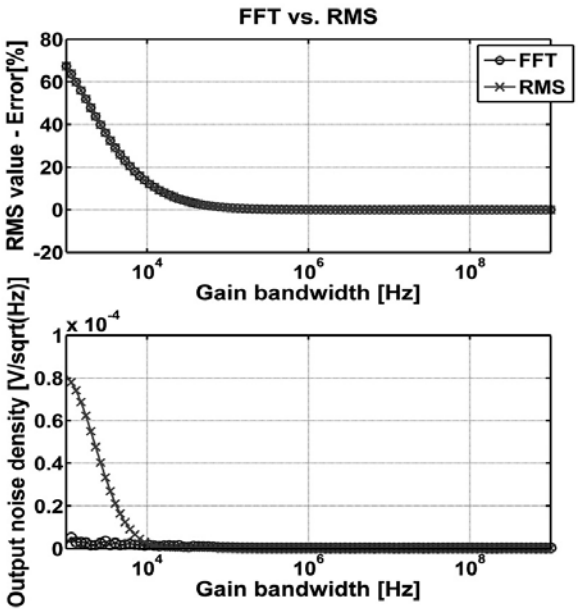

Fig. 10: RMS error and standard deviation of RMS as a function of unity gain bandwidth (o : FFT results, x: RMS results)

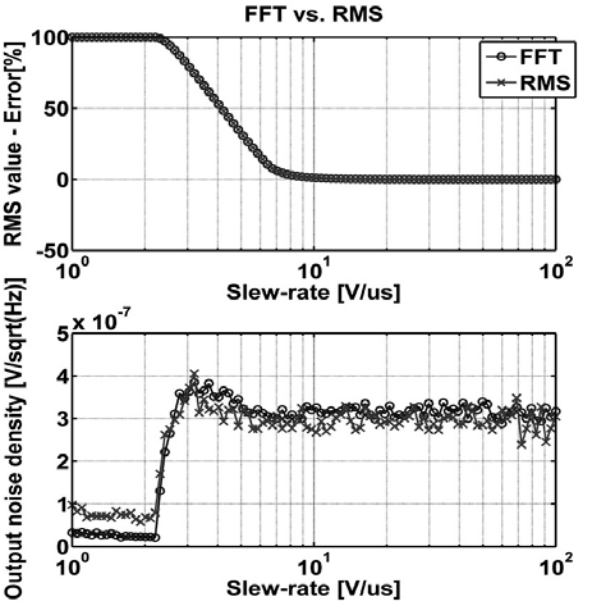

Fig. 9: RMS deviation and RMS noise density FFT as a function of slew-rate (o : FFT results, x: RMS results)

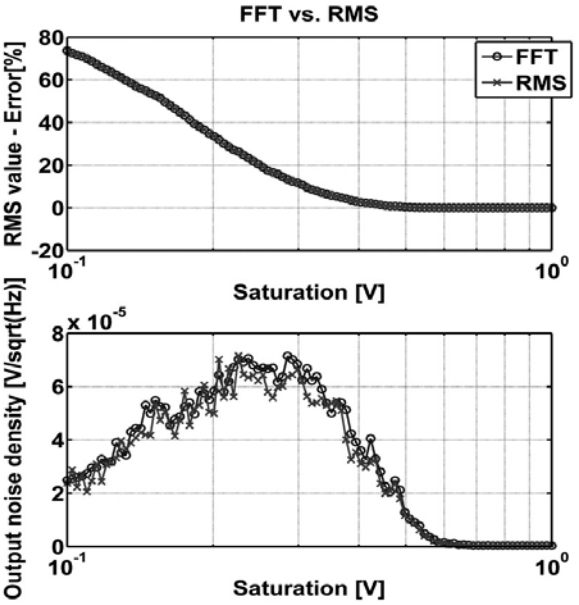

Fig. 11: RMS error and standard deviation of RMS value as a function of saturation region of the output of amplifier (o : FFT results, x: RMS results)

Comparison of the RMS error and noise density of the RMS value as a function of slew-rate is shown in Figure 9. In case that the first amplifier's slew-rate is small, the higher harmonics have big influence to the signal power, which can be seen from the RMS value.

The mismatch between FFT and RMS calculation results is present only for noise density calculations of standard deviation. The main reason for this is a small average RMS value, while standard deviation remains the same.

At maximum input signal the distortions may increase due to the non-linearity of the amplifier. Figure 11 shows the RMS error and the standard deviation of the RMS as a function of saturation limits of the first modulator's amplifier.

Changing the input noise density of the first amplifier does not influence the RMS value but only the output noise density (Figure 12).

In last example the simulation of a real BIST function is presented. In Figure 13 the response at the RMS output

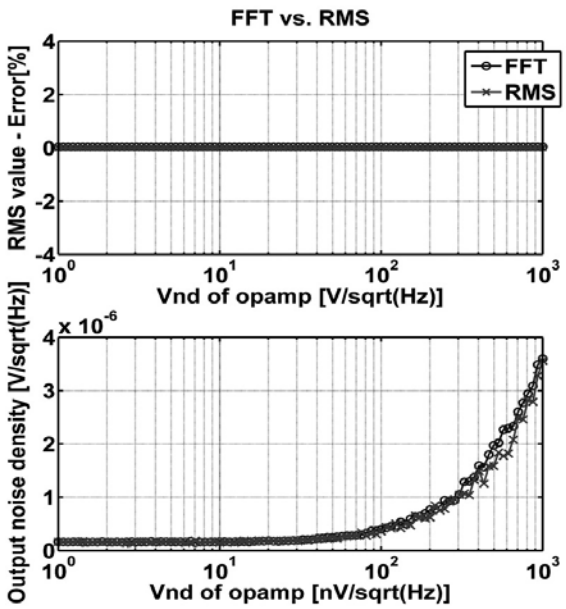

Fig. 12: RMS error and standard deviation of RMS as a function of input noise voltage of the first amplifier of the modulator (o : FFT results, x: RMS results)

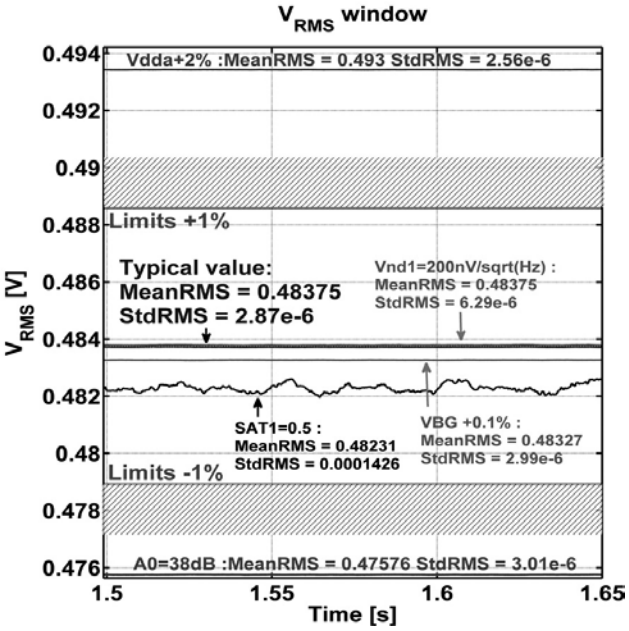

Fig. 13: RMS voltage from system level simulations at different parameters

block is presented together with accuracy limits. Different simulation results are included with different parameters deviated from their nominal values. The response is plotted together with accuracy limits. First, simulation results with typical parameters are shown and from this data the ±1% limits are set. In following simulations, the parameters like supply voltage (Vdda), reference voltage (VBG), open-loop gain (A0), saturation level (SAT1) and input noise voltage (Vnd1) were changed. The effects of these changes were monitored through average RMS value and standard deviation of RMS values and are all presented in Figure 13. If the supply voltage changes by 2% the average RMS value falls out of the desired specification. The same happens when the open-loop gain of the first amplifier decreases below 38 dB. By increasing the input noise voltage of the first amplifier, the average RMS value is the same as with typical parameters but standard deviation drastically increases. This parameter will not have a considerable effect on the accuracy because the data in the watt-hour meter are averaged over a long periods of time. The simulation results prove that most of the changes (like for example the change of reference voltage, saturation levels, slew-rates etc.) can be easily detected.

7. Conclusion

In this work an efficient BIST for a high precision electronic watt-hour meter was proposed. Using a Matlab model and system level simulations we prove that the use of a built-in RMS function gives comparable results to the FFT analysis. This method has many benefits: no testing equipment is required, testing time is reduced and it is possible to test the meter in the field during normal operation. Since new electronic watt-hour meters will have a built-in communication circuitry; so in addition to periodical test, they can also be tested in the field on demand by the distributing company.

Acknowledgments

This operation was partially financed by European Union, The European Social Found.

References

/1/ Uroš Bizjak, Drago Strle, "IEC 0.5 electronic watt-hour meter implemented with first-order sigma-delta converters", AEU – International Journal of Electronics and Communications, Volume 59, Issue 8, pp. 447-453, Dec 2005.

/2/ M. F. Toner and Gordon W. Roberts, "A BIST Scheme for an SNR Test of a Sigma-Delta ADC", Proc. of the IEEE, Test Conference, 1993. Proceedings., International, pp. 805-814, 1993.

/3/ W. Yong-Sheng, W. Jin-Xiang, L. Feng-Chang, Y. Yi-Zheng, "ΔΣ Modulator Based On-Chip Ramp Generator for ADC BIST", 2005 WSEAS Int. Conf. on Dynamical Systems and Control, pp. 512-516, Italy 2005.

/4/ Hao-Chiao Hong, Sheng-Chuan Liang and Hong-Chin Song, "A Built-in-Self-Test Σ-Δ ADC Prototype", Journal of Electronic Testing: Theory and Applications, Volume 25 Issue 2-3, June 2009.

/5/ Chee-Kian Ong, Kwang-Ting Cheng and Wang, L.-C., "A new sigma-delta modulator architecture for testing using digital stimulus" , Circuits and Systems I: Regular Papers, IEEE Transactions on, pp. 206 – 213, 2004.

/6/ Hao-Chiao Hong, Jiun-Lang Huang, Kwang-Ting Cheng, Cheng-Wen Wu and Ding-Ming Kwai, "Practical considerations in applying Σ-Δ modulation-based analog BIST to sampled-data systems", pp. 553 – 566, 2003.

/7/ Hogenauer, Eugene. "An Economical Class of Digital Filters For Decimation and Interpolation," IEEE Transactions on Acoustics, Speech and Signal Processing, Vol. ASSP-29, pp. 155-162, April 1981.

/8/ Richard G. Lyons, "Understanding Digital Signal Processing, Second Edition", Prentice Hall PTR, March 2004.

/9/ Schreider R.,Gabor C. Themes, "Understanding Delta-Sigma Data Converters", Wiley-IEEE Press, USA, November 2004.

/10/ I. N. Bronštejn, K. A. Semendjajew, G. Musiol, H. Muhlig, "Matematični priročnik", Tehniška založba Slovenije, Ljubljana, 1997.

/11/ Rok Ribnikar, Drago Strle, "Modeling of ΣΔ Modulator Non-idealities", Proc. MIDEM, International Conference of Microelectronics, Device and Materials, vol. 42 pp. 319-324, Strunjan, 2006.

/12/ Drago Strle, "Efficient Testing of High-Resolution Σ-Δ A/D Converters", Proc. MIDEM, International Conference of Microelectronics, Device and Materials, vol. 43 pp. 183-188, Bled, 2007.

Rok Ribnikar[1], Uroš Bizjak[1,3], Drago Strle[2,3]

[1]Iskraemeco, d.d. Savska loka 4, 4000 Kranj, Slovenia
[2]University of Ljubljana, Faculty of Electrical Engineering, Tržaška 25, 1000 Ljubljana
[3]Center odličnosti NAMASTE, Jamova 39, 1000 Ljubljana, Slovenia
e-mail: rok.ribnikar@iskraemeco.si

Prispelo: 17.02.2011 *Sprejeto: 23.08.2011*

THE INFLUENCE OF COOLING CONDITIONS ON CHARACTERISTICS OF THE LINEAR VOLTAGE REGULATOR

Krzysztof Górecki, Janusz Zarębski

Department of Marine Electronics, Gdynia Maritime University, Poland

Key words: Linear voltage regulators, selfheating

Abstract: In the paper the results of experimental investigations showing the influence of the selfheating phenomenon on characteristics of the monolithic voltage regulator 723 are presented. The ideal and real cooling conditions of the voltage regulator mounted in the packages DIL14 and TO-5 operating with a heat-sink and without any heat-sink are considered. The obtained results of measurements show a strong influence of selfheating on the output and transfer characteristics of the application circuits of the considered regulator.

Vpliv hlajenja na karakteristike linearnega napetostnega regulatorja

Kjučne besede: linearni napetostni regulatorji, lastno segrevanje

Izvleček: V članku predstavimo eksperimentalne rezultate vpliva lastnega segrevanja na lastnosti integriranega napetostnega regulatorja 723. Predstavimo vpliv idealnih in realnih pogojev hlajenja napetostnega regulatorja, vgrajenega v ohišja DIL14 in TO-5, prei delovanju z ali brez odvoda tolpote. Rezultati meritev kažejo močan vpliv lastnega segrevanja na izhodne in prenosne lastnosti vezij z regulatorjem.

1. Introduction 1

Linear and switched-mode voltage regulators commonly find application in power supplies /1, 2, 3, 4/. Of course, switched-mode voltage regulators have higher watt-hour efficiency, but on the other hand they are a source of electromagnetic interferences /5/. Therefore, linear voltage regulators are still used due to the short response time for pulse disturbances and a low level of the output ripple voltage /1, 4/.

There are two kinds of monolithic linear voltage regulators. The first are devices of the fixed value of the output voltage, whereas the other are adjustable voltage regulators of the programmable value of the output voltage. One of the most popular devices belonging to the second group of the considered regulators is the voltage regulator 723, manufactured by a lot of producers, e.g. LM723 (National Semiconductor), mA723 (Texas Instruments), MAA723 (Tesla), UL7523 (CEMI). The regulator 723 allows stabilizing the device output voltage in the range from 2 V to 37 V at the output current equal to 150 mA /3, 5, 6/. The use of the considered regulator in the application circuits described, e.g. in /1, 6/ allows broadening considerably broaden the range of stabilized voltages and currents.

The voltage regulator 723 is manufactured with two kinds of packages: the dual-in-line package DIL14 and the metal package TO-5. As it results e.g. from the papers /7, 8, 9/ selfheating affects considerably characteristics of linear voltage regulators. On the other hand, as it is commonly known, the increase of the device internal temperature over the ambient one, is determined by the device thermal resistance R_{th}. The value of R_{th} depends, among other things, on the kind of the device package and the size of the heat-sink included in this package /10/.

In the paper, which is an extended version of the paper /11/, some results of the measurements of the regulator 723 characteristics are presented. Moreover the influence of the device package cooling conditions on these characteristics is discussed in detail.

2. Investigated Circuits

The structure and principle of the considered voltage regulator operation are described e.g. in /2, 6, 7, 11/, whereas the most popular application circuits are shown in /2, 6, 7/.

The circuits shown in Figs. 1, 2 were selected for investigations. The nominal values of the circuit output voltage

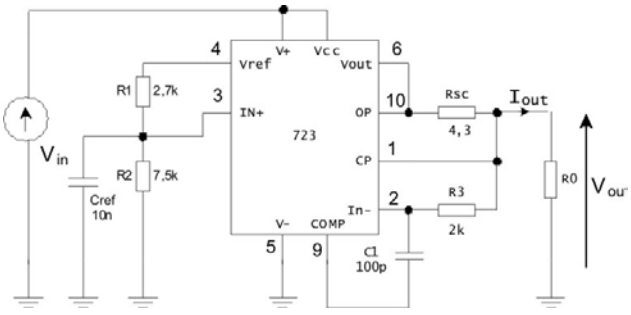

Fig.1. The application circuit of the voltage regulator 723 of the nominal output voltage equal to 5 V

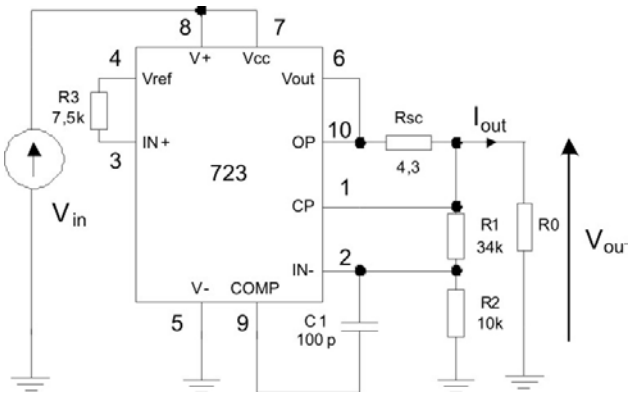

Fig.2. The application circuit of the voltage regulator 723 of the nominal output voltage equal to 30 V

are equal to 5 V and 30 V for the circuits from Fig.1 and Fig.2, respectively.

3. Measurement Results

The characteristics of the considered application circuits operating with different cooling conditions of the voltage regulator 723 were measured by the authors. Two kinds of such characteristics can be distinguished. The first are isothermal characteristics corresponding to the ideal conditions of the device cooling. The others are nonisothermal characteristics, in which the selfheating phenomenon is taken into account.

The isothermal characteristics were performed by the pulse method along with the measuring set described in /12/. On the other hand, the nonisothermal characteristics were obtained by the point-by-point method, which means that each point on the characteristics corresponds to the thermal steady state. Both the regulators were measured without any heat-sink, whereas the device in the package TO-5 was additionally situated on the aluminium heat-sink of the dimensions: 100x90x10 mm.

According to the catalogue data, the thermal resistance of the considered regulator in the package DIL14 and TO-5 is equal to 150 K/W and 165 K/W, respectively.

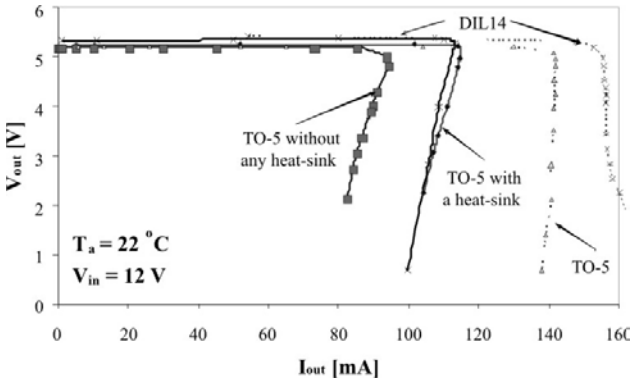

Fig.3. The measured output characteristics of the voltage regulator 723 operating in the application circuit from Fig.1

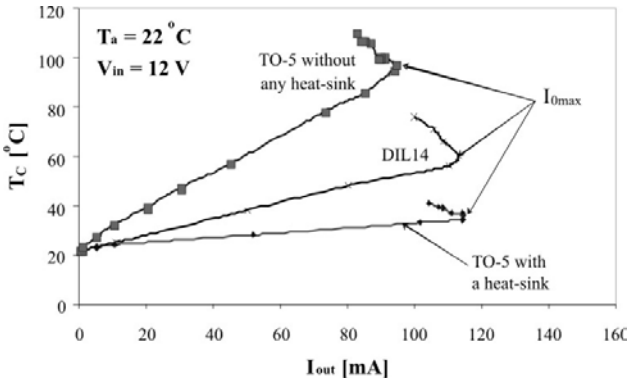

Fig.4. The measured dependences of the case temperature of the voltage regulator 723 operating in the application circuit from Fig.1 on the output current

The measuring results of the circuit from Fig.1 and Fig.2 are shown in Figs.3-7 and Figs. 8 -10, respectively. In these figures the isothermal and nonisothermal characteristics are denoted by the dashed lines and the solid lines, respectively.

Fig.3 and Fig.4 show the output characteristics and the dependence of the case temperature of the regulator from Fig.1 on the circuit output current. The device case temperature was measured with the use of the pyrometer Optex ST-3.

As seen from Fig.3, the maximum value of the circuit output current I_{0max} depends strongly on the device cooling conditions. For example, the value of the current I_{0max} corresponding to the package TO-5 is equal to 140 mA on the isothermal characteristics and less than 90 mA on the nonisothermal ones.

In turn, it is seen in Fig.4 seen, that at the same value of the circuit output current, an increase of the device case temperature (TO-5) is almost twice as high as in the second device (DIL14).

It is worth mentioning that the characteristics from Fig.3 show undercutting resulting from the activation of the overcurrent protection network built-in into the considered regulator.

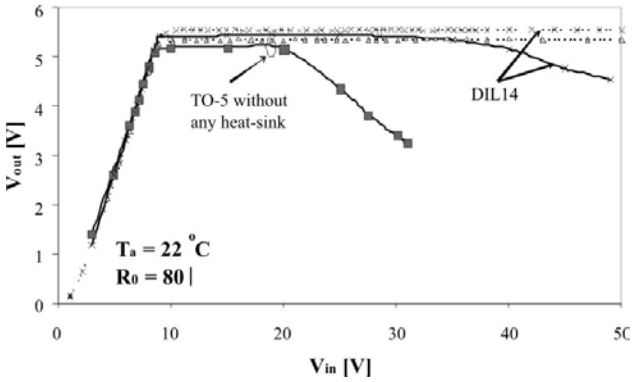

Fig.5. The measured transfer characteristics of the voltage regulator 723 operating in the application circuit from Fig.1 at R_0 = 80 W

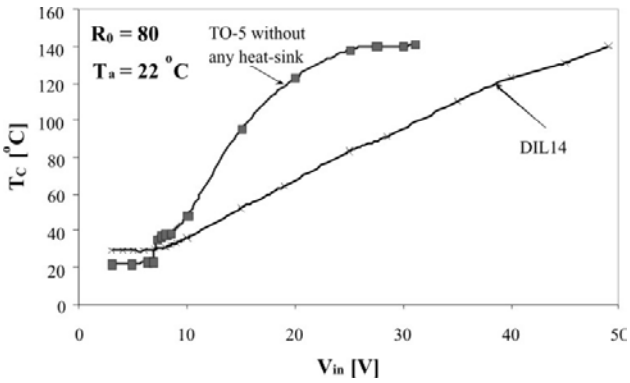

Fig.6. The measured dependences of the case temperature of the voltage regulator 723 operating in the application circuit from Fig.1 on the input voltage

Fig.5 and Fig.6 present the transfer characteristics and the corresponding to them dependences of the case temperature on the input voltage of the application circuit from Fig.1, with the load resistance R_0 = 80 W. As seen from Fig.5, the range of changes of the circuit input voltage corresponding to the fixed value of the circuit output voltage depends on the cooling conditions of the device. For isothermal conditions the stabilization range is limited only "from below" at the input voltage V_{in} = 9 V. Selfheating causes that the circuit stabilized output voltage is additionally limited "from the top" at the input voltage equal to 35 V (DIL 14) and 20 V (TO-5).

We see in Fig.6, that in the range of changes of the input voltage, for which the negative slope of the transfer characteristics is observed, the device case temperature is equal even more than 120°C.

As it was shown in Fig.5, selfheating results in narrowing the circuit stabilized output voltage. Fig.7 shows the transfer characteristics of the application circuit from Fig.1 with R_0 = 39 W. The circuit cannot stabilize the output voltage at all, when selfheating affects the $V_{out}(V_{in})$ characteristics. Note, that in the isothermal characteristics this phenomenon is not observed.

Figs.8 and 9 present the output characteristics and the corresponding to them dependences of the device case

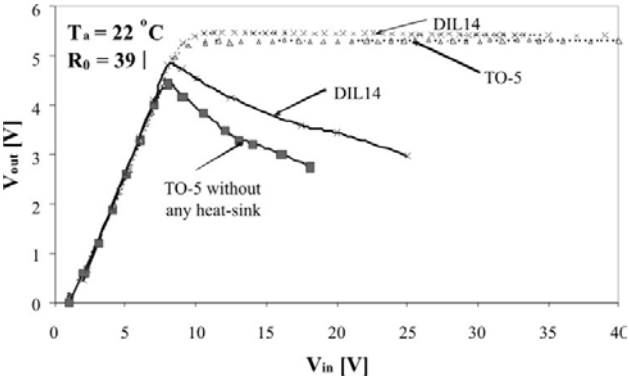

Fig.7. The measured transfer characteristics of the voltage regulator 723 operating in the application circuit from Fig.1 at R_0 = 39 W

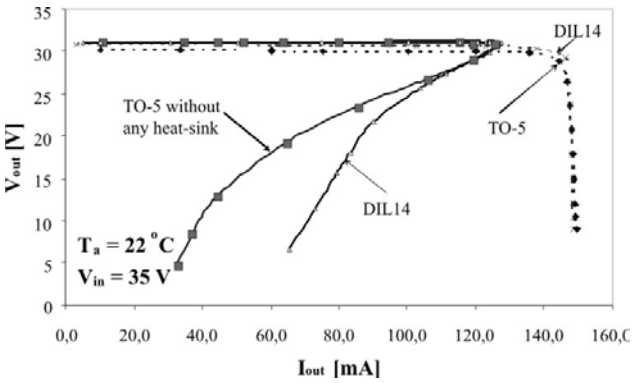

Fig.8. The measured output characteristics of the voltage regulator 723 operating in the application circuit from Fig.2

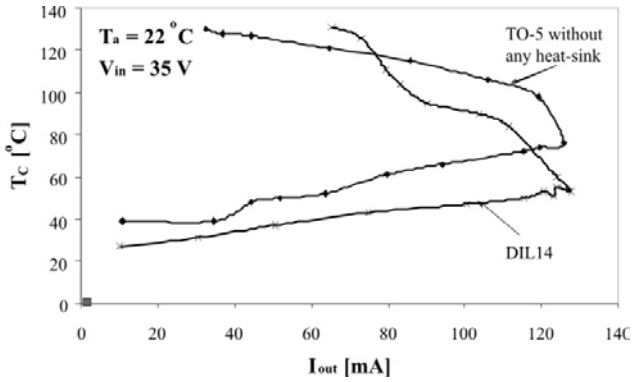

Fig.9. The measured dependences of the case temperature of the voltage regulator 723 operating in the application circuit from Fig.2 on the output current

temperature on the circuit output current. As seen, similarly as it was shown for the circuit from Fig.1, the value of the allowable circuit output current decreases due to selfheating. In the range, in which the overcurrent protection network is activated, the slope of the considered characteristic is much greater than it was in the circuit from Fig.1. In this range of changes of the output current, the strong increase of the device case temperature is observed.

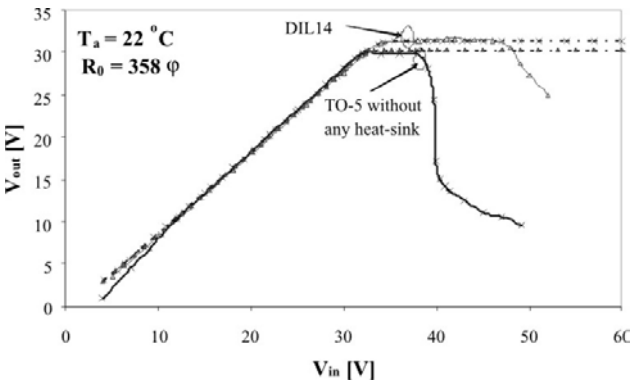

Fig.10. The measured transfer characteristics of the voltage regulator 723 operating in the application circuit from Fig.2

In Fig.10 the transfer characteristics of the application circuit from Fig.2 at the load resistance R_0 = 358 W are presented, whereas Fig.11 shows the dependences of the regulator case temperature on the input voltage, corresponding to these characteristics. As seen, a very narrow range of the stabilized circuit output voltage corresponds to the high value of the voltage V_{out} = 30 V. In particular, for the application circuit with the device package TO-5, a sudden decrease of the output voltage to the value equal to 13 V is observed after the input voltage crosses the value equal to 37 V. A further increase of the circuit input voltage causes a further decrease of the output voltage.

It is visible in Fig.11, that with the rapid increase of the case temperature, the big fall of the voltage regulator output voltage is observed. It is worth to notice, that the case temperature of the regulator is stabilized after achievement of the value 150°C.

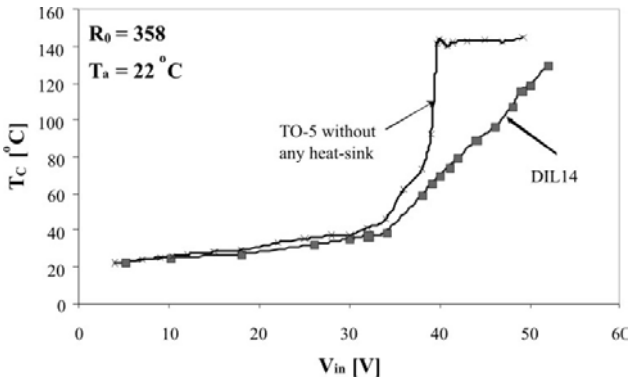

Fig.11. The measured dependences of the case temperature of the voltage regulator 723 operating in the application circuit from Fig.2 on the input voltage

4. Conclusions

In the paper the results of experimental investigations of the influence of cooling conditions of the monolithic voltage regulator 723 on the application circuits of this device are presented. It is seen from the presented results that selfheating causes strong restriction of values of the allowable circuit current and the output voltage. The influence of selfheating on the considered characteristics is more visible in the circuits of a higher nominal value of the output voltage.

Comparing the characteristics obtained from the different device cooling conditions it is seen that using the package TO-5 is less useful than the package DIL14. The characteristics of the device with both the packages are comparable, when the device with TO-5 is situated on the large heat-sink.

When the device case temperature crosses 120°C, the voltage regulator operates in the range of the restricted values of the output current, which results in changes of the shape of its output and transfer characteristics.

References

/1./ U. Tietze, Ch. Schenk: „Halbleiter-Schaltungstechnik". Springer-Verlag, Berlin, Heidelberg, 1993, in German.

/2./ A. Borkowski: „Zasilanie urządzeń elektronicznych". WKiŁ, Warszawa, 1990, in Polish.

/3./ Ö. Ferenczi: „Zasilanie układów elektronicznych. Zasilacze ze stabilizatorami o pracy ciągłej. Przetwornice DC-DC". WNT, Warszawa, 1988, in Polish.

/4./ M. H. Rashid: "Power Electronics Handbook", Elsevier, London, 2007.

/5./ N. Mohan, T.M. Undeland, W.P. Robbins: "Power Electronics: Converters, Applications, and Design". New York, John Wiley &Sons, 1995.

/6./ C. Rudnicki: „Układy scalone w sprzęcie elektroakustycznym". NOT-Sigma, Warszawa, 1987, in Polish.

/7./ K. Górecki, J. Zarębski: "Influence of selfheating on characteristics of linear voltage regulators with a power MOS transistor". XXXII International Conference on Fundamentals of Electrotechnics and Circuit Theory IC-SPETO 2009, Ustroń, 2009, pp. 69-70.

/8./ K. Górecki, J. Zarębski: "Analysis of the influence of selfheating on the characteristics of the linear voltage regulator including the MOS power transistor". Elektronika, No. 3, 2009, pp. 103-106.

/9./ J. Zarębski, K. Górecki: "The Electrothermal Macromodel of MA7800 Monolithic Positive Voltage Regulators Family". International Journal of Numerical Modelling: Electronic Networks, Devices and Fields, Wiley, Vol.19, No.4, 2006, pp. 331-343.

/10./ K. Górecki, J. Zarębski, M. Piotrowicz: „Measurements of the thermal parameters of the monolithic voltage regulator MAA723". Zeszyty Naukowe Akademii Morskiej w Gdyni, Nr 53, 2004, pp. 121-128.

/11./ K. Górecki, J. Zarębski: "The Influence of Cooling Conditions on Characteristics of the Linear Voltage Regulator". XXXIII International Conference on Fundamentals of Electrotechnics and Circuit Theory IC-SPETO 2010, Ustroń, 2010, pp. 57-58.

/12./ K. Górecki, J. Zarębski: „The circuit for the automatic measurement of the nonisothermal d.c. characteristics of Semiconductor devices". Metrology and Measuring Systems, Vol. VII, No.1, 2000, pp. 45-57.

Prof. Krzysztof Górecki
Prof. Janusz Zarębski
Gdynia Maritime University
Department of Marine Electronics
Morska 83, 81-225 Gdynia, POLAND,
Tel. ++48 58 6901448, ++48 58 6901599,
fax ++48 58 6217353
E-mail: gorecki@am.gdynia.pl, zarebski@am.gdynia.pl

Prispelo: 07.01.2011 *Sprejeto: 23.08.2011*

INFLUENCE OF SAR REDUCTION IN MUSCLE CUBE WITH METAMATERIAL ATTACHMENT

Mohammad Rashed Iqbal Faruque[1], Mohammad Tariqul Islam[2], Norbahiah Misran[1, 2]

[1]Dept. of Electrical, Electronic and Systems Engineering, Faculty of Engineering and Built Environment, Universiti Kebangsaan Malaysia, Bangi, Selangor, Malaysia.
[2]Institute of Space Science (ANGKASA), Universiti Kebangsaan Malaysia, Bangi, Selangor, Malaysia.

Key words: SAR, SAR reduction, muscle cube, metamaterial attachment, mobile communication equipment

Abstract: The purpose of this paper is to calculate the specific absorption rate (SAR) reduction in muscle cube with metamaterial attachment. The finite-difference time-domain (FDTD) method has been used to evaluate the SAR in a realistic anatomically based model of the muscle cube. We design the single negative metamaterials from periodic arrangement of split ring resonators (SRRS). By properly designing structural parameter of SRRS, the effective medium parameter can be trade negative at 900 MHz and 1800 MHz band in this paper. Numerical results of SAR values in muscle cube with presence of resonators exhibit SAR reduction. These results can provide useful information in designing safety mobile communication equipment compliance.

Zmanjšanje SAR v modelu mišične kocke z dodatkom metamateriala

Kjučne besede: SAR, zmanjšanje SAR, mišična kocka, dodatek metamateriala, mobilne komunikacijske naprave

Izvleček: Namen članka je izračunati zmanjšanje specifične stopnje absorpcije (SAR) v mišični kocki z dodatkom metamateriala. Za ocenjevanje SAR v realnem anatomskem modelu mišične kocke je bila uporabljena FDTD (finite-difference time-domain) metoda. Model metamaterialov smo izdelali s pomočjo periodične structure resonatorjev tipa SRRS (SRRS – split-ring resonator) Z ustrezno izbiro strukturnih parametrov SRRS lahko dosežemo negativno prepustnost pri frekvencah 900 MHz in 1800 MHz.

Numerični rezultati SAR vrednosti v mišični kocki ob prisotnosti resonatorjev SRRS kažejo na zmanjšanje SAR. Rezultati so tako uporaben vir informacij pri načrtovanju varnih mobilnih komunikacijskih naprav.

1. Introduction

The portable terminal devices are widely used in the human life. As usages of the mobile devices are increased, the study about the health risk from the hazard electromagnetic fields is widely in progress. The specific absorption rate (SAR) is defined parameter for evaluating power absorption in the human head. Radio frequency (RF) safety guidelines have been issued to prevent excessive electromagnetic-field exposure in terms of the SAR /1/. The exposure of the human head to the near field of a cellular phone has been evaluated by measuring the SAR in a human-head phantom, or by calculating it using a human-head numerical model. Therefore, it is important issue of the portable devices that reduction of SAR value. Previously, a ferrite sheet between the antenna and a head, a position study of the antenna feeding point; a use of the conductive material (such as aluminum), and electromagnetic band gap (EBG) structures to design high performance devices, were proposed to reduction of the SAR value /2-4/.

Recently, there are many interests on metamaterial with spilt ring resonator structure were proposed to reduction of the SAR value/5/. The negative permittivity can be obtained by arranging the metallic thin wires periodically /6/. On the other hand, an array of split ring resonators (SRRS) can exhibit negative effective permeability. The designed SRRS operated at 1.8 GHz and were used to reduce the SAR value in a lossy material. In /7/, the designed SRRS operated at 1.8 GHz were used to reduce the SAR value in a lossy material. The metamaterials are designed on circuit board so it may be easily integrated to the cellular phone. Simulation of wave propagation into metamaterials was proposed in /5-7/. The authors utilized the FDTD method with lossy-Drude models for metamaterials simulation. This method is a helpful approach to study the wave propagation characteristics of metamaterials /8-9/ and has been more developed with the perfectly matched layer (PML) and extended to three-dimension problem /7/.

At first, the SRRS are used to reduce the EM interface between a helix antenna and a muscle cube. With properly choosing geometry parameters of SRRS, the permeability can be negative at 900 MHz and 1.8 GHz, respectively. The SAR circulation in a muscle tissue with the presence of SRRS is studied. To explore the influence of SRRS to the antenna, the radiated power and radiation impedance of the antenna are also analyzed. Numerical results are established to confirm the effect of SAR reduction.

This paper is structured as follows. Section II describes the SRRS design and simulation between handset antenna and

the SAM phantom head, and SAR calculation in a muscle cube will be described in Section III, Section IV concludes the paper.

2. SRRS Design and Simulation

To construct the metamaterial for SAR reduction, we proposed one model of resonators namely the SRRS as shown in Fig. 1. We design the resonators for operation at the 900 MHz bands. The SRRS contains two square rings, each with gaps appearing on the opposite sides /5/. The SRRS was introduced by Pendry et al. in 1999 /8/ and subsequently used by Smith et al. for synthesis of the first left-handed artificial medium /9/. A lot of effort worldwide has been spent studying single negative metamaterials (SNMs), double negative metamaterials (DNMs), their properties /6/, applications in antennas /7/, and other microwave devices. In Fig. 1, the structures of resonators are defined by the following structure parameters: the ring thickness c, the ring gap d, the square ring size l, the split gap g, and c_0 is the speed of light in free space. The resonant frequency f is very sensitive to small changes in the structure dimensions of the SRRS. The frequency response can be scaled to higher or lower frequency by properly choosing these geometry parameters. After an extensive simulation study, we have found out a closed-form formula for the resonant frequencies of the SRRS:

$$f_{SRRS} = k_1 \frac{c_0}{2[4(2r_{ext} - c) - g]\varepsilon_r^{1/2}} \quad (1)$$

The SRRS is resonating at approximately half the guided-wavelength of the resonant frequency. There are two resonances from the split rings. We have given the formula for the resonance of the outer split ring, which has a lower resonance frequency.

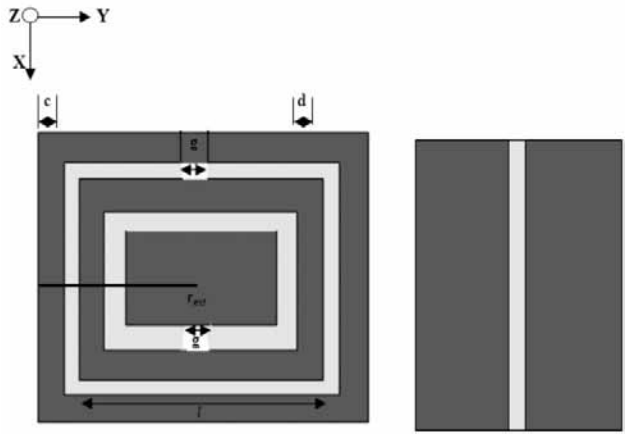

Fig. 1. The structure of SRRS (a) front-side and (b) back-side views

Numerical simulations could predict the transmission properties depend on various structure parameters of this system. Simulations of this complex structure are performed with FDTD method. To construct the SRRS for SAR reduction, the SRRS lie in the xz plane are considered. The EM wave propagates along the y direction. The electric polarization is kept along the z-axis and magnetic field polarization is kept along x axis. Periodic boundary conditions are used to reduce the computational domain and an absorbing boundary condition is used at the propagation regions. The total-field/scatter-field formulation is used to excite the plane wave. The regions inside of the computational domain and outside of the SRRS were assumed to be vacuum.

From this study, it is found that both of the two incident polarizations can produce a stop band. As shown in /4-6/, the stop band corresponds to a region where either the permittivity or permeability is negative. When the magnetic field is polarized along the split ring axes, it will produce a magnetic field that may either oppose or enhance the incident field. A large capacitance in the region between the rings will be generated and the electric field will be powerfully concentrated. There is strong field coupling between the SRRS and the permeability of the medium will be negative at the stop band. Because the magnetic field is parallel to the plane of SRRS, we imagine the magnetic effects are small, and that permeability is small, positive, and slowly varying. In this condition, these structures can be viewed as arranging the metallic wires periodically.

The stop bands of the SRRS are designed to be at 900 MHz and 1800 MHz. The periodicity along x, y, z axes are L_x = 63 mm, L_y = 1.5 mm, and L_z = 63 mm respectively. On the other hand, to obtain a stop band at 1800 MHz, the parameters of the SRRS are chosen as c = 1.8 mm, d = 0.6 mm, g = 0.6 mm, and r = 12.9 mm. The periodicity along the x, y, z axes are L_x = 50 mm, L_y = 1.5 mm, and L_z = 50 mm, respectively. Both the thickness and dielectric constant of the circuit boards for 900 MHz and 1800 MHz are 0.508 mm and 3.38 mm respectively. After properly choosing geometry parameters, the SRRS medium can display a stop band around 900 MHz and 1800 MHz. SRRS producing a good stop band and size are large. Therefore, SRRS are suitable for mobile phones as per size and recital point of view.

We have tried to use a high impedance surface configuration to reduce the peak SAR. However, we found that when these structures operate at 900 MHz, the sizes of these structures are too large for cellular phone application. A negative permittivity medium can also be constructed by arranging the metallic thin wires periodically /7/. However, we found that when the thin wires operate at 900 MHz, the size is also too large for practical application. Because the SRRS structures are significant due to internal capacitance and inductance, they are on a scale less than the wavelength of radiation. Fig.2 shows the modeled transmission coefficient. It can be clearly seen from this figure that after properly choosing geometry parameters, the SRRS medium can display a stop band around 900 MHz and 1800 GHz respectively.

3. SAR calculation in a muscle cube

To verify our FDTD simulation, the structure parameters of SRRS were chosen as same as /5/. Since a 3-D model of the whole head with the presence of SRRS structure requires a great amount of memory, a simplified muscle cube is used to validate the effect of SAR reduction. Fig. 3 shows the muscle cube used in SAR simulation. It is formed by muscle tissue with ε_r = 51.8, σ = 1.11, and ρ = 1040 for 900 MHz and ε_r = 49.4, σ = 1.53, and ρ = 1040 for 1800 MHz. A $\lambda/2$ helix antenna is placed near the muscle tissue. The distance between the antenna and the muscle cube is 20 mm. The radiated power from the antenna is assumed to be 600 mW for 900 MHz and 125 mW for 1800 MHz, respectively. The designed SRRS are placed between the antenna and the muscle cube. The medium with parameters Nx=1, Ny=10, and Nz,=1 unit elements along each direction are used. The sizes of the muscle cube are chosen to be the length of the $\lambda/2$ helix antenna.

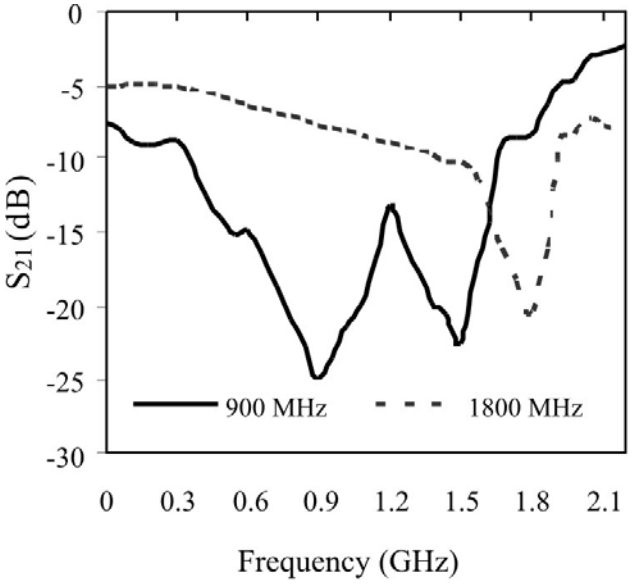

Fig.2. Modeled transmission spectra of the designed SRRS

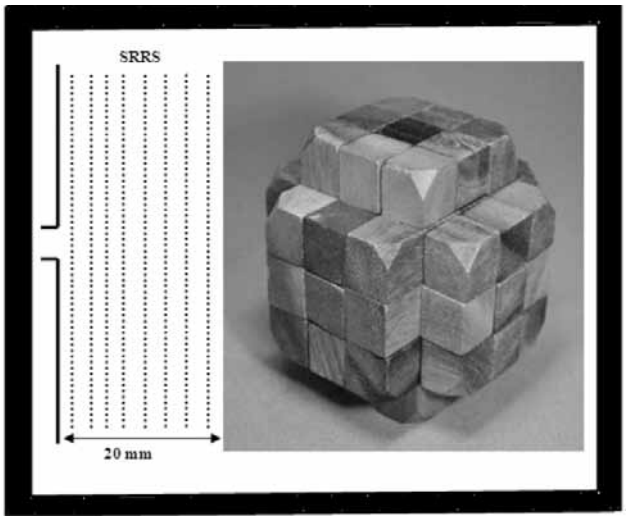

Fig. 3. Structure used in SAR calculation

To investigate the SAR distribution and antenna performance with SRRS, the power radiated from the antenna, the radiation impedance of the antenna, and the peak 1 gm averaged SAR values (SAR I gm) are analyzed. The free space radiation impedance of the antenna, in the absence of the SRRS and the muscle cube, is Z_{RO}. As in /7/, to evaluate the power radiated from the antenna, the source impedance (Zs) has been assumed equal to the complex conjugate of the free space radiation impedance (Z_S=Z_{Ro}). The source voltage (Vs) is chosen to obtain a radiated power P_R in free space ($V_S = \sqrt{P_R \times 8 \times R_{Ro}}$). When analyzing the influence of the metamaterials to the radiated power from the antenna, the source impedance and the source voltage are considered fixed at the Zs and Vs values. The power radiated from the antenna is evaluated by computing the radiation impedance in this situation (Z_R=R_R+ jX_R) and using the following equations:

$$P_R = \frac{1}{2} v_S^2 \frac{R_R}{|Z_R + Z_S|^2} \quad (2)$$

Table 1: Effects of srrs on the antenna performance

	900 MHz		1800 MHz	
	Without SRRS	With SRRS	Without SRRS	With SRRS
Z_R	49.48+ j48.81	37.32+ j42.94	61.81+ j85.86	81.63 + j93.94
P_R	600 mW	523.4 mW	125 mW	116.7 mW

The effects of SRRS on the performance of the antenna are studied. The radiation impedance and radiated power are given in Table I and compared with the results without SRRS placed between the antenna and the muscle cube. The free space radiation impedance is 49.48 + j48.81 Ω at 900 MHz. The source impedance is set to be 49.48 + j48.81 Ω and the amplitude of source voltage 21.25 V has been assumed to obtain a radiated power 600 mW in free space. The radiation impedance Z_R changes to 37.32 + j42.94 Ω with the presence of SRRS. From eqn. (2), the radiated power from the antenna with SRRS changes to 523.4 mW. The peak SAR I gm becomes 3.62 W/kg, a reduction of 44.73% with respect to the condition without SRRS. The antenna operated at 1800 MHz is considered. The free space radiation impedance is 61.81 + j85.86 Ω. The source impedance is set to be 61.81 + j85.86 Ω and the amplitude of source voltage 8.85 V has been assumed to obtain a radiated power 125 mW in free space. The radiation impedance Z_R changes to 81.63+ j93.94 Ω with the presence of SRRS. As a result, from eqn. (2) the radiated power with SRRS changes to 116.7 mW and the peak SAR 1 gm is equal to 0.45, a reduction of 48.27% with respect to the condition without SRRS. The radiated power is less affected while the peak SAR 1 gm is reduced more significantly. As a consequence, the designed SRRS can be used to reduce the EM interaction between the antenna and the muscle cube.

The SAR distribution is compared with the value reported in /5/ for validation, as shown in Table II. The calculated peak

SAR 1 gm value is 6.73 W/kg for 900 MHz and 0.87 W/kg for 1800 MHz, when the portable telephones is placed 20 mm away from the muscle cube without a metamaterial. This SAR value is better compared with the result reported in /8/, which is 8.85 W/kg at 900 MHz and 0.97 W/kg at 1800 MHz for SAR 1 gm. The SRRS is utilized in between the antenna and muscle cube, and it is found that the simulated value of SAR 1 gm 3.62 W/kg at 900 MHz and 0.45 W/kg at 1800 MHz for SAR 1 gm respectively. The reduction about of 44.73% for 900 MHz was observed in this study when a SRRS is attached between the antenna and muscle cube for SAR 1 gm and also 48.27% for 1800 MHz respectively This SAR reduction is better than the result reported in /5/, which is 36.8% at 900 MHz and 44.3 % at 1.8 GHz for SAR 1 gm. This is achieved due to the consideration of different thickness, different antenna, different size of metamaterial, different impedance factors, different positions and it is because the electromagnetic source is being moved away from the head.

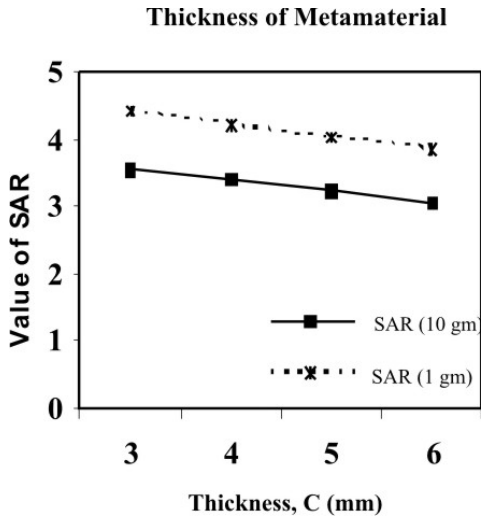

Fig.5 SAR value compared with the thickness of the metamaterial

Table 2: Comparisons of peak sar with metamaterial in a muscle cube

Tissue Type	900 MHz		1800 MHz	
	Without Metamaterial /W/kg/	With Metamaterial /W/kg/	Without Metamaterial /W/kg/	With Metamaterial /W/kg/
SAR value for /5/	8.85	5.59	0.97	0.54
SAR value with metamaterial for 1 gm	6.73	3.62	0.87	0.45

The influence of the distance, area and the thickness of the metamaterials on the SAR reduction effect are shown in Figs. 4, 5, and 6.

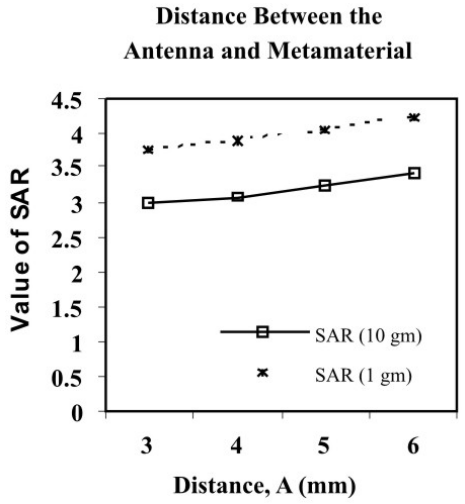

Fig. 4 SAR value compared with the distance between antenna and the metamaterial

In Fig. 4, it is shown that there is a great influence of the distance between the antenna and metamaterial on SAR reduction. If the distance between the antenna and metamaterial is increased from 3 mm to 6 mm, then the SAR value also increases from 2.9811 to 3.4112 W/kg for SAR 10 gm and 3.7505 to 4.2319 W/kg for SAR 1 gm respectively. This is because the dielectric constant, conductivity, density and magnetic tangent losses conductivity are also

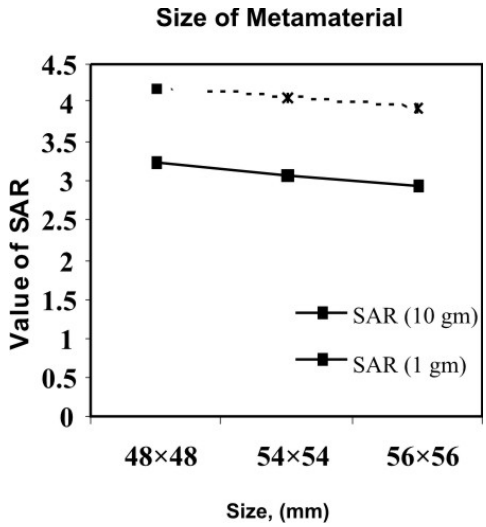

Fig.6 SAR value compared with the size of the metamaterial

varied. In Fig. 5, it can be observed that the SAR value increases with the decrease of the thickness of metamaterial. The SAR value reduces quickly when metamaterial size is large 48 mm × 48 mm to 56 mm × 56 mm then the SAR value also reduces from 3.2308 to 2.9211 W/kg for the cases of SAR 10 gm and 4.1831 to 3.9201 W/kg for SAR 1 gm as can be seen from Fig. 6.

4. Conclusion

The metamaterials has been designed to reduce SAR value in muscle cube in this paper. With properly choosing ge-

ometry parameters of SRRS, the stop band can be shifted around GSM 900 MHz and 1.8 GHz of the cellular phone. The SAR distribution in a simplified muscle tissue with the presence of SRRS is studied and a significant reduction can be obtained. The SAR value with metamaterial attachment for 900 MHz has been achieved of 44.73% with respect to the condition without SRRS and also SAR value has been for 1800 MHz achieved of 48.27% respectively. Numerical results can provide useful information in designing communication equipments for safety compliance.

References

/1/ International Non-Ionizing Radiation Committee of the International Radiation Protection Association, "Guidelines on Limits on exposure to radio frequency electromagnetic fields in the frequency range from 100KHz to 300GHz," Health Physics, vol.54 no. 1, pp. 115-123, 1988.

/2/ M. T. Islam, M. R. I. Faruque, and N. Misran, "*Design analysis of ferrite sheet attachment for SAR reduction in human head," Progress In Electromagnetics Research, PIER 98, pp. 191-205, 2009.*

/3/ S.I. Kwak, D.U. Sim, J.H. Kwon, and H.D. Choi, "Experimental tests of SAR reduction on mobile using EBG structures," Electron. Lett., vol. 44, no. 9, pp. 568–570, April 2008.

/4/ K. H. Chan, K. M. Chow, L. C. Fung, S. W. Leung, "Effects of using conductive materials for SAR reduction in mobile phones," *Vol. 44 no. 2, pp. 140 – 144, 2004.*

/5/ J. N. Hawang and Fu-chiarng chen. "Reduction of the peak SAR in the Human Head with Metamaterials" IEEE Trans. on antenna and propagation vol. 54 (12) 3763-3770, Dec. 2006.

/6/ J. Wang and O. Fujiwara, "FDTD computation of temperature rise in the human head for portable telephones," IEEE Trans. Microwave Theory Tech., vol. 47, no. 8, pp. 1528-1534, Aug.1999./

/7/ M. M. Sigalalas ,C. T. Chan ,K .M. Ho ,and Soukoulis, "Metallic photonic band gap materials," Phys. Rev. B.,vol.52, no.16, pp. 11744-11760.

/8/ J. B. Pendry, A. J. Holen, D. J. Robbins, and W. J. Stewart, "Magnetism from conductors and enhanced nonlinear phenomena," IEEE Trans. Microwave Theory Tech., vol. 47, no. 11, pp. 2075–2084, Nov. 1999.

/9/ D. R. Smith, D, R and Kroll, N. "Negative Refractive Index in left handed materials," phys. Rev. Lett., 85-14, 2933-2936. 2000.

Mohammad Rashed Iqbal Faruque[1],
Mohammad Tariqul Islam[2], Norbahiah Misran[1, 2]
[1]Dept. of Electrical, Electronic and Systems Engineering,
Faculty of Engineering and Built Environment,
Universiti Kebangsaan Malaysia, 43600 UKM,
Bangi, Selangor, Malaysia.
[2]Institute of Space Science (ANGKASA),
Universiti Kebangsaan Malaysia, 43600 UKM,
Bangi, Selangor, Malaysia.
rashedgen@yahoo.com, titareq@yahoo.com,
bahiah@vlsi.eng.ukm.my

Prispelo: 10.05.2010 *Sprejeto: 23.08.2011*

PERFORMANCES AND LIMITATIONS OF UNSLOTTED CSMA/CA MEDIA ACCESS IN IEEE 802.15.4 NETWORKS

Žarko F. Čučej

University of Maribor, Slovenia

Key words: wireless sensor network, standard IEEE 802.15.4, media access control, modeling, simulation

Abstract: Standard IEEE 802.15.4 offers three topology types and two channel access modes: slotted and unslotted CSMA/CA. The majority of a research work targets the performance of the slotted CSMA, despite the fact that wireless sensor networks are, by nature, intended to be multi-hop networks, where unslotted CSMA is the preferred media access control. This article analyzes the performance and limitations of the slotted CSMA channel access mechanism found in IEEE 802.15.4 devices. For this purpose, we have developed a model of a wireless sensor network node for the simulation-program OPNET.

Zmogljivosti in omejitve mehanizma dostopa do medija CSMA/CD brez rež v omrežjih IEEE 802.15.4

Kjučne besede: brezžična senzorska omrežja, standard IEEE 802.15.4, dostop do prenosnega medija, modeliranje, simulacije

Izvleček: Standard IEEE 802.15.4 določa tri topologije povezav omrežij in dva načina dostopa do prenosnega medija: CSMA/CA v definiranih režah in CSMA/CA v poljubnem času. Glavnina raziskav je usmerjena v mehanizme dostopa, ki so lahko aktivni le znotraj definiranih in med uporabniki omrežja sinhroniziranimi časovnimi intervali – režami, čeprav je dejstvo, da so brezžična radijska omrežja po naravi namenjena več-etapnemu prometu, kateremu je inherentna lastnost svobodni dostop do medija brez omejevanja s časovnimi režami.

V članku analiziramo zmogljivosti in omejitve dostopa do prenosnega medija brez organizacije časovnih rež, kot ga določa standard IEEE 802.15.4. V ta namen smo za simulacijski program OPNET razvili simulacijski model vozlišča v brezžičnem senzorskem omrežju.

1. Introduction

Wireless Sensor Networks (WSN) have two main advantages over wired networks:

1. the nodes can be mobile, and
2. they can be simply deployed in areas of interest, and at low-cost.

Both advantages require the following from network nodes: sensors with the ability to communicate with each other or with some central station. Their radio signals, on the one hand should have an autonomous energy source able to provide long-term sensor operations without maintenance, and on the other hand, have the capability of self-organization within the network.

A typical WSN consists of a large number, even a few thousand, nodes equipped with different types of sensors, microprocessors, radio transceivers etc, with goal of collecting measured data by sensors and transferring it through one or more data sinks, called User Access Point (UAP) or a Base Station (BS), to the end users of WSN services. The random-deployment of sensors, for example in battlefields or in plantations, usually means that the positions of the nodes are neither known exactly nor accessible for maintenance and local administration. Consequently, they should have the capabilities for self-organization on an ad-hoc multi-hop network fashion where, under normal working circumstances, the majority of traffic flows towards BS /1/

Within the implementation of WSN, the standard IEEE 802.15.4 developed by a working group for Wireless Personal Area Network (WPAN) /2/, is very popular. For example, the ZigBee alliance /3/ built their wireless sensor network solution on top of the 802.15.4 standard, which they used for the physical and medium access layer. ZigBee found its application area within home automation, plantations monitoring, health care, etc and even in the military field, where it is used, for example, for remote battlefield and Base-Camps, where surveillance became simpler and possible using wireless technology /4/. ZigBee's current focus is on defining a general-purpose, inexpensive, self-organizing mesh network that can be used for industrial control, embedded sensing, medical data collection, smoke and intruder warning systems, building automation, home automation, etc. The resulting network use very small amounts of power – individual devices would have to have a battery life of at least two years to pass ZigBee certification.

This article evaluates the multihop properties of the IEEE 802.15.4 standard through simulations in OPNET, using our own simulation model (SPaRCMosquitoModel), based on a WSN node prototype named SPaRCMosquito.

2. Standard IEEE 802.15.4

The IEEE 802.15.4-2003 Low-Rate Wireless Personal Area Network (WPAN) standard specifies the lower protocol layers: the physical layer (PHY), and the media access

control (MAC) portion of the data link layer (DLL). This standard specifies operations within the unlicensed 2,4 GHz (worldwide), 915 MHz (Americas), and 868 MHz (Europe) industrial, scientific, and medical (ISM) bands, where is defined 16, 10 and one channel, respectively. Channel bandwidth is 5 MHz. The raw, over-the-air data rate is 250 kb/s per channel in the 2,4 GHz band, 40 kb/s per channel in the 915 MHz, and 20 kb/s in the 868 MHz band. The transmission range is between 10 and 75 meters, and the output power of the radios is generally 0 dBm (1 mW) /5/.

The basic channel access mode is Carrier Sense, Multiple Access/Collision Avoidance" (CSMA/CA) channel access /6/. Their usage depends on their operating modes: beacon and non-beacon modes. In the beacon mode network, the coordinator creates a beacon message, called super frame, on which every client node is synchronized /5/. Super frame (Fig. 1) is divided on two types of slots and on an inactive period /2/.

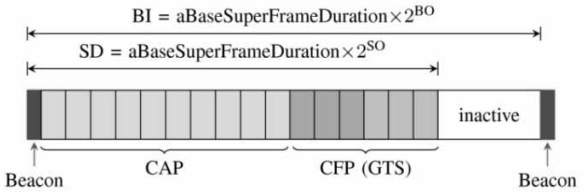

Legend:

CAP	Contention Access Period	BO/ SO	Beacon/Superframe Order
CFP	Contention Free Period	BI	Beacon Interval
GTS	Guaranteed Time Slots	SD	Superframe Duration

Fig. 1: Slotted CSMA/CA media access algorithm.

The first ten slots after beacon form so-called Contention Access Period (CAP), where the client uses a slotted CSMA/CA media access mechanism, which is similar to slotted Aloha media access control. CAP follows the Contention Free Period which, by definition, does not use CSMA. The same is valid for the beacon, which doesn't use any media access mechanism.

A. Non-beacon mode

The beacon mode is inappropriate for the multi-hop network, even though there are some scheduling techniques which propose the use of beacon mode in multi-hop networks /7/. The non-beacon mode standard specifies the use of unslotted CSMA/CA access mechanism (Fig. 2.)

Which, due to the specifics of WSN, differs from other IEEE 802.11x CSMA/CA mechanisms.

B. Non-beacon mode

The unslotted CSMA/CA mechanism uses random back-off time before sampling the channel (CCA). If the channel is found to be idle the node transmits data, otherwise it

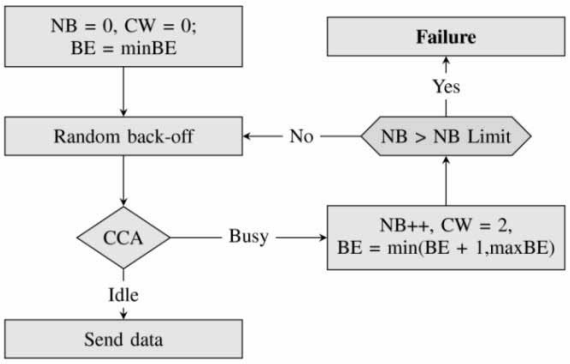

Fig. 2: Unslotted CSMA/CA media access control procedure. NB: Number of Backoffs, BE: Backoff Exponent, CW: Contention Window, CCA: Clear Channel Assessment.

repeats the back-off sequence until the channel is idle (or NB > NB Limit, see Fig. 2). The longest time to be channel accessed when channels is in the idle state considering initial back-off period and CCA sampling can be calculated as:

$$\text{backoff} + \text{CCA} = (2^3 - 1)\cdot\text{UBP} + \text{CCA} = 3{,}768 \text{ ms} \quad (1)$$

where CCA is defined as eight modulation symbol periods, and UBP (Unit Backoff Period) as 20 modulation symbol periods. A length of one modulation symbol period is determined by QPSK modulation and its duration is 1250 kHz = 16 micro second.

The IEEE 802.15.4 standard specifies a 127 bytes long MAC frame (data + header). Standard header is 25 bytes long. When using short addressing field (16 bits), the overhead is reduced to 13 bytes, leaving 114 bytes to payload /2/. Considering five bytes for Start of Frame Delimiter (SFD), one byte for data length (LEN) and MAC frame length, the duration of PHY frame is:

$$\frac{MACframe + \text{SFD} + \text{LEN}}{250\times10^3} = \frac{(127+5+1)8}{250\times10^3} = 4{,}256 \text{ ms} \quad (2)$$

Minimum time of MCU used for process the data is called turnaround time (TAT). In 802.15.4 standard the TAT is 0,192 ms. Inter frame separation period depends on PHY frame length. When sending frames shorter than 18 bytes, the short IFS (SIFS) is used (the length of SIFS is period of 12 symbols), and when frames are longer, the long IFS (LIFS) is used (the length of LIFS is period of 40 symbols). Acknowledge frame in IEEE 802.15.4 is 11 bytes in length and needs 0,352 ms of time to be send. Of course ACK duration of waiting period must be considered – normally it should not exceed 0,864 ms.

In the worst case scenario for traffic throughput all above elements should be considered when sending one frame. Without using ACK communications, which doesn't use CSMA/CA media access, the total time for sending one frame is around 6,816 ms, giving effective data rate approximately 133,8 kb/s, and with ACK communication this time is around 8,032 ms giving effective rate approximately 113,6 kb/s.

C. Open issues in non-beacon mode

The IEEE 802.15.4 faces with two significant problems, the both already known from 802.11x standard: hidden node and expose node problems.

The hidden-node problem is, in practice, solved with RTS/CTS frames /8/ in both networks 802.11x and 802.15.4 /9/, /10/. Some previous simulations stated that nearly 35 % of all traffic represents the control RTS/CTS packets /9/, /11/. On the other hand, without RTS/CTS packets, the network falls into congestion and only a low percentage of actual data is transmitted /9/, /11/.

In the case of the RTS/CTS frame usage channel saturation is about 48 % of the channels capability (120 kb/s). The use of RTS/CTS packets solves the hidden node problem, but the exposed node problem remain unresolved /9/ - /11/.

IEEE 802.15.4 does not consider any protocol or solution for either the hidden-node problem or the exposed-node problem.

3. Node model for OPNET

The OPNET model named "SPaRCMosquitoModel`` has been developed from a physical wireless sensor node, designed and created in the SpaRC[1] laboratory (Fig. 3).

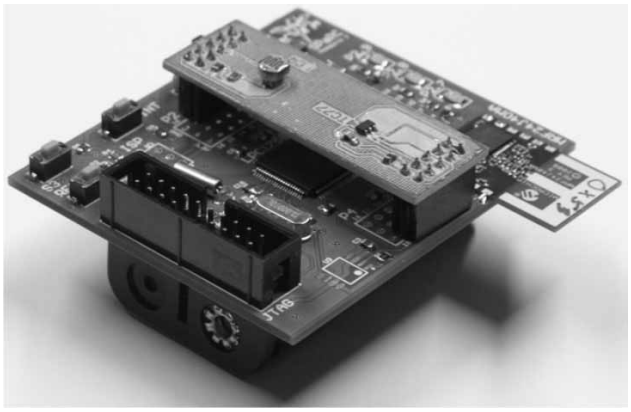

Fig. 3: WSN node SPaRCMosquito.

Calculations in simulations are based on real hardware data. Power consumption in simulations is calculated from measurements of real power consumption of the radio module MRF24J40 and CC2420, Cortex MCU, memory and integrated interface circuits. The figure 4 shows selection of data for simulation considering exact parameters as stated in data sheets.

The OPNET node model implements Physical layer, MAC layer with CSMA/CA access mechanism, routing and topology layers, a dispatcher and a data layer with source and sink processes at the top. The independent Battery process serves for separate calculation of power consumptions for CPU, sensors, and radio (Fig. 5).

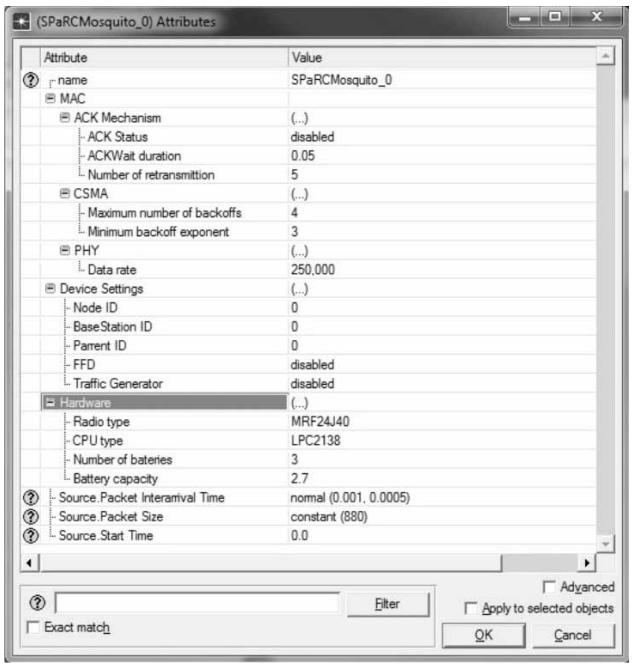

Fig. 4: Parameter selections for SPaRCMosquito OPNET model.

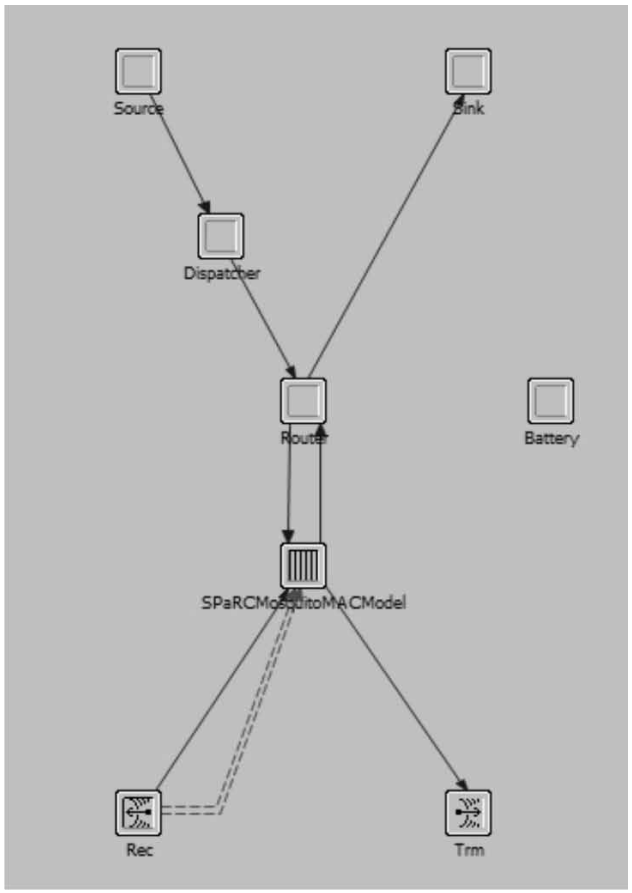

Fig. 5: Parameter selections for SPaRCMosquito OPNET model.

The source process is the data generator. Data is generated based on packet inter-arrival time and size selected in

1 *Laboratory for Signal Processing and Remote Control, \http://sparc.feri.uni-mb.si/*

node Attributes windows (Fig: 4). When created, the data packet is sent to the dispatcher process. The dispatcher process selects the targeted address (receiving node). In current setups around 95 % of data is sent towards the base-station. The rest of a packets are sent to random nodes within the network.

The routing process adds routing information to the packet (next hop destination) and sends data to MAC process, which allocates the channel and sends the data to TX process. TX process sends the data over the "air" simulated by one from many communication channel models provided within the OPNET. Packets are received in MAC process via the RX process. The consistency of a packet is done during the MAC process (CRC is checked, packet types and addresses are examined). If the packet is consistent then it is forwarded to the routing process. Inconsistent packets, ACK packets, and others are dropped in the MAC layer. The routing-process checks if the frame destination address is equal to node address. If it is, sends the data to the sink module, otherwise it calculates the next hop address and sends the data to MAC process, where it is treated like every other data packet.

The most important process for our simulation purposes is the "SPaRCMosquitoMACModel" (MAC model) – the model that implements CSMA-CA channel access. The SPaRCMosquitoMACModel (Fig. 6) is, as

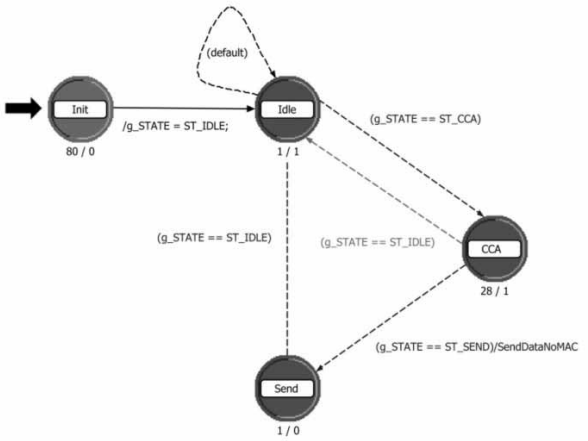

Fig. 6: SPaRCMosquitoMACModel process.

All others process models in OPNET based on the "state machine concept`` . In the idle state (Fig. 6), MAC process waits for the data from upper Network layer (from Routing process) or from lower Physical layer (from RX process).

If the data is passed from the upper layer, the model queues the data and starts the transmit protocol. The transmit protocol is based on a media accessed control procedure (Fig. 2). CCA scan duration is then simulated. During simulation, only two CCA samples are made: at the start and at the end of a CCA procedure which is 8 symbol-periods in length. If the medium is found to be idle, the data is sent. Alternatively, a new back-off duration is calculated and CCA sampling is repeated (Fig.2).

4. Network analysis by simulation in OPNET

For testing IEEE 802.15.4 throughput by simulations in OPNET the three scenarios were created:

1. scenario of the calculation for the worst case traffic throughput,
2. the traffic in the star topology (Fig. 7a), and
3. the traffic with 7 nodes creating a 6 hop network (Fig. 7b).

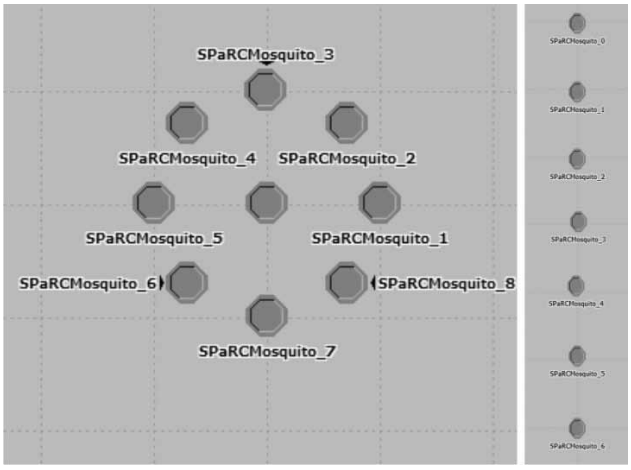

Fig. 7: SPaRCMosquitoMACModel process.

Traffic generators in the simulation scenario use normal distribution for packet inter-arrival times. Two parameters can be changed: mean outcome, defining the base time for data creation, and variance, defining the scattering. If, for example, the mean outcome is set at 0,5 and the variation to 0,1, a packet will be generated every 0,5 s within a possible variation of 0,1 s. Inversing the mean outcome give us the number of packets per second (mean outcome 0.5 means 2 packets/second), and vice-versa.

A. Throughput between two nodes

A comparison of the calculated results for the worst case scenario as it is described in subsection II-B with simulation of "real-life`` traffic with Gaussian pdf shows that simulation results give approximately 10 % to 20 % better throughput (Tab. 1).

Tabela 1: Comparison of computed worst case throughput and simulated average throughput between two nodes.

Traffic	calculated	simulated
non-ACK communication	~133,8 kb/s	155 kb/s
ACK	111 kb/s	~130 kb/s

This is expected results since the CSMA/CA mechanism implemented in ZigBee is accommodated for sparse traffic. Consequently calculated worst case throughput is actually upper bound for guaranteed utilization of raw channel capacity. Maximal throughput is obtained, when backoff

time is zero. In this case, as follows from calculation, the maximal throughput is approximately two times higher as at worst case scenario. Consequently, randomly generated traffic, obeying Gaussian pdf, should be clos to worst case scenario.

B. Single-hop network

Four single hop simulation groups were prepared: net-work with No-Acknowledgement and Acknowledgement settings simulated with two different node transmitting powers. Packets are generated on every node except base station in the middle of a circle (Fig. 7a). Packet generation is done via normal distribution with mean-value as the inverse number of packets per second and variation as half of the mean-value (Fig: 8).

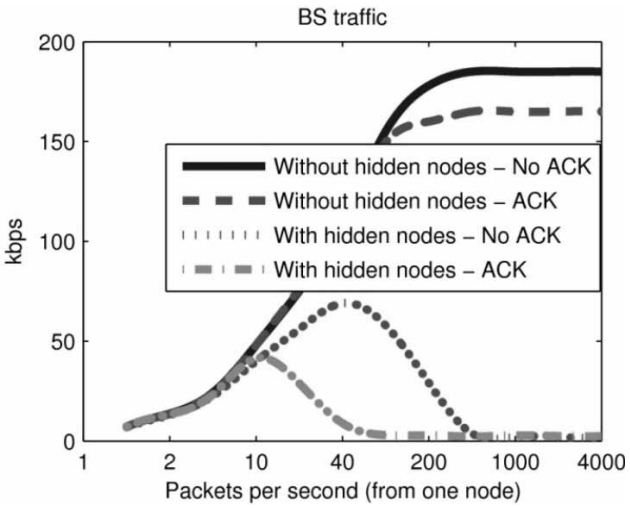

Fig. 8: Channel saturation.

In the first two simulations all nodes are in the same collision domain – no hidden nodes are present. The second simulation involves hidden nodes. This is accomplished by the selection of a transmission power, which enables 66,7 % of nodes to be visible to each other, and 33,3 % nodes to be hidden from certain nodes.

When considering the graphs (Fig. 4) it can be seen that without the hidden nodes' presence, the network throughput grows and stays saturated. The saturation limit for networks is acknowledged to be expectedly lower, as shown in Fig. 4 – acknowledgement frames must be sent from the receiver to the sender.

When dealing with hidden nodes, it can be seen that throughput rises to the point of maximum traffic still allowed and then drastically falls to a few received packets per second. Of course, the traffic with no acknowledges is again more successful. Sending ACK packets increases the chance of collision during the data send.

C. Multi-hop network

No-Acknowledge traffic setting was selected for multi-hop communication. The transmitting power was reduced to the levels can only hear the next node in chain (in scenario simulation radio sight was limited to 510 m; nodes were 500 m apart).

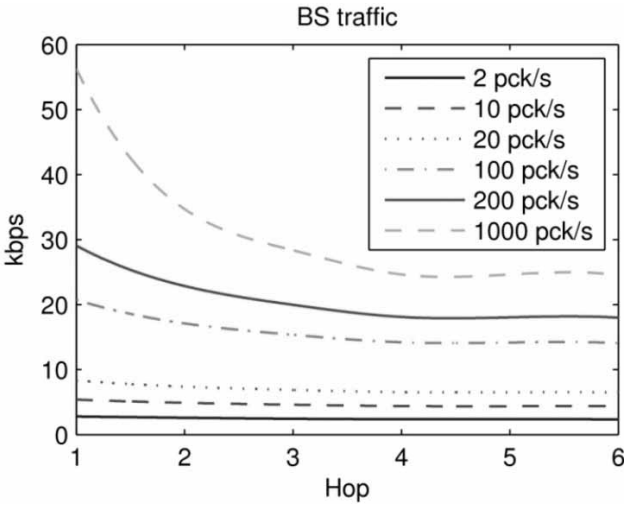

Fig. 9: Multihop saturation.

Packets were generated in the same manner as in the single-hop simulation (via normal distribution with mean value as the inverse number of packets per second, and variation as half of the mean-value) only on the last node in the chain (Fig. 3b.: SPaRCMosquito_6). Other nodes only resent data towards the base-station (Fig. 3b: SPaRCMosquito_0).

From the simulation results (Fig. 5.), it can be seen that the data rate in each hop decreases. Data rate decreasing can be clearly seen with 1000 packets/second where, in the first hop data rate drastically decreased (about 38 %), but at the last hop the decrease is hardly noticeable (2 %).

5. Conclusion

The goal of this simulation was to define the limits for data rate within IEEE 802.15.4 based networks.

IEEE 802.15.4 standards are intended for low power low data rate wireless sensor networks, meaning that sensor nodes only send a few messages per second and the upper data rate limit is never reached. Due to the lack of standardized hardware supporting higher data rates, the IEEE 802.15.4 standardized hardware is often used as PHY layer for higher data rates.

It can be assumed that IEEE 802.15.4 is intended for those networks without hidden nodes which is, in practice, very hard (or often impossible) to achieve. From the simulation point of view the data rate in channel must not exceed 40 kb/s in order to achieve stable and useful communication but, in practice, this data rate falls down to less than 20 kb/s.

Wireless sensor networks based on IEEE 802.15.4 would tend to use the minimum number of hops as possible if the

data rates are high, regardless of the energy efficiency hypothesis which claims that shorter hops provide greater energy-efficiency than a few longer jumps – when using high data rates, energy must be sacrificed at the data rate's expense.

Network traffic should be evenly distributed over the network in order to achieve better throughput and efficiency.

6. Acknowledgement

This work was financial supported by Research programs ARRS, P2-0065 "Telematics`` financed by Slovenian Ministry of Higher Education, Science and Technology.

References

/1/ H. Dai and R. Han, "A node-centric load balancing algorithm for wireless sensor networks." in Proc. of the Global Telecommunications Conference, vol. 1, San Jose, Ca, USA, January 2003, pp. 548–552.

/2/ IEEE 802.15 WPAN Task Group 4. IEEE 802.15.4. standard. /Online/. Available: http://www.ieee802.org/15/pub/TG4.html

/3/ Zigbee alliance. /Online/. Available: http://www.zigbee.org/

/4/ B. Ames, "Electronics are central to 21st century warfare tactics," Military and Aerospace Electronics, 2004.

/5/ A comprehensive simulation study of slotted CSMA/CA for IEEE 802.15.4 wireless sensor networks, 2006. /Online/. Available:http://ieeexplore.ieee.org/xpls/abs_all.jsp?arnumber=1704149

/6/ L. Kleinrock, Fouad, and A. Tobagi, "Carrier sense multiple-access modes and their throughput-delay characteristics," IEEE Trans. Comm, vol. 23, pp. 1400–1416, 1983.

/7/ B. Carballido Villaverde, R. De Paz Alberola, Rodolfo. Susan, and P. Dirk, "Experimental Evaluation of Beacon Scheduling Mechanisms for Multihop IEEE," in Proc. of the Fourth International Conference on Sensor Technologies and Applications, vol. 1, August 2010, pp. 229–234.

/8/ R. S, C. J. B, and S. D, "RTS/CTS-induced congestion in ad hoc wireless LANs," in WCNC, vol. 3, March 2003, pp. 1516–1521.

/9/ K. Benkič, "Prometno uravnoteženi usmerjevalni algoritmi za brezži˘cna senzorska omrežja," Ph.D. dissertation, Univerza v Mariboru, Fakulteta za elektrotehniko, ra˘cunalništvo in informatiko, Maribor, Slovenia, 2010.

/10/ K. P, "Maca - a new channel access method for packet radio," in ARRL/CRRL Amateur Radio 9th Computer Networking Conference, vol. ?, Lake Buena Vista, FL, USA, ? 1900, pp. 134–140.

/11/ U. Pešović, "Hidden node avoidance mechanism for IEEE 802.15.4/zigbee wireless sensor networks," Master of Science thesis, Univerza v Mariboru, Fakulteta za elektrotehniko, ra˘cunalništvo in informatiko, Maribor, Slovenia, 2009.

Žarko F. Čučej
University of Maribor, Slovenia
elektronska pošta: zarko.cucej@uni-mb.si

Prispelo: 03.01.2011 *Sprejeto: 23.08.2011*

Informacije MIDEM
Strokovna revija za mikroelektroniko, elektronske sestavine dele in materiale

NAVODILA AVTORJEM

Informacije MIDEM je znanstveno-strokovno-društvena publikacija Strokovnega društva za mikroelektroniko, elektronske sestavne dele in materiale - MIDEM. Revija objavlja prispevke s področja mikroelektronike, elektronskih sestavnih delov in materialov. Ob oddaji člankov morajo avtorji predlagati uredništvu razvrstitev dela v skladu s tipologijo za vode-nje bibliografij v okviru sistema COBISS.
Znanstveni in strokovni prispevki bodo recenzirani.

Znanstveno-strokovni prispevki morajo biti pripravljeni na naslednji način:

1. Naslov dela, imena in priimki avtorjev brez titul, imena institucij in firm
2. Ključne besede in povzetek (največ 250 besed).
3. Naslov dela v angleščini.
4. Ključne besede v angleščini (Key words) in podaljšani povzetek (Extended Abstract) v anglešcčini, če je članek napisan v slovenščini
5. Uvod, glavni del, zaključek, zahvale, dodatki in literatura v skladu z IMRAD shemo (Introduction, Methods, Results And Discsussion).
6. Polna imena in priimki avtorjev s titulami, naslovi institucij in firm, v katerih so zaposleni ter tel./Fax/Email podatki.
7. Prispevki naj bodo oblikovani enostransko na A4 stra-neh v enem stolpcu z dvojnim razmikom, velikost črk namanj 12pt. Priporočena dolžina članka je 12-15 strani brez slik.

Ostali prispevki, kot so poljudni cčlanki, aplikacijski članki, novice iz stroke, vesti iz delovnih organizacij, inštitutov in fakultet, obvestila o akcijah društva MIDEM in njegovih članov ter drugi prispevki so dobrodošli.

Ostala splošna navodila

1. V članku je potrebno uporabljati SI sistem enot oz. v oklepaju navesti alternativne enote.
2. Risbe je potrebno izdelati ali iztiskati na belem papirju. Širina risb naj bo do 7.5 oz.15 cm. Vsaka risba, tabela ali fotografija naj ima številko in podnapis, ki označuje njeno vsebino. Risb, tabel in fotografij ni potrebno lepi-ti med tekst, ampak jih je potrebno ločeno priložiti članku. V tekstu je treba označiti mesto, kjer jih je potrebno vstaviti.
3. Delo je lahko napisano in bo objavljeno v slovenščini ali v angleščini.
4. Uredniški odbor ne bo sprejel strokovnih prispevkov, ki ne bodo poslani v dveh izvodih skupaj z elektronsko verzijo prispevka na disketi ali zgoščenki v formatih ASCII ali Word for Windows. Grafične datoteke naj bodo priložene ločeno in so lahko v formatu TIFF, EPS, JPEG, VMF ali GIF.
5. Avtorji so v celoti odgovorni za vsebino objavljenega sestavka.

Rokopisov ne vračamo. Rokopise pošljite na spodnji naslov.

Uredništvo Informacije MIDEM
MIDEM pri MIKROIKS
Stegne 11, 1521 Ljubljana, Slovenia
Email: Iztok.Sorli@guest.arnes.si
tel. (01) 5133 768, fax. (01) 5133 771

Informacije MIDEM
Journal of Microelectronics, Electronic Components and Materials

INSTRUCTIONS FOR AUTHORS

Informacije MIDEM is a scientific-professional-social publication of Professional Society for Microelectronics, Electronic Components and Materials – MIDEM. In the Journal, scientific and professional contributions are published covering the field of microelectronics, electronic components and materials.
Authors should suggest to the Editorial board the classification of their contribution such as : original scientific paper, review scientific paper, professional paper…
Scientific and professional papers are subject to review.

Each scientific contribution should include the following:

1. Title of the paper, authors' names, name of the institution/ company.
2. Key Words (5-10 words) and Abstract (200-250 words), stating how the work advances state of the art in the field.
3. Introduction, main text, conclusion, acknowledgements, appendix and references following the IMRAD scheme (Introduction, Methods, Results And Discsussion).
4. Full authors' names, titles and complete company/institution address, including Tel./Fax/Email.
5. Manuscripts should be typed double-spaced on one side of A4 page format in font size 12pt. Recommended length of manuscript (figures not included) is 12-15 pages
6. Slovene authors writing in English language must submit title, key words and abstract also in Slovene language.
7. Authors writing in Slovene language must submit title, key words and extended abstract (500-700 words) also in English language.

Other types of contributions such as popular papers, application papers, scientific news, news from companies, institutes and universities, reports on actions of MIDEM Society and its members as well as other relevant contributions, of appropriate length , are also welcome.

General informations

1. Authors should use SI units and provide alternative units in parentheses wherever necessary.
2. Illustrations should be in black on white paper. Their width should be up to 7.5 or 15 cm. Each illustration, table or photograph should be numbered and with legend added. Illustrations, tables and photographs must not be included in the text but added separately. However, their position in the text should be clearly marked.
3. Contributions may be written and will be published in Slovene or English language.
4. Authors must send two hard copies of the complete contributon, together with all files on diskette or CD, in ASCII or Word for Windows format. Graphic files must be added separately and may be in TIFF, EPS, JPEG, VMF or GIF format.
5. Authors are fully responsible for the content of the paper.

Contributions are to be sent to the address below.

Uredništvo Informacije MIDEM
MIDEM pri MIKROIKS
Stegne 11, 1521 Ljubljana, Slovenia
Email: Iztok.Sorli@guest.arnes.si
tel.+386 1 5133 768, fax.+386 1 5133 771

MIDEM
DRUŠTVO-SOCIETY
Slovenia Chapter

M I D E M

Strokovno društvo za mikroelektroniko,
elektronske sestavne dele in materiale
MIDEM pri MIKROIKS
Stegne 11, 1521 Ljubljana
SLOVENIJA

TEL.: +386 (0)1 5133 768
FAX: +386 (0)1 5133 771
Email / WWW
iztok.sorli@guest.arnes.si
http://paris.fe.uni-lj.si/midem/

MIDEM SOCIETY REGISTRATION FORM

1. First Name .....Last Name.....

   Adress .....

   City .....

   Country .....Postal Code .....

2. Date of Birth .....

3. Education (please, circle whichever appropriate)

   PhD MSc BSc High School Student

3. Profession (please, circle whichever appropriate)

   Electronics Physics Chemistry Metallurgy Material Sc.

4. Company .....

   Adress .....

   City .....

   Country .....Postal Code .....

   Tel.: .....FAX: .....

   Email .....

5. Your Primary Job Function

   Fabrication Engineering Facilities QA/QC
   Management Purchasing Consulting Other

6. Please, send mail to a) Company adress b) Home Adress

7. I wil regularly pay MIDEM membership fee, 25,00 EUR/year

MIDEM member recive Journal "Informacije MIDEM" for free !!!

Signature .....Date .....

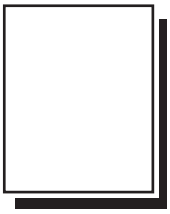

MIDEM at MIKROIKS
Stegne 11

1521 Ljubljana
Slovenija

ORGANI DRUŠTVA MIDEM - BOARDS OF MIDEM

Predsednik društva MIDEM
MIDEM President

Prof. dr. Marko Topič, univ. dipl. inž. el., UL Fakulteta za elektrotehniko, Ljubljana, Slovenija

IZVRŠILNI ODBOR MIDEM - MIDEM EXECUTIVE BOARD

Podpredsednika
Vice-presidents

Prof. dr. Barbara Malič, univ. dipl. kem., Institut Jožef Stefan, Ljubljana, Slovenija
Dr. Iztok Šorli, univ. dipl. inž. fiz., MIKROIKS, d. o. o., Ljubljana, Slovenija

Tajnik
Secretary

Igor Pompe, univ. dipl. inž. el., Ljubljana, Slovenija

Člani izvršilnega odbora MIDEM
Executive Board Members

Prof. dr. Janez Trontelj, univ. dipl. inž. el., UL Fakulteta za elektrotehniko, Ljubljana, Slovenija, blagajnik
Darko Belavič, univ. dipl. inž. el., HIPOPT-RR, d.o.o., Šentjernej, Slovenija
Prof. dr. Bruno Cvikl, univ. dipl. fiz., UM Fakulteta za gradbeništvo, Maribor, Slovenija
Leopold Knez, univ. dipl. inž. el., Iskra TELA d.d., Ljubljana, Slovenija
Dr. Miloš Komac, univ. dipl. kem., UL Fakulteta za kemijo in kemijsko tehnologijo, Ljubljana, Slovenija
Jožef Perne, univ. dipl. inž. el., Zavod TC SEMTO, Ljubljana, Slovenija
Prof. dr. Slavko Amon, univ. dipl. fiz.; UL Fakulteta za elektrotehniko, Ljubljana, Slovenija
Prof. dr. Miran Mozetič, univ. dipl. fiz. , Institut Jožef Stefan, Ljubljana, Slovenija
Prof. dr. Marija Kosec, univ. dipl. kem., Institut Jožef Stefan, Ljubljana, Slovenija
Dr. Werner Reczek, Infineon AG, Austrija
Prof. dr. Giorgio Pignatel, University of Perugia, Italija
Prof. dr. Leszek J. Golonka, Technical University, Wroclaw, Poljska

Nadzorni odbor
Supervisory Board

Prof. dr. Franc Smole, univ. dipl. inž. el., Fakulteta za elektrotehniko, Ljubljana
Mag. Andrej Pirih, univ. dipl. inž. el., Iskra - Zaščite, d. o. o. , Ljubljana
Dr. Slavko Bernik, univ. dipl. inž. kem., Institut "Jožef Stefan", Ljubljana

Častno razsodišče
Court of Honour

Zasl. prof.dr. Jože Furlan, univ. dipl. inž. el.,Ljubljana, Slovenija
Prof. dr. Radko Osredkar, univ. dipl. inž. el., UL Fakulteta računalništvo in informatiko, Ljubljana
Franc Jan, univ. dipl. fiz., Kranj, Slovenija

Sponzorji MIDEM

MIDEM Sponsors

JAVNA AGENCIJA ZA RAZISKOVALNO DEJAVNOST RS, Ljubljana

INSTITUT "JOŽEF STEFAN", Odsek za elektronsko keramiko, Ljubljana

FAKULTETA ZA ELEKTROTEHNIKO - LMFE, Ljubljana

FAKULTETA ZA ELEKTROTEHNIKO - LMSE, Ljubljana

FAKULTETA ZA ELEKTROTEHNIKO - LPVO, Ljubljana

MIKROIKS, d.o.o., Ljubljana

TC SEMTO, Ljubljana

ISKRA ZAŠČITE d.o.o., Ljubljana

RLS, d.o.o., Ljubljana

Informacije MIDEM, 41(2011)3, Ljubljana, SEPTEMBER 2011, ISSN 0352-9045, UDK 621.3:(53+54+621+66)(05)(497.1)=00

Strokovna revija za mikroelektroniko, elektronske sestavne dele in materiale

Journal of Microelectronics, Electronic Components and Materials

Publikacija informacije MIDEM izhaja po ustanovitvi Strokovnega društva za mikroelektroniko, elektronske sestavne dele in materiale - MIDEM kot nova oblika publikacije Informacije SSOSD, ki jo je izdajal Zvezni strokovni odbor za elektronske sestavne dele in materiale SSOSD pri Jugoslovanski zvezi za ETAN od avgusta 1969 do 6. oktobra 1977 in publikacije Informacije SSESD, ki jo je izdajala Strokovna sekcija za elektronske sestavne dele, mikroelektroniko in materiale - SSESD pri Jugoslovanski zvezi za ETAN od 6. oktobra 1977 do 29. januarja 1986.

Časopis Informacije MIDEM je vpisan v register časopisov pri Ministrstvu za informiranje pod registrsko številko 809.